Delft University of Technology

Computational aeroacoustic approaches for wind turbine blade noise prediction

van der Velden, Wouter

DOI
10.4233/uuid:ea709745-7238-47e0-90d1-c8381fd34f39

Publication date
2017

Document Version
Final published version

Citation (APA)
van der Velden, W. (2017). *Computational aeroacoustic approaches for wind turbine blade noise prediction*. [Dissertation (TU Delft), Delft University of Technology]. https://doi.org/10.4233/uuid:ea709745-7238-47e0-90d1-c8381fd34f39

Important note
To cite this publication, please use the final published version (if applicable).
Please check the document version above.

Copyright
Other than for strictly personal use, it is not permitted to download, forward or distribute the text or part of it, without the consent of the author(s) and/or copyright holder(s), unless the work is under an open content license such as Creative Commons.

Takedown policy
Please contact us and provide details if you believe this document breaches copyrights.
We will remove access to the work immediately and investigate your claim.

This work is downloaded from Delft University of Technology.
For technical reasons the number of authors shown on this cover page is limited to a maximum of 10.

COMPUTATIONAL AEROACOUSTIC APPROACHES FOR WIND TURBINE BLADE NOISE PREDICTION

COMPUTATIONAL AEROACOUSTIC APPROACHES FOR WIND TURBINE BLADE NOISE PREDICTION

Proefschrift

ter verkrijging van de graad van doctor
aan de Technische Universiteit Delft,
op gezag van de Rector Magnificus prof. ir. K.C.A.M. Luyben,
voorzitter van het College voor Promoties,
in het openbaar te verdedigen op vrijdag 31 maart 2017 om 15:00 uur

door

Wouter Cornelis Pieter VAN DER VELDEN

Ingenieur in de Lucht- en Ruimtevaart,
Technische Universiteit Delft, Nederland,
geboren te Rotterdam, Nederland.

Dit proefschrift is goedgekeurd door de

promotor: prof. dr. ir. drs. H. Bijl
copromotor: dr. ir. A.H. van Zuijlen

Samenstelling promotiecommissie:

Rector Magnificus,	voorzitter
Prof. dr. ir. drs. H. Bijl	Technische Universiteit Delft & Universiteit Leiden
Dr. ir. A.H. van Zuijlen	Technische Universiteit Delft
Onafhankelijke leden:	
Prof. dr. P.F. Joseph	University of Southampton
Prof. dr. W.Z. Shen	Technical University of Denmark
Prof. dr. C. Schram	Von Kármán Institute
Prof. dr. D. Casalino	Technische Universiteit Delft & Exa Coorporation
Dr. ir. S. Oerlemans	Siemens Wind Power
Prof. dr. ing. F. Scarano	Technische Universiteit Delft, reservelid

Keywords: Wind turbine noise, Aeroacoustics, CAA, CFD

Printed by: Ridderprint BV, the Netherlands

Front & Back: Wouter van der Velden captured mounting serrations on a DU-96 airfoil during a wind tunnel campaign in the LTT at Delft University of Technology. Picture taken by Carlos Arce-León, modified by Darryll Atema.

Copyright © 2017 by W.C.P. van der Velden

This research is funded and supported by Siemens Wind Power A/S, Brande, Denmark.

ISBN 978-94-6186-756-8

An electronic version of this dissertation is available at
`http://repository.tudelft.nl/`.

When I'm working on a problem, I never think about beauty.
I think only how to solve the problem.
But when I have finished, if the solution is not beautiful,
I know it is wrong.

R. Buckminster Fuller

SUMMARY

HIGH fidelity computational aeroacoustic approaches have been applied in this thesis, for the purpose of predicting noise from wind turbine blades. For a large modern wind turbine, aerodynamic noise from the blades is generally considered to be the dominant noise source, provided that mechanical noise is adequately treated. Most of the aerodynamic blade noise sources, such as tip noise and blunt-trailing-edge noise, can be prevented by good design, leaving turbulent boundary layer trailing edge noise to be the dominant noise source.

This thesis demonstrates how both incompressible and compressible computational fluid dynamics solutions can be employed to obtain both qualitative and quantitative description of the aeroacoustic sources, underlying mechanism and predicted far-field acoustic pressure. Both Navier-Stokes and Lattice Boltzmann relations have been studied to obtain high fidelity flow field results. In combination with acoustic analogies, solved either as integral solution or as boundary element method, an estimation of the acoustic radiation in the far field can be obtained.

To obtain a fully developed turbulent boundary layer, both recycling and rescaling planes as well as bypass transition strips were analyzed. A staggered grid of cubic blocks for transition was analyzed and compared with a more conventional, zigzag strip using flow results from the Lattice Boltzmann method. The trips were shown to be successful to enforce transition, but the observed transition scenario suggested that a zigzag strip is more efficient as a bypass transition process compared to the staggered grid of cubes, since the spanwise vortices were undulated more effectively from the trip.

Furthermore, the prediction of the streamwise and spanwise coherence length of the pressure field below a turbulent boundary layer at low Reynolds number generated using a recycling inflow method, were estimated using different numerical large eddy simulation models in an open-source finite volume based computational fluid dynamics package. It was found that the spanwise coherence length was significantly smaller than the streamwise coherence length, indicating low amplitude structures. For both spatial directions, the decay obtained from the simulations matched the Corcos model and experimental results at intermediate and high frequencies.

Trailing edge noise has been analyzed by considering the flow around a plate with an asymmetrically beveled 25° trailing edge. Both integral and boundary element method were employed on incompressible flow data, with the latter method also predicting the scattered acoustic pressure. It was concluded that, when performing aeroacoustic computations with incompressible flow data, a scattering correction is essential to properly represent the acoustic spectra.

The flow and acoustic field around the beveled plate was further analyzed by the Lattice Boltzmann equations in combination with a Ffowcs-Williams and Hawkings aeroacoustic analogy. To validate the coupling of these computational approaches for the prediction of trailing edge noise, a comparison was made between experimental data. The flow and pressure field dynamics show similar trends and compare well for both the mean velocity field and turbulent fluctuations, while deviations of 2 dB for surface pressure spectra were found. Furthermore, the non-dimensional shedding frequency value agreed well between experiment and simulation. Broadband noise was in excellent agreement with a similar maximum deviation as for the surface pressure spectra.

Many passive mitigation strategies have been proposed to reduce trailing edge noise. In the past, using both experiments and simulations, a serrated trailing edge has been shown to be efficient in reducing this type of noise. Although serrations are now used quite often on wind turbine blades, the noise reduction mechanism is not fully understood. Therefore, in this thesis, the flow topology and noise emission around a teeth, combed teeth and straight edge configuration retrofitted on a NACA 0018 airfoil at zero angle of attack is studied in order to understand the working mechanisms of serrations. The numerical results confirmed that the combed teeth give a larger noise reduction than the standard teeth. Furthermore, the acoustic far-field results and boundary layer characteristics obtained from the simulation of the teeth configuration matched the earlier experiments. It was hypothesized that the main noise-suppression mechanism, due to the application of the combs, is the change of the angle of the streamlines. Other experimental methods, such as the analysis of boundary layer characteristics, surface pressure fluctuations, the individual segment analysis and the flow induced noise detection revealed that most noise is generated at the root of the teeth rather than the tip. It was observed that surface pressure fluctuations at low frequencies are dependent of the streamwise location. It suggested a variable intensity of the scattered pressure waves.

With that in mind, a shape optimization on the teeth has been proposed in this thesis, resulted in a iron-like geometry. The iron-like geometry reduced far field noise more of approximately 2 dB with respect to the conventional teeth geometry. The analysis of the time-averaged near-wall velocity components showed that the main effect of the proposed geometry is to mitigate both the outward and downward motion near the root of the serration. It resulted in a less strong interaction between the two sides of the airfoil at the root location and in a larger effective angle seen by the turbulent flow approaching the edges.

SAMENVATTING

GEDETAILLEERDE betrouwbare aeroakoestische benaderingen zijn toegepast in dit proefschrift, met het oog op het voorspellen van het geluid afkomstig van windturbine bladen. Voor een grote moderne windturbine wordt het aerodynamisch geluid afkomstig van de bladen gezien als de meest dominante geluidsbron, mits mechanisch geluid op gepaste wijze wordt behandeld. De meeste aerodynamische geluidsbronnen, zoals het tipgeluid of geluid door een stompe achterrand kan worden voorkomen door een goed ontwerp. Hierdoor wordt het geluid dat ontstaat door de interactie van de turbulente grenslaag en de achterrand, de belangrijkste geluidsbron.

Dit proefschrift laat zien hoe zowel onsamendrukbare als volledig samendrukbare stromingssimulaties kunnen worden gebruikt voor het verkrijgen van kwalitatieve en kwantitatieve beschrijvingen van de aeroakoestische bronnen, de onderliggende mechanismen en het voorspelde akoestische verre veldsignaal. Zowel Navier-Stokes vergelijkingen als Lattice Boltzmann vergelijkingen zijn onderzocht om een hoge betrouwbaarheid van het stromingsveld te verkrijgen. In combinatie met verschillende akoestische analogieën, opgelost als integraal oplossing of als randelementmethode, kan een schatting worden gemaakt van het gestraalde akoestische verre veld.

Om een volledig ontwikkelde turbulente grenslaag te krijgen zijn zowel recyclings- en herschaalmethoden als verschillende transitiestrips bekeken. Een raster van vierkante blokken voor transitie werd geanalyseerd en vergeleken met een conventionele, zigzagstrip met behulp van stromingsresultaten van de Lattice Boltzmann-methode. Beide transitiestrips waren succesvol om een overgang naar een turbulente grenslaag af te dwingen. Het waargenomen scenario suggereerde dat een zigzagstrip efficiënter werkt als bypasstransitieproces dan transitie met een raster van vierkante blokken, gezien het feit dat de spanwijdterichting wervels beter vermengd werden.

In een andere studie werden in stroom- en spanwijdterichting de coherentielengtes van de randdrukken voorspeld onder een turbulente grenslaag bij lage Reynolds getallen. De grenslaag was gegenereerd door een recycling instroommethode en verschillende numerieke grove structuursimulatiemodellen door middel van een open-bron, eindige volume, stromingssimulatiepakket. Het bleek dat de coherentielengte in spanwijdterichting significant kleiner was dan de coherentielengte in stromingsrichting, wat duidde op structuren met lage amplitudes. Voor beide ruimtelijke richtingen en voor middelhoge en hoge frequenties was het verval van de coherentielengte gelijk aan het model van Corcos en de experimentele resultaten.

Vervolgens is achterrandgeluid geanalyseerd door te kijken naar de stroming rond een plaat met een asymmetrische schuine achterrand van 25°. Zowel een integraal oplossing als een randelementmethode waren getest met data van een onsamendrukbare stromingssimulatie, waarbij de laatste methode tevens ook een voorspelling kan doen van het verstrooide akoestische veld. Er kon worden geconcludeerd dat wanneer berekeningen uitgevoerd werden met aeroakoestische, onsamendrukbare stromingsdata, een correctie voor de verstrooiing van het geluid noodzakelijk was om het correcte akoestische spectra weer te geven.

Verder werd de stroming en geluid rond de afgeschuinde plaat bekeken door middel van de Lattice Boltzmann vergelijkingen in combinatie met een Ffowcs-Williams-Hawking afgeleide aeroakoestische analogie. De koppeling van deze twee methodes werd gebruikt voor het voorspellen en valideren van het achterrandgeluid tegen experimentele data. Het stromingsveld en drukveld vertoonden gelijkwaardige trends met de experimenten, en toonden nauwe overeenkomsten voor zowel de gemiddelde snelheid als de turbulente fluctuaties. Een maximum afwijking van 2 dB werd gevonden voor de spectra van de wanddrukken, terwijl de dimensieloze frequentiewaarde van de afscheiding van wervelingen goed overeenkwam tussen experiment en simulatie. De vergelijking van het breedbandgeluid was uitstekend, met een maximale afwijking overeenkomstig met het resultaat van de wanddrukken.

Veel passieve mitigatiestrategieën zijn voorgesteld om achterrandgeluid te reduceren. In het verleden hebben zowel experimenten als simulaties aangetoond dat een getande achterrand efficiënt kan zijn in het verminderen van achterrandgeluid. Hoewel zaagtanden nu vaak gebruikt worden op windturbinebladen wordt het exacte mechanisme van de geluidsonderdrukking nog niet volledig begrepen. Vandaar dat in dit proefschrift de stroming en geluidsemissie rond zaagtanden, gekamde zaagtanden en een rechte achterrand configuratie gemonteerd op een NACA 0018 vleugelprofiel onder een invalshoek van nul graden zijn bestudeerd om achter de werking van het reductiemechanisme te komen. De numerieke resultaten bevestigden dat de gekamde zaagtanden een grotere geluidsreductie geven in vergelijking met de standaard zaagtanden. Bovendien komen de akoestische verre veldresultaten en de grenslaageigenschappen van de conventionele zaagtand nauw overeen met data verkregen uit eerdere experimenten. De resultaten suggereerden dat het belangrijkste geluidonderdrukking mechanisme, door toepassing van de kammen tussen de zaagtanden, de verandering van de hoek van de stroomlijnen is. Uit andere methoden van experimentele aard, zoals de analyse van de grenslaageigenschappen, het onderzoek naar de oppervlakte drukfluctuaties, de individuele segmentanalyse en de stromingsgeïnduceerde geluidsdetectiemethode kon worden geconcludeerd dat het meeste geluid werd gegenereerd tussen de basis van de zaagtanden in plaats van de tip van de tand. Er werd waargenomen dat bij lage frequenties de druk fluctuaties afhankelijk zijn in de stromingsrichting. Dit suggereert een variabele intensiteit van de verstrooide drukgolven.

Met dit in het achterhoofd is er in dit proefschrift een optimalisatie van de zaagtand voorgesteld, die veel weg heeft van de vorm van een strijkijzer. De strijkijzergeometrie verhoogt de geluidsreductie met ongeveer 2 dB vergeleken met een conventionele zaagtand. Uit onderzoek van de tijdsgemiddelde snelheidscomponenten bij de wand is gebleken dat het hoofdeffect van de voorgestelde geometrie de vermindering van zowel de heen- als neerwaartse beweging bij de basis van de vertanding is. Dit resulteerde in een minder sterke interactie tussen beide zijden van het aerodynamisch profiel bij de basis van de vertanding en in een grotere, meer efficiëntere, hoek van de stroomlijnen bij de randen van de geometrie.

VOORWOORD

It always seems impossible until it's done

Nelson Mandela

Soms lijken dingen inderdaad eindeloos, maar het is gelukt; voor u ligt mijn proefschrift ter verkrijging van de graad van doctor. Na wat voelt als vier korte jaren, ben ik trots op wat er is behaald.

Mijn dank gaat daarom ook uit naar Hester Bijl en Alexander van Zuijlen, respectievelijk mijn promotor en copromotor tijdens vrijwel mijn hele academische leven. Het was een uitdagende tijd waarin ik heel veel van jullie hebt kunnen leren. Dank voor alle tijd die jullie met mij en mijn onderzoek hebben beziggehouden.

Ik wil graag Siemens Wind Power bedanken voor alle middelen waarmee zij mijn PhD-project gesteund hebben. Kennis en expertise op gebied van aeroakoestiek kwam van Stefan Oerlemans. Ook zonder de financiële ondersteuning afgelopen jaren zou mijn proefschrift niet kunnen zijn wat het nu is.

Tot slot, als allerbelangrijkste, wil ik mijn familie bedanken voor de volledige en altijd aanwezige ondersteuning, zorg en liefde. Laten we niet vergeten dat mijn ouders, Cees en Anne, mij hier gebracht hebben. Tot op de dag van vandaag heb ik altijd op ze kunnen rekenen en ik weet dat het in de toekomst ook zo zal zijn, ongeacht waar ik heen ga en beland. Bedankt Wijnand en Willemijn dat ik jullie grote broer mag zijn, en ik wens jullie ook voorspoed in jullie academisch leven. Mama en papa zijn nu al trots op ons!

WCPvdVelden

Wouter Cornelis Pieter van der Velden
Delft, December 2016

CONTENTS

Summary **vii**

Samenvatting **ix**

Voorwoord **xi**

Prologue **1**

1 Introduction **3**

1.1 Wind energy and noise nuisance . . . 4
1.2 Sources of wind turbine noise. . . . 4
1.3 Airfoil noise 4
  1.3.1 Inflow turbulence noise 6
  1.3.2 Laminar boundary layer instability noise 6
  1.3.3 Turbulent boundary layer trailing edge noise 6
  1.3.4 Trailing edge bluntness noise 7
  1.3.5 Separation and stall noise 7
  1.3.6 Tip noise 7
1.4 Characteristics of trailing edge noise 7
1.5 Measurement and prediction 10
  1.5.1 Wind tunnel experiments 10
  1.5.2 Field measurements 11
1.6 Computational aeroacoustics 11
  1.6.1 Flow source field 13
  1.6.2 Direct methods 13
  1.6.3 Hybrid methods 14
1.7 Reduction of wind turbine noise 17
1.8 Motivation and objectives. 18
1.9 Outline of the thesis. 19

I Turbulent boundary layer **21**

2 Physical modeling of bypass transition strips **23**

2.1 Introduction 24
2.2 Methodology 25
2.3 Case setup 26
2.4 Result and discussion 28
  2.4.1 Bypass transition process 28
  2.4.2 Downstream development of the boundary layer 33
2.5 Conclusion 37

3 Pressure coherence under a turbulent boundary layer **39**
3.1 Introduction 40
3.2 Methodology 40
3.2.1 Governing fluid equations 40
3.2.2 Sub grid scale models 41
3.2.3 Recycling method 42
3.2.4 Definition and estimation of coherence 42
3.3 Model set-up 43
3.4 Results 44
3.4.1 Mean velocity and Reynolds stresses 44
3.4.2 Wall pressure spectrum and coherence 46
3.5 Conclusion 50

II Trailing edge noise **53**

4 Non-compactness using incompressible flow data **55**
4.1 Introduction 56
4.2 Methodology 57
4.2.1 Source field flow simulation 57
4.2.2 Acoustic analogy 58
4.3 Test case 59
4.4 Results and discussion 60
4.4.1 Flow field 60
4.4.2 Acoustic emission 61
4.5 Conclusion 64

5 Beveled trailing edge flow field and noise emission **65**
5.1 Introduction 66
5.2 Measurement and simulation 68
5.2.1 Test case 68
5.2.2 Experimental set-up 69
5.2.3 Numerical simulation 71
5.3 Results and discussion 75
5.3.1 Flow field 75
5.3.2 Unsteady surface pressure measurements 79
5.3.3 Acoustic emission 80
5.4 Conclusion 84

III Noise suppression add-ons **89**

6 Noise reduction mechanisms of serrated trailing edges **91**
6.1 Introduction 92
6.2 Computational methodology 94
6.2.1 Flow source field 94
6.2.2 Acoustic prediction 96
6.2.3 Noise source detection 97

6.3 Computational setup and test cases. 98
6.4 Results 100
6.4.1 Boundary layer development over the airfoil. 100
6.4.2 Noise emission and directivity 100
6.4.3 Mean flow over the serrated edge 106
6.4.4 Boundary layer characteristics over the serrated edge 106
6.4.5 Surface pressure fluctuations 109
6.4.6 Convection velocity over edge 112
6.4.7 Spanwise coherence 113
6.4.8 Source detection and localization 115
6.5 Conclusion 119

7 Shape optimization of serrated trailing edges 121
7.1 Introduction 122
7.2 Methodology and solver 123
7.3 Computational test-case 124
7.4 Results 127
7.4.1 Far field noise 127
7.4.2 Mean and turbulent flow features 130
7.4.3 Wall-pressure fluctuations 131
7.4.4 Detection of noise source 134
7.5 Conclusions. 135

Epilogue 137

8 Conclusion 139
8.1 Introduction 140
8.2 Turbulent boundary layer. 140
8.3 Trailing edge noise 141
8.4 Noise suppression add-ons 143
8.5 Recommendations 144

References 147

Appendix 161

A Variables for acoustics 163

B Sampling for aeroacoustics 165

C Statistical data analysis 167

Acknowledgements 171

Curriculum Vitæ 175

List of Publications 177

PROLOGUE

1

INTRODUCTION

The thesis must be an original work of the candidate.

PhD Examination Regulations, Delft University of Technology

There is nothing new under the sun.

Ecclesiastes

As wind is a clean and inexhaustible source of energy, a tremendous growth of the application of wind energy is seen in the past decades. However, as the noise from wind turbines, and in particular trailing edge noise, constitutes an important hindrance to the environment, efficient tools and methodology for the prediction of trailing edge noise gained substantial interest within the wind turbine industry. To provide a solution for complex flow problems and acoustic prediction, computational aeroacoustic methods have received increased attention. This chapter provides background information on the history of blade noise, quantification of sources, recent developments and perspectives. Furthermore, a detailed analysis of computational aeroacoustics is given to provide the reader some insights in the different options to model sound. The chapter concludes with thesis objectives and an outline of the current thesis.

1.1. WIND ENERGY AND NOISE NUISANCE

WIND energy; the solution to deal with an increasingly recognized and critical challenge ever faced for human mankind. In order to reduce the greenhouse gasses, the demand for renewable energy, such as wind energy, is growing and growing. Turbines are either placed onshore or offshore, and each has its corresponding advantages and disadvantages. Although placing wind turbines onshore seem to be a good idea in terms of installation and maintenance costs, controversy exists about placement of turbines near inhabited places, due to for example noise pollution and obstruction of view. A recent study from van den Berg [1] showed that noise, and especially the swishing character of the noise, is one of the most annoying aspects of onshore wind turbines. The hindrance significantly reduces when people have an economic benefit from the turbines. These days, in order to protect public health, governments apply strict noise regulations for both maximum, average and modulated noise levels for wind turbines [2]. This now constitutes an important barrier for the widespread application of wind energy [3] as many wind turbines have to operate at reduced power during the night. This barrier could lead to a lower power output from the turbines, which will lead to an overall reduction of the annual energy production. Potentially, in some cases, even plans for complete wind farms could fail and be canceled due to stricter noise regulations. Hence, for the design of new wind turbines, noise emission becomes a key design parameter. Therefore, potential noise sources should be analyzed, understood and reduced as much as possible.

1.2. SOURCES OF WIND TURBINE NOISE

In the last few decades, some studies aimed to quantify wind turbine noise [4, 5]. The sound from a wind turbine can be divided into mechanically created and aerodynamically generated noise. Mechanical noise can be generated in the hub, such as the gearbox or the generator and may contain tonal noise. However, if one adequately isolates this type of noise by, for example, sound absorbing materials, the aerodynamically generated noise is the most dominant noise source. This type of noise is caused by the interaction between the incoming flow and the tower and/or rotor blades. This noise is difficult to block or to reduce because the sound sources are located at the outside of the blades, making isolation useless. In order to reduce the aeroacoustic noise the sources should therefore be mitigated using various complex mechanisms [6].

1.3. AIRFOIL NOISE

The different aerodynamic noise source mechanisms can be divided into two sections according to Brooks et al. [7]: airfoil inflow turbulence noise and airfoil self-noise, while the latter can be subdivided into five different components; inflow turbulence noise, laminar boundary layer instability noise, turbulent boundary layer trailing edge noise, trailing edge blunt noise, separation and stall noise and tip noise. Below, the main mechanisms are addressed and characterized. An illustration can be found in Fig. 1.1.

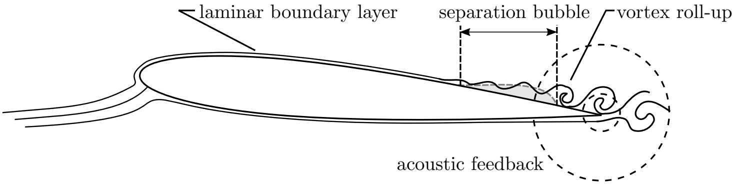
laminar boundary layer
separation bubble
vortex roll-up
acoustic feedback

(a) Laminar boundary layer instability noise.

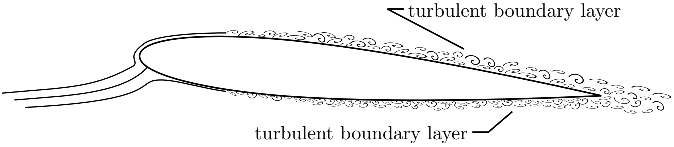
turbulent boundary layer
turbulent boundary layer

(b) Turbulent boundary layer trailing edge interaction noise.

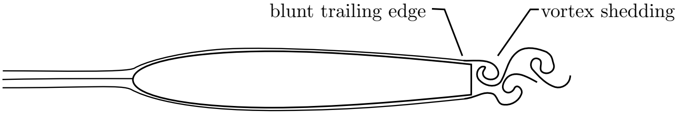
blunt trailing edge
vortex shedding

(c) Trailing edge bluntness vortex shedding noise.

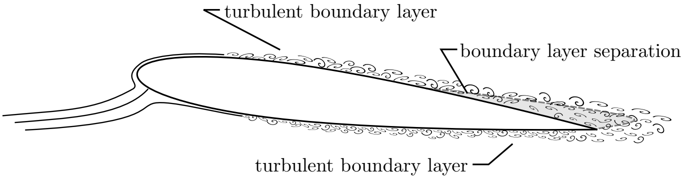
turbulent boundary layer
boundary layer separation
turbulent boundary layer

(d) Boundary layer separation noise.

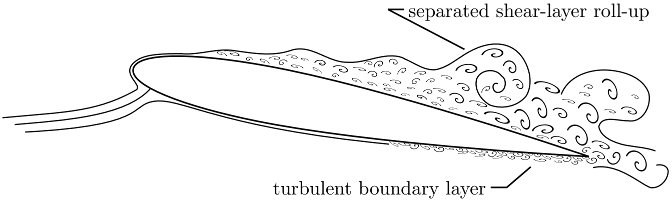
separated shear-layer roll-up
turbulent boundary layer

(e) Separation stall noise.

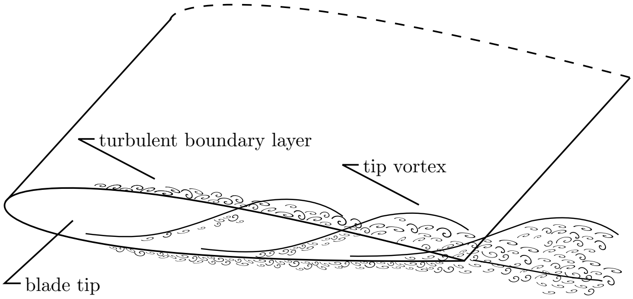
turbulent boundary layer
tip vortex
blade tip

(f) Tip noise.

Figure 1.1: Mechanisms of airfoil noise generation. Adapted from Brooks [7] and Pröbsting [8]

1.3.1. INFLOW TURBULENCE NOISE

The interaction between the incident eddies and the blade surface may cause inflow turbulence noise. This source is not considered to be self-noise, as it is dependent on local atmospheric conditions or on the local site conditions (e.g. wake of upstream wind turbine). Inflow turbulence noise can be a large contributor to the total far-field noise when the inflow is highly turbulent, however it is an open issue to what extent inflow turbulence noise contributes to the overall sound level of a wind turbine under normal conditions [6]. Under those normal conditions, it will only have a marginally effect on the overall sound pressure level.

1.3.2. LAMINAR BOUNDARY LAYER INSTABILITY NOISE

If the Reynolds number over the wind turbine blade is smaller than 1 million, the boundary layer on either side of the airfoil can remain laminar. The small perturbations in this laminar layer are amplified coherently, thereby creating instabilities. These instabilities can roll up into larger vortical structures, which then pass the trailing edge. During the interaction with the edge, acoustic waves are generated. These waves can travel upstream, thereby creating additional instabilities, such as triggering laminar to turbulent transition or Tollmien-Schlichting waves [9]. This then radiates towards the trailing edge and causes trailing edge noise, as sketched in Fig. 1.1a. If such feedback loop occurs, high tonal noise may be generated. Tonal noise is defined as well defined peaks, i.e. about 30 dB above background noise in the acoustic power spectrum.

1.3.3. TURBULENT BOUNDARY LAYER TRAILING EDGE NOISE

On the outer part of most large scale wind turbine blades, typically, high Reynolds number flow ($Re > 1 \cdot 10^6$) is present. Here, a turbulent boundary layer is formed with a large range of scales. Either natural transition or forced transition enhances the boundary layer to be random and turbulent (details in Ch. 2 of this thesis), which will convect over the trailing edge. When such conditions appear, periodic conditions are no longer present at the trailing edge. Instead, the motion is random and has to be described in a statistical manner. As the eddies pass the trailing edge, their pressure fluctuation is scattered at the trailing edge, causing noise. A sketch is found in Fig. 1.1b, showing that in principle the mechanism is similar to laminar boundary layer noise; a sudden jump in boundary condition in combination with differences in pressure fluctuations acting on both the pressure and suction side [7]. The main difference is now that the structures are random and chaotic, resulting in a broadband noise spectrum. This also makes acoustic feedback less relevant. Different turbulent boundary layer trailing edge noise case are discussed in this thesis, e.g. Ch. 3-7. A very good example is the well-known swish noise produced by a wind turbine at the blade passing frequency [10], which is caused by the interaction of the turbulent boundary layer with the trailing edge at the blade traveling towards the receiver, normally located on the ground. Trailing edge noise usually defines the lower bound of wind turbine noise, and is considered to be the most important noise source for modern large wind turbines [6].

1.3.4. TRAILING EDGE BLUNTNESS NOISE

Both laminar and turbulent boundary layer noise are seen as the most important airfoil self-noise sources on a sharp trailing edge and proper mitigation is therefore essential. However, in case of a blunt trailing edge, a different noise mechanism occurs as seen in Fig. 1.1c. When the trailing edge thickness exceeds a critical value, perodic Von Karman type vortex shedding forms at the trailing edge. In this case, the vorticity is not shed from the turbulent boundary layer convecting over the edge, but due to the roll-op of vortices in the near wake. As the turbulent length scale is fixed in this case (bluntness of the airfoil), a narrowband or tonal noise peak appears in the acoustic power spectrum [11]. This can be avoided by a proper design of the trailing edge. Part of Ch. 5 of this thesis is devoted to this type of noise.

1.3.5. SEPARATION AND STALL NOISE

As the angle of attack increases, at some point the flow will separate from the suction side and produce noise due to the shedding of vorticity, Fig. 1.1d. This causes so called boundary layer separation noise. At even higher angles of attack, conditions of deep-stall appear; large scale separation far upstream the trailing edge of the airfoil, illustrated in Fig. 1.1e. Stall causes a substantial level of unsteady flow around the airfoil with large scale vortex shedding, which may lead to a significant increase in low frequency noise [7, 12]. Stall noise is considered to be of minor importance for modern pitch-controlled wind turbines.

1.3.6. TIP NOISE

The last mechanism, only occurring on finite wings, is related to the tip vortex, which is formed due to the pressure difference between the pressure and suction side of the blade and can be highly unsteady and turbulent (Fig. 1.1f). When turbulence convects over the tip edge, separation may occur. The interaction between the turbulent flow and the tip surface may cause tip noise to appear. Furthermore, a steady wing tip vortex can lead to convection of fluctuations within the boundary layer past the edge, thereby acting as a noise mechanism similar to the turbulent trailing edge noise. This type of noise can be present on a modern wind turbine [10].

1.4. CHARACTERISTICS OF TRAILING EDGE NOISE

Let's consider the flow around the outer part of a wind turbine blade, with a local Mach number of the order $M = u/c = 0.2$, with c the speed of sound approximated at 340 m/s and u the incoming velocity at the blade trailing edge section (i.e. $u = 68$ m/s). At these low Mach numbers, flow is assumed to be incompressible [13] and free turbulence away from the blade surface is a very inefficient noise source [14]. Therefore, the radiated far-field noise from an airfoil will be dominated by the interaction between the turbulence and the airfoil wall. The characteristic length of the turbulence; Λ, is a key parameter for the efficiency of the increasing acoustic scattering effect [11]. For trailing edge noise cases, this is normally the boundary layer displacement thickness $\delta^\star$ at the local trailing edge location, while for inflow turbulence this is often set to the incident eddy size, typically in the order of the size of the airfoil. With the disturbances occurring at

$f \sim u/\Lambda$, while the frequency of the emitted sound is defined as $f = c/\lambda$ (with λ denoting the acoustic wavelength), information about the source can be obtained. When the eddies are larger than the chord of the airfoil l, i.e. when the ratio of the chord to the wavelength is $l/\lambda \ll 1$, the acoustic wavelength will also be much larger than the chord. Hence, this results in an acoustically compact airfoil. The eddies will cause an interaction on the complete airfoil, resulting in low frequency noise sources which will radiate as a compact dipole. Curle showed, that in this specific case, the acoustic power which is proportional to the square of the acoustic pressure, scales with the sixth power of the flow speed; $p^2 \sim u^6$ [14]. The directivity of the sound, also known as radiation, behaves like a dipole. Analytically, this can be written as $p^2 \sim \sin^2\theta$, where θ is the angle with respect to the incoming flow direction. Details are found in Fig. 1.2.

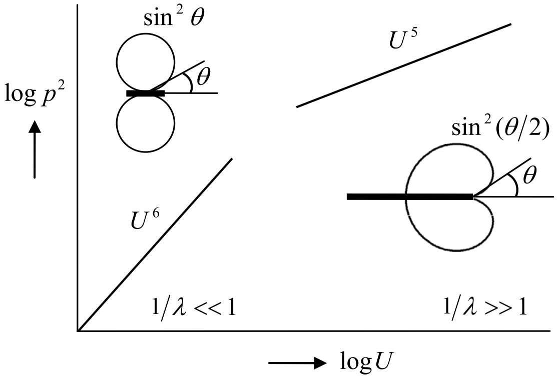

Figure 1.2: Noise radiation and speed dependence for compact and non-compact sources under the assumption of subsonic Mach number. Adapted from Blake [11]

In case of trailing edge noise, the eddies are way smaller than the airfoil chord, i.e. $l/\lambda \gg 1$, and will only locally induce the pressure fluctuations. The sound is scattered at the trailing edge and brings high frequency noise to the acoustic spectra from all radial segments of the blade. Characteristics of this type of noise can be characterized by their local Strouhal number based on the displacement thickness as local length scale, defined as $St = f\delta^\star/u$, which for modern wind turbines, showing a broadband spectrum around $St = 0.1$ [6]. Using a semi-infinite flat plate approximation derived by Ffowcs-Williams and Hall [15], the level of non-compact trailing edge noise can be estimated:

$$p^2 \sim u^5 \frac{b\delta^\star}{r^2} \cos^3\gamma \sin^2(\theta/2)\sin\phi. \tag{1.1}$$

In this equation, b is the span of the blade section, r the distance between source and observer. The angles are defined as in Fig. 1.3. The analytic formulation shows some interesting properties of trailing edge noise. First of all the dependence on b/r^2 is obvious, doubling the span results in a doubling of acoustic energy (i.e. +3 dB), whereas a doubling of observer distance results in a 75% reduction in acoustic energy (i.e. −6 dB). Furthermore, it is shown that in this case the acoustic power scales with the fifth power

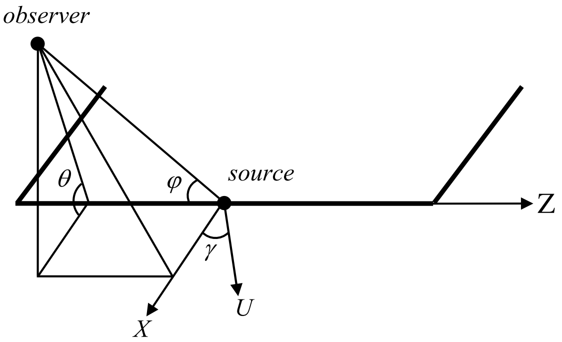

Figure 1.3: Definition of angles at the trailing edge [15]

of the flow speed: $p^2 \sim u^5$, while its directivity is given by $p^2 \sim \sin^2(\theta/2)$. As seen in Fig. 1.2, this means that the maximum radiation occurs in the upstream direction for trailing edge noise ($\theta = \Pi$), hence in the direction of the leading edge. Both the velocity and directivity dependence are the main reason why the swishing sound of a wind turbine is only observed when the outer part of a blade (higher velocity) moves towards the observer (trailing edge noise is emitted towards the leading edge). Generally speaking, transition from the compact to the non-compact regime on a fixed airfoil can occur by either a change in characteristic length scale or by an increase in flow speed, as $f \sim u/\Lambda$. However, since with trailing edge noise the characteristic length scale is much smaller than the airfoil chord, it mainly exhibits in the non-compact regime. Details are further discussed in Ch. 4. It should be further noted that both suction side and pressure side radiate in symmetry, as depicted in Fig. 1.4 [6]. Since the boundary layer displacement thickness on the suction side is normally larger than on the pressure side, the sound produced by the suction side usually attains higher values at lower frequencies compared to the sound produced at the pressure side. As both sides radiate in anti-phase, a silent zone will be created in front of the airfoil. This is further discussed in Ch. 5.

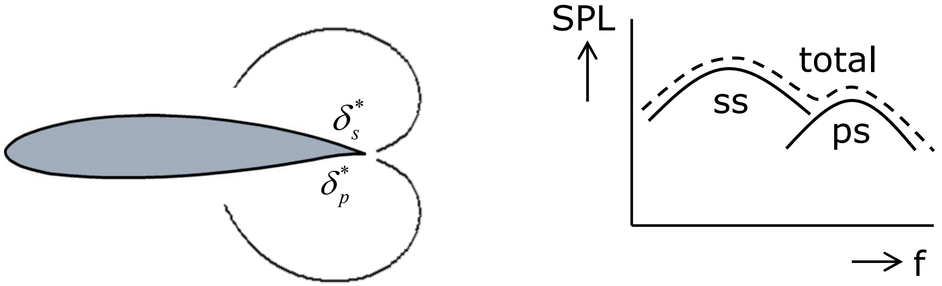

Figure 1.4: Directivity of trailing edge noise on both suction (ss) and pressure side (ps), as well as their contribution to the overall acoustic sound spectrum. Adapted from Leventhall et al. [6]

1.5. MEASUREMENT AND PREDICTION

Wind turbine noise can be experimentally measured and predicted via various methods. The following two sub-sections describe in-field measurements, as well as the predictions being made using scaled wind tunnel models.

1.5.1. WIND TUNNEL EXPERIMENTS

Already in the early days of aeroacoustic experimental research, wind tunnels were used to obtain information about the sound spectra of two-dimensional airfoil sections [16]. These facilities generally contained an open jet. The airfoil is mounted between two acoustically lined side plates and the test section is surrounded by an anechoic chamber to prevent any reflections and spurious noise sources in the far-field spectrum. A microphone is placed outside the tunnel to prevent flow induced noise from turbulence and can be translated during the experiment to characterize the directivity. Multiple microphones can also be used, mainly to filter out the incoherent part of the noise, thus focusing on the actual source region [17]. These days, it is more common to use a complete array of phased microphones, to localize the noise sources on the airfoil. The data from multiple microphones is collected and post-processed using so-called beamforming algorithms to obtain an image of the acoustic source [18].

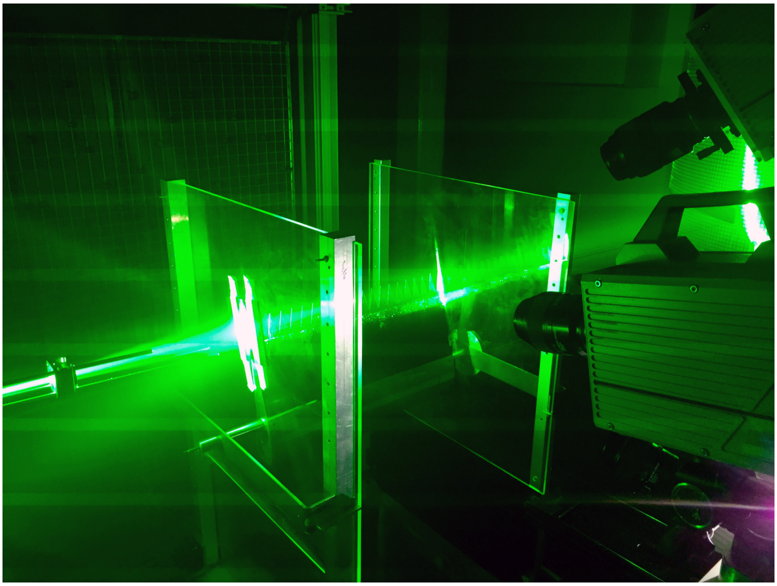

Figure 1.5: PIV campaign on trailing edge noise at the V-tunnel at the Delft University of Technology

Several parameters can be easily adjusted during a wind tunnel campaign, e.g. wind tunnel speed, airfoil angle of attack and shape. Furthermore, a spanwise roughness strip is often used on the airfoil to enforce boundary layer transition from a laminar to turbulent state. In this way higher Reynolds numbers, where transition is normally performed intrinsically, can be simulated. They also can provide information regarding surface roughness, which can occur on a real wind turbine as dirt or insects. To mimic similar conditions in a simulation, a bypass transition can also be performed. In Ch. 2 of this thesis, it is analyzed whether or not it is feasible to obtain uncorrelated boundary layers from different trips, to be later used in numerical trailing edge noise cases.

A classical tool to qualitatively describe aeroacoustic sources is by means of flow vizualization in wind tunnels. Here, the focus lies on capturing the turbulent source region adequately so that a prediction of the aeroacoustic sources can be made. Examples are smoke visualizations and the application of shadowgraphy, put also point measurement techniques such as hot-wire and laser-doppler velocimetry are tools often used in the field of experimental aeroacoustics, mostly to give insight in the aeroacoustic source [19, 20]. To better characterize the noise, in the last decade, many studies have been performed using Particle Image Velocimetry (PIV). This tool is also used in Ch. 5 to validate the computations performed on a trailing edge noise case. As the aeroacoustic source is mostly distributed in space and time, PIV can be used to resolve the flow evolution over time and obtain measurement data in a volume. With this data, and coupled with an acoustic analogy, a estimation of the far-field noise can be made [8, 21]. An example set-up of a recent PIV campaign in Delft can be found in Fig. 1.5.

1.5.2. FIELD MEASUREMENTS

As wind tunnel experiments deal with airfoil sections only, it is essential for wind turbine manufacturers to perform aeroacoustic tests also on-site. Both single microphone as well as detailed analyses with acoustic arrays are used to quantify the noise sources. With a single microphone in field, the overall sound pressure level of an entire wind turbine platform can be measured and compared to the IEC norms set by governments. With an acoustic array [22], a map of sound sources can be plotted as illustrated in Fig. 1.6 which enables one to pinpoint different noise sources. This image depicts the main sound sources at mid frequencies; the rotor hub and the outer part of the downstroke going blade (i.e. not the tip). As mentioned before, trailing edge noise scatters towards the leading edge. This is also confirmed when looking at Fig. 1.6, where the source position is located on the ground.

Instead of study averaged sound pressure levels, in field measurements, it is also possible to study the sound level as function of time, to investigate the importance of the blades passing by. This so called amplitude modulation of the broadband aerodynamic blade noise at the blade passing frequency is often referred to as a swish.

1.6. COMPUTATIONAL AEROACOUSTICS

As an alternative to experimental methods a very efficient, though low fidelity tool to obtain an estimation of the far-field noise levels of a wind turbine is to use empirical models [23]. These methods generally require experimental input (such as the displacement thickness and spanwise coherence length) and can predict noise level trends. More time-consuming is to computationally determine both the noise sources and its propagation. As the source definition of noise is quite complex, accurate tools are needed to predict the acoustic source terms generated by the flow together with its subsequent propagation of waves.

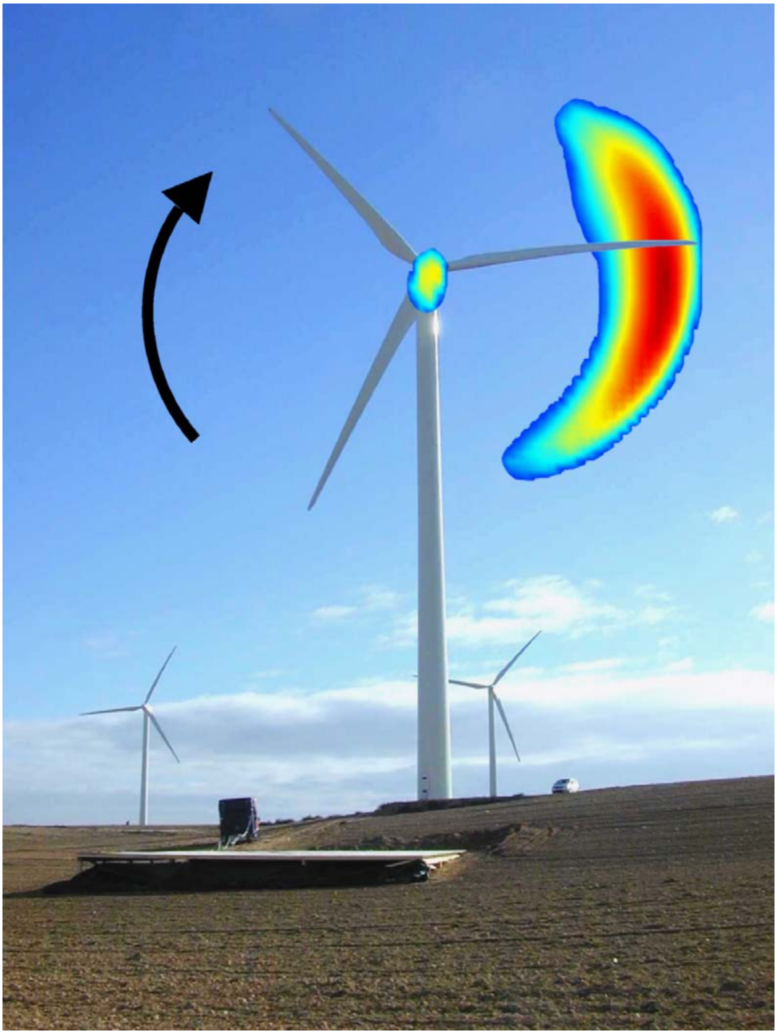

Figure 1.6: Noise sources on a G58 wind turbine extracted from field measurement tests [22]

The modeling of aeroacoustic problems gains interest when computatational resources became affordable to solve the source field accurately and time resolved. The field of Computational Aero Acoustics (CAA) provides an alternative for the prediction of sound compared with empirical and experimental methods. In conjunction with advances in Computational Fluid Dynamics (CFD), CAA has matured over the years. This section gives a comprehensive, but an incomplete list of available methods for Computational Aero Acoustic (CAA) research. For more information the reader is referred to review papers of both Wang et al. [24] and Colonius and Lele [25]. Firstly, in short, different options for the source field are discussed. Next, a distinction is made between direct CAA methods and hybrid CAA methods.

1.6.1. FLOW SOURCE FIELD

Acoustic methods require source data from computational fluid algorithms. Conventionally, in CFD, the flow is solved using a discretized set of partial differential equations, the Navier-Stokes (N-S) equations, together with mass and energy conservation equations (Ch. 3 & 4 of this thesis). Several methods of discretization can be applied, with the Finite Volume (FVM), Finite Element (FEM) and Finite Difference (FDM) method being employed most often in order of appearance [26]. As an alternative, the Boltzmann equations can be solved for simulating fluid flows [27]. The Lattice Boltzmann Method (LBM) starts from a mesoscopic kinetic equation in order to determine the macroscopic fluid dynamics (Ch. 2, 5, 6 & 7 of this thesis). It is solved on a Cartesian mesh, known as a lattice, by explicit time-stepping and collision modeling. The explicit time-stepping makes the computational time for LBM simulations significant shorter than for implicit N-S simulations.

Fully resolving the entire turbulent spectrum up to the so-called Kolmogorov' length scales is preferable for CAA purposes as even the smallest turbulent scales can emit noise. This type of flow simulation is known as a Direct Numerical Simulation (DNS) [24]. There exist other, less computational demanding options, where the discretization generally involves larger cells. When the smallest eddies for acoustics can be neglected, a Large Eddy Simulation (LES) [28–30] can be computed. A LES is modeling the smallest eddies by means of a turbulence closure model, while solving the larger eddies directly [26]. The cut-off is important and could affect the CAA computations. Both DNS and LES are transient and can be employed for both N-S and LBM simulations. Lower fidelity flow simulations such as Reynolds Averaged Navier-Stokes (RANS) can also be applied for aeroacoustic computations, where all eddies are modeled, but care should be taken in the selection of turbulence model as well as the stochastic model for turbulence modeling. Both unsteady [31, 32] and steady [33–35] simulations were performed for CAA purposes in the past using the N-S equations, as the LBM methodology is intrinsically transient.

1.6.2. DIRECT METHODS

When dealing with direct methods in a computational framework, the acoustic propagation to the far-field is computed simultaneously with the simulation of the aeroacoustic source region. One can solve a set of compressible flow equations, using a direct numerical simulation. Nevertheless, the computation of both hydrodynamic and acoustic pressure in one computational tool poses several computational difficulties, which are related to either scale differences or boundary conditions. Difficulties are, for example:

1. For low Mach number flows there exists a large length and time scale separation between the acoustic and flow field [24].

2. There is a large difference between the magnitudes of the acoustic and aerodynamic disturbances [25] and hence, numerical errors may overshadow sound production due to its low efficiency if both flow and sound are calculated simultaneously.

3. Special treatment of the boundaries is essential, since reflection from outward propagating waves back into the computational domain distorts the solution [36].

4. Commonly used levels of artificial dissipation and dispersion in conventional CFD can largely attenuate the waves as they propagate to the far field, putting high demands on the numerical scheme [25, 37].

When the above mentioned difficulties are properly addressed, it is possible to obtain an accurate description of both the near-field or far-field acoustics.

1.6.3. HYBRID METHODS

On the other hand, a hybrid method can be employed. In contrast to direct methods, the source region simulation for the hybrid methodology does not aim to capture the near-field and far-field radiated sound field directly, but relies on a second calculation for predicting the acoustic propagation. The source region usually encapsulates the entire turbulent part of the flow as well the close surfaces which interact with it. The boundary is usually placed in the near-field, extending only the most important regions, avoiding excessive computational times but taken into account reflection at the outer boundaries. A schematic overview is found in Fig. 1.7.

Flow data in the source region are obtained similar to the methodology in a direct CAA method; again using a set of compressible flow equations if possible. The flow source data should have sufficient spatial and temporal resolution, hence a DNS or LES are often employed [39]. Generally, the more accurate CAA computations, the more details one needs to resolve, the more computational power it will cost.

Wang et al. [24] stated that at a low Mach number, incompressible flow solutions could also adequately approximate the acoustic source terms. Schram [40] on the other hand showed that, when solving an incompressible flow solution, only compact acoustic sources can be captured as the code is unable to determine the scattering effects. However, if one would like to incorporate the scattering effect, which appears when the unsteady flow produces sound at or below wavelengths comparable to the body dimensions, the source term should be adjusted to incorporate non-compact acoustic sources. And as trailing edge noise appears to be mainly in the non-compact regime [6], where the ratio of the wavelength to chord is smaller than one, a correction has to be found. The correction applied by Schram [40] to use incompressible flow data is further described and investigated later in this thesis (Ch. 4).

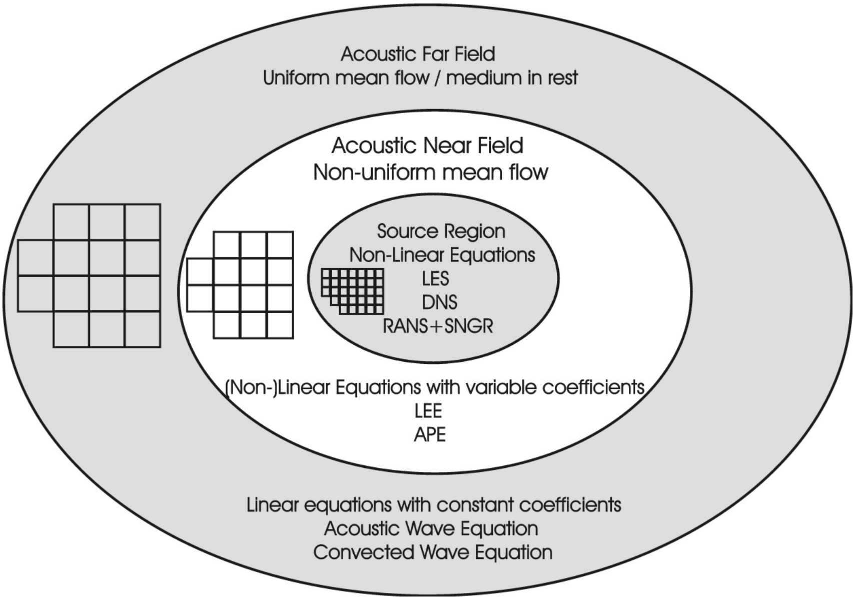
Acoustic Far Field
Uniform mean flow / medium in rest
Acoustic Near Field
Non-uniform mean flow
Source Region
Non-Linear Equations
LES
DNS
RANS+SNGR
(Non-)Linear Equations with variable coefficients
LEE
APE
Linear equations with constant coefficients
Acoustic Wave Equation
Convected Wave Equation

Figure 1.7: Domain division using CAA [38]

NEAR-FIELD METHODS

In order to reduce the computational effort of the direct noise computation, a variety of methods exist which can extend the near-field sound sources from CFD, to remote distances. Mostly, it consists of a domain extension using an improved mesh more suitable for acoustic propagation, for example a cartesian mesh instead of an unstructured mesh. In the turbulent source field location and extended domain, the near-field, a simplified set of governing fluid equations can be employed, such as the Linearized Euler Equations (LEE) [37] or the acoustic wave equation. The coupling scheme simplifies in this case to a transfer of acoustic data from one domain mesh to another domain mesh, and relaxes the strict requirements on the scale length difference between hydrodynamic and acoustic pressure fluctuations. Special care has to be taken to ensure accurate and stable transfer of information at the grid interface, as well as avoiding reflections at the boundary [36]. More advanced methods, derived from the LEE can also be found in literature, e.g. the acoustic perturbation equations [41] and the perturbed compressible equations [42].

Near-fields methods can still be computational expensive, but offer a solution when non-uniform mean flow plays an important role so that refraction and convection effects are taken into account. The importance of addressing non-uniform mean flow for aeroacoustic problems has been addressed earlier by Si et al. [43]. As noise induced by turbulent flows often propagates from near field to far field in a non-quiescent medium, the effect of non-uniform mean flows on the propagation of acoustic waves is important to be considered. A LEE simulation seems to be sufficient to tackle this problem. The necessity of higher order schemes for the discretization of the acoustics problem limit the user to solve aeroacoustic problems on, for example, complex geometries on large domains. Solutions to this are found by decomposition of the waves, by using wave characteristics to solve acoustic problem [44, 45].

FAR-FIELDS METHODS

When more engineering approaches are required for fast turn-around times, free-field integral methods based on acoustic analogies can be used. The idea here is to replace the whole sound generating flow field by specific sources, denoted by quadrupole, dipole and monopole sources. This method is appealing for industry due to its simplicitiy and straightforwardness in implementing this in, e.g. the wave equation, as it only requires to collect the right hand side source from the fluid simulation. The coupling is much easier then with near-field methods, and the accuracy mainly depends on the accuracy of the CFD simulation. Furthermore, it can be translated to an integral formulation solving the relation using a free-field Green's function only at observer and source location. This way, no set of equations has to be discretized and solved, as an analytical formulation is obtained. This approach has as major advantage that no additional numerical errors are made in the propagation of the acoustics waves [39], but shows disadvantages in the fact that no non-linear flow interaction is taken into account as well as the fact that both observer and source should be located at a significant distance away from each other.

The history of the acoustic analogy started off with the theory of Lighthill [46]. He considered the problem of jet noise and investigated the acoustic sources; turbulence. Using a rearrangement of the governing fluid equation, a wave equation with a source term was obtained. The source term consists of free turbulence in the form of a Lighthill stress tensor, and can be visualized in a quadrupole like shape in the far-field. However, quickly after the release of Lighthill's analogy [46] it was found that, in case of low Mach number flow, the presence of solid boundaries in the flow changes the radiation of sound significantly. Therefore, Curle [14] suggested to incorporate the influence of solid bodies upon the radiation of sound in the wave equation earlier described. This resulted in a dipole source term which encapsulates the fluctuating pressure force on a body. In low Mach number flow, the scattering of this dipole source is more effective (compact dipole source scales with M^6 while a quadrupole source scales with M^8), and hence advantage is obtained by only storing the dipole surface data instead of the, more computationally demanding, quadrupole volume data. For trailing edge noise cases, one can imagine that (non)-compact dipole sources are the main source of interest, as the edge was found to be an effective scattering object.

After the release of Curle's analogy [14], a further improvement was obtained by incorporation of the movement of solid surfaces, which resulted in a monopole source term, which scales with M^4. The Ffowcs Williams-Hawkings analogy [47] can be considered as the most general form of the wave equation, and is useful for, for example, noise studies with helicopter rotors as the sources are in constant motion. The integral formulation-1A by Farassat and Succi [48] provides the solution for this wave equation, while Bres et al. [49] extended the analogy by incorporating mean convective effects. A further improvement was found by Casalino [50], by taking into account a new interpretation of the retarded time approach.

Since the release of Lighthill's analogy [46] many people contributed to simplified and derived forms of the wave equation, mostly varying in source terms [14, 47, 51–57].

Physically noise sources are expected to be unique and definite, although in practice these acoustic analogies strongly depend on the choice of source variables, incorporation of convection and refraction effects and the acoustic wave operator. Which source terms are a more accurate representation of reality is strongly dependent on the type of flow being analyzed. However, as this thesis focus is on trailing edge noise, surface dipole sources are highly appreciated in the physical representation of the far-field noise.

1.7. REDUCTION OF WIND TURBINE NOISE

In the previous sections characteristics of the most dominant noise source are given, as well as many options to measure, estimate and predict the far-field acoustic spectrum. When it is possible to predict noise, it is time to look forward and investigate devices which can reduce noise. When reducing noise, 1) turbines do not have to operate at reduced power during the night due to noise constraints, 2) more wind turbines can be erected on a given site within the same overall noise levels, 3) sites can be placed closer to the end user, so that they become more accessible and 4) when more quiet blades can be designed, it enables a larger rotor diameter and higher RPM, hence an increase in energy production for a given turbine [6].

To discover ways to reduce trailing edge noise, Eq. 1.1 is further analyzed. As can been seen, the acoustic pressure scales with u^5 and hence, decreasing the RPM of the blades directly leads to noise reduction. This strategy is sometimes employed during nighttime. However, a decrease of RPM also drastically reduces the power production. The same disadvantage holds for a decrease in displacement thickness, which can be obtained by an increase in blade pitch angle which results in a reduction of local angle of attack. This gives a reduction of lift, and therefore a reduction in energy production. Solutions have to be found which do not result in a loss of energy production.

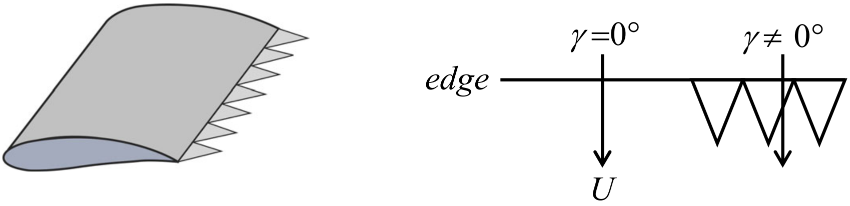

Figure 1.8: Sketch of trailing edge serrations [6]

A solution to reduce noise while maintaining the same performance would be the redesign of the airfoil; creating optimized airfoils reducing the displacement thickness, while maintaining the aerodynamic performance [58]. Another option would be to alter the acoustic radiation efficiency of the trailing edge, defined with the angles in Eq. 1.1. The factor $\cos^3\gamma$ shows that trailing edge noise is scattered most effectively when the path of the turbulent eddies is perpendicular to the trailing edge. This implies that sound can be reduced by sweeping the edge with respect to the flow direction, basically aligning the streamlines with the edge. This can be achieved by applying serrations, as depicted in Fig. 1.8. Here, the angle between the incoming eddy and the edge is less than 90 degrees, resulting in less efficient sound scattering [59]. Serrations are designed to alter the acoustic scattering only, while having a small effect on the total aerodynamic performance of the blade. The actual mechanisms, though are still a matter of discussion and will be further addressed in Ch. 6 & 7 of this thesis.

1.8. MOTIVATION AND OBJECTIVES

Due to the rapid advances in computer technology the field of CAA has become a valid alternative to empirical and experimental methods for the prediction of far-field sound production and propagation. As part of a long-term research strategy, the industry would like to build-up competence on CAA methods for blade noise prediction. On the longer term, such methods might enable quantitative comparisons between different blades and/or trailing edge noise suppression add-ons within current industrial turn-around times, thereby reducing for example the required amount of field and wind-tunnel test work. Therefore, the main, final, objective of this study is:

> *to develop a fast, reliable and accurate computational aeroacoustic methodology to identify, visualize and quantify primary noise sources and their underlying mechanisms on a wind turbine blade with and without noise suppression add-ons.*

Before acoustic sources can be captured accurately, one should gain knowledge about the fidelity of the flow solution. Therefore, the first sub-goal would be to investigate different governing flow equations and their corresponding solvers, and comment on their accuracy, easiness and effectiveness to generate turbulent boundary layers (Part I) required for the analysis of turbulent boundary layer trailing edge noise. When uncorrelated boundary layers can be physically correctly generated, flow around trailing edges (Part II) can be investigated. The final step would then be the analysis of the flow field around noise-suppression add-ons (Part III). Furthermore, the resulting flow field should closely resemble a physically correct flow field and hence validation of the software used is essential to reach the overall objective of this study. A proper validation of the simulated results with experimental data is required and should be applied to both the flow and pressure field (Part I, II & Part III).

Another sub-goal in this thesis is the acoustic solver; a fast and accurate method has to be obtained to interpolate the sources from the flow field to the acoustic field, as well as propagation to the far-field. The focus should lie on the analysis of parameters that could influence the acoustic scattering (Part I) before the actual problem of turbulent trailing edge noise scattering can be studied Part II). Scattering could here play an important role.

Once both goals are reached, the main objective can be finalized by looking into the noise sources and underlying mechanisms of airfoils with and without complex noise suppression add-ons (Part III). Furthermore, new trailing edge designs can be tested and quantitative comparisons can be made.

1.9. OUTLINE OF THE THESIS

This thesis contains five parts; prologue, turbulent boundary layer noise (Part I), trailing edge noise (Part II), noise suppression add-ons (Part III) and the epilogue.

In the prologue, an extensive introduction to the topic as well as a motivation and research objectives are given. These research objectives led to the three parts in this thesis, analyzed using two flow modeling approaches (vertical axis) and four acoustic propagation (horizontal axis) approaches. The outline is graphically summarized in Tab. 1.1 and further briefly discussed in the next paragraphs.

Table 1.1: Test matrix of studies performed in this thesis. On the horizontal axis, the different acoustic approaches are presented while the vertical axis denotes the two flow methods employed in this thesis.

	None - Coherence length with Corcos model	**Direct** - Near field pressure microphones	**FEM/BEM** - Tailored Green's function - Incompressibility correction - Dipole sources - Solid surface	**FW-H analogy** - Free field Green's function - Dipole and monopole sources - Solid surface and porous membrane
Navier-Stokes - Incompressible - LES, ILES	Part I: Turbulent boundary layer noise, Ch. 3		Part II: Trailing edge noise, Ch. 4	Part II: Trailing edge noise, Ch. 4
Boltzmann - Compressible - DNS, VLES, ILES	Part I: Turbulent boundary layer noise, Ch. 2	Part II: Trailing edge noise, Ch. 5 Part III: Noise suppression add-ons, Ch. 6 & 7		Part II: Trailing edge noise, Ch. 5 Part III: Noise suppression add-ons, Ch. 6 & 7

Part I deals with studies related to fluid dynamics modeling of turbulent boundary layers. No acoustics is considered but related properties are considered. First, a detailed analysis of the bypass transition process is given and downstream conditions are analyzed to ensure an uncorrelated fully developed boundary layer. While Ch. 2 focuses on the tripping mechanism, Ch. 3 will focus on the downstream characteristics of the boundary layer, in particularly related to aeroacoustic properties such as the spanwise coherence length.

In Part II, the tonal and broadband noise emission from a beveled plate is estimated using different computational methods, varying in flow modeling and acoustic propagation modeling. Both an incompressible Navier-Stokes (Ch. 4) and compressible Lattice Boltzmann (Ch. 5) are used for the prediction of the turbulent boundary layer flow convecting over an edge, and its resulting acoustic source field. In addition, Ch. 4 discusses the importance of scattering effects by looking at non-compact acoustic sources from incompressible flow simulation using the comparison between free-field and tailored-made Green functions. Ch. 5 validates the computational methodology by means of experimental PIV, hot wire and acoustic data using computational acoustic input from direct probes in the computational domain and the FW-H acoustic analogy integral relation.

Part III discusses the scattering mechanism of noise-suppression add-ons, in particularly of serrations. The flow topology and noise emission of a NACA 0018 airfoil with conventional and improved serrations is analyzed in Ch. 6, focusing on the noise reduction mechanisms of serrations. The computational approach is validated by means of PIV and acoustic array data. An improvement of a serrated trailing edge design is discussed in Ch. 7, showing the possibility to further increase the noise reduction on wind turbine blades.

This thesis is concluded with an epilogue, containing the conclusion (Ch. 8) and acknowledgments. For the interested reader, the appendices contain general formula's to describe the fundamentals of acoustics, as well as information on sampling and statistical data analysis methods used in this thesis.

I

TURBULENT BOUNDARY LAYER

2

PHYSICAL MODELING OF BYPASS TRANSITION STRIPS

> *It would be possible to describe everything scientifically,*
> *but it would make no sense;it would be without meaning,*
> *as if you described a Beethoven symphony*
> *as a variation of wave pressure.*
>
> Albert Einstein

To force the flow from a laminar state into a turbulent state at a specific position of interest, a boundary layer transition trip is generally used. During more recent applications, transition strips were used to match transition locations and boundary layer growth so that similar trailing edge flow characteristics were obtained when comparing, e.g. airfoil noise simulations with acoustical experiments. The motivation for the current chapter is to understand the properties of simulated transition strips for future aero-acoustic simulations. A staggered grid of cubic blocks for transition is analyzed and compared with a more conventional, zigzag strip using flow results from a direct numerical simulation of the fully transient, explicit and compressible Lattice Boltzmann equations. The staggered grid of blocks is more efficient in stopping the flow and creating large, coherent flow structures of the size of the blocks, which results in a stronger transition. However, the downstream merging of spanwise created structures is relatively long, in the order of $80\delta_0$*, resulting in more strongly correlated boundary layers. If the variation of the zig-zag strip in spanwise direction is small, the streamwise vortices created merge quicker, resulting in an uncorrelated boundary layer after* $40\delta_0$.

2.1. INTRODUCTION

TO force the flow from a laminar state into a turbulent state at a specific position of interest, a boundary layer transition trip is generally used. As an additional effect, boundary layer transition often prevents laminar separation bubbles on airfoils from occurring, thereby reducing drag and improving the airfoil performance [60, 61]. During more recent applications, transition strips were used to match transition locations and boundary layer growth so that similar trailing edge flow characteristics were obtained when comparing, e.g. airfoil noise simulations with acoustical experiments. Although passive bypass transition offers a good solution to enforce transition, it is known that it will introduce disturbances which remain coherent far downstream, making it a challenge to have a fully conical turbulent boundary layer. In general, due to the large introduced disturbances by a tripping device, questions as: 1) which and what kind of flow structures are actually initiated by these passive devices, 2) how long do these structures persist downstream and 3) how do they develop into a fully developed turbulent boundary layer, would remain of crucial interest [62].

Though the flow topology arising from the so-called bypass transition process [63] has been extensively addressed in the past, several issues are left open. Both experimental [64–69] studies, devoted to the description of the transition process by means of two-dimensional roughness strips, and numerical studies [70–72], describing the challenges with immersed boundary (IB) methods to represent the trip, have been conducted in the past. Previous attempts into the analysis of the flow topology included oil film surface flow visualizations and Particle Image Velocimetry (PIV) behind a zigzag strip [67, 68]. The oil flow visualizations revealed backflow in small regions directly downstream of the upstream pointing spike, which are followed by clear oil stripes, indicating streamwise flow streaks. These streamwise streaks are confirmed by the PIV analysis as streamwise vortices and experience maximum spatial energy growth after which they develop into turbulence [73]. The spanwise vortical related structures directly behind the trip break up slowly into individual arches and start to develop into hairpin structures which are typical for wall turbulent bounded flows [68]. These elongated streaks of mostly low speed flow are a common feature in multiple bypass transition studies, and unwanted since they promote coherence in the flow. They are present by either flows tripped by roughness as well as by free-stream turbulence [74, 75]. The far downstream effects of various trips are also investigated by, e.g. Erm [69]. They showed that the influence of various trips far downstream of the trip disappear and that velocity statistics return to their common values for a fully developed turbulent boundary layer, which is a good effect for an uncorrelated boundary layer.

The motivation for the current research is to understand the properties of simulated transition strips for future aero-acoustic simulations. Particularly, the effect of boundary layers generated by these strips on trailing edge noise. The pressure and flow coherence downstream of a transition strip can influence the evaluation of trailing edge noise when the velocity statistics do not normalize in a sufficient downstream length. The study will compare different geometries and conclude on their effectiveness to generate a physical correct and uncorrelated boundary layer, focusing on the streamwise length it would take.

In recent years, an efficient and highly parallelizable approach for the simulation of fluid flows, known as the Lattice Boltzmann Method (LBM) receives increased attention [76–81]. The LBM solves the discrete Boltzmann equations in combination with a collision model to compute the flow of a Newtonian fluid. By modeling the convection and collision processes of particles with a limited number of directions, the flow is represented on a macroscopic scale. The LBM methodology is used in the present study to analyze the low Mach number fluid flow around a zigzag trip and a staggered grid of cubic blocks.

2.2. METHODOLOGY

Within the current study, the discrete Boltzmann equations are solved for computing the fluid flow [27]. The LBM method starts from a mesoscopic kinetic equation, i.e. the Boltzmann equation, to determine the macroscopic fluid dynamics. The commercial software package Exa PowerFLOW 5.0b is used to solve the discrete Lattice-Boltzmann equations for a finite number of directions. The discretization considers 19 discrete velocities in three dimensions (D3Q19) involving a third order truncation of the Chapman-Enskog expansion, which has been shown sufficient to recover the Navier-Stokes equations for a perfect gas at low Mach number in isothermal conditions [82].

The kinetic equations are solved on a Cartesian mesh, known as a lattice, by explicit time-stepping and collision modeling. Defining the particle density distribution function as f_i, the Lattice-Boltzmann equation may be written as:

$$f_i(\mathbf{x}+\mathbf{c}_i\Delta t, t+\Delta t) - f_i(\mathbf{x}, t) = C_i(\mathbf{x}, t), \tag{2.1}$$

where the particle density distribution function can be interpreted as a typical histogram representing a frequency of occurrence at a position x with a discrete particle velocity $\mathbf{c}_i$ in the i direction at time t. $\mathbf{c}_i\Delta t$ and Δt are space and time increments respectively. The collision term on the right hand side of the LBM equation adopts the simplest and also the most popular form known as the Bhatnagar-Gross-Krook (BGK) form [83]:

$$C_i(\mathbf{x}, t) = -\frac{\Delta t}{\tau}\left[f_i(\mathbf{x}, t) - f_i^{eq}(\mathbf{x}, t)\right]. \tag{2.2}$$

This term drives the particle distribution to the equilibrium with a relaxation time parameter τ. The variable f_i^{eq} is the local equilibrium distribution function, relates the LBM to hydrodynamic properties and is essential for the local conservation criteria to be satisfied. The equilibrium distribution of Maxwell-Boltzmann can be approximated by a 2nd order expansion valid for small Mach number [84]:

$$f_i^{eq} = \rho\omega_i\left[1 + \frac{\mathbf{c}_i\mathbf{u}}{a_s^2} + \frac{(\mathbf{c}_i\mathbf{u})^2}{2a_s^4} + \frac{|\mathbf{u}|^2}{2a_s^2}\right], \tag{2.3}$$

where ω_i are the weight functions related to the velocity discretization model [84] and $a_s = \frac{1}{\sqrt{3}}$ is the non-dimensional speed of sound. The equilibrium function is related to the macroscopic quantities density ρ and velocity $\mathbf{u}$, which can be computed by summing up the discrete momentum of the particle distribution:

$$\rho(\mathbf{x}, t) = \sum_i f_i(\mathbf{x}, t), \qquad \rho\mathbf{u}(\mathbf{x}, t) = \sum_i \mathbf{c}_i f_i(\mathbf{x}, t). \tag{2.4}$$

The single relaxation time used is related to the dimensionless kinematic viscosity: [84]:

$$\nu = a_s^2(\tau - \frac{\Delta t}{2}). \tag{2.5}$$

A direct simulation of the LBM relations is employed. A variable resolution is allowed, where the grid size changes by a factor of two for adjacent resolution regions. Due to the explicit time-stepping characteristics of the LBM scheme, the time-step size is increased with cell size in factors of two as well. Larger cells will therefore not be evaluated every time-step. This gives rise to the notation of time-step equivalent number of cells, which is the number of cells scaled to operation at the shortest time-step in addition to the total number of cells.

2.3. CASE SETUP

The flow topology around two different transition strips along the upper part of a l = 350 mm long, 0.0857l wide flat plate is simulated. The tripping, seen in Fig. 2.1 is applied by either a staggered grid of blocks or zigzag strip of each 2 mm height. The small cubic blocks of 2 mm each are 6 mm located away from each cubic center. In total, 4 rows of blocks are placed in a staggered grid, starting at 9 % of the flat plates chord. The second trip, a 9 times V-shaped zigzag strip of 5.5 mm length is also applied at 9 % of the flat plate chord.

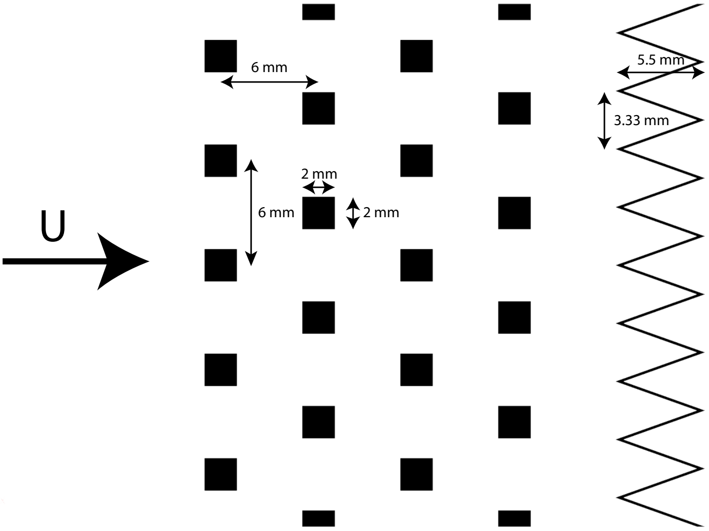

Figure 2.1: Schematic view of both bypass transition devices; (left) the staggered grid of cubes and (right) the zig-zag strip

The simulation domain is bounded by a no-slip boundary condition at the location of the plate and by a frictionless wall at a 0.1l distance in wall-normal direction, making sure that the frictionless wall is in undisturbed flow and does not interfere with the development of the boundary layer. At the inlet, a streamwise velocity of 45 m/s is prescribed to run simulations at a chord based Reynolds number of $1.5 \cdot 10^5$, the maximum which could be reached within a turn-around time of 15 days for 0.1 physical second of computational time on a system of 80 cores of Intel Xeon X5670 (hex-core) platform at 2.93 GHz. The outlet is modeled by a fixed static pressure, while maintaining a free flow direction. The LBM scheme is discretized over lattices of different sizes. The finest lattices of 32 cells per mm are positioned near the wall and at a larger area around the trip, including a wake refinement making it a direct, wall resolved, simulation. The viscous grid spacing ($x^+ = y^+ = z^+$) is directly extracted from the downstream friction velocity and equals 0.4. The DNS simulation in PowerFLOW® allows us to solve the boundary layer at a dense mesh, while outside the boundary layer, the mesh coarsens. In total, seven volumes of refinement (VR) are used as indicated in Fig. 2.2 resulting in a total of 666 million voxels, or 438 million fine equivalent voxels.

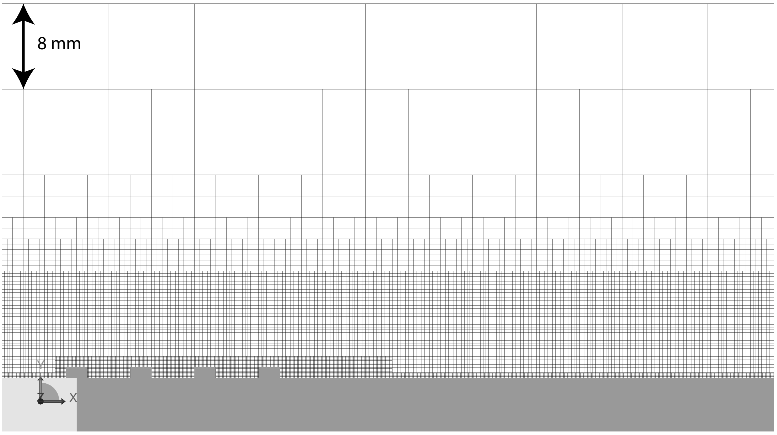

Figure 2.2: Detailed view of the VR's near the block trip. Similar refinement regions are used for the zigzag strip model.

The experimental Mach number is about 0.13, but in the simulation the Mach number has been increased to 0.31 in order to obtain a proper DNS resolution in all the refinement regions, keeping the same viscosity and speed of sound in every single refinement region. When converting the physical quantities into dimensionless lattice quantities, the velocity is increased by approximately a factor of three while keeping the Reynolds number constant by increasing viscosity. After the computations, the data is converted back to the experimental values. If the Reynolds number is kept constant, similar flow conditions are expected. The Courant-Friedrichs-Lewy (CFL) stability number is intrinsically set to unity by the solver, leading to a time step of 1.3×10^{-7} s, assuming a maximum velocity of $1.3 \cdot u_\infty$. In physical time, the simulations are run for 0.3 s, where the last 0.25 s (i.e. 32 flow passes) are used for recording statistics at a frequency of 30 kHz (App. B). Spectra are obtained using a Hamming window with 50 % overlap, 22,000 frames with a FFT window width of 5400, resulting in an optimal smoothing.

The physical quantities from the LBM solution like velocities, pressures and distances are made dimensionless in the next section using the free-stream velocity (u_∞ = 45 m/s) and the atmospheric pressure (p_∞), as well as the undisturbed laminar boundary layer thickness, δ_0, which will be determined at the location where the trip starts ($x_0 = 0.09c$). If the thickness is determined using a Blasius profile, it results in:

$$\delta_0 = 5.0\frac{x_0}{\sqrt{Re_{x0}}} \qquad \text{with} \qquad Re_{x0} = \frac{u_\infty x_0}{\nu_\infty} \tag{2.6}$$

which results in a Reynolds number of $1.4 \cdot 10^4$ and thickness of δ_0 = 1.4 mm for the current setup. The undisturbed Reynolds number of the laminar boundary layer, $Re_{\theta 0}$ is estimated to be 80 which is far below the thresholds of a transitional and turbulent boundary layer given by [85] (i.e. $Re_\theta = 162$ and 320 respectively). This implies the usage of an imposed tripping device to bypass the transition process to provide a large disturbance and an added momentum loss.

The optimum trip height can be compared against some engineering tools for forcing a boundary layer available in literature from both Braslow [61] and Gibbings [86]. The minimum roughness height $k_c r$ is determined based on the roughness height Reynolds number Re_k, which is obtained by extensive wind tunnel research. For two-dimensional tripping devices, Braslow [61] and Gibbings [86] predicted a Reynolds number of Re_k = 300 and 850 respectively, leading to a roughness height of $k_c r$ = 0.7 mm and 2.0 mm respectively. Van Rooij [60] suggested on the other hand, when three-dimensional trips are applied, the Reynolds number is reduced to $Re_k = 200$. This would imply a trip thickness of 0.5 mm. The large discrepancy between the values is illustrative for the differences in the results of aforementioned studies. It can be seen that the current test case ($Re_k = 800$) is slightly over-tripped, based on the other studies presented before.

2.4. RESULT AND DISCUSSION

2.4.1. BYPASS TRANSITION PROCESS

The three-dimensionality of the mean flow is analyzed using figures of streamlines around both bypass transitions strips, colored by their wall normal height. The results in Fig. 2.3 show a uniform flow before it is disrupted by the bypass transition strip. Clearly, for both trips, spanwise periodicity and symmetry is found back in the figure by means of compressed bundle of streamlines behind the trip. The staggered grid of blocks seems to disturb the incoming flow less. The flow is either moved around blocks (blue streamlines at the second and third row) or is flowing over a block (red streamlines at the last row) instead of fully stagnation, which appears at the entire frontal surface of the zigzag strip. The vortices created by the first rows are pushing the low-speed and back flow fluid away from the wall resulting in the higher fluid streaks over the last row. In case of the zigzag strip, the incoming laminar boundary layer encounters a larger initial frontal area which covers the entire span. This enhances a wedge of continuous turbulence behind the trip, resulting in larger friction forces. Because of these additional disturbances in the flow, momentum drag is added, after which transition occurs [13]. The streamlines reach their highest point directly after the downstream tip after which the high speed fluid is moved in the direction of the wall again. The overall drag is measured to be four times larger with a zigzag strip when comparing with the first row of blocks. The average drag coefficient is similar though if all rows of blocks are taken into account, with the first row contributing the most.

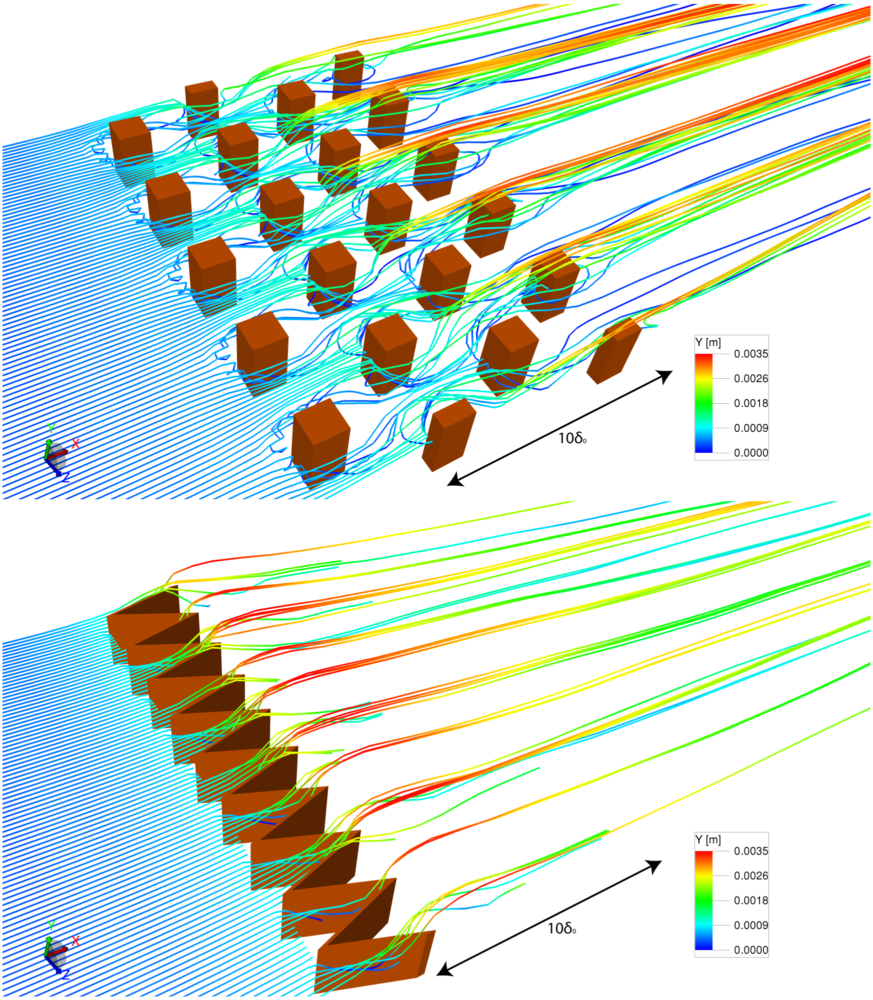

Figure 2.3: Streamwise colored by wall-normal height illustrating the mean flow topology of the bypass transition behind blocks (top) and zig zag strip (bottom). Note that half of the trip is placed in the floor of the plate, resulting in a trip which is effectively half of displayed here.

The results for the different velocity components are displayed in a wall-parallel plane in Fig. 2.4 and 2.5. For the zig-zag strip, streak-like structures are present directly behind the trip, which extends at least $10\delta_0$. This is a common trend and observed in, for example, the study from Elsinga [68]. One thing though to observe in Fig. 2.4 is that, by applying the staggered grid of blocks as a bypass transition device, this results in a clearly less effective merging of the lower speed streaks. Visible streaks are present up to $80\delta_0$.

For the staggered grid of blocks, back flow is observed behind every single block

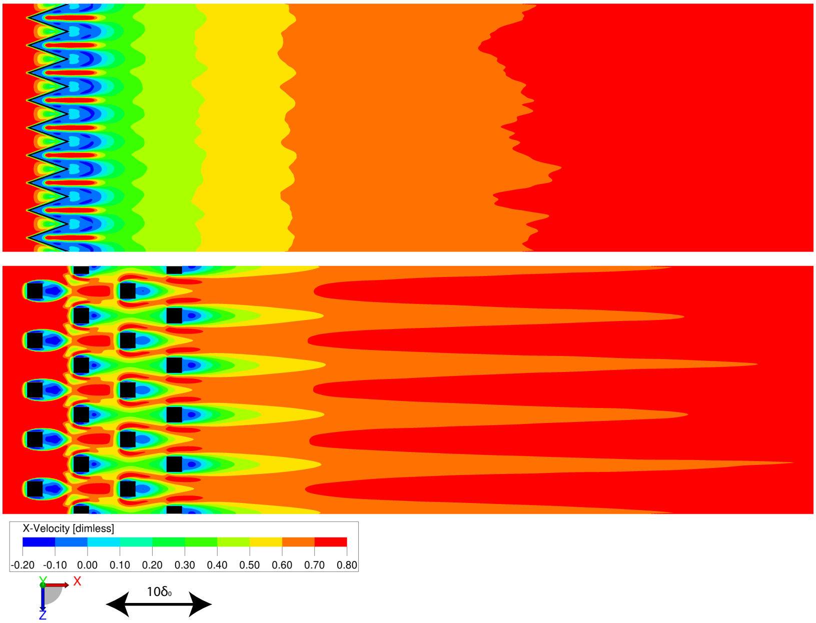

Figure 2.4: Mean streamwise velocity behind the zig-zag strip (top) and staggered grid of blocks (bottom) in a plane parallel to the wall at $y/\delta_0 = 1$

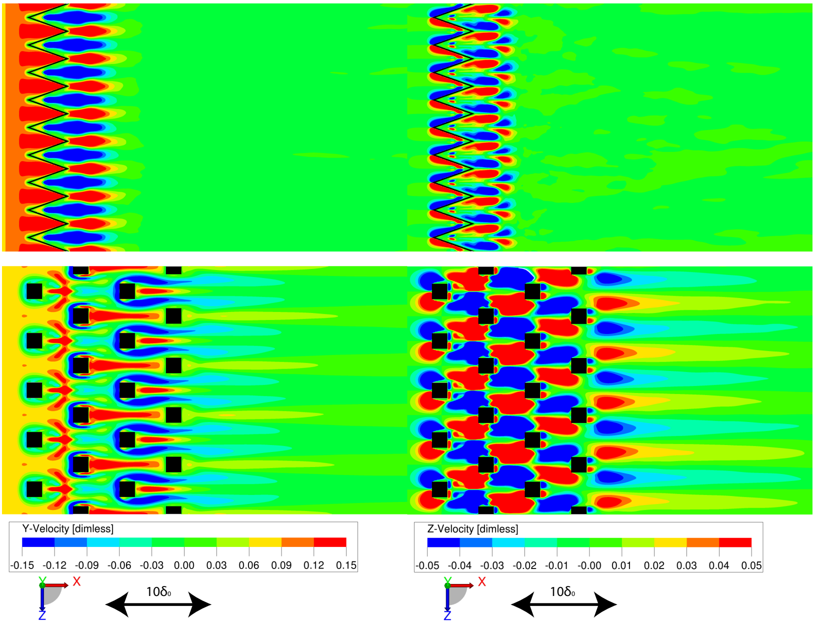

Figure 2.5: Mean wall-normal (left) and spanwise (right) velocity behind the zig-zag strip (top) and staggered grid of blocks (bottom) in a plane parallel to the wall at $y/\delta_0 = 1$

which is made visible by the negative streamwise velocity component in the figure. The size of the backflow is a variable for each row of blocks, where the largest backflow can be seen in the first row. This backflow gradually decreases per row of block due to the increased drag of the blocks, resulting in a lower convective velocity. Less energetic boundary layer profiles (see Reynolds stresses in Fig. 2.7 and Fig. 2.8) hits the next row of blocks while energy transfer takes place vertically in the boundary layer. Similar conditions are found back in applications, e.g. energy extraction from a row of aligned wind turbines. Numerical studies, such as the modeling of rows of actuator disks have been performed in the past [87]. Furthermore, the flow moves towards the wall before a block appears and away from the wall behind a block. This wall-normal movement (denoted by negative velocities in Fig. 2.5) is the strongest behind the second row of blocks, where it appears as a long streak of upward moving fluid flow. The interaction of the first row and second row also results in flow moving away from the wall while the interaction between the second and third row creates flow structures being pushed towards the wall (see also Fig. 2.3). The spanwise velocity component alters (positive and negative) as expected around a single block, creating a diverging and converging pattern around the staggered grid. Behind the last row of blocks, the non-uniformity stays for about $20\delta_0$, which could indicate periodical rows of packages of horseshoe vortices, to be confirmed in a later stage.

For the zigzag strip, uncorrelated flow features with minor streamwise, wall-normal and spanwise variations are observed earlier than by using a staggered grid of blocks (within $5\delta_0$). Directly behind the trip, the streaks are visible and backflow is observed together with a flow going away from the wall (as seen by the red streaks in the wall-normal velocity plot from Fig. 2.5). This behavior starts behind a downstream pointing tip of the zigzag strip. The upstream pointing tip on the other hand show a region with positive, but relatively small streamwise velocity ($u > 0$) with flow pointing towards the wall ($v < 0$). The spanwise component (Fig. 2.5) is clearly smaller using a zigzag strip compared to using a staggered grid of blocks. However, close to the downstream pointing tip, an altering pattern is present for the zigzag case. Positive oriented vortices (red and pointing down) are canceled and merged with negative orientated vortices (blue and pointing upwards) at the tip at a downstream location of the trip, enhancing the mixing which is useful for smaller and quicker recovery [69]. After the initial region with streaks a region follows where the average flow regains its spanwise uniformity, merges and further accelerates in streamwise direction and is slightly directed towards the wall. This region covers approximately $10\delta_0$, see Fig. 2.4, where after little variations is seen for the streamwise direction. This is expected for a fully developed turbulent boundary layer [73, 88].

In Fig. 2.6, iso-surfaces of Λ_2 colored by velocity magnitude (low speed blue, high speed red) illustrates the instantaneous flow topology around the bypass transition process, with a limited domain width in streamwise direction. The general trend due to the three-dimensional nature of the trip show a shear layer in which vortices roll up into spanwise coherent structures. These spanwise structures break up into individual arches that remain aligned according to the periodic nature of the trip. In both trip cases the arches are inclined at about 45 degrees with the wall, which can be associated with increasing wall-normal fluctuations, which were already observed in $u'v'$ fluctuations

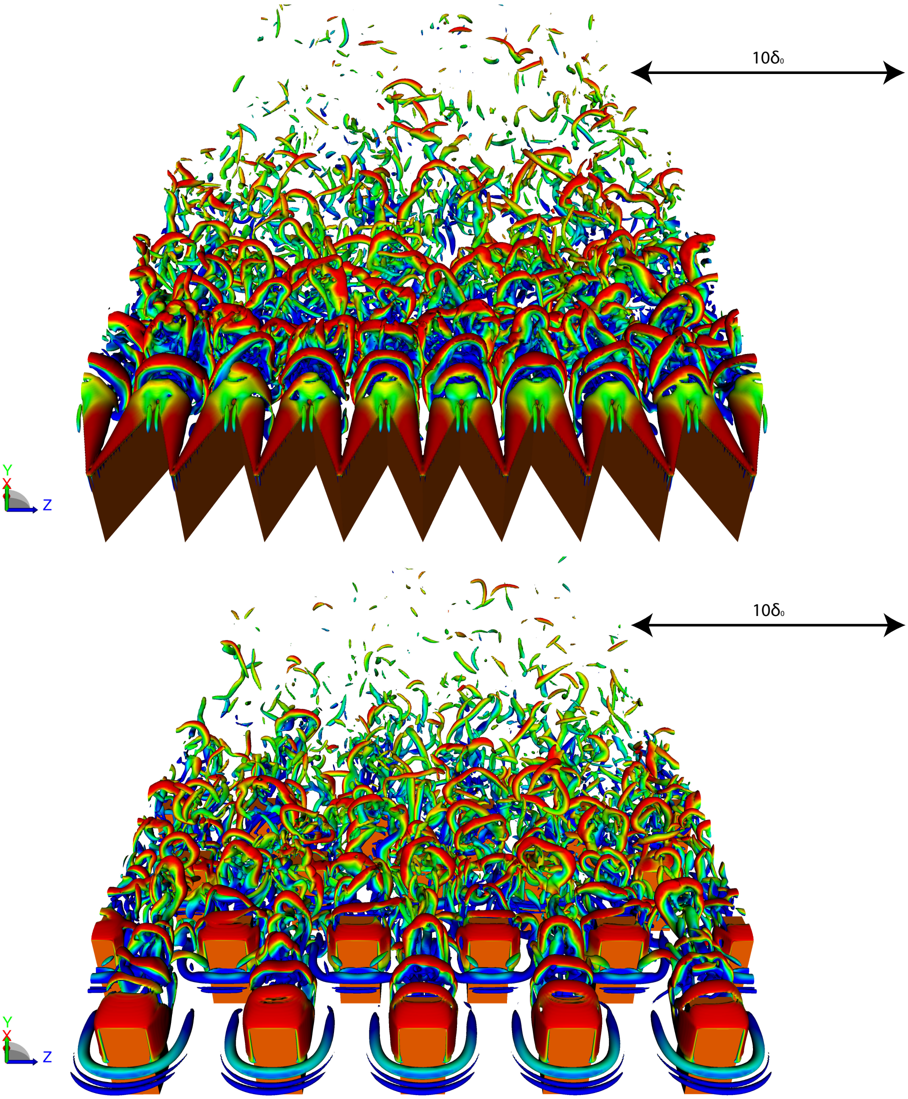

Figure 2.6: Iso-surface of Λ_2 colored by velocity magnitude illustrating the instantaneous flow topology of the bypass transition behind the zig-zag strip (top) and staggered grid of blocks (bottom)

in the previous section. This roll-up and orientation has been described by Ghaemi [89] before. Further downstream, the arches are merged with low speed quasi streamwise vortices (blue and green structures), resulting in the formation of hairpin like structures [90]. These legs become stretched because of the acceleration of the flow after the trip (Fig. 2.4) and rotate corresponding to their spanwise and wall-normal variations. These hairpin-like structures form packages after which they convect and dissipate further downstream [68, 89].

A difference between the staggered grid of cubic blocks and the zigzag strip is the spanwise merging of horseshoe vortices. The staggered grid enhances the effect of streaks of packages with hairpins, whereas the short spanwise wavelength between the arches of the zigzag strip enhances the merging process, so that, further downstream, no streamwise elongated streaks are present. This observation was already confirmed using Fig. 2.4 and 2.5.

The Reynolds spanwise normal stresses ($w'w'$) and shear stresses ($u'v'$) are presented in a streamwise-wall-normal plane through the last row of blocks and a downstream pointing tip for the staggered grid of blocks and zigzag strip respectively, see Fig. 2.7 and 2.8. The Reynolds stresses presented are about 5 times higher downstream then those in a general canonical developed turbulent boundary layer presented by, e.g. Klebanoff [91], which are $w'w' = 1.6 \cdot 10^{-3}$ and $u'v' = -0.8 \cdot 10^{-3}$. However, the order of magnitudes are similar to other, more recent studies behind turbulent transition [68, 92, 93]. This would imply that at least the current measurement domain shown in the figures (approximately $80\delta_0$) remains affected by trip.

Both shear stress plots ($u'v'$) show the occurrence of a shear layer emanating from the trailing edge of either a block or zigzag strip. The trailing edge of the trip separates the reversed flow near the wall from the higher speed streaks in the outer flow. In the velocity plot, this introduced an inflection point which is a clear source of the generation of turbulence. For the staggered grid of cubic blocks, the thickness of the layer is influenced by the next row of blocks as can been seen from Fig 2.7. The flow is compressed and pushed upwards by the individual blocks, resulting in a less thick shear layer compared to the results from the zigzag strip.

The spanwise normal stress levels ($w'w'$ in Fig. 2.8) are larger close the wall behind the separation compared to the trends found in shear stress levels. Behind the zigzag strip, the spanwise normal stress levels attain higher values compared to the other tripping mechanism. This is an indication for enhanced mixing towards a homogeneous turbulent boundary layer. This result is also in agreement with Fig. 2.5, where the breakup of spanwise structures is superior for a zigzag strip compared to a staggered grid of cubic blocks.

2.4.2. DOWNSTREAM DEVELOPMENT OF THE BOUNDARY LAYER

The downstream development of the Reynolds stresses suggests the proper transition towards a fully developed boundary layer. To confirm this result, line plots at $10\delta_0$ till $80\delta_0$ are plotted in Fig. 2.9, showing both mean streamwise velocity and Reynolds normal stresses. The mean flow seems to be heavily affected by both transition strips within a $20\delta_0$ downstream distance. On the other hand, the normal stresses seem to take at least $60\delta_0$ to recover the flow. The zig-zag strip shows a slightly larger boundary layer,

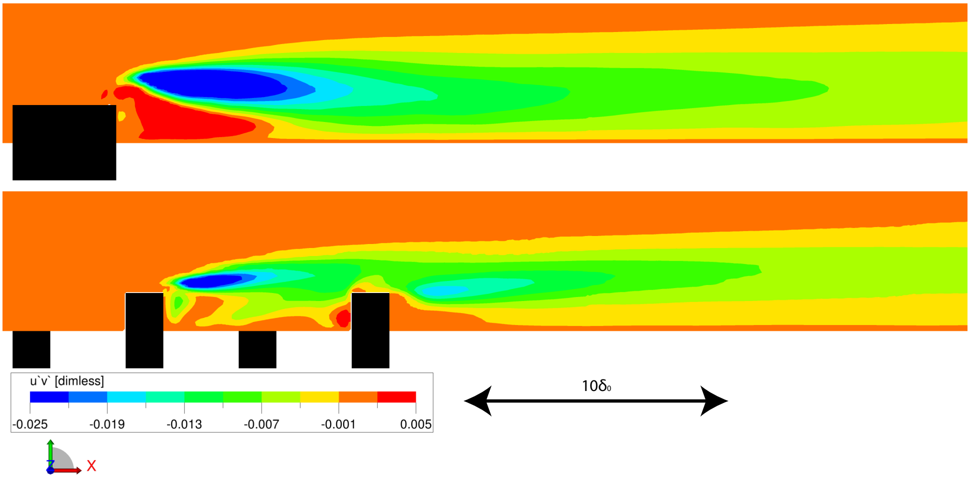

Figure 2.7: Reynolds shear stresses of streamwise, wall-normal direction in a streamwise-wall-normal plane behind the zig-zag strip (top) and staggered grid of blocks (bottom)

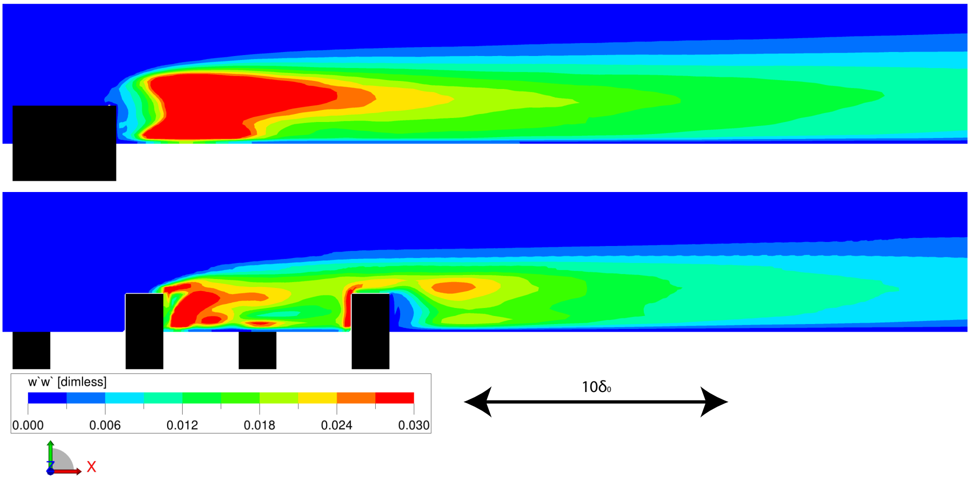

Figure 2.8: Reynolds normal stresses in spanwise direction in a streamwise-wall-normal plane behind the zig-zag strip (top) and staggered grid of blocks (bottom)

as already concluded in Fig. 2.7. In both bypass transitions, the shear layer thickness increases downstream while remaining at approximately the same height, while the average flow rebuilds towards a fully developed boundary layer. The indication of high local shear flow indicates the transport of energy from near the wall fluid towards the higher momentum-fluid available in the flow. This effectively results in re-energizing the boundary layers.

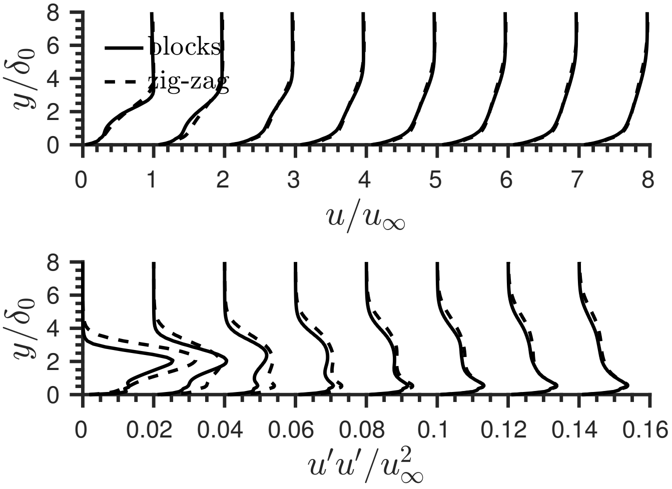

Figure 2.9: Line plots of the downstream development of the boundary layer. Mean streamwise velocity (top) and Reynolds normal stresses (bottom), separated by $10\delta_0$

To further investigate the recovery of the boundary layer, the shape factor at the same planes as before are extracted and plotted in Fig. 2.10. While the staggered grid of blocks attain slightly higher values close to the trip, both strips convergence to a shape factor of $H = 1.5$. Clearly, the zig-zag strip reaches this threshold earlier, at around $40\delta_0$, while the staggered grid of blocks needs to double the downstream distance to convergence.

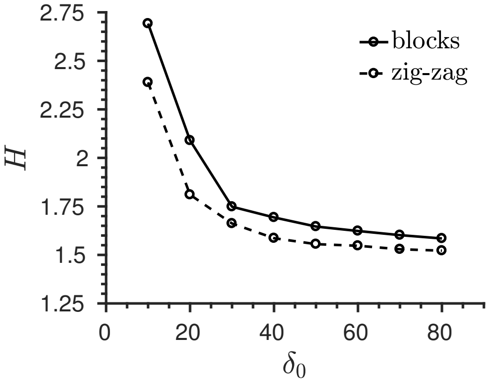

Figure 2.10: Development of shape factor downstream the transition strip

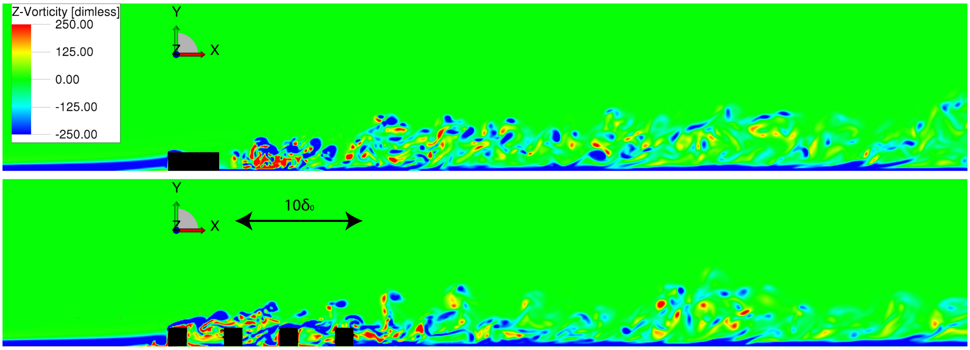

Figure 2.11: Instantaneous spanwise vorticity behind the zig-zag strip (top) and staggered grid of blocks (bottom) in a plane at mid-span

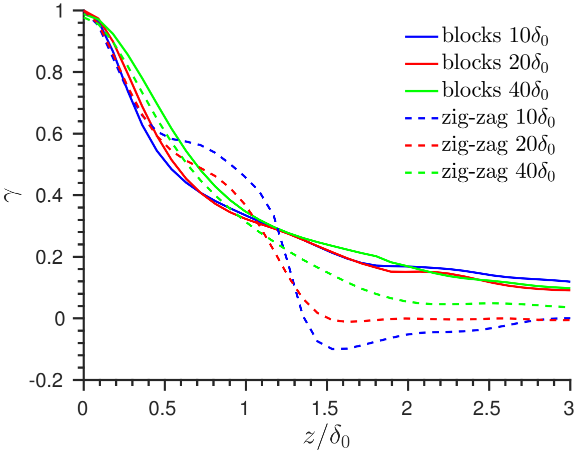

Figure 2.12: Wall pressure spanwise cross-correlation at different planes behind the transition strip

To further analysis the development of the boundary layer, an instantaneous view of the spanwise vorticity is plotted in Fig. 2.11. Spanwise vortices are present over the entire computational domain, but the largest, locally bundled, spanwise vortices are present until $10\delta_0$ downstream the zigzag strip, emphasizing the effective merging process of the hairpin like vortices. The staggered grid of blocks on the other hand only show a minor increase in spanwise vorticity directly downstream the last row of blocks (Fig. 2.6). It is thought that the spanwise wavelength of both trips will play an important role in this merging effect, in order to speed up the development of the boundary layer.

The visualization of the vortical structures as well as the mean velocity plots implies that the spanwise periodicity of arches gradually disappear downstream. While vortical structures as horseshoes, arches and low speed streaks keep present in the flow, the initial structures from the tripping brings in an important spanwise coherence to the flow. To investigate the spanwise coherence (App. C), the auto spanwise correlation of wall pressure fluctuations is analyzed downstream the trips (Fig. 2.12). The resulting profiles for the staggered grid of blocks show less of a decay compared to the zigzag trip results at the three downstream locations behind the trip. The zigzag strip on the other hand shows some dominating spanwise oscillations corresponding to the strong streaks behind the downstream pointing tips. The height of the correlation peaks drops quickly when going downstream, while a constant plateau around 0.0 is maintained at $40\delta_0$ spanwise distance. The staggered grid of blocks however shows a constant plateau around 0.075, which is evidence that large spanwise coherence structures remain present at downstream locations.

2.5. CONCLUSION

To force the flow from a laminar state into a turbulent state at a specific position of interest, a boundary layer transition trip is generally used. During more recent applications, transition strips were used to match transition locations and boundary layer growth so that similar trailing edge flow characteristics were obtained when comparing, e.g. airfoil noise simulations with acoustical experiments. Though the flow topology arising from the so-called bypass transition process is extensively addressed in the past, several issues are left open. The motivation for the current research is to understand the properties of simulated transition strips for future aero-acoustic simulations. A staggered grid of cubic blocks for transition is analyzed and compared with a more conventional, zigzag strip using flow results from the Lattice Boltzmann relation.

The velocity and pressure field is used to quantitatively visualize the flow topology field around both tripping devices. The trips are shown to be successful to enforce transition, but the observed transition scenario suggests that a zigzag strip is more efficient as a bypass transition process compared to the staggered grid of cubes since the spanwise vortices are undulated more effectively from the trip. This could be a result of a larger frontal area of the trip as well as a smaller wavelength of the zig-zag strip. These spanwise instabilities enhances the development of a canonical fully turbulent boundary layer. Visualizations of the mean flow reveals periodic streamwise streaks behind the transition strips, with the most distinctive streaks being visible behind the staggered grid of cubes. In general, a canonical fully turbulent boundary layer is experienced after $40\delta_0$ for a zig-zag strip, while the staggered grid of blocks need at least $80\delta_0$ to convergence. This is confirmed by analyses of shape factor, vorticity and spanwise coherence.

3

PRESSURE COHERENCE UNDER A TURBULENT BOUNDARY LAYER

> *as Sir Cyril Hinshelwood has observed,*
> *fluid dynamicists were divided into hydraulic engineers,*
> *who observed things that could not be explained,*
> *and mathematicians who explained things*
> *that could not be observed.*
>
> Sir James Lighthill

Important parameters for efficient acoustic scattering of a turbulent boundary layer are its auto-spectral density and spanwise coherence. In this chapter, the prediction of the streamwise and spanwise coherence length of the pressure field below a turbulent boundary layer at low Reynolds number generated using a recycling inflow method is estimated using different numerical LES models in an open-source Finite Volume based CFD package. Results are compared with DNS results, as well as with time resolved tomographic PIV data. Matching results are found for outer scaling mean and fluctuating velocity data as well as for the pressure spectrum data. The coherence function shows a similar decay with respect to various references. An exponential fit is applied to determine the coherence length. Agreement within one displacement thickness in streamwise and spanwise direction is found for the coherence length with semi-empirical data. The spanwise coherence length is considerably smaller than the streamwise coherence length, but indicates a clear peak in the low frequency regime originating from large coherent structures with relatively small amplitudes.

Parts of this chapter have been published in the AIAA Journal (2015) [94].

3.1. INTRODUCTION

IMPORTANT characteristics of the unsteady surface pressure field are its auto-spectral density and spanwise coherence. Several authors, such as Amiet [95] and Howe [55] have discussed diffraction theory regarding trailing edge noise. Here, the auto-spectral density and spanwise correlation length of hydrodynamic pressure fluctuations were used to estimate the acoustic far field spectrum. Amiet [95] and Howe [55] assumed that the incident pressure fluctuations on the surface below the turbulent boundary layer convect over the trailing edge, acting as an impedance discontinuity, where the fluctuations are scattered in the form of acoustic waves. In most aeroacoustic analyses, Corcos [96] model was used for the estimation of the spanwise coherence length instead of predicting it numerically. The theory of numerical predicting coherence forms the basis of the current study, as well as previous published experimental and numerical studies, such as the Large Eddy Simulation study of Christophe [97], the surface pressure measurements of Brooks and Hodgson [17], and the recent study of Pröbsting et al. [98] with high-speed tomographic Particle Image Velocimetry based pressure reconstruction.

The present study is set to validate the applicability of a Navier-Stokes based computational tool with boundary layer recycling function to simulate an infinite flat plate in order to determine the spanwise wall pressure coherence under a fully developed turbulent boundary layer of low Mach number flow. Numerical data is obtained from a Large Eddy Simulation (LES) approach that solves the larger turbulent scales, but models the smaller scales by means of both explicit and implicit closure models. Validation is performed based on Particle Image Velocimetry (PIV) and Direct Numerical Simulation (DNS) data, earlier presented by Pröbsting et al. [99].

3.2. METHODOLOGY

3.2.1. GOVERNING FLUID EQUATIONS

Since a low Mach number flow over an infinite flat plate is considered, the incompressible Navier-Stokes equations are used to describe the fluid dynamics. Furthermore, Newtonian fluid properties are assumed and gravity forces and other body forces are neglected, resulting in the following simplified set of equations, describing the conservation of mass and momentum [100]:

$$\nabla \cdot \mathbf{u} = 0, \tag{3.1}$$

$$\frac{\partial \mathbf{u}}{\partial t} + \nabla \cdot (\mathbf{u}\mathbf{u}) = -\frac{\nabla p}{\rho} + \nabla \cdot (\nu \nabla \mathbf{u}), \tag{3.2}$$

wherein $\mathbf{u}$ are the different velocity components, p is the pressure, ρ the density and ν the kinematic viscosity.

The governing fluid equations are solved by means of a Large Eddy Simulation (LES). This methodology resolves all large eddy scales, while smaller eddy scales are modeled. This methodology is known as the intermediate form between completely modeling the turbulence (Reynolds Averaged Navier-Stokes, RANS) and completely solving the turbulence (Direct Numerical Simulation, DNS). To obtain the acoustic near and far field from an incompressible flow simulation, a hybrid approach coupled with a tailored made Green function could be used which corrects for the non-compactness of the local, acoustic, source [40]. In this case, the acoustic scattering correction solves for the lack of acoustical data in an incompressible flow solution. Details are found in Ch. 4.

The discretized set of equations is solved in the open-source package OpenFOAM 2.2.0 using the Finite Volume Method on an collocated unstructured grid [101]. Time discretization is done by the second order backward difference scheme. For the spatial discretization, the velocity and pressure gradient are discretized using a second order, Gaussian linear interpolation (central differencing), while the velocity divergence is interpolated using a second order, Gaussian linear interpolation with filtering for high frequency ringing. For all other quantities defined in the turbulence model, the divergence term is interpolated using a second order, limited Gaussian linear interpolation. A linear upwind scheme is used instead when considering a simulation without eddy viscosity closure model (implicit simulation). Finally the Laplacian of the kinematic viscosity and the velocity is discretized using the second order, Gaussian unbounded, conservative scheme. Details are summarized by Jasak [100]. The transient solver for incompressible flow, PIMPLEFOAM, is used using the PIMPLE (merged PISO-SIMPLE) algorithm. PISO is an acronym for Pressure Implicit Splitting of Operators for time dependent flows while SIMPLE stands for Semi-Implicit Method for Pressure Linked Equations which is used for steady state problems [100]. The PISO algorithm neglects the velocity correction in the first step, but then performs one in a later stage, which leads to an additional correction for the pressure [102].

3.2.2. SUB GRID SCALE MODELS

Two sub-grid-scale (SGS) models, used for determining the eddy viscosity, are validated and compared; the homogeneous dynamic Smagorinsky model [103] and the selective Smagorinsky model [104]. In addition an implicit LES (ILES) is considered, where numerical schemes are used such that the inviscid energy cascade through the inertial range is captured accurately and the inherent numerical dissipation emulates the effect of the dynamics beyond the grid-scale cut-off [105].

The homogeneous dynamic Smagorinsky model is an algebraic eddy viscosity SGS model founded on the assumption that local equilibrium prevails [103]. In the homogeneous dynamic version, the eddy viscosity coefficient is calculated from the smallest resolved scales during the simulation. Averaging is performed in spanwise direction, i.e. homogeneous turbulence is assumed [100]. The selective Smagorinsky model on the other hand, is a local method validated specifically for wall bounded flows which is derived by Sagaut [104]. This SGS model is a combination of the basic Smagorinsky model together with a selection function, which will be locally turned on and off on a specific value of the local angular fluctuations of the instantaneous vorticity. This parameter determines the three dimensionality of the flow, and in this case, the angle between the vorticity vectors. The selection function, f_s, can be mathematically written as:

$$f_s(\theta,\theta_0) = \begin{cases} 1 & \text{if } \theta \le \theta_0 \\ r(\theta,\theta_0)^{1/2} & \text{else} \end{cases}, \tag{3.3}$$

with $r(\theta,\theta_0)$ defined as

$$r(\theta,\theta_0) = \frac{\tan^2(\theta/2)}{\tan^2(\theta_0/2)}. \tag{3.4}$$

Here θ is defined as the angle between the average vorticity of all neighbors cells and the own cell's vorticity, while the threshold has been set at $\theta_0 = 20°$.

3.2.3. RECYCLING METHOD

To reduce computational demands, a recycling method is used. The main idea behind the recycling and rescaling inflow modeling approach is to extract data at a station downstream of the inflow, and rescale it to account for boundary layer growth. In the approach by Lund [106], the flow at the extraction station is averaged in spanwise direction and in time, to allow the decomposition of the flow field in a mean and fluctuating part. The mean velocities ($\bar{u}_i$) and fluctuations (u'_i) are then rescaled according to the law of the wall in the inner region and the defect law in the outer region, and blended together using a weighted average of the inner and outer profiles:

$$\begin{aligned}(u_i)_{in} &= \left\{(\bar{u}_i)_{in}^{inner} + (u'_i)_{in}^{inner}\right\}\left[1 - W(\eta_{in})\right] \\ &+ \left\{(\bar{u}_i)_{in}^{outer} + (u'_i)_{in}^{outer}\right\}\left[W(\eta_{in})\right], \end{aligned} \tag{3.5}$$

with the weighting function defined as:

$$W(\eta) = \frac{1}{2}\left\{1 + \frac{1}{\tanh(\alpha)}\tanh\left[\frac{\alpha(\eta - b)}{(1-2b)\eta + b}\right]\right\}, \tag{3.6}$$

wherein $\eta = y/\delta$ indicates the outer coordinate scaling and $\alpha = 4$ and $b = 0.2$ are prescribed constants [106]. The inlet boundary layer thickness and momentum thickness are fixed on 5 mm and 0.5 mm respectively, so that the experimental conditions in a plane downstream are met.

3.2.4. DEFINITION AND ESTIMATION OF COHERENCE

For determination of the coherence length, first the coherence function should be evaluated. The coherence function ($\gamma^2(\omega, \Delta z)$) is the auto-power and cross-power density of the signals (App. C). Determining the coherence is valid for the case that the flow statistics are homogeneously distributed along the spatial dimension, stationary in time and for an infinite observation period. For a flat plate the first criterion is fulfilled when considering the spanwise direction. With restriction to very short separations, this is also valid for the streamwise direction. By definition, the coherence length is related to the integral of coherence function over the spatial separation Δz and therefore reduces to a function of frequency only:

$$l_z(\omega) = \lim_{L\to\infty}\int_0^L \gamma(\omega, \Delta z)\, d\Delta z. \tag{3.7}$$

This relation can be used to obtain the coherence length. However, due to convergence issues, first observed by Christophe [97] for his LES data with a finite observation period, the coherence does not approach zero for very large separations Δz and therefore, the integral might be unbounded. Instead, in this study a curve fitting approach based on an exponential function is applied (see [107]):

$$\gamma(\omega, \Delta z) = e^{-\frac{|\Delta z|}{l_z(\omega)}}. \tag{3.8}$$

The fit is performed for each discrete frequency and has shown to be a robust alternative to Eq. 3.7.

3.3. MODEL SET-UP

The current study investigates a turbulent boundary layer on a flat plate of 400 mm chord, with a wetted span of 40 mm (Fig. 3.1). The domain stretches 30 mm in wall-normal direction. Reference length and velocity scales are the boundary layer thickness and the free stream velocity at a plane 250 mm downstream. At a free stream velocity of $u_\infty = 10$ m/s the Reynolds number based on the local boundary layer thickness $\delta = 10.4$ mm is $Re_\delta \approx 6{,}800$ and based on the momentum thickness $\theta = 1.1$ mm is $Re_\theta \approx 750$. A complete overview of all model parameters from the current study is found in Tab. 3.1.

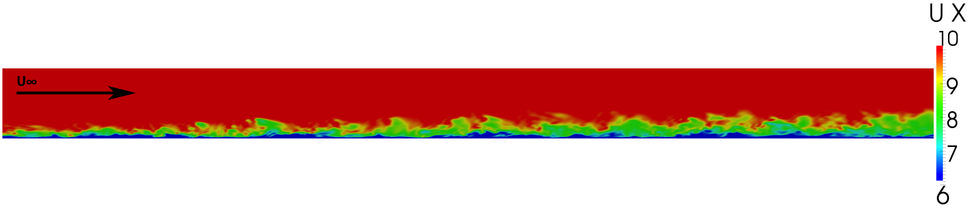

Figure 3.1: Snapshot at $t = 0.5$ s of streamwise velocity over the plate, clearly indicating the generation of a turbulent boundary layer

The domain is discretized in $800 \times 100 \times 80$ cells, resulting in vector sampling of $\Delta x/\delta \approx 0.048$ and $\Delta z/\delta \approx 0.048$ in streamwise and spanwise direction respectively. In wall-normal direction the sampling resolution ranges from $\Delta y/\delta \approx 0.004$ near the wall to $\Delta y/\delta \approx 0.1$ in the free stream. For the given Reynolds numbers, this results in $\Delta x^+ = 15$, $\Delta y^+ = 1.25$ and $\Delta z^+ = 15$. Vector spacing for the DNS and PIV reference results are $\Delta x/\delta \approx 0.033$, $\Delta y/\delta \approx 0.004$, $\Delta z/\delta \approx 0.030$ and $\Delta x/\delta \approx 0.036$, $\Delta y/\delta \approx 0.018$, $\Delta z/\delta \approx 0.036$ respectively [99]. Marching in time is variable in such a way that the flow Courant number stays below unity. In practice this yields time-steps of approximately $\Delta t \approx 2 \cdot 10^{-5}$ s. Pressure and velocity fluctuations are stored each four steps, which results in a temporal sampling of $\Delta t u_\infty/\delta \approx 0.07$ ($\omega\delta^\star/u_\infty \approx 13.3$). For the present study, approximately 4,000 samples equivalent to a non-dimensional time interval of $T u_\infty/\delta \approx 300$ are used for the analysis (App. B).

At the inlet of the model, a recycle inflow condition is used for a turbulent boundary layer. At the outlet and top of the model, velocity is imposed by a Neumann boundary condition. The wall is modeled with a no-slip condition. Both sides of the domain are periodic, to simulate an infinite span. Regarding pressure boundary conditions, the top boundary is fixed, while all other boundaries are modeled using a zero gradient condition.

Table 3.1: Boundary layer parameters

Parameter	**Symbol**	**LES**	**PIV** [99]	**DNS** [99]
Boundary layer thickness [mm]	δ	10.4	9.4	9.4
Displacement thickness [-]	$\delta^\star/\delta$	0.16	0.16	0.18
Momentum thickness [-]	θ/δ	0.11	0.12	0.12
Wall shear velocity thickness [-]	u_τ/u_∞	0.045	0.052	0.053
Shape factor [-]	H	1.48	1.45	1.50
Reynolds number [-]	Re_δ	6,800	6,240	8,185
	Re_θ	750	730	1,000
	Re_τ	310	436	325

3.4. RESULTS

Now that the methodology and boundary layer characteristics are defined, the results of the downstream plane are discussed. The boundary layer is investigated using mean velocity and Reynolds stresses plots. Furthermore the wall pressure under the boundary layer is analyzed and the streamwise and spanwise coherence function are determined. Using this function, an estimation is made for the coherence length.

3.4.1. MEAN VELOCITY AND REYNOLDS STRESSES

At a plane 250 mm downstream of the inlet, measurements were taken for this study. All boundary layer characteristics are summarized in Tab. 3.1. The PIV results are obtained from planar PIV measurements performed by Pröbsting et al. [99] on a flat plate in a low speed wind tunnel facility, where, at the leading edge, the flow was tripped using a strip with 3D roughness elements. The DNS results on the other hand are obtained from a compressible direct simulation of a turbulent boundary layer using the algorithm described by Pirozzoli and Bernardini [108, 109].

The mean velocity profiles for the different models scaled with inner and outer scaling variables are depicted in Fig. 3.2 and 3.3 respectively. The lines closely correspond to the analytical expression in the viscous sublayer: $y^+ = u^+$. For the law of the wall, a Von Karman constant of $\kappa = 0.35$ is used to fit well, which is in line with the boundary layer flow analysis from [110]. As an average for each LES model, a shape factor of $H = \delta^\star/\theta = 1.5$ is found, which confirms the presence of a developed turbulent boundary layer. Close agreement is found for all simulations and comparison data.

The distribution of the Reynolds stress tensor is depicted in Fig. 3.4. The considered closure models show perfect agreement with each other in all parts of the boundary layer. An overestimation of the $u\prime u\prime$ Reynolds stresses is observed close to the wall when comparing the results to the DNS results, whereas it matches the PIV results well. Wall normal fluctuations on the other hand are under predicted with respect to the DNS results. This discrepancy could possibly be assigned to the slight variance in displacement thickness $\delta^\star/\delta = 0.16$ for the LES versus 0.18 for the DNS, indicating a slightly more turbulent profile for the LES simulations.

As an indication for the outer time scale the eddy turn over time is estimated with $\delta/u_\infty \approx 1$ ms or a non-dimensional frequency of $\omega\delta^\star/u_\infty \approx 1$. Regarding the inner scale,

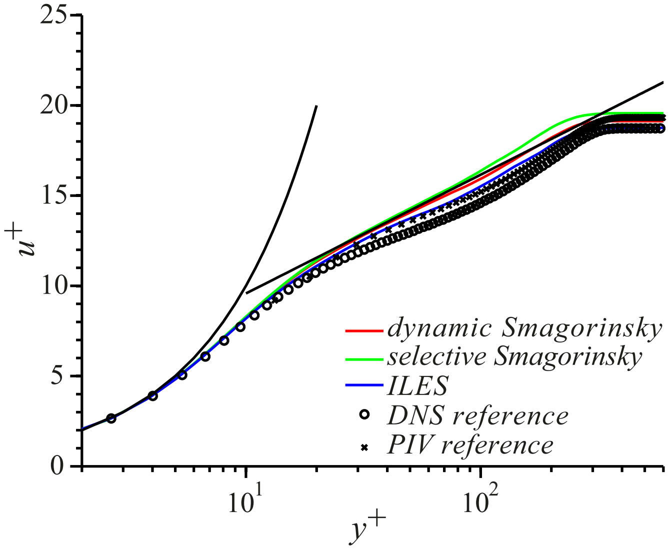

Figure 3.2: Mean velocity in outer scaling

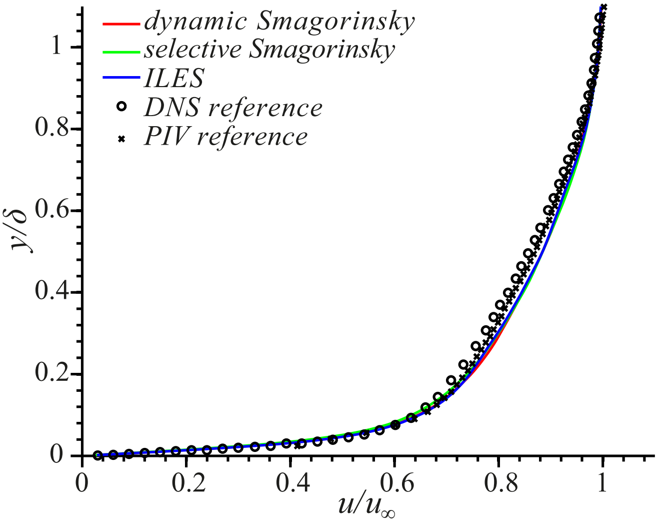

Figure 3.3: Mean velocity in outer scaling

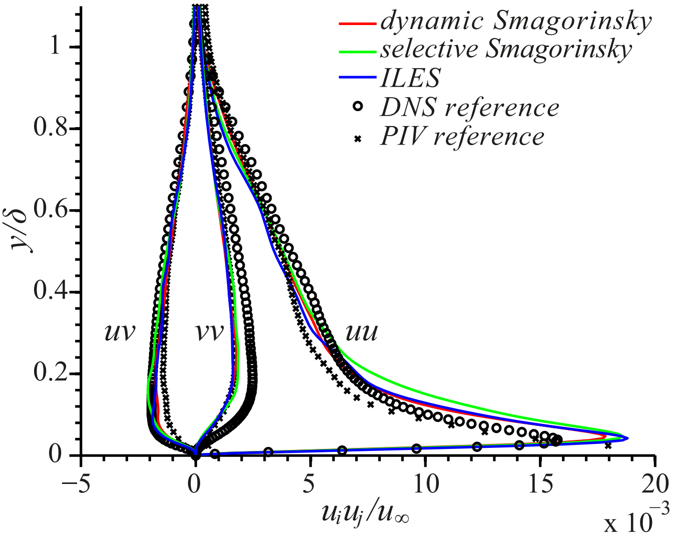

Figure 3.4: Reynolds stress profiles in outer scaling

$\delta_\nu/u_\tau \approx 73$ μs with $\delta_\nu = \nu/u_\tau$. In non-dimensional units, this results in $\omega\delta^\star/u_\infty \approx 14.5$. Since the temporal sampling of the LES was set at $\omega\delta^\star/u_\infty \approx 13.3$, it is sufficient to sample the outer time scale, but not the inner one. In the remainder of this study, $\delta^\star/u_\infty$ and $\delta^\star$ are used as outer time and length scale respectively, while δ_ν/u_τ and δ_ν are used as inner scales.

To further discuss the velocity results, the spatial resolution is considered by means of an instantaneous visualization of the streamwise iso-surface at $u/u_\infty = 0.6$ in Fig. 3.5. The organization of the turbulent boundary layer is illustrated by streamline aligned low- and high-speed regions. The distance between regions of low and high speed velocity in the inner region of the boundary layer, about half the spanwise distance between two velocity iso-surfaces, is on the order of 100 viscous lengths δ_ν, typically for Reynolds numbers $Re_\theta < 6,000$ ([90]).

The unsteady organization and evolution of coherent structures within the turbulent boundary layer is investigated by means of Fig. 3.6, where the second invariant of the velocity gradient tensor (Q) is plotted. Multiple low- and high-speed regions illustrate the organization of the turbulent boundary layer. The interaction between the low-speed streaks (blue) and vortical structures (red) are shown by means of hairpin packets, full hairpins, legs and cane vortices.

3.4.2. WALL PRESSURE SPECTRUM AND COHERENCE

Pressure fluctuations on the wall are recorded mid-span in the considered plane. In Fig. 3.7, an instantaneous image of the wall pressure field at the location of interest is displayed. Examination shows slightly spanwise elongated patches of low and high pressure. This result is also found in the comparison study.

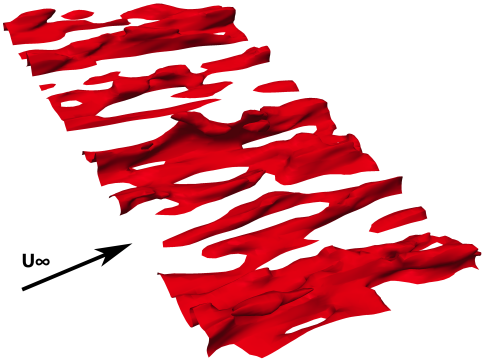

Figure 3.5: Instantaneous visualization of streamwise velocity iso-contours ($0.6U_\infty$)

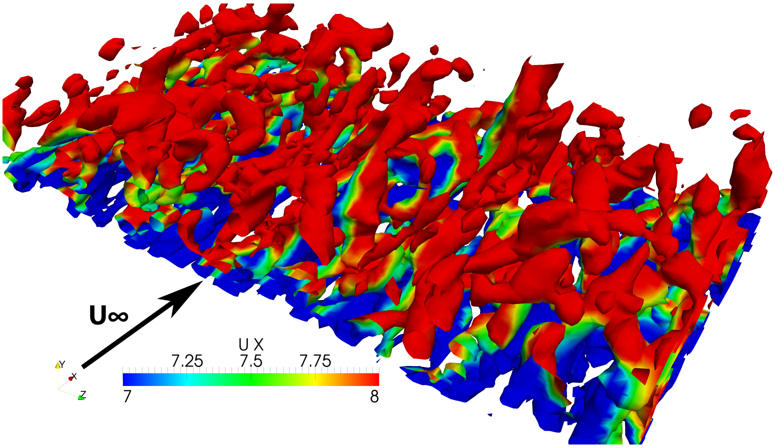

Figure 3.6: Instantaneous visualization of second invariant of the velocity gradient tensor iso-contours ($Q = 0.2 \cdot 10^6$), colored by the streamwise velocity

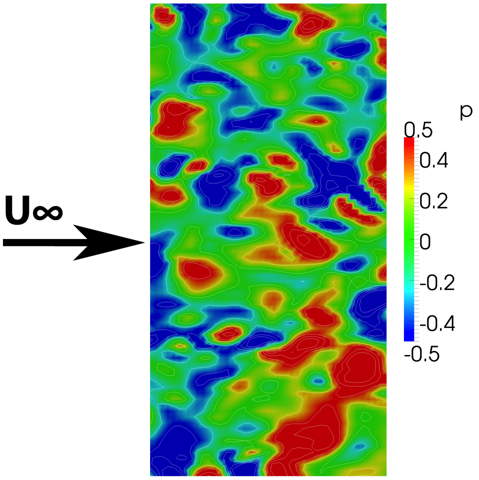

Figure 3.7: Instantaneous visualization of the wall pressure field visualized by contours of p'

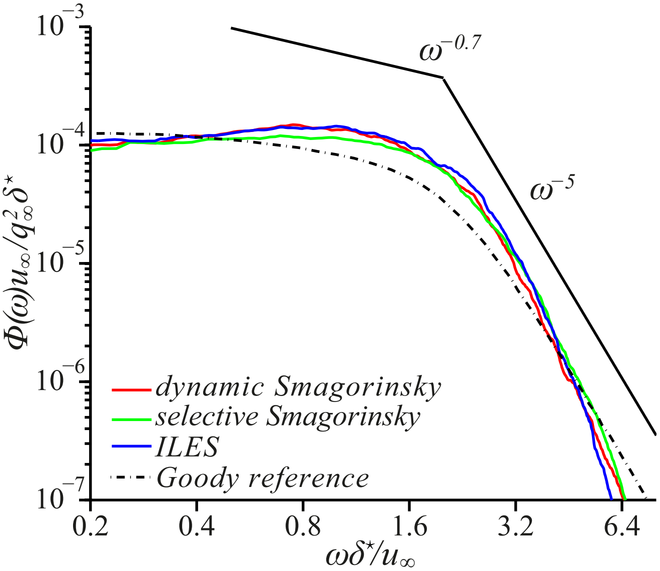

Figure 3.8: Pressure spectrum scaled with outer variables

The raw mid plane microphone signal is transferred to a Power Spectral Density (PSD) signal using Welch's [111] method, together with a Hanning window of 128 samples with 50 % overlap, normalized using $q = \frac{1}{2}\rho_0 u_\infty^2$ and $\delta^\star$ and plotted in Fig. 3.8 as well as an estimation of the spectrum provided by the model of Goody [112]. The selective Smagorinsky model seems to follow the decay the best, but still at a slope slightly larger then ω^{-5}. At the mid frequencies, the LES overestimates the PSD compared to the analytic Goody model result with $1-3$ dB. The indicated slope of $\omega^{-0.7}$ is characteristic for the overlap region, which becomes narrow for very low Reynolds numbers [112].

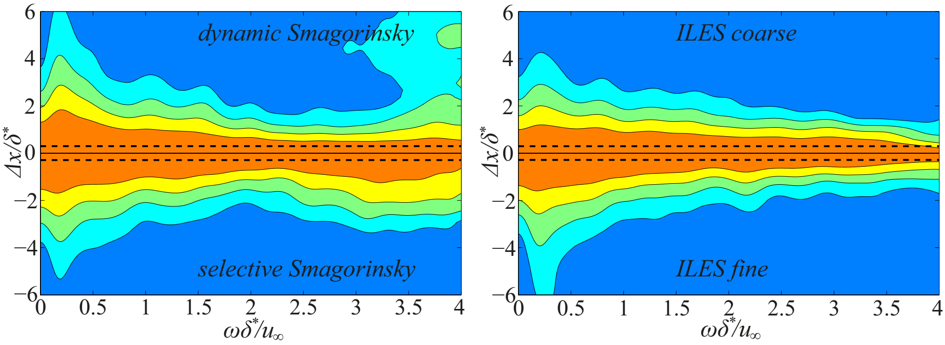

Figure 3.9: Streamwise magnitude squared coherence function $\gamma_p^2(\omega,\Delta x)$ of pressure fluctuations on the surface, indicated by iso-surface limits of: $0.0-0.2$ (blue), $0.2-0.4$, $0.4-0.6$, $0.6-0.8$ and $0.8-1.0$ (orange)

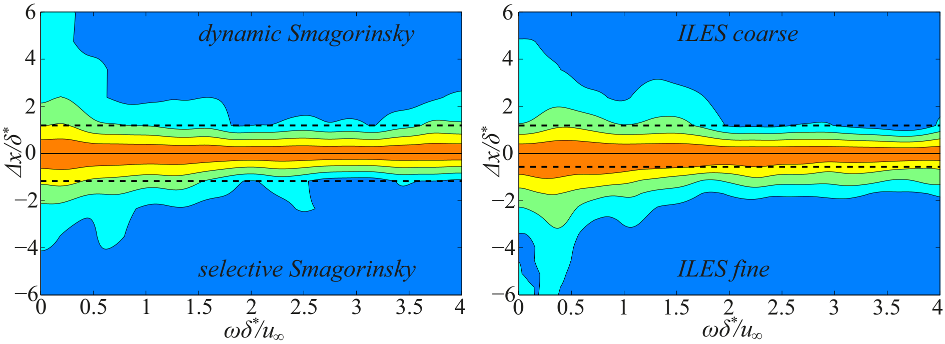

Figure 3.10: Spanwise magnitude squared coherence function $\gamma_p^2(\omega,\Delta z)$ of pressure fluctuations on the surface, indicated by iso-surface limits of: $0.0-0.2$ (blue), $0.2-0.4$, $0.4-0.6$, $0.6-0.8$ and $0.8-1.0$ (orange)

The results for the wall pressure coherence in streamwise and spanwise direction are found in Fig. 3.9 & 3.10 by means of a contour plot. In general, the coherence along the streamwise direction attains much higher values at low frequencies and decays beyond the resolvable scales at frequencies higher than $\omega\delta^\star / u_\infty \geq 4$ compared to its spanwise counterpart. At moderate frequencies, coherence increases for both Smagorinsky models again, resulting in erroneous results. This type of noise could possibly be introduced by the dynamics of constantly changing the eddy viscosity coefficient in the closure model. However, this hypothesis needs further research.

The coherence of pressure fluctuations over the span show a substantially faster decay compared to the streamwise direction, indicating that the resolution of the simulation is a key parameter. Therefore, an implicit simulation with finer spanwise resolution ($\Delta z/\delta \approx 0.024$) is also run and compared with the standard mesh ($\Delta z/\delta \approx 0.048$). Results of the pressure coherence function in spanwise direction is also found in Fig. 3.10. Apparently, decreasing the cell size increases the prediction of coherent structures at all frequencies. The peak around $\omega\delta^\star/u_\infty = 0.35$ is frequently found in literature, e.g. in [99].

The results of the final estimation of the coherence length involves the integration of the coherence function. The results are depicted in Fig. 3.11 & 3.12. The streamwise coherence length is considerably larger than the spanwise coherence length, especially for low frequencies. As a comparison, the PIV and DNS results are added as well as the analytic prediction from Corcos model [96].

Regarding the streamwise coherence length, a closer correspondence is found with the DNS data. A decay in l_x is found for increasing frequencies, which is consistent with the reference results. Only the homogeneous dynamic Smagorinsky and selective Smagorinsky start to deviate from this empirical solution by a sudden increase in coherence length at high frequencies, which were already visible in the results from Fig. 3.9. The result from the implicit simulation shows that a mesh refinement is required for a better match with the DNS results. The streamwise coherence estimate from Corcos [96] start to match at $\omega\delta^\star/u_\infty \approx 1.0$ and continue showing a similar decay. Please note that the Corcos model rely on empirical constants and have been validated for considerably higher Reynolds numbers only, which might explain the large discrepancies at the lowest frequencies. Another reference model should be considered for a better comparison, such as the model from Efimtsov [113] which predicts a decrease of coherence at lower frequencies.

The spanwise coherence result in Fig. 3.12 also match with the decay and values of the empirical model of Corcos [96] in the higher frequency regions, whereas in the lower frequency region the model is likely to behave incorrect. In the lower frequency regions, the error does not exceed one displacement thickness error with respect to the DNS and PIV results. Note that the coherence length estimate is only a small fraction of the displacement thickness $\delta^\star$, which implies that the majority of the spanwise elongated structures are of the order of the displacement thickness. Therefore, at low frequencies, the decrease in spanwise cell size enables better capturing of these structures, as seen in Fig. 3.10. But still, the spatial resolution and the limited measurement dynamic range are considered as the main limiting factors.

3.5. CONCLUSION

In the present study, the prediction of the streamwise and spanwise coherence length of the pressure field below a turbulent boundary layer at low Reynolds number generated using a recycling inflow method is estimated using different numerical LES models in an open-source Finite Volume based CFD package. Results have been compared to DNS and PIV results from Pröbsting et al. [99], as well as empirical models from Goody [112] and Corcos [96].

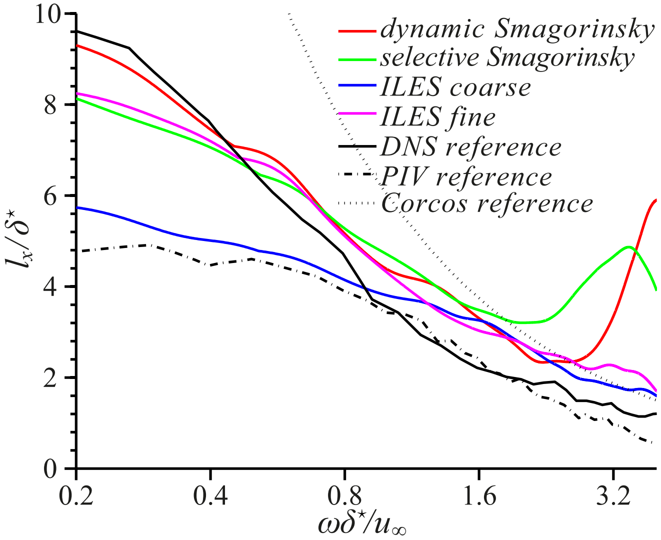

Figure 3.11: Streamwise coherence length

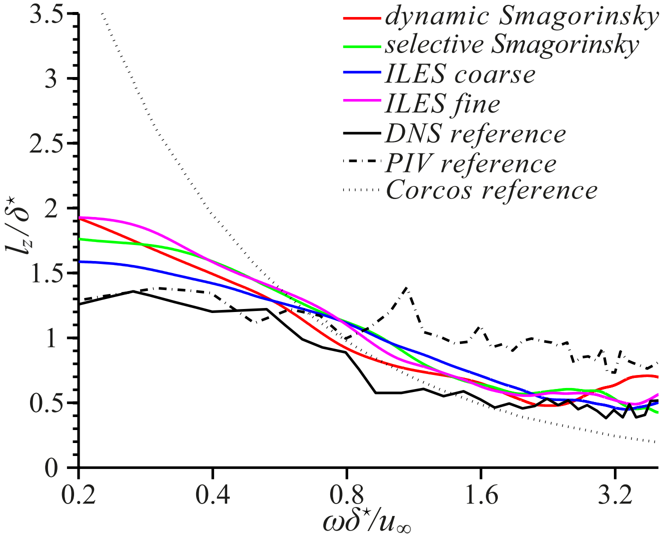

Figure 3.12: Spanwise coherence length

Results for outer scaling mean and fluctuating velocity data are in good agreement with the PIV data, whereas the comparison with the DNS results shows discrepancies in the viscous sub-layer. The trend of the pressure spectrum is confirmed by the empirical model of Goody [112], with a slightly faster decay at the higher frequencies for the LES models. Regarding the streamwise and spanwise pressure coherence, the spanwise coherence length is significantly smaller than the streamwise coherence length, indicating low amplitude structures. For both spatial directions, the decay matches the analytic and reference result at intermediate and high frequencies. A mismatch in the low frequency regime of the coherence length estimation is found between Corcos [96] model and the numerical and experimental results, which likely will be solved when considering a higher fidelity reference model such as the model presented by Efimtsov [113]. A close look into the spanwise coherence shows that it is mainly limited by its small length and strength relatively to the mesh resolution. Increasing the spanwise mesh resolution enables a better prediction of the coherent structures at the lower frequencies, shown in Fig. 3.10, but this need further examination in a future study.

II

TRAILING EDGE NOISE

4

NON-COMPACTNESS USING INCOMPRESSIBLE FLOW DATA

> *There are two possible outcomes:*
> *If the result confirms the hypothesis,*
> *then you've made a measurement.*
> *If the result is contrary to the hypothesis,*
> *then you've made a discovery*
>
> Enrico Fermi

Efficient tools for the determination of acoustic sources around wind turbines are necessary to further reduce its noise footprint. These simulations should be computational efficient and should be able to capture acoustic sources in the compact and non-compact regime, as the frequency range of interests covers both regimes. Many researches attempted to use Curle's analogy, which determines the acoustic spectra while taken into account acoustic dipole sources in the vicinity of a surface. When considering an incompressible flow solution, this theory provides accurate result when only a compact source body is involved, but lacks of accuracy when the order of the acoustic wavelength is smaller then the source body. To overcome this problem of an inaccurate acoustic source formulation, scattering has to be taken into account. A Boundary Element Method that uses Curle's analogy in combination with a correction for the scattering is used to predict the sound and compared to a general formulation of Curle's analogy. This is shown in this study by predicting trailing edge noise from a 25 *degrees beveled plate with different rounding radii under low Mach number, high Reynolds number conditions. The flow result is obtained by solving the incompressible Navier-Stokes equations using an open-source Finite Volume based package.*

Parts of this chapter have been published in the AIAA Journal (2017) [114].

4.1. INTRODUCTION

As mentioned in the introduction of this thesis, the airfoil self-noise originates from unsteady flow over an airfoil. Local disturbances of the surface pressure, introduced by and convected with the turbulent eddies, are scattered over the trailing edge. Due to the small length scale and high convection velocity of the turbulent eddies, the surface pressure fluctuations are typically encountered at high Strouhal number and its directivity pattern shows a bias towards the leading edge (i.e. in upstream direction) [7, 11].

A different situation is encountered at beveled trailing edges. Here, flow separation is observed at the beveled surface upstream of the trailing edge and separation noise can occur [115]. This flow separation introduces a shedding component to the wake flow with large, coherent, velocity fluctuations. The associated length scale is often characterized in terms of the wake thickness and associated to the bluntness of the trailing edge, for instance the thickness of the plate. If this length scale is large compared to the boundary layer thickness, the tonal noise component associated to such coherent vortex shedding processes becomes a prominent feature of the acoustic emission [11]. Beveled trailing edge geometries have served for validation purposes in the past, such as the study of Wang and Moin [29].

Generally speaking, the problem of sound generated aerodynamically has been successfully addressed in the past by Lighthill's theory [46] and extended by Curle [14] to include sound produced in the vicinity of solid surfaces. This theory proved its ability to predict sound from compact acoustic sources, for example sound originating from shedding. However, if one would like to incorporate the scattering effect, which appears when the unsteady flow produces sound around wavelengths comparable to the body dimensions, the source term should be adjusted to incorporate the so called, non-compact sources. Examples of non-compact sources are high frequency components of the noise produced by turbulence convecting over the trailing edge of a plate, but also retarded time differences between different parts of sound produced by the body over itself. Non-compactness should be included in the source term when applying an integral solution based on an aeroacoustic analogy, such as Curle's analogy. A straightforward solution to include this acoustical information would be by applying a high-fidelity, compressible flow solution using high-order schemes with low dissipation and dispersion. This will then both include the incident and scattered pressure effects. However, the numerical costs associated with these methods is still too expensive for industrial solutions [39].

To overcome erroneous results when determining non-compact acoustic souces from an incompressible trailing edge noise calculation, this study proposes an acoustic correction for when the surface source term is lacking acoustic scattered information. An earlier study by Schram [40] proposed a novel correction for taking into account scattering information, and validated the code by means of two vortex filaments in an infinite two-dimensional duct. More advanced methods nowadays are for example the stochastic noise generation and radiation (SNGR) models [116], used for the prediction of trailing edge noise cases. The current study presents acoustic results from a 25 degree beveled trailing edge, where the flow data is obtained from an open-source, transient, Finite Volume (FV) based Computational Fluid Dynamic (CFD) solution of the incompressible Navier-Stokes (N-S) equations [100]. Small scale turbulence is modeled by means of a Large Eddy Simulation (LES), using a dynamic Smagorinsky model. A turbulent boundary layer along the entire flat plate is generated using Lund's rescaling theory. The acoustic far-field pressure is obtained by successfully decoupling the system, since the amplitudes of the acoustic fluctuations are much smaller compared to the fluid fluctuations. The sound is predicted by Curle's analogy using the following two source field approaches: the incompressible source description without and with numerical treatment such that the solution will account for scattering of the sources.

4.2. METHODOLOGY

4.2.1. SOURCE FIELD FLOW SIMULATION

Since a low Mach number flow over an infinite flat plate is considered, the incompressible Navier-Stokes equations are used to describe the fluid dynamics. Furthermore, Newtonian fluid properties are assumed and gravity forces and other body forces are neglected, resulting in the following simplified set of equations, describing the conservation of mass and momentum [100]:

$$\begin{aligned} \nabla \cdot \mathbf{u} &= 0, && (4.1) \\ \frac{\partial \mathbf{u}}{\partial t} + \nabla \cdot (\mathbf{u}\mathbf{u}) &= -\frac{\nabla p}{\rho} + \nabla \cdot (\nu \nabla \mathbf{u}), && (4.2) \end{aligned}$$

wherein $\mathbf{u}$ are the different velocity components, p is the pressure, ρ the density and ν the kinematic viscosity. The governing fluid equations are solved by means of a Large Eddy Simulation (LES). This methodology resolves all large eddy scales, while smaller eddy scales are modeled. This methodology is known as the intermediate form between completely modeling the turbulence (Reynolds Averaged Navier-Stokes, RANS) and completely solving the turbulence (Direct Numerical Simulation, DNS).

The discretized set of equations is solved in the open-source package OPENFOAM [100], based on the Finite Volume Method (FVM). Time discretization is performed via a second order backward difference scheme. Regarding the spatial discretization, the velocity gradient is discretized using a cell limited Gaussian linear integration with filtering for high frequency ringing, while the velocity divergence is interpolated using a second order, Gaussian linear upwind interpolation. All other flow quantities are discretized using the van Leer interpolation scheme. These schemes are in general more dissipative than standard linear schemes, but with the current spatial mesh resolution, the numerical diffusion will stay sufficiently small to maintain enough resolution into the inertial range. Finally, the Laplacian operator is discretized using the second order, Gaussian explicit non-orthogonal correction scheme. Further details of the discretization schemes are summarized by Jasak [100]. The large time-step transient solver for incompressible flow, PIMPLEFOAM, is used using the PIMPLE (merged PISO-SIMPLE) algorithm. PISO is an acronym for Pressure Implicit Splitting of Operators for time dependent flows while SIMPLE stands for Semi-Implicit Method for Pressure Linked Equations which is used for steady state problems [100]. The PISO algorithm neglects the velocity correction in the first step, but then performs one in a later stage, which leads to additional correction for the pressure [102].

The proposed subgrid scale (SGS) model in this study is the dynamic Smagorinsky model [103]. This model is an algebraic eddy viscosity SGS model in which the

Smagorinsky coefficient is calculated dynamically. These coefficients are determined as part of the flow calculations, and use the energy content of the smallest resolved scales to locally determine the value of the closure coefficients. This implies, however, the behavior of the smallest resolved scale is analogous to that of the subgrid scales.

To perform a LES on an infinite flat plate within current computational demands, a recycling method is used. The main idea behind the recycling and rescaling inflow modeling approach is to extract data at a station downstream from the inflow, and rescale it to account for boundary layer growth. In the approach found by Lund [106], the flow at the extraction station is averaged in spanwise direction and time, to allow the decomposition of the flow field in a mean and fluctuating part. The mean velocities ($\bar{u}_i$) and fluctuations (u'_i) are then rescaled according to the law of the wall in the inner region and the defect law in the outer region, and blended together using a weighted average of the inner and outer profiles:

$$\begin{aligned}(u_i)_{in} &= \left\{(\bar{u}_i)_{in}^{inner} + (u'_i)_{in}^{inner}\right\}\left[1 - W(\eta_{in})\right] \\ &+ \left\{(\bar{u}_i)_{in}^{outer} + (u'_i)_{in}^{outer}\right\}\left[W(\eta_{in})\right], \end{aligned} \tag{4.3}$$

with the weighting function defined as:

$$W(\eta) = \frac{1}{2}\left\{1 + \frac{1}{\tanh(\alpha)}\tanh\left[\frac{\alpha(\eta - b)}{(1-2b)\eta + b}\right]\right\}, \tag{4.4}$$

wherein $\eta = y/\delta$ indicates the outer coordinate scaling and $\alpha = 4$ and $b = 0.2$ are prescribed constants [106].

4.2.2. ACOUSTIC ANALOGY

Within the field of Computational Aero-Acoustics (CAA) a distinction is made between direct and hybrid methods. Direct CAA methods solve the full compressible flow equations for determining both the hydrodynamic and acoustic pressure fluctuations. The domain covers both the flow field and at least the source and near acoustic field. Due to the high computational cost originating from the large scale separation of hydrodynamic fluid and acoustic pressure fluctuations, a direct calculation is restricted to simple geometries and low and moderate Reynolds numbers. In a hybrid method, the flow and acoustic field are calculated separately, so that the numerical method can be optimized for the physics to be solved. In this study, the sound is predicted by two approaches.

Firstly, the acoustic field is determined based on the non-homogeneous wave equation from Lighthill [46], but extended with surface sources in presence of turbulent fluctuations near a solid body. Curle's analogy [14] is translated to the frequency domain [117], resulting in an equation known as the Helmholtz equation. Furthermore, by assuming subsonic rectilinear motion of all acoustic sources, an efficient and easy implementable form is obtained which determines the far field noise from non-linear near-field flow quantities in an integral solution purely containing surface sources:

$$c_0^2\rho'(\mathbf{y},\omega) = -\int_{f=0} F_i(\mathbf{x},\omega)\frac{\partial G(\mathbf{y};\mathbf{x})}{\partial y_i}\,ds, \tag{4.5}$$

wherein G indicates the three dimensional free-field Green function including convective and Doppler effects [117] and F includes the source term from the incompressible flow simulation, which in time domain reads:

$$F_i = p\hat{n}_i. \tag{4.6}$$

Herein, p being the hydrodynamic pressure on the wall and $\hat{n}_i$ the outward pointing normal vector on the surface in the ith direction. Furthermore, $\mathbf{x}$ denotes the three-dimensional source coordinates while $\mathbf{y}$ indicates the current observer position. The methodology is implemented in MATLAB and correctly predicts sound for the compact body regime.

A numerical adaption to this method for non-compact bodies, to account for the missing acoustical information of scattering effects, is applied in the BEM formulation as presented by Schram [40]. This approach consists of the discretization of the boundary integral solution of the Helmholtz equation, assuming a free-field Green's function for the calculation of the acoustic field to the far field microphone position. Similar efforts have been done by Takaishi et al. [118], which derived a numerical tailored Green's function by means of a BEM for non-compact bodies. When placing the listener directly on the source surface instead of far away from the sound production region in a uniform region, as done in Curle's analogy, an adapted form of Eq. 4.5 is found. Without any loss of generality, we can further decompose the pressure fluctuations in a hydrodynamic part, which can be obtained from an incompressible flow model, and an acoustic part, which will be the solution to our problem. This implicit integral equation is resolved using a BEM in SYSNOISE [119]. Once the acoustical part of the wall pressure fluctuation is obtained, it is summed with the hydrodynamic component from the fluid flow simulation to yield the complete dipole source term for Curle's analogy. Further details on the numerical implementation are summarized in the paper by Schram [40].

4.3. TEST CASE

The geometry of interest used in the simulations was a 20 mm thick (h), $1.5h$ span (d) flat plate with an asymmetrically 25 degrees trailing edge, characterized by a radius of curvature of $R/h = 0$. Modeled chordwise extension of the plate is $l = 18h$. The uniform flow under consideration is 10 m/s, which ensures a chord based Reynolds number of $270,000$. The domain stretches for $3h$ in both wall normal directions and extends $9h$ in the wake region. Final mesh resolution after resolution study in streamwise, wall-normal and spanwise direction at the beveled plate is $x^+ = 55$, $y^+ = 1$ and $z^+ = 11$ respectively, corresponding to a total cell size of 11.4×10^6 cells. This is, according to Wagner [39], sufficient enough to encapsulate the acoustic problem. A close up near the beveled edge of the mesh is found in Fig. 4.1.

The velocity inflow is prescribed according to the recycling method discussed in the previous section. The velocity outlet is modeled using a Neumann condition. A no-slip condition for the flat plate wall is used and top and bottom are modeled as a frictionless wall. The front and back patches are periodic, which physically simulates an infinite span condition. Regarding the boundary condition for the pressure, zero gradient conditions are used for the inlet, outlet and wall. The top and bottom are modeled using a fixed value condition, imposing atmospheric free stream condition.

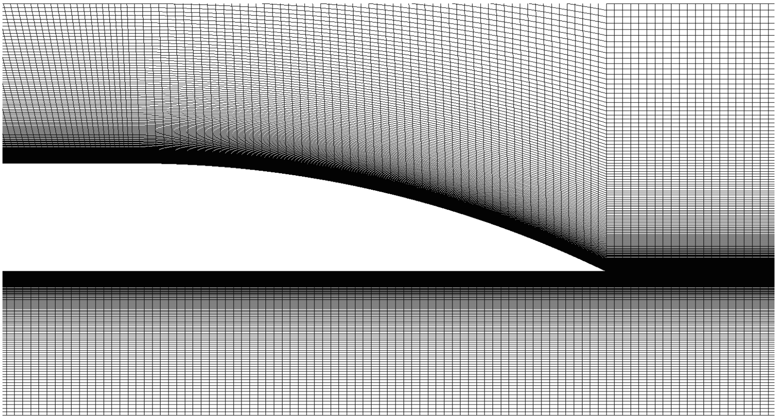

Figure 4.1: Indication of the quality of the mesh around the beveled edge

4.4. RESULTS AND DISCUSSION

4.4.1. FLOW FIELD

The understanding of the flow field over beveled edges is of major importance before considering the acoustic emissions. The source term should be formulated adequately, and correctly obtained and transferred to the acoustic analogy. In general, flow over the beveled edge encounters an adverse pressure gradient on the top (suction) side, which magnitude depends on the curvature of the profile. The turbulent boundary layer on both sides reaches it characteristic state with conditions of $\delta_{99}/h = 0.25$ and $H = 1.3$, where the maximum velocity is defined as the inflow velocity. A quantitative image is depicted in Fig. 4.2, where similar parameters are plotted at 6 stations along the vertical axis (i.e. $x/h = -6, -5, -4, -3, -2, -1, 0$).

The separation and forming of the shear layer is induced by the increasingly unstable and fluctuating velocity profile downstream over the beveled edge, subjected by an adverse pressure gradient. When approaching separation, the inflection point of the boundary layer and therefore the center of the shear layer is separated by a larger distance from the wall. This is visible in Fig. 4.2. A thick and slightly angled shear layer is visible at a distance away from the wall, while, close to the wall and directly behind the corner point, a recirculation zone with backflow is formed.

Due to the rapid change at the obtuse corner, larger accelerations in the outer part of the boundary layer resulting in a larger velocity gradient close to the wall will appear which will stretch out the vortical structures in streamwise direction. This is evidenced by plotting Q iso-surfaces of the flow in Fig. 4.3, which denotes the second invariant of the velocity Jacobian. It detects local pressures smaller than surrounding pressure. Larger structures can be identified upstream, while the region below the shear layer reveals more smaller structures due to the turbulent nature of the flow in combination with lower convection speed. Furthermore, a shedding component in the near wake is visible. The shedding frequency of the model can be qualitatively estimated by measuring the distance between two vortices: $\approx 1.92h$, which results in a Strouhal number of

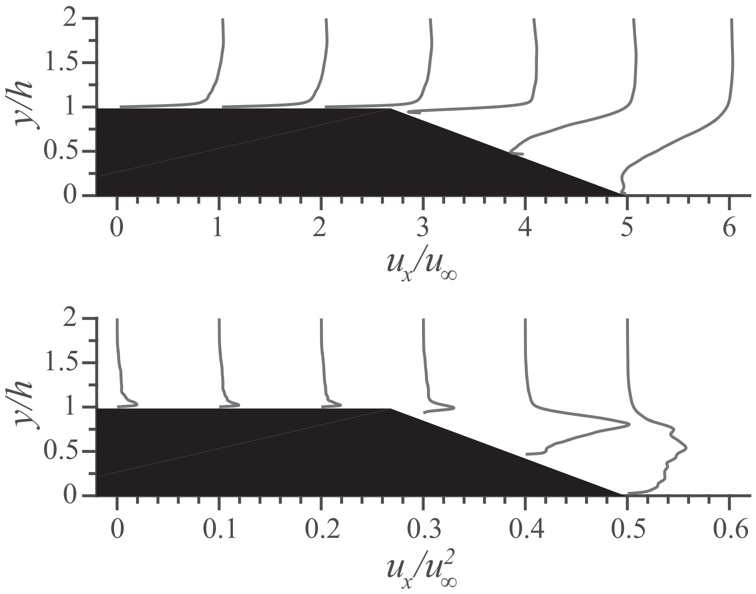

Figure 4.2: Mean streamwise velocity (left) and normal streamwise Reynolds stresses(right) for six different stations over the beveled edge

$St_h = \frac{h}{2\Delta x} \approx 0.26$, assuming that mean flow in the far wake is equal to the undisturbed flow. This result is in close agreement with the experimentally determined values from Blake [11], Bearman [120] and Greenway and Wood [121] which vary between 0.24 and 0.28 for high and low Reynolds number flows for beveled trailing edges respectively.

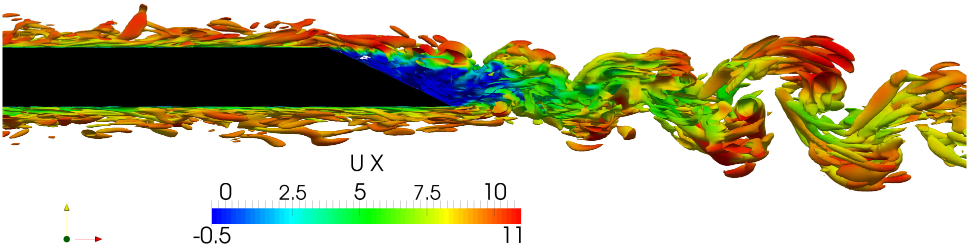

Figure 4.3: $Q = 1 \cdot 10^5$ iso-surfaces colored by streamwise velocity

4.4.2. ACOUSTIC EMISSION

The acoustic power spectra in the far-field, Φ_{aa} is obtained by applying a Fast Fourier Transform (FFT) on the time signal obtained from the acoustic analogy. In total, around 7000 signals, sampled at 30 kHz, were used, with a Hamming window of 4096 with 50% overlap (App. B & C). This ensured capturing the shedding peak, although it did not result in an optimal smoothing of the higher frequency ranges. Results are presented in

Fig. 4.4, together with the experimental reference data from van der Velden et al. [81] (see Ch. 5). Both experimental and numerical data predict the shedding frequency well at $St_h \approx 0.26$, although the numerical data underpredicts the amplitude by about 4 dB with respect to the experimental results. Broadband noise from both numerical methodologies in the compact regime is in excellent agreement with the experimental data. The cut-off frequency where non-compactness of the source appear, is found to be $f = \frac{c}{\lambda} = \frac{340}{0.36} \approx 950$ Hz, with λ and c being the wavelength (in this case the plate chord) and speed of sound respectively. This results in a Strouhal number of $St_h \approx 1.9$. As expected, above this Strouhal number, both numerical results start to deviate, with the BEM method following similar trends as the experimental sound pressure spectra.

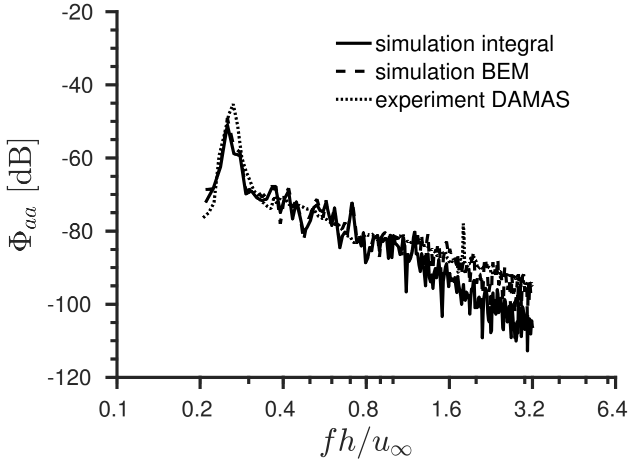

Figure 4.4: Power spectra of the far field pressure fluctuations (Φ_{aa}) for both integral method and BEM against experimental data at $10l$ distance right above the trailing edge

The characteristics of non-compact acoustical sources in the far field commonly manifest in a multilobe directivity [7, 11]. To visualize this, acoustic dipole directivity contours of Sound Pressure Level (SPL) around the trailing edge are visualized using both the integral and the BEM method. Fig. 4.5 shows a comparison of the result of the integral solution and BEM solution for a low Strouhal number case. The ratio of the wavelength λ to the acoustic chord of the plate l is $\lambda/l = 7.5$. The result implies that the approximation of acoustically compactness is well satisfied at this frequency.

Fig. 4.6 shows the comparison at a Strouhal number of $St_h = 3.2$. Here, the ratio of λ/l equals 0.6, meaning that the compact approximation is no longer valid. The integral solution in Fig. 4.6 still visualizes a compact dipole, although a bit deformed due to other sources present on the airfoil wall. The BEM solution on the other hand depicts multiple lobes on the plate wall and the far field, while the trailing edge noise is more directed towards the leading edge, compared to the integral solution.

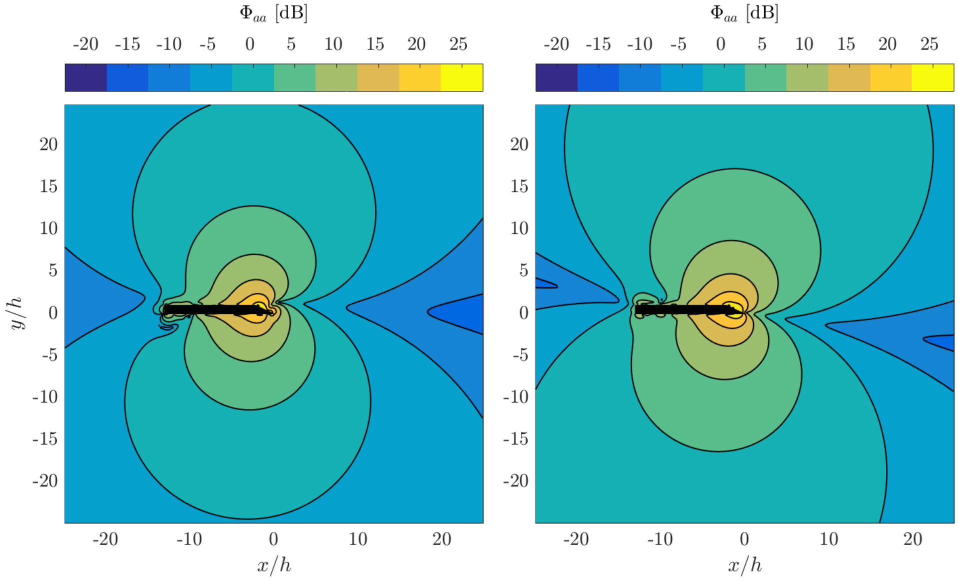

Figure 4.5: Acoustic directivity for low Strouhal numbers ($St_h = 0.25$) for integral method (left) and BEM (right)

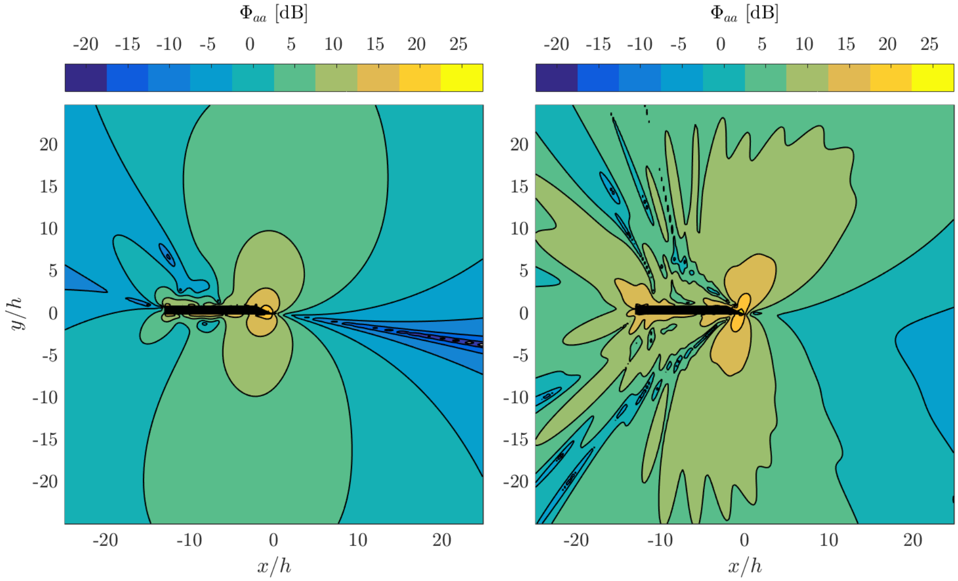

Figure 4.6: Acoustic directivity for high Strouhal numbers ($St_h = 3.2$) for integral method (left) and BEM (right)

4.5. CONCLUSION

Efficient tools for the determination of acoustic sources around wind turbines are necessary to further reduce its noise footprint. These simulations should be computational efficient and should be able to capture acoustic sources in the compact and non-compact regime, as the frequency range of interests covers both regimes. Therefore, this study is focused on the non-compact prediction and computation of acoustic sources in the vicinity of a trailing edge. Both integral and boundary element method (BEM) are analyzed, while the latter also predicts the scattered acoustic pressure as well as proper propagation of the sources. The numerical model under consideration is a 25 degrees asymmetric beveled plate.

The compact source approximation is found to be valid for low frequencies up until the wavelength-chord ratio $\lambda/l = 1$ when comparing an integral solution with a BEM, which include scattering effects. The integral solution start deviating from the other solution when $\lambda/l > 1$, while the BEM start showing non-compactness by forming different lobes around the trailing edge. Similar turn-around times are found for both methodologies, making the current presented methodology suitable for further complex industrial cases.

5

BEVELED TRAILING EDGE FLOW FIELD AND NOISE EMISSION

The scientists of today think deeply instead of clearly.
One must be sane to think clearly,
but one can think deeply and be quite insane.

Tesla

The trailing edge noise of a wind turbine blade is currently one of the most dominant noise sources on a wind turbine and, therefore, understanding and modeling of the physics associated with the generation and propagation of noise are of paramount importance for the design of silent wind turbines. Based on the Lattice Boltzmann Equation in combination with a Ffowcs-Williams and Hawking aeroacoustic analogy, an estimation of the acoustic radiation in the far field is obtained of an asymmetric 25° *beveled trailing edge with obtuse corner. Flow field dynamics are compared to data obtained experimentally from Particle Image Velocimetry and Hot Wire Anemometry, and compare favorably in terms of mean velocity field and turbulent fluctuations. Moreover, the characteristics of the unsteady surface pressure, which are closely related to the acoustic emission, show good agreement between simulation and experiment. Finally, the prediction of the radiated sound is compared to the results obtained from acoustic phased array measurements in combination with a beamforming methodology. Vortex shedding results in a strong narrowband component centered at a constant Strouhal number in the acoustic spectrum. At higher frequency, a good agreement between simulation and experiment for the broadband noise component is obtained and a typical cardioid-like directivity is recovered.*

Parts of this chapter have been published in the Journal of Sound and Vibration (2016) [81].

5.1. INTRODUCTION

THE trailing edge noise of a wind turbine blade is currently one of the most dominant noise sources on a wind turbine and, therefore, understanding and modeling of the physics associated with the generation and propagation of noise are of paramount importance for the design of silent wind turbines [22]. Brooks et al. [7] defined the fundamental airfoil self-noise mechanisms associated with the trailing edge, such as the noise produced by the transitional or turbulent boundary layer flow with the trailing edge or that due to vortex shedding. In the case of the interaction between the boundary layer flow and the trailing edge, perturbations of the unsteady surface pressure field, introduced and convected with the turbulent eddies, are scattered at the discontinuity posed by the trailing edge. The acoustic radiation depends largely on the length scale of the individual turbulent eddies [11]. In the case of a developed turbulent boundary layer, the surface pressure is only affected within a confined area by various turbulent eddy sizes and, therefore, the overall aerodynamic force acting on the airfoil remains comparatively constant [11]. Due to the small length scale and high convective velocity of the eddies, this situation is typically encountered at high frequencies with respect to the human ear frequencies of interest. At such high frequency, where non-compactness arises due to the fact that the acoustic wavelengths are much smaller than the airfoil chord, the directivity pattern of the acoustic radiation shows a bias towards the leading edge (i.e. in upstream direction) [7, 11]. For convecting turbulent boundary layers over sharp trailing edges, where the spanwise correlation associated with turbulent eddies is by far smaller than the airfoil span, an appropriate length scale is the local boundary layer displacement thickness $\delta^\star$ [122].

A slightly different situation is encountered for an asymmetrically beveled trailing edge, which is defined by the trailing edge angle θ and the radius of curvature R, normalized by the maximum airfoil thickness h. For the special case of an obtuse corner, the radius of curvature is identically zero ($R = 0$). This model was selected as the test case for the present study and Fig. 5.1 shows the truncated trailing edge section. For asymmetrically beveled trailing edges with small radius of curvature, flow separation is observed over the beveled surface upstream of the trailing edge [11, 115, 123, 124]. This flow separation can introduce a shedding component into the wake flow, which is associated with coherent vortex roll-up and velocity fluctuations at a shedding frequency f_s. The associated length scale is often characterized in terms of the wake thickness parameter or by the plate thickness h. If the bluntness $h/\delta^\star$ (> 3.3) is large, the tonal noise component associated with such coherent vortex shedding becomes a dominating feature of the acoustic emission [11]. For the case of the obtuse corner, the separation point is fixed at the upstream corner point on the upper surface and its location is therefore independent of Reynolds number [124]. Beveled trailing edge geometries have served for validation purposes in the past, for instance in the studies of Wang and Moin [29, 125, 126] and Shannon and Morris [115, 123].

Several authors, for instance Amiet [95] and Howe [55], have discussed trailing edge noise in the light of incident turbulent flow and diffraction theory, respectively. Within this framework, the relevant characteristics for noise radiation due to boundary layer interaction with the trailing edge are the auto-spectral density (ASD), the spanwise correlation length (l_z) of the unsteady surface pressure, and its convective velocity, which

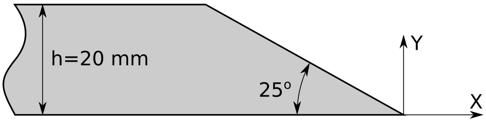

Figure 5.1: Representation of the truncated trailing edge section of the beveled plate

are all a function of frequency ω. Amiet [95] and Howe [55] assumed that the incident pressure gust on the surface of the airfoil convects past the trailing edge, which represents an impedance discontinuity and at which the fluctuations are scattered in the form of acoustic waves. This theory forms the start of multiple experimental and numerical studies, such as the Large Eddy Simulations (LES) of Christophe [97] and van der Velden et al. [94], the surface pressure measurements of Brooks and Hodgson [17], and the recent study of Pröbsting et al. [8, 98], who proposed a methodology for trailing edge noise diagnostics based on high-speed tomographic Particle Image Velocimetry (PIV). Numerical studies towards the prediction of beveled trailing edge noise have been presented by Wang and Moin [29] and by van der Velden et al. [127, 128]. However, simulations using conventional equations (as the Navier-Stokes relations) could be computationally expensive because they have to be solved implicitly and under compressible flow conditions to accurately predict noise levels within decent turn-around-times.

As an alternative therefore, in recent years, the Lattice Boltzmann Method (LBM) experienced increased attention in industry as an efficient and highly parallelizable approach for the simulation of fluid flows [76–80, 129]. The LBM solves the discrete Boltzmann equations in combination with a collision model to simulate a Newtonian fluid. The flow is represented on a mesoscopic scale, modeling the convection and collision processes of a limited number of distributions of particles. The method is intrinsically transient and can therefore capture flow characteristics such as flow separation, vortex shedding, and shear layer development. Due to its efficiency in computing unsteady compressible flows, the LBM was proposed as an alternative to previous Navier-Stokes based numerical schemes, especially for complex flow and various acoustic problems (e.g. [80]). Since the compressible flow equations are solved, sound pressure waves from aeroacoustic sources are captured [27] in a time-resolved manner. Moreover, due to the treatment of boundaries using a cut-cell approach, the simulation of complex geometries and even entire engineering applications, such as wind turbines, becomes feasible with a considerably smaller increase in computational time when compared to solving similar studies with conventional tools [78]. Previous studies applying the LBM include an acoustic analysis of a full-scale wind turbine [78], where the acoustic prediction was obtained by means of a Ffowcs-Williams Hawking (FW-H) aeroacoustic analogy [15] in the far-field and direct probes in the near-field. More recently, a validation of a methodology combining an LBM simulation with the FW-H aeroacoustic analogy for trailing edge self-noise prediction was reported (Lew, Yazdi and Mongeau [130]) on beveled trailing edges with an obtuse corner of 45° degrees, where transition was incorporated by the wall model. The mean flow topology showed a good comparison with the experimental data from Shannon & Morris [123], although the spanwise correlation in the simulation did not match with the experimental results, due to poor laminar-turbulent transition.

Furthermore, the study left open questions regarding the comparison of the acoustic results as the conditions were not exactly the same with respect to the experiment (e.g. no boundary layer tripping device for enforced transition). Discrepancies between simulation and experiment were found for the broadband noise component at moderate and high Strouhal numbers, which can be mainly assigned to the interaction of the turbulent boundary layer convecting over the trailing edge. Therefore, in view of the questions raised by previous studies, further validation is required.

The present study is set to further validate the applicability of a LBM against PIV, wall pressure and acoustic far field array measurements to predict trailing edge tonal and broadband noise. It focuses on a flat plate with turbulent boundary layers encountering an asymmetric 25° beveled trailing edge with an obtuse corner in a low Mach number flow. The LBM methdology is validated for correctly modeling the flow and noise sources at different Reynolds and Mach numbers, to directly propagate the acoustic sources in the near field and to efficiently couple the source data with external acoustic propagation methods. Validation of the numerical results and methodology is based on experimental data obtained from PIV, hot-wire anemometry (HWA), unsteady surface pressure, and acoustic phased-array measurements on the same geometry and at identical Reynolds and Mach number. The acoustic far-field and near-field radiation is predicted by means of a FW-H approach by integrating the unsteady surface pressure and the results are compared to those obtained directly from the LBM solution.

5.2. MEASUREMENT AND SIMULATION

5.2.1. TEST CASE

The geometrical model, which was used in the experiments, and modeled numerically, is a flat plate with an elliptical leading edge and thickness $h = 20$ mm, chord $l/h = 18$, and span $b_{exp}/h = 20$. The trailing edge was asymmetrically beveled with an angle of $\theta = 25$ degree and radius of curvature $R/h = 0$, which results in an obtuse corner upstream of the slanted trailing edge section (Fig. 5.1). The $x-$, $y-$, and $z-$coordinate directions is aligned with the streamwise, transverse, and spanwise directions, respectively, and the origin is located at the trailing edge (Fig. 5.2).

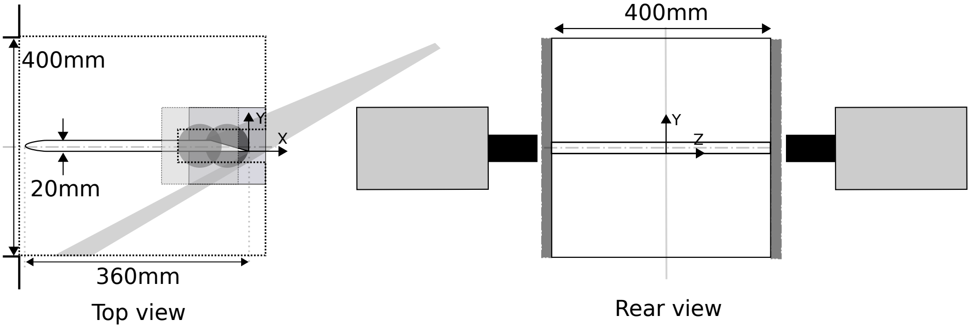

Figure 5.2: Experimental set-up for 2-component planar PIV flow field measurements

To ensure a turbulent boundary layer upstream of the trailing edge, $l/h = 0.5$ mm wide bands of randomly distributed 3D roughness elements (carborundum, nominal grain size of $d/h = 0.042$) were applied as tripping devices on both sides of the plate at $x/h = 4.5$ downstream of the leading edge. Experiments with the same baseline model and different beveled trailing edges were reported by Pröbsting et al. [131] and Guan et al. [124] before. In the numerical simulation, Fig. 5.3, with span $b_{sim}/h = 2.56$ a fully developed turbulent boundary layer was obtained by the use of a zig-zag tripping device at $x/h = 0.9$ downstream of the leading edge with a height of $d/h = 0.075$ and a streamwise length of $l/h = 0.27$. The wavelength of the zig-zag pattern is $\lambda/h = 0.28$, resulting in a total of nine wavelengths over the width of the domain. This geometry ensures similar trailing edge conditions as in the experiment. In the simulation, the flat plate was modeled as an infinite plate, hence no leading edge is present. A frictionless wall condition (slip condition) was applied up to the actual leading edge of the plate, to model a similar chordwise plate length as in the experiment.

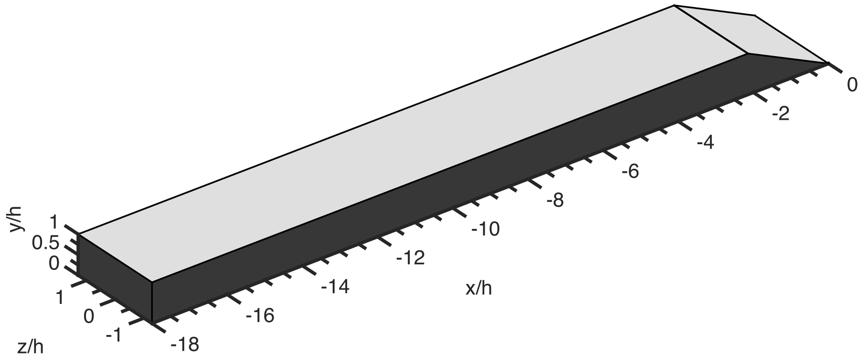

Figure 5.3: Discrete representation of semi-infinite flat plate with finite spanwise dimension

5.2.2. EXPERIMENTAL SET-UP

PIV and HWA measurements were performed to provide an experimental reference for the flow field around the edge and the incoming boundary layer on both sides. Furthermore, unsteady surface pressure measurements using remote microphone probes were used to quantify the pressure fluctuations at various locations. In addition, acoustic phased array measurements in an anechoic facility were acquired for comparison with the computationally predicted noise levels.

FLOW FIELD MEASUREMENTS

High-speed PIV experiments were performed in an open-jet, low-speed wind tunnel with a rectangular outlet of $0.4 \times 0.4\ m^2$ at Delft University of Technology. The model was mounted vertically between span end-plates, which were placed tangentially to the exit nozzle to avoid 3D flow effects. The free-stream velocity was set to $u_\infty = 20 m/s$, equivalent to a chord-based Reynolds number of $Re = u_\infty l/\nu = 480{,}000$, where ν is the kinematic viscosity of air.

The flow was seeded with evaporated water-glycol based fog fluid with a mean droplet diameter of 1 μm. A Quantronix Darwin Duo Nd:YLF laser ($2 \times 25\ mJ$ at 1 kHz) illuminated the tracer particles over the field of view (FOV) and two Photron Fastcams SA1.1 (1 Mpx, 12 bit resolution, 20 μm pixel pitch) were used for image acquisition. Both cameras were equipped with Nikon Micro-Nikkor 105 mm prime lenses and positioned on opposite sides of the test section with a small offset in the streamwise ($x-$)coordinate direction (see Fig. 5.2). The resulting FOV encompassed the beveled surface (suction side) of the trailing edge and a part of the near wake.

For flow statistics, images were acquired at 125 Hz in double-frame mode with a pulse separation equivalent to a tracer particle displacement of approximately 15px in the free-stream. The image sequence was correlated with an iterative multi-grid, multi-pass correlation technique with Gaussian window weighting, window deformation, and a final interrogation window size of $16 \times 16\ px^2$ [98]. Parameters related to the planar PIV measurements are listed in Tab. 5.1.

Table 5.1: Parameters for planar PIV measurements

Parameter	Symbol	Value
Field of view $[mm^2]$	FOV	45×21
Magnification $[-]$		0.42
Interrogation window size $[mm]$	δ_x, δ_y	0.76
Focal ratio $[-]$	$f_\#$	5.6
Free-stream displacement $[px]$	$\mathrm{d}x$	15
Sampling frequency $[kHz]$	f_x	0.125
Number of samples $[-]$	$-$	1,000

UNSTEADY SURFACE PRESSURE MEASUREMENTS

Unsteady surface pressure measurements were conducted in the $0.6 \times 0.6\ m^2$ open jet Anechoic Wind Tunnel facility (AWT) at the University of Notre Dame. The model was placed vertically in the center of the test section. To adapt the dimensions of the test section to those of the model and to avoid 3D flow effects, a 19 mm wooden splitter plate with an elliptical leading edge was placed at a height of 0.4 m from the bottom surface of the exit nozzle and reached 1.22 m downstream. All surfaces of the surrounding chamber are treated with sound absorbent glass fiber wedges with an absorption coefficient greater than 99% for frequencies exceeding 100 Hz. Details on the experimental facility can be found in Mueller et al. [132].

The linear array of remote microphone probes (RMP) consisted of five elements located on the suction side ($x/h = -0.6, -1.2, -1.8, -2.4, -3.0$). Pinholes of diameter 0.5 mm were connected through hypodermic tubing to the remote sensing elements (Knowles FG-23629-C36 electret-condenser microphones) and a 4 m tygon tube provided an anechoic termination. The RMPs were calibrated by simultaneous measurements of a white noise signal with a B&K 2679 reference microphone with Nexus amplifier placed 1mm above the pinhole of each RMP. A transfer function, correcting both the amplitude and phase shift, was computed and applied. A similar set-up has been described previously by Bilka et al. [133] and Guan et al. [134]. Data were acquired for free-stream velocities $u_\infty = 20$, 25 and 30 m/s, equivalent to chord based Reynolds numbers of $Re = 480{,}000$, $600{,}000$ and $720{,}000$, respectively.

ACOUSTIC MEASUREMENTS

Acoustic phased array measurements were also conducted in the AWT over an extended range of free-stream velocities (10−35 m/s). The phased array consisted of 40 condenser microphones arranged in a streamwise elongated logarithmic spiral configuration. It had an aperture of approximately 120×60 cm^2 and was placed parallel to the chord plane at a distance of 2.38 m with its center aligned with the trailing edge of the model. Data were acquired at a frequency of 40 kHz in an ensemble of 64 windows with 32,768 samples (total acquisition time 52.43 s). For beamforming, a Cross-Spectral Matrix (CSM) method (Conventional Beamforming) as well as DAMAS (Deconvolution Approach for the Mapping of Acoustic Sources) [135] was employed under the assumption of a point source distribution, taking into account the modified propagation path due to shear layer refraction effects [136] with a simplified correction as described by Sijtsma [18]. To distinguish the trailing edge noise source from parasitic noise sources, the source power was summed over an integration area around the trailing edge. The result of this integration procedure represents the average source power over the aperture of the array. Results presented later in the discussion are further scaled to the acoustic pressure ASD at the center location of the array under the assumption of a simple point source. Details on the microphone array, the beamforming technique, and the source power integration methodology can be found in Shannon & Morris [123].

In addition, hot-wire measurements were performed to characterize the boundary layer upstream of the trailing edge at $x/h = -1$ and $x/h = -2.5$ on the pressure and suction side, respectively. An AA Lab System AN-1003 hot-wire system with low-pass filter at 14 kHz was used and the hot-wire probe was mounted on a 3D computer-controlled translation stage. At each data point, the signal was sampled at a frequency of 40 kHz for a period of 26 s. Data were acquired for a free-stream velocity of $u_\infty = 20$ m/s ($Re = 480,000$).

5.2.3. NUMERICAL SIMULATION

SOURCE FIELD SIMULATION

For the numerical simulation of the trailing edge flow, the commercial software package Exa PowerFLOW 5.0b was used to solve the Lattice-Boltzmann equations for a finite number of directions. The discretization considers 19 discrete velocities in three dimensions (D3Q19) involving a third order truncation of the Chapman-Enskog expansion, which has been shown sufficient to recover the Navier-Stokes equations for a perfect gas at low Mach number in isothermal conditions [82].

The kinetic equations were solved on a Cartesian mesh, known as a lattice, by explicit time-stepping and collision modeling. Defining the particle density distribution function as g_i and the discrete velocity vector as c_i, the Lattice-Boltzmann equation were written as:

$$g_i(\mathbf{x}+\mathbf{c}_i\Delta t, t+\Delta t) - g_i(\mathbf{x}, t) = C_i(\mathbf{x}, t), \tag{5.1}$$

where the particle density distribution function can be interpreted as a typical histogram representing the likelihood of the presence of particles at a position $\mathbf{x}$ with a discrete particle velocity $\mathbf{c}_i$ in the i direction at time t. $\mathbf{c}_i\Delta t$ and Δt are space and time increments respectively. The collision term on the right hand side of the LBM equation adopts the form known as the Bhatnagar-Gross-Krook (BGK) form [83]:

$$C_i(\mathbf{x},t) = -\frac{\Delta t}{\tau}\left[g_i(\mathbf{x},t) - g_i^{eq}(\mathbf{x},t)\right]. \tag{5.2}$$

This term drives the particle distribution to the equilibrium with a relaxation time parameter τ. The variable g_i^{eq} is the local equilibrium distribution function and relates the LBM to hydrodynamic properties. The equilibrium distribution of Maxwell-Boltzmann was approximated by a 2nd order expansion valid for small Mach numbers [84]:

$$g_i^{eq} = \rho\omega_i\left[1 + \frac{\mathbf{c}_i\mathbf{u}}{a_s^2} + \frac{(\mathbf{c}_i\mathbf{u})^2}{2a_s^4} + \frac{|\mathbf{u}|^2}{2a_s^2}\right], \tag{5.3}$$

where ω_i are the weight functions related to the velocity discretization model [84] and $a_s = \frac{1}{\sqrt{3}}$ is the non-dimensional speed of sound. The equilibrium function was related to the macroscopic quantities density ρ and velocity $\mathbf{u}$, which can be computed by summing up the discrete momentum of the particle distribution:

$$\rho(\mathbf{x},t) = \sum_i g_i(\mathbf{x},t), \qquad \rho\mathbf{u}(\mathbf{x},t) = \sum_i \mathbf{c}_i g_i(\mathbf{x},t). \tag{5.4}$$

The single relaxation time used was related to the dimensionless kinematic viscosity by: [84]:

$$\nu = a_s^2(\tau - \frac{\Delta t}{2}). \tag{5.5}$$

For the Very Large Eddy Simulation (VLES), the subgrid scale model was implemented as a viscosity model through the relaxation time τ to locally adjust the numerical viscosity of the scheme [137]:

$$\tau_{eff} = \tau + C_\mu \frac{k^2/\epsilon}{(1+\eta^2)^{1/2}}, \tag{5.6}$$

where $C_\mu = 0.09$ and η is a combination of a local strain parameter $(k|S_{ij}|/\epsilon)$, local vorticity parameter $(k|\Omega_{ij}|/\epsilon)$, and local helicity parameters. The model consisted of a two-equation $k-\epsilon$ Renormalization Group (RNG) modified to incorporate a swirl based correction that reduces the modeled turbulence in presence of large vortical structures [79]. This VLES methodology was implemented as standard turbulence model in Exa PowerFLOW 5.0b.

Fully resolving the near wall region is prohibitively expensive for high-Reynolds number turbulent flow with the lattice concept of the LBM scheme. Therefore, a turbulent wall model was used to provide approximate boundary conditions. In the current study, the following wall-shear stress model based on the extension of the generalized law of the wall model was used [84, 138]:

$$u^+ = f\left(\frac{y^+}{A}\right) = \frac{1}{\kappa}\ln\left(\frac{y^+}{A}\right) + B, \tag{5.7}$$

with

$$A = 1 + f\left(\frac{\mathrm{d}p}{\mathrm{d}x}\right). \tag{5.8}$$

This relation was iteratively solved to provide an estimated wall-shear stress for the wall boundary conditions in the LBM scheme. A slip algorithm [84], a generalization of a bounce-back and specular reflection process, was then used for the boundary collision process.

A variable resolution was allowed, where the grid size changes by a factor of two for adjacent resolution regions. Due to the explicit time-stepping characteristics of the LBM scheme, the time-step size was increased with cell size in factors of two as well. Larger cells will therefore not be evaluated every time-step. This creates the parameter time-step equivalent number of cells, which is defined as a scaled number of cells to be evaluated each single time-step, scaled to the operation at the shortest time-step in addition to the total number of cells.

The simulation domain size was $270h$ in both the streamwise and wall normal directions, where the outer $37.5h$ were modeled as an anechoic outer layer to damp acoustic reflections. The third dimension was dependent on the span of the model, and was modeled using periodic boundary conditions. Multiple refinement regions were applied such that, near the boundary, the first cell was placed in the viscous sub layer (Fig. 5.4). In total, around 160 million voxels were used to completely discretize the problem, with a total of 100 million time-step equivalent voxels. Data were acquired for a free-stream velocity of 20, 25 and 30 m/s, corresponding to a chord-based Reynolds number of $480,000$, $600,000$ and $720,000$ respectively. Sampling was started after reaching a steady transient solution, i.e. after 35 flow passes (see App. B). The Courant-Friedrichs-Lewy (CFL) was dependent on the wave propagation velocity and smallest voxel size in this compressible simulation and fixed to unity for each single simulation. Therefore, the physical time step was fixed at $1.7 \cdot 10^{-7}$ s. Mean and fluctuating statistics in the streamwise plane at a centered span were sampled for the 20, 25, and 30 m/s case at a Strouhal number of $St = \frac{fh}{u_\infty} = 23$, 18.4 and 15.3 ($f = 23$ kHz is constant) respectively, while the characteristics of the boundary layer were obtained at $St = 46$, 36.8 and 30.7 ($f = 46$ kHz is constant) respectively. The wall pressure probes had the size of their local voxel size (i.e. $0.005h$) and were sampled at a frequency of $St = 92$, 73.6 and 61.3 ($f = 92$ kHz is constant) respectively, after which the ASD was obtained by a Hanning window with 50 % overlap, to optimally smooth out the spectra.

PREDICTION OF ACOUSTIC RADIATION

Due to the fact that the LBM is inherently compressible and provides a time-resolved solution, the sound pressure field can directly be extracted from the computational domain, provided that there is sufficient resolution to capture the acoustic waves. Sufficient accuracy is obtained when considering at least $12-16$ cells per wavelength for the LBM methodology [79]. At the location of the direct probes, this yielded accurate predictions up to Strouhal numbers of $St = \frac{fh}{u_\infty} = 4.8$, 3.8 and 3.2 for the three different velocities, respectively.

To validate the acoustic propagation and source capturing inside the computational domain, an acoustic analogy was used to obtain the far-field sound radiation. To recover the acoustic far-field, the Ffowcs-Williams and Hawkings [47] (FW-H) equation was employed. The time-domain FW-H formulation developed by Farassat, known as formulation 1A [48], and extended based on the convective form of the FW-H equation was used

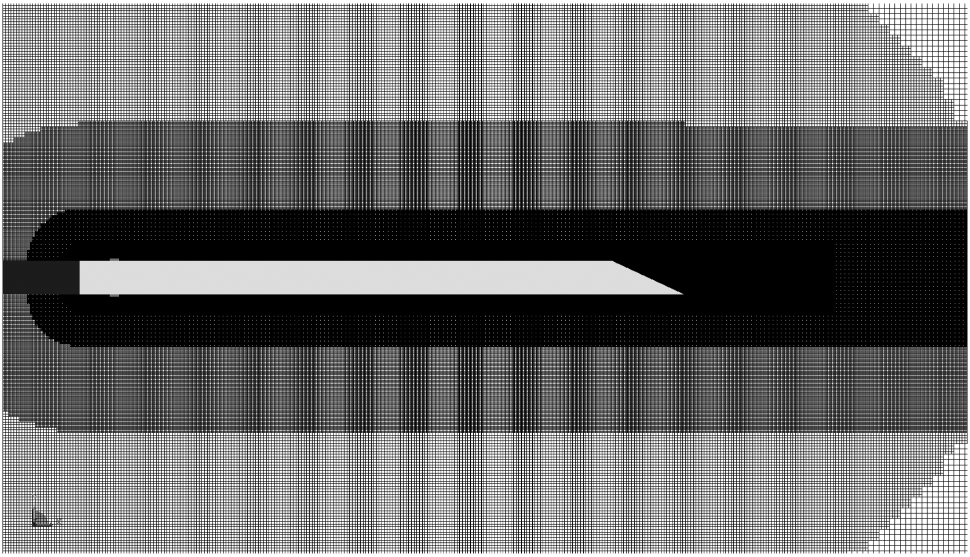

Figure 5.4: Detailed view of the grid around the beveled trailing edge

to predict the far-field sound radiation of the beveled trailing edge in a uniformly moving medium [49]. The formulation was implemented in the time domain using a source-time dominant algorithm also referred to as an advanced time approach [49, 50]. The input to the FW-H solver were the time-resolved flow field quantities on a surface mesh provided by the transient LBM simulations. This surface mesh can be defined either as a solid surface corresponding to the physical body or as a permeable surface surrounding the solid body. In the present study, the solid formulation was chosen with pressure information sampled on the surface of the airfoil. Hence, acoustic dipole sources L_i were the only source term for the current analogy, defined as:

$$L_i = (p - p_0)n_i \tag{5.9}$$

with $p - p_0$ the fluctuating pressure on the solid surface and n_j the unit surface normal. With r representing the effective acoustic distance rather than the geometric distance between the source and the observer in terms of time delay between emission and reception:

$$r = \frac{-M_0(x_1 - y_1) + r^\star}{\beta^2}, \tag{5.10}$$

with

$$r^\star = \sqrt{(x_1 - y_1)^2 + \beta^2\left[(x_2 - y_2)^2 + (x_3 - y_3)^2\right]}, \tag{5.11}$$

and

$$\beta = \sqrt{1 - M_0^2}. \tag{5.12}$$

With this in mind, the unit radiation vector was written as:

$$\hat{r}_i = \left[\frac{-M_0 r^\star + (x_1 - y_1)}{\beta^2 r}, \frac{x_2 - y_2}{r}, \frac{x_3 - y_3}{r}\right]. \tag{5.13}$$

With the source term L_i and the observer distance from the source R defined, the following integral relation was solved in order to compute the acoustic pressure field at the observer location **x** [49]:

$$\begin{aligned} 4\pi p'_{aa}(\mathbf{x},t) &= \frac{1}{a}\int_{g=0}\left[\frac{\dot{L}_i\hat{r}_i}{r(1-M_i\hat{r}_i)^2}\right]_{ret}\mathrm{d}S \\ &+ \int_{g=0}\left[\frac{L_i\hat{r}_i-L_iM_i}{r^2(1-M_i\hat{r}_i)^2}\right]_{ret}\mathrm{d}S \\ &+ \int_{g=0}\left[\frac{L_i\hat{r}_i(M_i\hat{r}_i-M^2)}{r^2(1-M_i\hat{r}_i)^3}\right]_{ret}\mathrm{d}S. \end{aligned} \tag{5.14}$$

The subscript ret denotes the evaluation of the integrand at the time of emission based on the effective acoustic distance, i.e. the retarded time.

The acoustic pressure was sampled at locations distributed at uniform spacing in a circle around and at a distance of two chords from the trailing edge in the mid-span plane. FW-H analogy results were obtained at a distance of ten chords from the trailing edge in the mid-span plane. The ASD was obtained using an average periodogram approach of the fluctuating signal [111] with a Hanning window and 50 % overlap from signals sampled at a frequency of $St = 92$, 73.6 and 61.3 (92 kHz) and $St = 46$, 36.8 and 30.7 (46 kHz) for the direct probes and FW-H surface respectively (App. B).

5.3. RESULTS AND DISCUSSION

5.3.1. FLOW FIELD

The quality of the turbulent boundary layer convecting over the trailing edge in the simulation is depends on the bypass transition process. Therefore, firstly, the flow features around the trip are analyzed. A detailed organization of the structures downstream of the trip was depicted before in Ch. 2 using iso-surfaces of the λ_2 criterion, see Fig. 2.6. The trip causes the roll-up of vortices into spanwise coherent structures, which later evolve into arch-like structures, typical for a turbulent boundary layer [90]. However, due to the spanwise periodic arrangement of the zig-zag trip, these arches show a high level of organization initially. Further downstream, these vortical structures merge with low-speed quasi-streamwise vortices (blue and green structures), resulting in the formation of hairpin structures [89, 90]. Towards the trailing edge, this boundary layer flow assumes a turbulent state.

The incoming boundary layer for both the experiment and simulation shows characteristics of a generic, flat-plate turbulent boundary layer. The magnitude, $V = (u_x^2 + u_y^2)^{1/2}$, of the normalized mean velocity, $\overline{V}/u_\infty$, and root mean square (rms) velocity, $(\overline{V\prime^2})^{1/2}/u_\infty$ as a function of distance from the wall are shown in Fig. 5.5 and Fig. 5.6 for the pressure ($x/h = -1$) and suction ($x/h = -2.5$) side, respectively. The comparison shows a good agreement between simulation and experiment. When observing the mean boundary layer profile on both the pressure and suction sides, the boundary layers in both the experiment and simulation attain a turbulent state near the trailing edge with slightly different shape factors ($H^s_{exp} = 1.40$, $H^p_{exp} = 1.55$ and $H^s_{sim} = 1.27$, $H^p_{sim} = 1.33$) for suction and pressure side in the experiment and simulation, respectively. The rms velocity data from the simulation shows the expected behavior of a turbulent boundary layer, with larger fluctuations and shifted away from the wall in the inner layer. The HWA measurements agree with the numerical solution in the outer layer, but show a 10% smaller amplitude of velocity fluctuations in the viscous layer, as well as a small wall normal location shift towards the wall. The displacement thickness on the pressure side is $h/\delta^\star = 14$ and 13 in the experiment and simulation, respectively, and $h/\delta^\star = 20$ and 17, respectively, on the suction side.

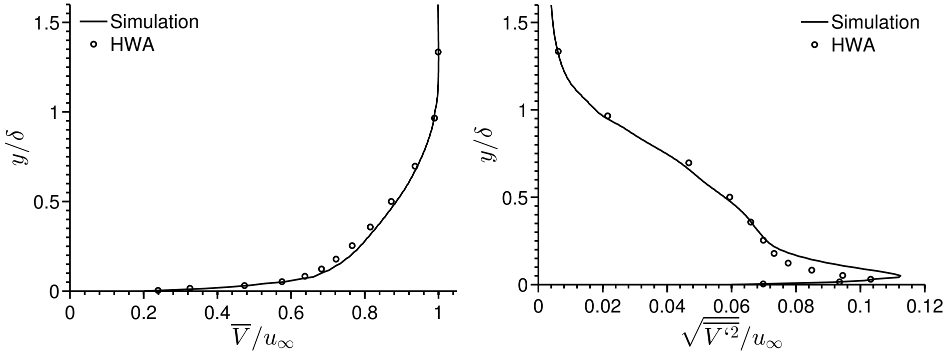

Figure 5.5: Mean (left) and rms (right) velocity magnitude, $V = \sqrt{u_x^2 + u_y^2}$, at the pressure side measurement location $x/h = -1$ for $Re = 480,000$

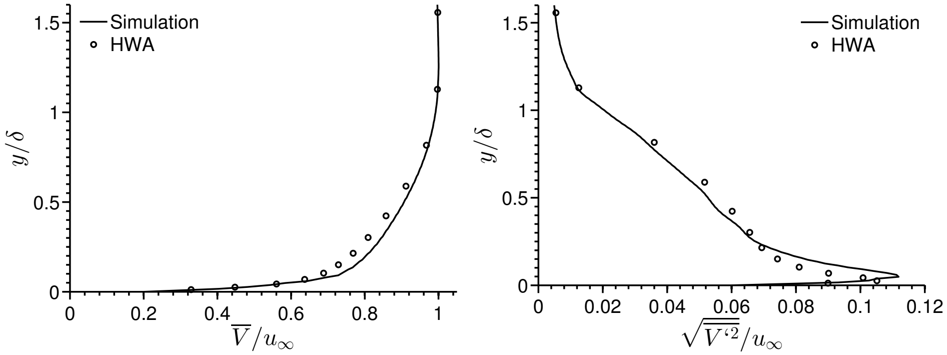

Figure 5.6: Mean (left) and rms (right) velocity magnitude, $V = \sqrt{u_x^2 + u_y^2}$, at the suction side measurement location $x/h = -2.5$ for $Re = 480,000$

The shedding of the larger vortical structures from the beveled edge is a process of both shear layers originating from the beveled trailing edge. Fig. 5.7 shows a visualization of the process for a single snapshot by iso-contours of λ_2. The vortical structures in the turbulent boundary layer are convected into the wake after separation. The large-scale shedding motion is visible through the sinusoidal arrangement of the wake behind the trailing edge, which translates to a flapping over time. To assess the shedding behind the beveled plate, Fig. 5.7 can be further analyzed. The streamwise distance between the upper and lower vortex (the wavelength of the shedding) is measured to be $1.925h$ in the far wake (outside the figure), where the convective velocity is assumed to be similar to the free-stream velocity. This results in a shedding frequency of approximately $\frac{u_\infty}{2\Delta_x} = \frac{25}{0.0385\times 2} = 325$ Hz, corresponding to a Strouhal number based on the plate thickness (h) of $St = \frac{fh}{u_\infty} = 0.26$. This result is in close agreement to the experimentally determined values of Blake [11], Bearman [120] and Greenway and Wood [121] which vary between 0.24 and 0.28 for high and low Reynolds numbers for beveled trailing edges respectively.

Fig. 5.8 shows a contour plot of the normalized mean streamwise velocity component. The numerical solution (Fig. 5.8, left) shows an attached boundary layer on the lower surface (pressure side) up to the point of the sharp trailing edge and both the numerical and experimental data show a separated zone over the upper surface (suction side) starting from the obtuse corner. Flow separation is fixed at the obtuse corner on the suction side as previously noted by Guan et al. [124]. A slight downwash is observed behind the trailing edge, which is caused by the slight camber of the plate introduced by the asymmetric edge, indicating that lift is generated [133]. Behind the obtuse corner, two recirculation zones form; a smaller one at the trailing edge and a larger one downstream of separation at the suction side of the upper-side corner point. These observations are similar to the ones reported by other authors [29, 115]. The contours of both the numerical and PIV results show close resemblance and display the separation point and recirculation region at similar locations. Some discrepancies are noted for the thickness of the incoming boundary layer, visible on the suction side in Fig. 5.8, and in the magnitude of the reversed flow. These discrepancies may be assigned the slightly differing ratio of the upstream turbulent boundary layer to airfoil thickness between the experiment and numerical simulation. Also, the finite width of the open jet in the experiments may give rise to discrepancies in the details of the flow around the trailing edge.

For trailing edge aeroacoustics in low Mach number flows, unsteady surface pressure fluctuations are of paramount importance [95]. In a turbulent boundary layer, these fluctuations are primarily caused by the interaction of the fluctuating wall-normal velocity component and the mean velocity gradient normal to the wall [139]. Hence, there exists a direct relation between wall-normal velocity fluctuations and sound generation [55]. Fig. 5.9 shows contour plots of the variance, or Reynolds stress $\overline{v\prime v\prime}$, of the y-velocity component. A thin, horizontal, shear layer appears at the obtuse corner for both the simulation and experimental results. At the trailing edge the highest values of the v-velocity component Reynolds stresses are found in the pressure-side shear layer, which contains unsteady fluctuations due to vortex shedding. The shear layer originating from the shedding process at the trailing edge, appears as a thin region of locally increased $\overline{v\prime v\prime}$. These regions are captured in the LBM and show a minor discrepancy with the PIV results with respect to the inclination of the shear layer. In the experimental results, the center of the shear layer developed from the obtuse corner point remains aligned with the x-coordinate direction, whereas in the simulation it is slightly inclined towards the pressure side. This may be explained by the boundary volume mesh in the simulation, which smoothed the first cell after the obtuse corner by $R/h = 0.012$ dependent on the local voxel resolution, causing a smoother transition towards the trailing edge. On

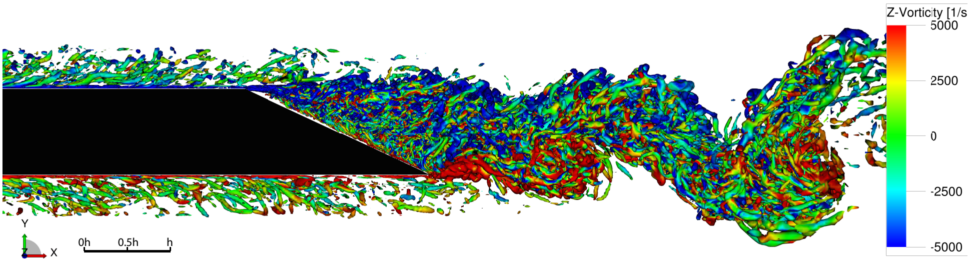

Figure 5.7: λ_2 iso-surfaces of the instantaneous flow around the beveled trailing edge, colored by spanwise vorticity for $Re = 600,000$

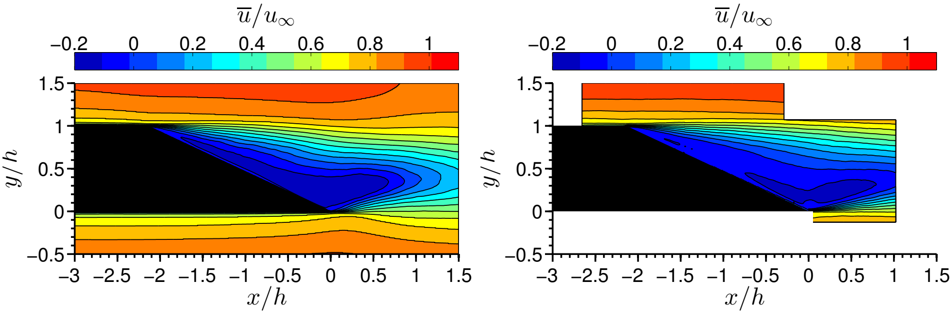

Figure 5.8: Contour plot of the normalized mean streamwise component, $\overline{u}/u_\infty$, for the numerical simulation (left) and the PIV experiment (right) for $Re = 480,000$

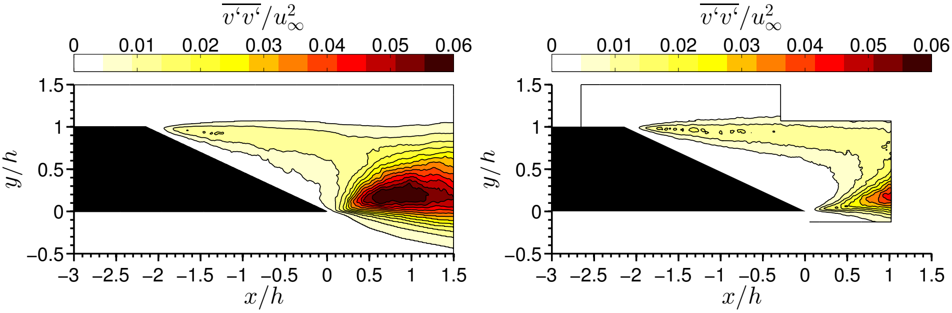

Figure 5.9: Contour plot of the normalized fluctuating y-velocity component, $\overline{v'v'}/u_\infty^2$, for the numerical simulation (left) and the PIV experiment (right) for $Re = 480,000$

the other hand, Bilka et al. [133] also found different shear angles for his experimental analyses of various beveled edges, but these were mainly assigned by differences in displacement thickness of the incoming turbulent boundary layer, which is also the case with the incoming boundary layer in the current study.

5.3.2. UNSTEADY SURFACE PRESSURE MEASUREMENTS

To asses the unsteadiness of both the turbulent boundary layer and the trailing edge flow, unsteady surface pressure measurements are performed in the experimental and numerical campaign. Fig. 5.10 shows the normalized ASD of the surface pressure measurements on the suction side for both the simulation and experiment. These data were normalized by the dynamic pressure (q_∞), free-stream velocity (u_∞) and the plate thickness (h). Effectively, this leads to an amplitude scaling by the free-stream velocity to the power of three, which is common for pressure fluctuations in close proximity of a wall [140, 141]. The figures illustrate the pressure spectra under the turbulent boundary layer at various locations along the suction-side surface of the plate. The first measurement is located in the upstream turbulent boundary layer, and the last measurement close to the trailing edge. Both the experimental and numerical results show a tonal peak and broadband components with a high frequency decay indicating the shedding and the turbulent boundary layer, respectively.

For the broadband component of the signal, there is an overall agreement in the shape of the spectra between the numerical and experimental results for all locations between Strouhal numbers of 0.2 – 1.6. At lower Strouhal numbers, the numerical results start deviating, likely due to the limited sampling time. The experimental results all show a strong, narrowband peak at the shedding frequency $\frac{fh}{u_\infty} = 0.26$. Similar peaks are found in the LBM solution before and after $x/h = -1.2$, albeit lower in amplitude. This amplitude decrease for the simulated results could be explained by the inclination of the shear layer, as well as the local increase in wall normal fluctuations close to the trailing edge compared to the experimental result, as indicated in the rms plot in Fig. 5.9. Bilka et al [133] stated that this difference could be assigned to variations in boundary layer characteristics, in particular the ratio $\delta^\star/h$. The numerical results in the middle of the recirculation region around $x/h = -1.2$, represents an outlier, where no acoustic tonal peak is observed for all cases considered in the simulation. The energy level of the peak could be too low in comparison with the higher turbulence intensity from the tilted shear layer, which appears to be closer to the wall compared to the experimental result. However, this question cannot be answered conclusively based on the data acquired in the present study.

Closer to the trailing edge, the decay is steeper at higher Strouhal numbers when compared to the results in the undisturbed, fully turbulent boundary layer. This difference is related to the presence of small-scale structures in the boundary layer upstream, which are associated to a broad range of frequencies, while the instability of the separated shear layer over the separated flow region leads to a large-scale shedding motion and concentrates kinetic energy at low frequencies. Downstream of and close to the separation point, at $x/h = -1.8$, the experimentally obtained data show a good collapse when scaled on the reference velocity, whereas the spectra obtained from the numerical solution show pronounced differences exceeding 5 dB for the broadband part of the signal. It is argued that the local y^+ values increases significantly at the obtuse corner point for the different Reynolds numbers, thereby altering the characteristic flow pattern. This strong Reynolds number dependence of the broadband part requires further attention. At the shedding frequency though, and at higher frequencies, strong agreement between experiments and simulations are found.

5.3.3. ACOUSTIC EMISSION

Acoustic waves are often visualized by density dilatation fields, defined as $\frac{1}{\rho}\frac{\partial \rho}{\partial t}$ [39]. Fig. 5.11 shows the dilatation for the case $Re = 480,000$ band-pass filtered around the shedding frequency with lower and upper cut-off frequencies $fh/u_\infty = 0.25$ and 0.27, respectively. The alternating pattern of positive and negative dilatation in the wake (near $x > 0$ and $y = 0$) is due to the large-scale vortex shedding, which introduces pressure fluctuations and, therefore, density changes, and shows a comparatively short wavelength on the order of the plate thickness. Moreover, acoustic waves propagate radially outward from the trailing edge and possess a wavelength larger by an order of magnitude when compared to the convected scales in the wake. This large difference in wavelength between hydrodynamic and acoustics perturbations at the same frequency arises due to large ratio of the speed of sound and the convective velocity in the wake, or the low Mach number $M \approx 0.06$. It should be noted that the acoustic pressure on the suction and pressure sides shows a phase opposition, which is reminiscent of a dipole, and displays the directivity characteristics of trailing edge noise for the non-compact case [142] with higher amplitudes for upstream propagating waves. Without the frictionless wall, the suction and pressure side waves would cancel in front of the leading edge, creating a zone of silence.

The FW-H analogy, described in the methodology section, is applied without the frictionless wall. The experimental results, obtained from post-processing the beamforming results reflect the average source power over the aperture of the array [143]. In the numerical results, this is modeled by averaging the source power over the angle covered by the aperture of the microphone array (α), i.e., between 75 and 105 degree above the trailing edge. A similar procedure for comparison between model equations and beamforming results was described by Pröbsting et al. [98]. The spectra are shown in terms of the reduced frequency and non-dimensionalized Sound Pressure Levels (SPL), and made non-dimensional by the dynamic pressure (q_∞), free-stream velocity (u_∞), the plate thickness (h), the model span (b), the observer location (r) and the Mach number (M_∞). Effectively, this leads to an amplitude scaling by the free-stream velocity with the fifth power. This is an often used scaling for typical problems of trailing edge scattered noise problems, where non-compact noise sources are the main source of interest [11, 140, 141]. Due to the cyclic boundary conditions and limited span, the acoustic pressure field in the numerical solution contains contributions from mirrored coherent image sources of the airfoil arriving through the cyclic domain boundaries to the microphone location. This problem is visualized in Fig. 5.12. To correct for this, in addition to previous mentioned scaling parameters, another correction has to be applied to the sound spectra. Oberai [144, 145] derived a three-dimensional, frequency dependent,

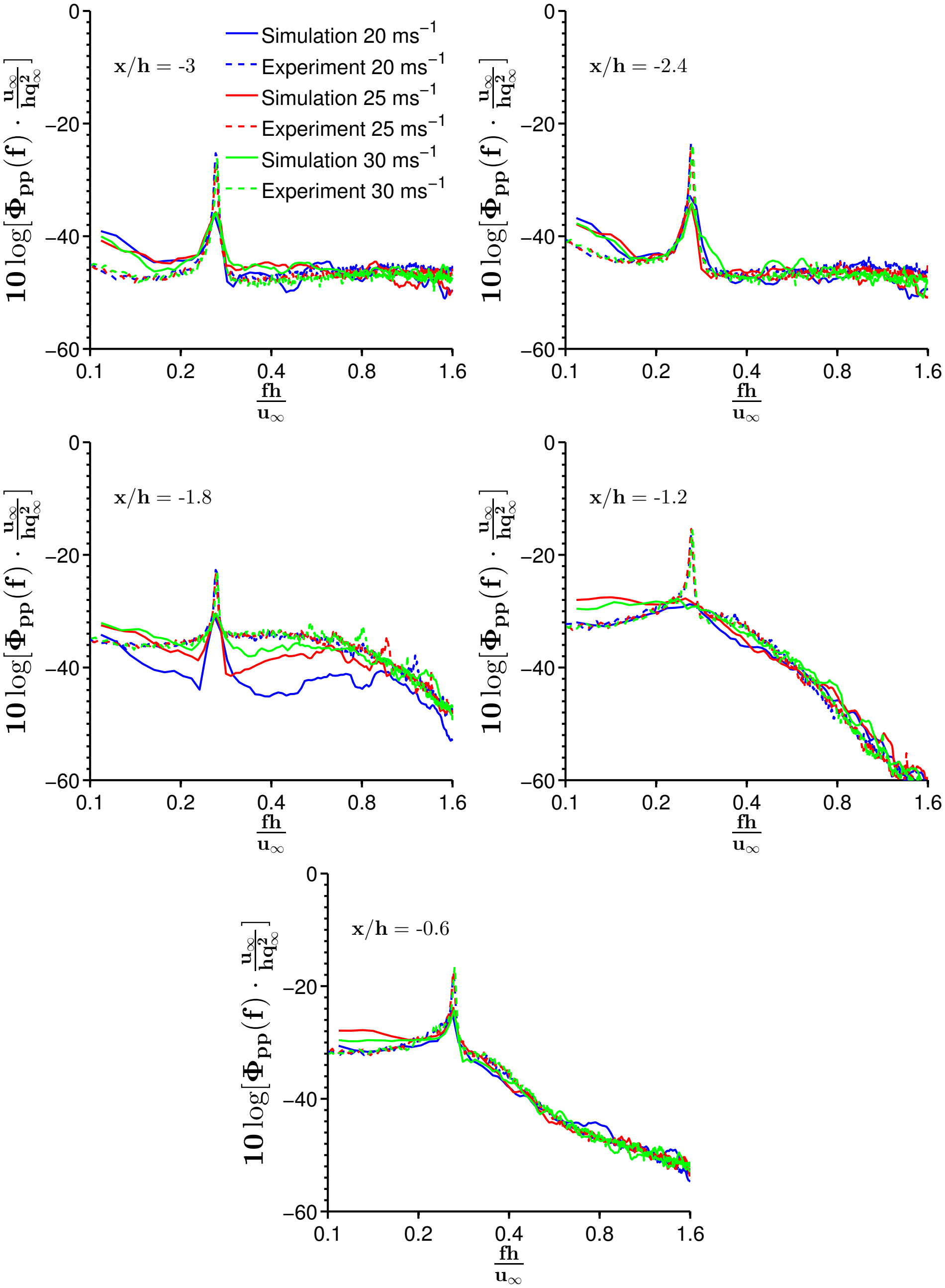

Figure 5.10: Normalized, unsteady, wall pressure spectra Φ_{pp} for $Re = 480,000$ (20 m/s), 600,000 (25 m/s) and 720,000 (30 m/s)

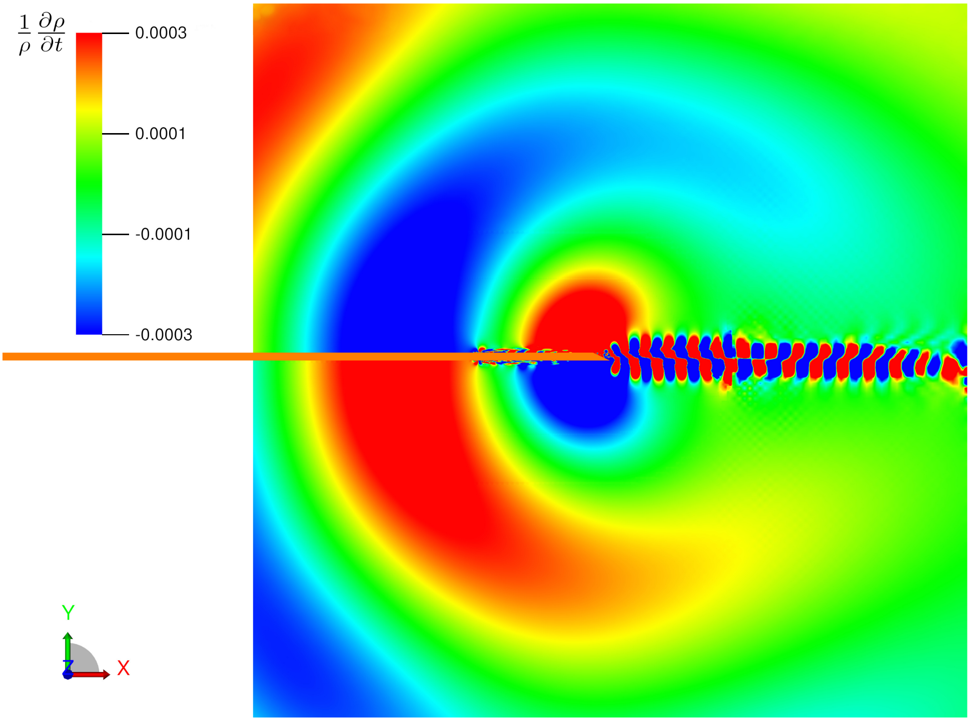

Figure 5.11: Non dimensionalized dilatation instantaneous field indicating the acoustic propagation around the shedding frequency ($St = 0.25 - 0.27$) for $Re = 480,000$

correction for low Mach number flows, which can be rewritten in a dB form as:

$$\Phi_{cor} = 10\log_{10}(fb^2/ar). \tag{5.15}$$

This correction has been applied on the direct probes measured in the simulated domain.

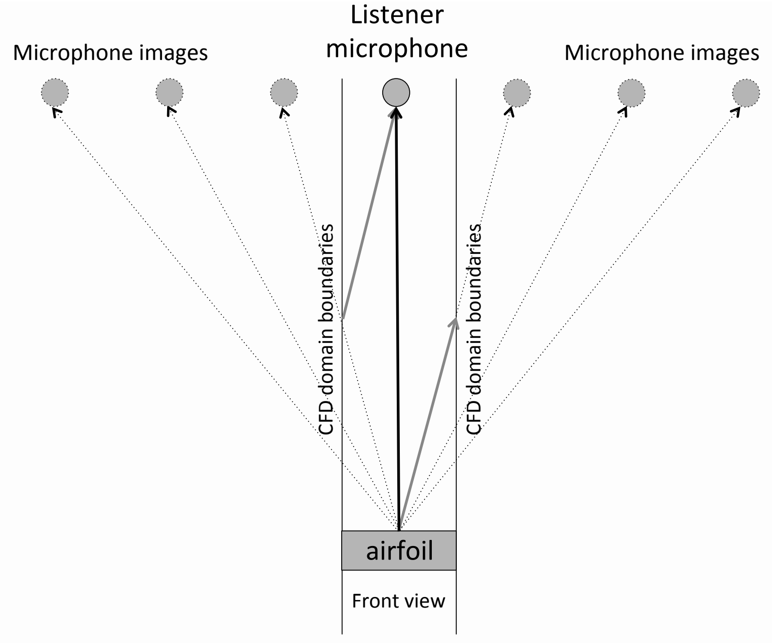

Figure 5.12: Acoustic images due to the spanwise simulated periodic boundaries [77]

Fig. 5.13 shows the non-dimensionalized, experimental and numerical acoustic far-field spectra for $Re = 600,000$ for the different numerical and experimental approaches. The results show a good agreement between the experimentally obtained data and the simulation at low and moderate Strouhal numbers. The tonal peak, at a thickness based Strouhal number of 0.26, corresponding to vortex shedding at the trailing edge, is present in both the simulated and measured spectra. At low frequency, the DAMAS results underestimate the actual source power due to spectral leakage through the boundaries of the fixed integration domain. Shannon and Morris [123] suggested that the DAMAS technique is superior to the CSM approach at high frequency, while the CSM is recommended for range of interest including the shedding peak. In the mid-frequency regime, where broadband noise from the incoming turbulent boundary layer is present, a good match between simulation and experiments is observed. The amplitude decay at higher Strouhal numbers is similar between experiment and simulation, with a maximum deviation of 2 dB. On the other hand, the sound pressure levels of the direct microphone probes within the simulation domain starts to reach a plateau above $St = 0.8$. This plateau is possibly caused by the coarsening of the mesh away from the beveled plate, resulting in a lower cut-off frequency. Due to the nature of the lattice Boltzmann scheme, particle distributions are always in movement. This implies that on average, background noise is larger in a lattice Boltzmann methodology when compared to a conventional Navier-Stokes based solution, where flow can be stagnant. This hypothesis is confirmed by running the same simulation in a double precision mode, see Fig. 5.13. Indeed, the spectra decay for the direct probes improves at higher frequencies when considering double precision mode.

Fig. 5.14 shows the acoustic far-field spectra for $Re = 480,000$, $600,000$ and $720,000$ and compares the results obtained from experiment (DAMAS) and simulation (FW-H). The different spectra collapse well and a close agreement is found between measured and simulated results for the broadband regime. A small discrepancy in the amplitude of the shedding peak amplitude of a maximum of 5 dB, as earlier discussed with the unsteady wall pressure microphones, is present on each simulated spectrum for both experimental and numerical cases. This difference has been addressed earlier by a small deviation in flow features, as the inclination of the shear layer and different ratio of $\delta^\star/h$. Furthermore, because the plots are scaled for non-compact dipole sources, the Mach scaling could cause a small discrepancy as well. A scaling for compact sources will improve the low frequency amplitude results.

In the simulation, the acoustic field was sampled around the trailing edge with a resolution of 10 degrees. With this information, it is possible to discuss directivity effects for different ranges of frequencies. In Fig. 5.15, the mean-square acoustic pressure for four different frequency regimes are depicted. It is known from experiments and analytical investigations that the acoustic radiation of trailing edge-noise has the highest sound pressure level in an oblique upstream direction [7]. Also the maximum radiation appears at higher upstream angles with increasing frequency. This behavior is recovered in Fig. 5.15, where the mean pressure levels between Strouhal numbers of 0.2 and 0.4 show compact dipole behavior whereas at higher frequency, non-compactness appear and a typical cardioid-like directivity pattern is present.

5.4. CONCLUSION

Based on the fully explicit and transient solution of the compressible Lattice Boltzmann Equation in combination with a Ffowcs-Williams and Hawking aeroacoustic analogy, an estimation of the acoustic radiation in the far field was obtained. To validate the coupling of these computational approaches for the prediction of trailing edge noise, the flow around a plate with an asymmetrically beveled 25° trailing edge in a low Mach number flow was analyzed. The flow field dynamics show similar trends and compare with a maximum deviation of less than 7% favorably for both the mean velocity field and turbulent fluctuations when compared to the experimental data. The simulations exhibit a slightly thicker boundary layer near the trailing edge, which may be a residual of the conservative tripping geometry selected for the simulation. The non-dimensional shedding frequency $\frac{fh}{u_\infty} = 0.26$ agrees well between experiment and simulation also shows a good agreement with previous experimental studies [11, 29, 120, 121]. After separation at the obtuse corner, the shear layer shows an inclination downwards towards the surface in the simulation, whereas it remains horizontal in the experimental results. This deviation

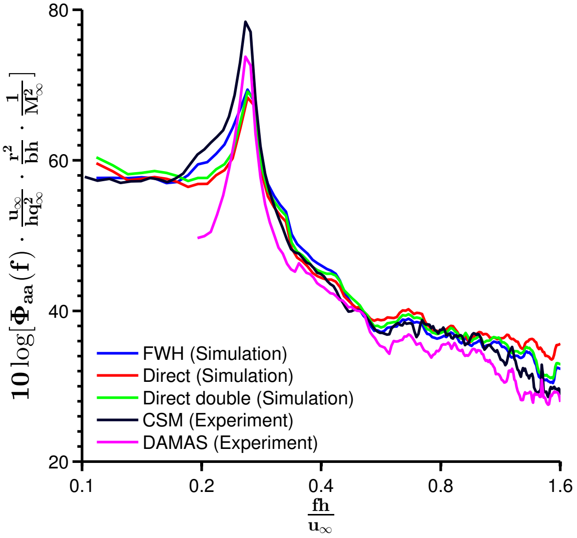

Figure 5.13: Non-dimensionalized, experimental and numerical acoustic far-field spectra for $Re = 600,000$

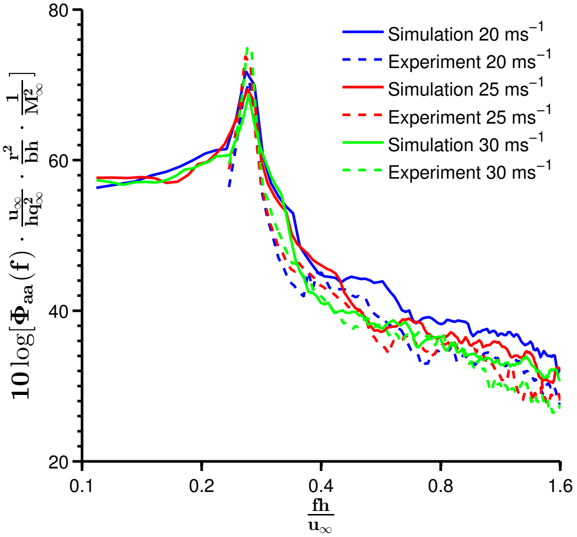

Figure 5.14: Experimental and numerical acoustic far-field spectra for $Re = 480,000$ (20 m/s), 600,000 (25 m/s) and 720,000 (30 m/s)

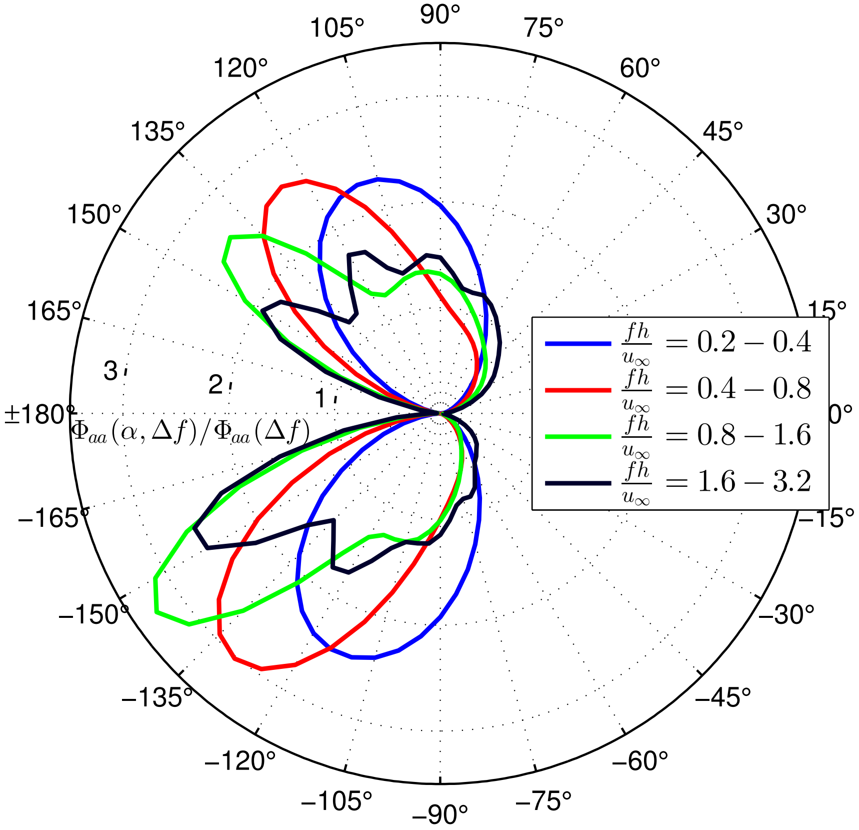

Figure 5.15: Mean-square acoustic pressure directivity plot for different frequency regimes obtained from the numerical simulation using the FWH analogy for $Re = 600,000$

may be the result of the surfel discretization at the sharp corner, the locally increased y^+ value, or the slightly thicker boundary layer at the trailing edge.

Unsteady surface pressure measurements over the edge with the obtuse corner produced spectra for the turbulent boundary layer upstream of the edge and for the separated flow region. The general trends found in the simulated wall-pressure spectra show deviations of less than 2 dB when compared to their experimental counterparts for the broadband noise regime. A peak, originating from the coherent vortex shedding around the trailing edge, is present and similar for both experiment and simulation. At the shedding frequency, simulated and experimental results show a maximum deviation of 5 dB with the simulated results being lower. The tilted shear layer enforces a small Reynolds dependence, which was observed at the pressure microphones close to the separation point. This dependency was not found in the experimental campaign, where the freestream velocity scaling of u_∞^3 was sufficient for collapse. Further away, downstream and upstream of the separation point, the wall pressure results were shown to be Reynolds independent for both experimental and numerical results.

Results of the acoustic far-field prediction were compared to acoustic measurements obtained from phased array measurements in combination with two beamforming methodologies. Vortex shedding results in a strong narrowband component centered at a fixed Strouhal number in the acoustic spectrum for both the simulation and experiment. Broadband noise is in excellent agreement with a similar maximum deviation of 2 dB as for the surface pressure spectra for $\frac{fh}{u_\infty} > 0.3$. The typical cardioid-like directivity behavior is found for the acoustic pressure obtained from the FW-H analogy.

In conclusion, the comparison between experiment and simulation presented here shows good agreement when compared to similar previous research efforts [29, 130]. In general, the methodology is thus regarded to be sufficiently accurate for trailing edge noise prediction, in particular for broadband noise. Turn-around time for a 0.1 physical second was 730 CPU hours on a Linux Xeon E5-2690 (eight-core) platform, clocked at 2.9 GHz. Exact reproduction of the experimental conditions is regarded to be the major obstacle for an even closer agreement of the results. The major differences include numerical modeling of the tripping device, finite jet width in the experiment, and discretization of the geometry near the sharp corners.

III

NOISE SUPPRESSION ADD-ONS

6

NOISE REDUCTION MECHANISMS OF SERRATED TRAILING EDGES

If we knew what it was we were doing,
it would not be called research, would it?

Albert Einstein

To reduce the trailing edge noise described in the previous chapter, noise suppression add-ons can be used. The current chapter investigates the flow topology and noise emission from an airfoil with a combed teeth trailing edge geometry, to understand the noise reduction mechanisms observed in earlier experiments. A comparison is made to a straight trailing edge and a serrated trailing edge without combs. The different trailing edges are retrofitted to a NACA 0018 airfoil at zero angle of attack. The flow field is analyzed by evaluating the fully explicit, transient, compressible Lattice Boltzmann equation. The acoustic far-field is obtained by means of a Ffowcs-Williams and Hawkings integral solution. The simulated acoustic farfield results and boundary layer characteristics for the teeth configuration match earlier experiments well. Furthermore, the numerical results confirm that the combed teeth give a larger noise reduction than the standard teeth. It is hypothesized that the main noise-suppression mechanism of the combs is an improvement of the streamline angles with respect to the conventional serration: in general, the flow tends to be less three-dimensional and more aligned with the serration edge. As a result, less vorticity is produced, especially at the root of the serrations.

Parts of this chapter have been published in the 35th ASME Wind Energy Symposium (2017) [146]

6.1. INTRODUCTION

SERRATED trailing edges have shown to be an good trailing edge add-on to suppress noise within the wind turbine industry for the last decade, as many manufacturers attach it to their turbines primary for a decrease in overall sound pressure level and secondary for an increase in annual energy production [147]. Although serrations are now used quite often, the noise reduction mechanism is not fully understood. Therefore, understanding and modeling the physics associated with the generation and propagation of noise is of paramount importance for the design of more silent wind turbines.

Brooks [7] defined the fundamental airfoil self-noise mechanisms associated with the trailing edge, such as the noise produced by the transitional or turbulent boundary layer flow interacting with the trailing edge or that due to vortex shedding. For turbulent boundary layer trailing edge noise, the unsteady surface pressure field, introduced by and convected with the turbulent eddies, is scattered at the discontinuity posed by the trailing edge. The acoustic radiation depends largely on the length scale of the turbulent eddies [11]. In the case of a developed turbulent boundary layer, the surface pressure is only affected over a highly localized area by various turbulent eddy sizes [11], a situation typically encountered at high frequency. At high frequency, the directivity pattern of the acoustic radiation shows a bias towards the leading edge (i.e. in upstream direction) [7, 11]. This asymmetry arises due to the fact that the acoustic wavelengths are much smaller than the airfoil chord, known as non-compactness of the acoustic source. For convecting turbulent boundary layers over sharp trailing edges, where the spanwise correlation associated with turbulent eddies is by far smaller than the airfoil span, an appropriate length scale is the local boundary layer displacement thickness $\delta^\star$ [122]. In the current study, the boundary layer thickness is kept constant while varying the trailing edge geometry, fixing the appropriate length scale.

Several authors, for instance Amiet [95] and Howe [55], have discussed trailing-edge noise in the light of incident turbulent flow and diffraction theory respectively. Within this framework, the relevant characteristics for noise radiation due to boundary layer interaction with the trailing edge are the auto-spectral density (ASD), the spanwise correlation length (l_z), and the convection velocity of the unsteady surface pressure. Amiet [95] and Howe [55] assumed that the incident surface pressure wave on the airfoil convects past the trailing edge. Howe [59, 148] analyzed a sawtooth trailing edge using a theoretical model for a flat plate, and concluded that the intensity of radiation at the trailing edge could be reduced by such a modification. The magnitude of the reduction depends on the length and spanwise spacing of the teeth, as well as the frequency of the radiation. It was determined that the dimensions of an individual serration should be at least of the order of the turbulent boundary layer thickness and that longer, narrower teeth should yield a greater intensity reduction [59, 148].

Several experiments have confirmed that trailing edge serrations indeed reduce trailing edge noise [149–156]. Airfoils and flat plates were tested in the past by Dassen et al. [149]. A maximum of 10 dB noise reduction for the flat plate and a 8 dB reduction for the airfoil was observed, both only in the low frequency range. Parchen et al. [152] continued the experimental investigation on trailing edge serrations, but considered full wind turbine blades and wind tunnel models. Slightly lower noise reductions were found as compared with the study from Dassen et al. [149]. This study was continued by Oerlemans et al. [151], however only a 2 to 3 dB noise reduction at low frequencies was observed. Both Parchen et al. [152] and Oerlemans et al. [151] reported noise increases at high frequencies. More recently, Gruber et al. [150] attempted to investigate the aeroacoustic effects of trailing edge serrations, slits and more complex add-ons on airfoils. On average, 3 – 5 dB reduction at low frequencies was observed using sharp sawtooth serrations, while at high frequencies, noise increases up to 5 dB were found. It was suggested that the significant noise decrease could be ascribed to a significant reduction of phase speed near the sawtooth edges, in combination with a slight reduction of pressure coherence along the edge. Gruber et al. [150] confirmed the results from Azarpeyvand et al. [157] and also concluded that the slitted-sawtooth trailing edge add-ons were the most effective noise-suppression add-on, with large noise reductions in the low frequency area and minor noise increases (< 1 dB) in the high frequency range. More recent experiments were performed by Arce-León et al. [154] on sawtooth, slitted-sawtooth and straight trailing edges on a NACA 0018 airfoil. The study confirmed the effectiveness of noise-suppression add-ons, even at zero angle of attack. However, the sawtooth design outperformed the slitted-sawtooth with a maximum of 5 dB at low frequencies. It was argued that, when applying the slitted-sawtooth design, still a straight trailing edge discontinuity appeared at the trailing edge location. Important to note though are the variations in terms of serration thickness as well as the bending capabilities of the slits with respect to other studies.

Based on the results from previous experimental studies, Howe's theory seems to overestimate the measured noise reductions. This may be because of the assumptions of the flow field, such as the assumption of frozen turbulence and the correct modeling of sound radiation and scattering. The latter might be Green function related [158]. Recently, Lyu et al. [159, 160] developed a new semi-analytical model applying Amiet's trailing edge noise theory [95] to sawtooth trailing edges. Results showed that the predicted noise reduction are closer to experiments [149–152]. Lyu et al. [159, 160] detected two non-dimensional parameters that substantially affect the noise reduction: $k_1 \times 2h$ and $l_{zp}(f)/\lambda$, where λ and $2h$ are the serration wavelength and length respectively, k_1 is the wavenumber in the chordwise direction of the convective velocity, and $l_{zp}(f)$ is the spanwise correlation length of the pressure fluctuations on the surface of the airfoil. The studies of Lyu et al. [159, 160] concluded that far-field noise can be reduced when both $k_1 \times 2h$ and $l_{zp}(f)/\lambda$ are much larger than unity. This implies that the serration should be long enough to ensure a considerable phase difference of the scattered pressure waves at the edge of the serration. In addition, if the spatial range of these phase differences, i.e. λ, is sufficiently small compared to the correlation length in the spanwise direction, radiated sound waves may destructively interfere with each other.

Numerical solutions of the flow source field and acoustic propagation have also been performed in the past on serrated trailing edges [80, 153, 161, 162]. By doing simulations one has the advantage of solving both flow and pressure fields, and obtaining the surface pressure fluctuations that are experimentally difficult to obtain. Jones & Sandberg [161] showed that serrations do not affect the flow upstream of the trailing edge significantly. Furthermore, the flow is found to be highly three-dimensional [153, 161], with formation of horse-shoe vortices in the space between the serrations, in combination with a mean flow through the teeth from pressure to suction side. Similar to experiments, lower noise reductions were found in comparison with the theoretical model of Howe [59, 148]. The recent numerical study of van der Velden et al. [153] complemented the experimental campaign of Arce-León et al. [155] by applying the Lattice Boltzmann equations to complex trailing edge add-ons, such as slitted-sawtooths retrofitted on a NACA 0018 airfoil at zero angle of attack. The results were found to be in close agreement with the experimental results and opened the door towards the optimization of serrated designs.

Although many attempts have been made, the underlying noise reduction mechanism of serrated trailing edges is still not fully understood. Possible explanations include, a variation in the hydrodynamic field, a reduction in acoustical source strength, a shift of low frequency acoustic energy to higher frequencies, or a change in sound diffraction due to the complex geometry. Especially the three dimensionality of the flow raises questions, as it is currently unclear how this directly affects the acoustic behavior of the flow. Better understanding of the physics may lead to improvements in serration design, and possibly the development of alternative concepts based on similar mechanisms and principles.

This current study aims to explore the flow topology and noise emission from an airfoil with a combed teeth trailing edge geometry, to understand the large noise reduction observed in experiments [147]. Comparison is made to a straight trailing edge and to a serrated trailing edge without the combs. The different trailing edges are retrofitted on a NACA 0018 airfoil at zero angle of attack. This zero-lift setup was chosen to focus on acoustic diffraction effect rather than aerodynamic effects induced by the large pressure differences over the teeth. The flow field is analyzed by evaluating the fully explicit, transient, compressible Lattice Boltzmann equation with a wall model in the inner region. The numerical results are validated against experimental data. Acoustic perturbations are obtained by means of a Ffowcs-Williams and Hawkings [47] integral solution. This makes it possible to study the actual noise reduction mechanism and compare to earlier studies and experiments. A similar numerical methodology has been validated against experiments before, as presented by van der Velden et al. [81, 153] (see Ch. 5).

6.2. COMPUTATIONAL METHODOLOGY

The following section describes the numerical methods used for determining the flow field, acoustic prediction and propagation, and noise source detection.

6.2.1. FLOW SOURCE FIELD

The commercial software package `Exa PowerFLOW 5.3b` was used to solve the discrete Lattice-Boltzmann (LB) equations for a finite number of directions. A detailed description of the equations used for the source field computations is given by Succi [27]. The LB method starts from a mesoscopic kinetic equation, i.e. the Boltzmann equation, to determine the macroscopic fluid dynamics. The discretization used for this particular application consisted of 19 discrete velocities in three dimensions (D3Q19) involving a third-order truncation of the Chapman-Enskog expansion, which has been shown to be sufficient to recover the Navier-Stokes equations for a perfect gas at low Mach number in isothermal conditions [82].

The distribution of particles was solved using the kinetic equations on a Cartesian mesh, known as a lattice, by explicit time-stepping and collision modeling. The Lattice-Boltzmann equation can then be written as:

$$g_i(\mathbf{x}+\mathbf{c}_i\Delta t, t+\Delta t) - g_i(\mathbf{x}, t) = C_i(\mathbf{x}, t), \tag{6.1}$$

where the particle density distribution function g_i can be interpreted as a histogram representing a frequency of occurrence at a position x with a discrete particle velocity $\mathbf{c}_i$ in the i direction at time t. $\mathbf{c}_i\Delta t$ and Δt are space and time increments respectively. The collision term on the right hand side of the LBM equation, $C_i(\mathbf{x}, t)$, adopts the simplest and also the most popular form known as the Bhatnagar-Gross-Krook (BGK) form [83]:

$$C_i(\mathbf{x}, t) = -\frac{\Delta t}{\tau}\left[g_i(\mathbf{x}, t) - g_i^{eq}(\mathbf{x}, t)\right]. \tag{6.2}$$

This term drives the particle distribution to the equilibrium with a relaxation time parameter τ. The variable g_i^{eq} is the local equilibrium distribution function. It relates the LB equations to hydrodynamic properties and is essential for the local conservation of mass and momentum to be satisfied. The equilibrium distribution of Maxwell-Boltzmann is approximated by a 2nd order expansion valid for small Mach number: [84]

$$g_i^{eq} = \rho\omega_i\left[1 + \frac{\mathbf{c}_i\mathbf{u}}{c_s^2} + \frac{(\mathbf{c}_i\mathbf{u})^2}{2c_s^4} + \frac{|\mathbf{u}|^2}{2c_s^2}\right] \tag{6.3}$$

where ω_i are the fixed weight functions related to the velocity discretization model D3Q19 [84] and $c_s = \frac{1}{\sqrt{3}}$ is the non-dimensional speed of sound in lattice units. The equilibrium function is related to the macroscopic quantities density ρ and velocity $\mathbf{u}$, which can be computed by summing up the discrete momentum of the particle distribution:

$$\rho(\mathbf{x}, t) = \sum_i g_i(\mathbf{x}, t), \qquad \rho\mathbf{u}(\mathbf{x}, t) = \sum_i \mathbf{c}_i g_i(\mathbf{x}, t). \tag{6.4}$$

A single relation for the relaxation time is used to relate to the dimensionless kinematic viscosity [84]:

$$\nu = c_s^2(\tau - \frac{\Delta t}{2}). \tag{6.5}$$

A Very Large Eddy Simulation (VLES) was implemented as viscosity model through the relaxation time τ, to locally adjust the numerical viscosity of the scheme [137]:

$$\tau_{eff} = \tau + C_\mu \frac{k^2/\epsilon}{(1+\eta^2)^{1/2}}, \tag{6.6}$$

where $C_\mu = 0.09$ and η is a combination of a local strain parameter ($k|S_{ij}|/\epsilon$), local vorticity parameter ($k|\Omega_{ij}|/\epsilon$) and local helicity parameters. The model consists of a two-equation $k-\epsilon$ Renormalization Group (RNG) modified to incorporate a swirl based correction that reduces the modeled turbulence in presence of large vortical structures [79].

Fully resolving the near wall region is computationally too expensive for high Reynolds number turbulent flow with the lattice concept of the LBM scheme. Therefore, a turbulent wall model is used to provide approximate boundary conditions until y^+ values of

250. In the current study, the following wall-shear stress model based on the extension of the generalized law of the wall model is used [84, 138]:

$$u^+ = f\left(\frac{y^+}{A}\right) = \frac{1}{\kappa}\ln\left(\frac{y^+}{A}\right) + B, \tag{6.7}$$

with

$$A = 1 + f\left(\frac{\mathrm{d}p}{\mathrm{d}x}\right). \tag{6.8}$$

This relation is iteratively solved to provide an estimated wall-shear stress for the wall boundary conditions in the LBM scheme. A slip algorithm [84], a generalization of a bounce-back and specular reflection process, is then used for the boundary process. Within the current test case, the wall model has negligible effect as the boundary is fully resolved until the viscous sub layer, leaving the last part to be modeled.

6.2.2. ACOUSTIC PREDICTION

Due to the fact that the LBM is inherently compressible and provides a time dependent solution, the sound pressure field can directly be extracted in the near field from the computational domain, provided that there is sufficient resolution to accurately capture the acoustic waves. Sufficient accuracy is obtained when considering at least $12-16$ cells per wavelength for the LBM methodology [79].

In addition, as for most trailing edge noise problems, an acoustic analogy is used to obtain the far-field noise. To recover the acoustic far-field, the Ffowcs-Williams and Hawkings [47] (FW-H) equation is employed. The time-domain FW-H formulation developed by Farassat known as formulation 1A [48], and extended based on the convective form of the FW-H equation is used to predict the far-field sound radiation of the trailing edge in a uniformly moving medium [49].

The formulations are implemented in the time domain using a source-time dominant algorithm also referred to as an advanced time approach [49]. The input to the FW-H solver is the time-dependent flow and pressure field on a surface mesh provided by the transient LBM simulations. This surface mesh is defined either as a solid surface corresponding to the physical body or as a permeable surface surrounding the solid body. The current study considers the solid surface methodology and hence, acoustic dipole sources L_i are the only source term for the current analogy [14]:

$$L_i = (p - p_0)n_i \tag{6.9}$$

with $p - p_0$ the fluctuating pressure on the solid surface and n_i the surface normal in the ith direction. To determine the far field pressure spectra, the distance between the observer ($\mathbf{x}$) and the source position ($\mathbf{y}$), R needs to be defined. It can be written as:

$$R = \frac{-M_0(x_1 - y_1) + R^\star}{\beta^2}, \tag{6.10}$$

with

$$R^\star = \sqrt{(x_1 - y_1)^2 + \beta^2\left[(x_2 - y_2)^2 + (x_3 - y_3)^2\right]}, \tag{6.11}$$

and

$$\beta = \sqrt{1 - M_0^2}. \tag{6.12}$$

R represents the effective acoustic distance rather than the geometric distance between the source and the observer in terms of time delay between emission and reception. The unit radiation vector then reads:

$$\hat{\mathbf{R}} = \left[\frac{-M_0 R^{\star} + (x_1 - y_1)}{\beta^2 R}, \frac{x_2 - y_2}{R}, \frac{x_3 - y_3}{R} \right]. \tag{6.13}$$

With the source term L_i and the observer distance from the source R defined, the following integral relation is solved [49]:

$$\begin{aligned} 4\pi p\prime_{aa}(\mathbf{x}, t) &= \frac{1}{a_0} \int_{g=0} \left[\frac{\dot{L}_i \hat{R}_i}{R(1 - M_i \hat{R}_i)^2} \right]_{ret} \mathrm{d}S \\ &+ \int_{g=0} \left[\frac{L_i \hat{R}_i - L_i M_i}{R^2 (1 - M_i \hat{R}_i)^2} \right]_{ret} \mathrm{d}S \\ &+ \int_{g=0} \left[\frac{L_i \hat{R}_i (M_i \hat{R}_i - M^2)}{R^2 (1 - M_i \hat{R}_i)^3} \right]_{ret} \mathrm{d}S. \end{aligned} \tag{6.14}$$

The subscript ret denotes the evaluation of the integrand at the time of emission, i.e. the retarded time. The acoustic probes are equally distributed in a circle around the trailing edge, 1.5 chords away, while for the FW-H analogy, data at 10 chords away is analyzed.

6.2.3. NOISE SOURCE DETECTION

To determine the location of the noise sources in the near field, Powell's [53] analogy is employed by looking into the dynamics of co-rotating flow structures. This so-called Flow-Induced Noise Detection (FIND) tool automatically detects and tracks flow structures in the flow field in order to locate and characterize the co-rotating vortices which produce noise. This, current experimental numerical technique, quantifies the acoustic radiation properties based on the theory of vortex sound [163]. This implies that in general at low Mach number flow, quadrupole sources are detected rather than more efficient scattering dipole sources [14]. Since dipole sources are presumably dominant for the serrated trailing edges studied here, the FIND results should be interpreted with care. To quantify the acoustic source, the following expression is found by Powell [53] for the far-field acoustic density fluctuations due to vortex motion:

$$\rho'(\mathbf{x}, t) \approx -\frac{\rho_\infty}{4\pi a_0^2 |x|} \frac{x_i x_j}{|x|} \frac{\partial^2}{\partial t^2} \int_V z_j (\Gamma \times \mathbf{u})_i \; \mathrm{d}V(\mathbf{z}), \tag{6.15}$$

with z_j being the projection of the integration vector z on e_z, ω the vorticity vector, dV the elementary volume of the fluid and ρ_∞, $\mathbf{x}$, $\mathbf{u}$, a_0 and t prescribed before as free-stream density, observer position, velocity, speed of sound and time, respectively. The volume of integration will be discretized in terms of vortex coreline elements. When assuming a system of two co-rotating vortex pairs at a distance of $2z$ with similar circulation Γ resulting in an angular velocity of $\Omega = \Gamma/(4\pi z^2)$, the far-field approximation can be written as:

$$\rho'(\mathbf{x},t) \approx -\rho_\infty 4\sqrt{\pi}\sqrt{\frac{\Delta l}{R}}\cos\left(2(\mathbf{x},\mathbf{e_1}) - 2\Omega t^* + \frac{\pi}{4}\right)\left(\frac{\Omega z}{2a_0}^{7/2}\right), \tag{6.16}$$

with Δl being the length of the vortex coreline element. The total radiated power, emitted by a pair of co-rotating vortices, then becomes:

$$P_{tot} = \oiint \frac{\rho'^2(\mathbf{x},t)a_0^3}{\rho_\infty}\,\mathrm{d}^2 S = \frac{\rho_\infty \Delta l \pi^2 \Omega^7 z^7}{8a_0^4}. \tag{6.17}$$

6.3. COMPUTATIONAL SETUP AND TEST CASES

A NACA 0018 airfoil with a chord of $l = 0.2$ m and straight trailing edge is considered as baseline model in an undisturbed, turbulence-free (< 0.1%) flow field under zero angle of attack of 20 m/s ($M = 0.06$), resulting in a chord based Reynolds number of $Re_l = 280{,}000$. Spanwise, cyclic boundary conditions are applied with a modeled span of $b = 0.08$ m ($b = 0.4l$). Transition is enforced by a zig-zag transition strip of height $t_{trip} = 0.6$ mm ($t_{trip} = 0.003l$) and streamwise length $l_{trip} = 3$ mm ($l_{trip} = 0.015l$) on both upper and lower sides of the airfoil at $x = -0.8l$, i.e. 20% of the chord. This trip height corresponds to half the local incoming boundary layer thickness δ_0, but is rather more dependent to the ratio of trip height to cell size (six in this case). More information can be found in Ch. 2. One zig-zag spans $b_{trip} \approx 3$ mm ($b_{trip} \approx 0.015l$), resulting in a repetitive pattern of 27 triangles.

Besides the straight trailing edge reference case, a serrated tooth trailing edge is tested, as well as a combed teeth design. A sketch of the geometry is found in Fig. 6.1. The serration model considered in this study has teeth of $2h = 0.04$ m ($2h = 0.2l$) length and $\lambda = 0.02$ m ($\lambda = 0.1l$) width, resulting in a length-width ratio of $2h/\lambda = 2$. The width of the combs is similar to their spacing $d = 0.5$ mm ($d = 0.0025l$). Both trailing edge add-ons are of flat-plate type, with a constant 1 mm ($t_{ser} = 0.005l$) thickness throughout the entire span and length, thus not changing the nominal thickness of the straight airfoil trailing edge. The first serration was placed mid-span, with a total of 4 serrations being modeled with the chosen span. This geometry has been presented before by van der Velden et al. [153].

The simulation domain size is a block of $12l$ in both streamwise and wall normal direction. Outside a circular refinement zone of $10l$ diameter an anechoic outer layer is used to damp acoustic reflections. A total of 10 refinement regions are applied such that, near the boundary, the first cell is placed in the viscous sub layer, i.e. at $0.00039l$. This results in an average y^+ value over the airfoil surface trailing edge of 3. In total, around 150 million voxels were used to completely discretize the problem, with a total of 65 million time-step equivalent voxels. 0.1 seconds of simulation time (10 flow passes) took 6,300 CPU hours on a Linux Xeon E5-2690 2.9 GHz platform of 80 cores.

After the transient phase of 10 flow passes, sampling is started. The Courant-Friedrichs-Lewy (CFL) number is dependent on the wave propagation velocity and smallest voxel size in this compressible simulation and fixed to unity for each single simulation. Therefore, the physical time step is fixed at $1.3 \cdot 10^{-7}$ s. Data is sampled at 30 kHz ($St = fl/u =$

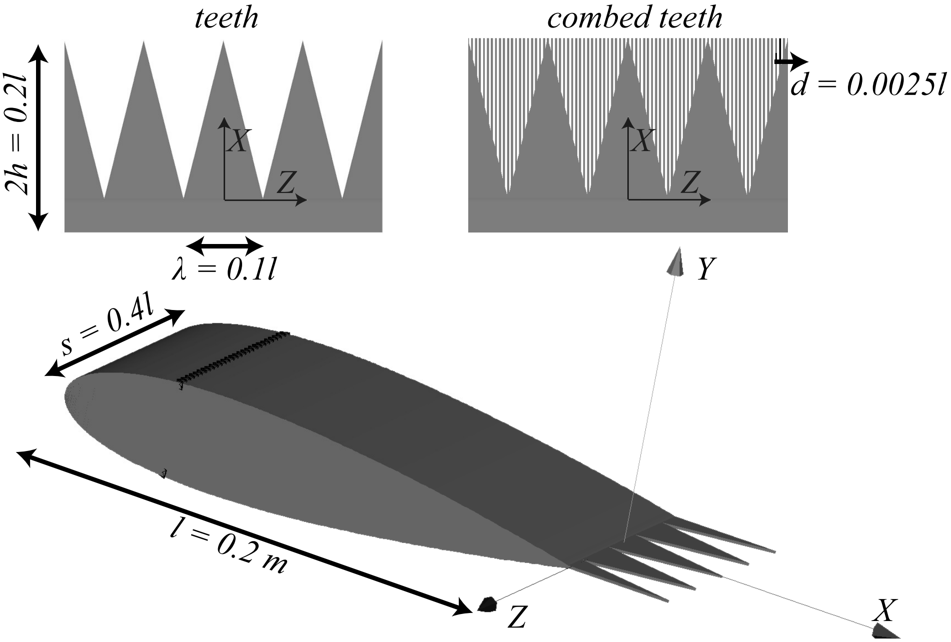
teeth
combed teeth
2h = 0.2l
d = 0.0025l
λ = 0.1l
X
Z
X
Z
Y
s = 0.4l
l = 0.2 m
Z
X

Figure 6.1: Airfoil and serration geometry and dimensions

300) for 0.2 physical seconds at local lattice size, resulting in a recording of 20 flow passes or 6,000 samples. Fourier transformed data are obtained with a Hamming window with 50 % overlap, to smooth the spectra (App. B & C).

The adopted Cartesian coordinate system, as shown in Fig. 6.1, for each case is defined as follows: the origin is chosen at the location of the baseline airfoil trailing edge; the z-axis coincides with the airfoil trailing edge; the x-axis is aligned with the chord of the airfoil (i.e., on the serration centerline); and the y-coordinate is perpendicular to the surface of the serrations. In presence of serrations, the origin coincides with the projection along the chord direction of a serration tip on the trailing edge of the baseline model.

Given the flow similarities over the repeated serrations in the computation domain, and in order to further reduce the uncertainty on the velocity fields, in the following, the computed fields are spatially averaged along the spanwise direction at points with the same relative spanwise location with respect to the serration root. This procedure reduces the uncertainty by increasing the number of samples available for averaging, and has been successfully applied before [161].

6.4. RESULTS

In this section, first the computed boundary layer development will be validated against experiments. Next, the computed far-field noise emission for the difficult configurations is evaluated against experiments on the same cases. Furthermore, the directivity pattern is analyzed. In the remaining sub-sections of this section, possible mechanisms for the observed noise reduction will be explored; mean flow direction, boundary layer characteristics, surface pressure, convection, spanwise coherence and noise source detection by a new, experimental, splitting tool.

6.4.1. BOUNDARY LAYER DEVELOPMENT OVER THE AIRFOIL

A verification and validation of the boundary layer information at the trailing edge location is essential for trailing edge noise comparisons. To visualize the transition process and the growth of the turbulent boundary layer over the airfoil edge using this computational setup, an instantaneous view is displayed in Fig. 6.2. As the airfoil is placed at zero angle of attack, the mean flow is symmetric on both sides of the airfoil and hence, with zero lift. The attached turbulent boundary layer convects over the sharp trailing edge, and a wake with almost zero shedding component is visible.

The boundary layer profile of the mean streamwise velocity component and time-averaged turbulent statistics [13] were inferred from the computed velocities from the straight trailing edge. They are reported in Fig. 6.3 and summarized in Tab. 6.1. Results agree well with the measured boundary layer integral parameters reported by Arce-León et al. [155].

6.4.2. NOISE EMISSION AND DIRECTIVITY

The acoustic waves in the computational domain coming from the interaction between the hydrodynamic pressure fluctuations and the airfoil trailing edge can be depicted by means of dilatation snapshots. Dilatation is defined as $\frac{1}{\rho_\infty}\frac{\partial \rho}{\partial t}$ [39], and is visualized by

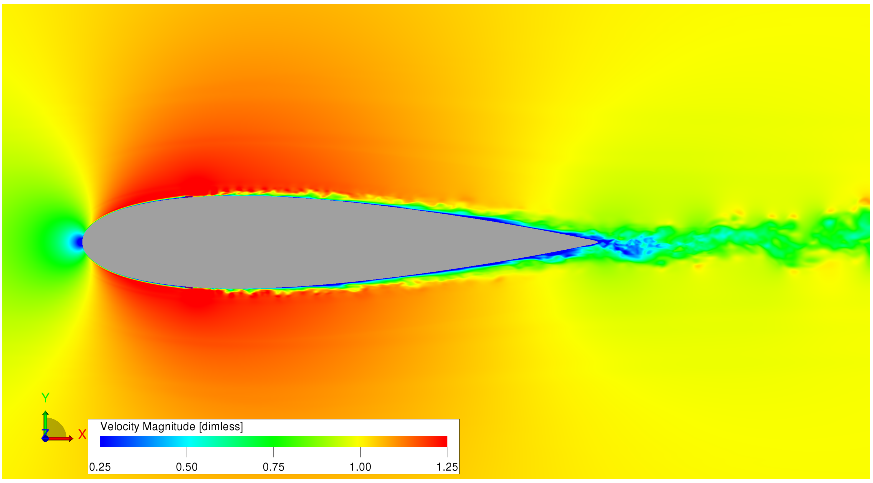
Y
X
Velocity Magnitude [dimless]
0.25
0.50
0.75
1.00
1.25

Figure 6.2: Instantaneous view of the flow around a NACA 0018 airfoil with straight trailing edge

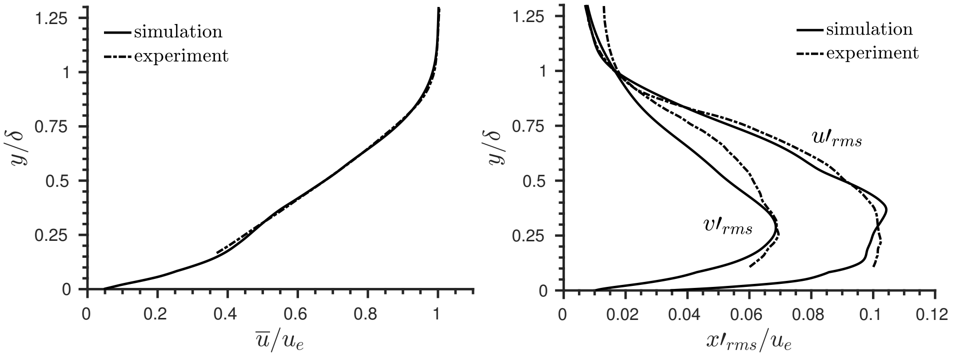

Figure 6.3: (left) Mean streamwise velocity component and (right) time-averaged turbulent statistics for the baseline airfoil with straight trailing edge at $x/l = 0$. u_e is the local edge velocity. Experimental data is extracted from Arce-León et al. [155].

Table 6.1: Boundary layer characteristics at $x/l = 0$

Parameter	**Symbol**	**Quantity**
Free stream velocity	u_∞	20 m/s
Edge velocity	u_e	18.75 m/s
Displacement thickness	$\delta^\star$	3.3 mm
Momentum thickness	θ	1.5 mm
Boundary layer thickness	δ	9.5 mm
	δ_{95}	7.9 mm
Reynolds number	Re_c	280,000
	$Re_{\delta^\star}$	4,600
	Re_θ	2,100
	Re_δ	13,300
Shape factor	H	2.2

one single snapshot in Fig. 6.4 for three different Strouhal numbers. An alternating pattern of positive and negative dilatation on the airfoil wall and in the wake is present due to the presence of the instability in the turbulent boundary, generating pressure fluctuations and therefore density changes, while growing over the airfoil surface and in the wake. At low Strouhal numbers, it shows a high wavelength compared to the order of the airfoil chord. This relation, defined by Λ/l gives information on the compactness of the source. Non-compactness appears when $\Lambda/l < 1$.

Moreover, acoustic waves propagate radially outward from the trailing edge and possess a wavelength larger by an order of magnitude when compared to the convected scales in the wake. This large difference in wavelength between hydrodynamic and acoustics perturbations at the same frequency arises due to the large ratio of the speed of sound to the convective velocity in the wake. It should be noted that the acoustic pressure on the suction and pressure side shows a phase opposition, which is characteristic for a dipole, and displays the expected directivity characteristics of trailing edge noise for the convected dipole case [142] with higher amplitudes for the upstream propagating waves. The acoustic waves from both airfoil sides cancel each other out upstream of the leading edge, creating a zone of silence and resulting in a directivity of a compact, dipole-like, behavior. At the highest presented Strouhal number (right image of Fig. 6.4), non-compact behavior is observed, in line with the lower ratio of Λ/l.

At a location directly positioned above the airfoil trailing edge, the time series of the pressure fluctuations are recorded (Φ_{meas}). The power spectrum is extracted from the FW-H analogy, as described in previous section. To enable comparison with experiments, the data presented in Fig. 6.5 is normalized for Mach number M, observer radius R and a span b by means of:

$$\Phi_{aa} = \Phi_{meas} + 10\log_{10}\left(\frac{R^2}{bM^5}\right). \tag{6.18}$$

Effectively, this leads to an amplitude scaling by the free-stream velocity to the power five. This is an often used scaling for typical problems of trailing-edge scattered noise problems, where non-compact noise sources are the main source of interest [11, 140,

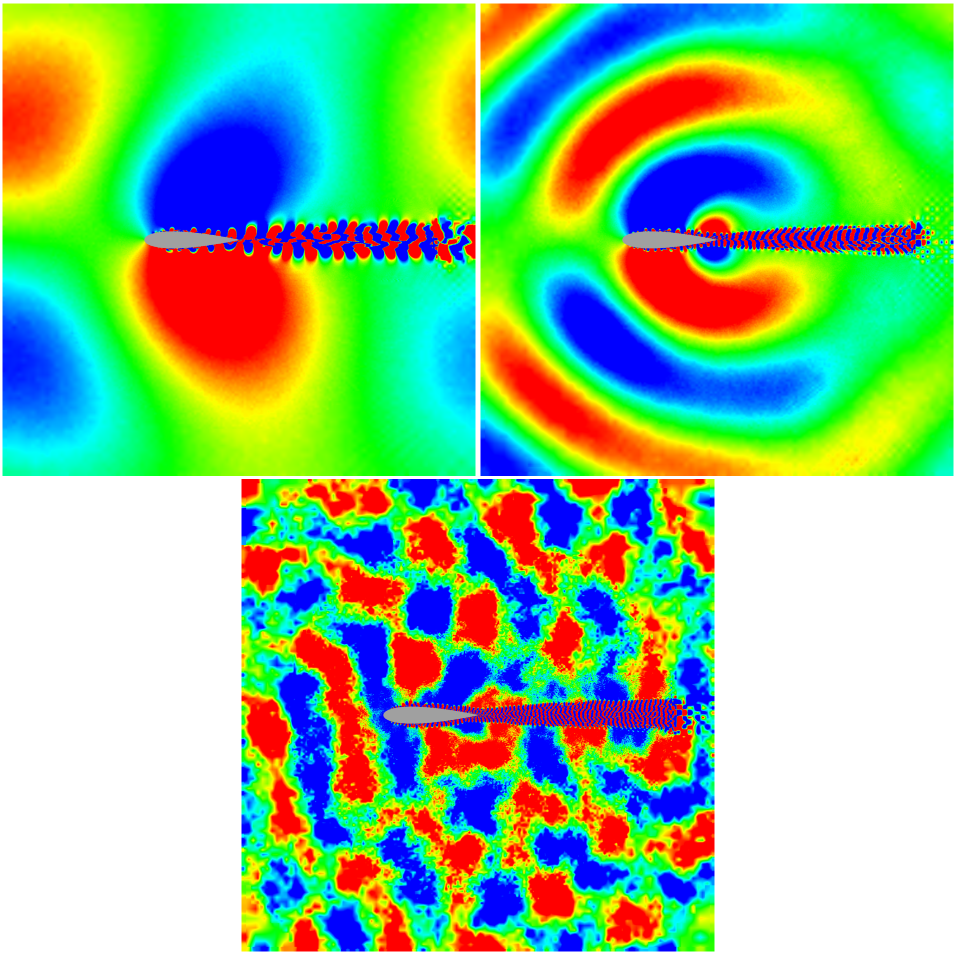

Figure 6.4: Instantaneous snapshots of the dilatation field around the straight trailing edge, band passed at (left) $St_l = fl/u_\infty = 4$ ($\Lambda/l = 4.25$), (right) $St_l = fl/u_\infty = 10$ ($\Lambda/l = 1.7$), (bottom) $St_l = fl/u_\infty = 20$ ($\Lambda/l = 0.85$) respectively

141]. The results of the scaled calculated acoustic pressure spectrum (Φ_{aa}) as well as the measured noise reduction ($\Delta\Phi_{aa}$) with respect to the straight trailing edge (positive is reduction) is presented in Fig. 6.5. As reference, acoustic wind tunnel data for the teeth trailing edge configuration was obtained from the study of Arce - León et al. [155].

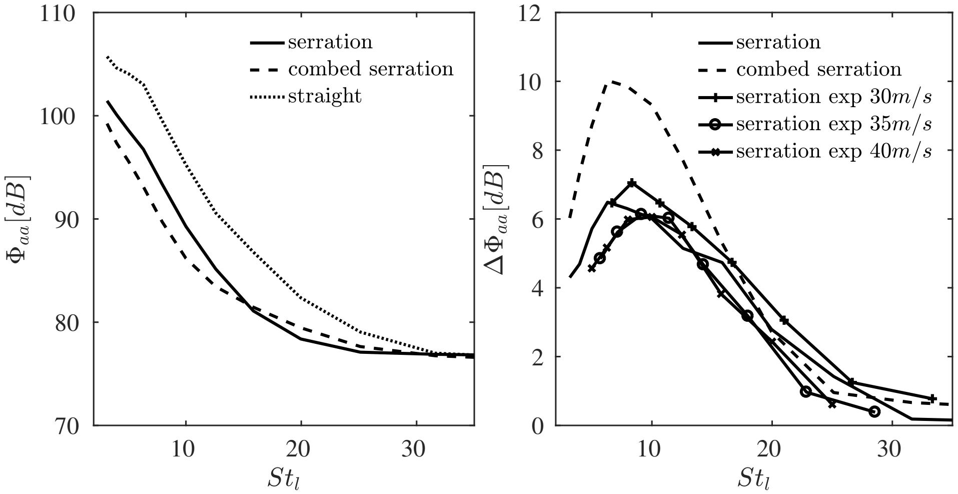

Figure 6.5: Left: normalized computed far-field sound pressure levels (left). Right: computed and measured noise reduction with respect to the straight edge at an observer position above the trailing edge. Experimental data is extracted from Arce-León et al. [155].

The spectral trends are similar for all three trailing edges; high sound pressure levels at low frequencies and a decay towards high frequencies. There are no significant peaks, indicating no distinctive shedding present in the computational model. In general, the noise is of broadband type, with the dilatation field (Fig. 6.4) clearly pinpointing the source region near the trailing edge of the airfoil. Both serrated trailing edges show noise reductions up to $St_l = 32$, corresponding to a $St_\delta = 1.5$. The teeth model reaches a maximum of 6 dB and the combed teeth configuration a maximum of 10 dB around $St_l \approx 8$. This large noise reduction for the combed teeth configuration is in line with experimental observations on this concept on a full-scale wind turbine [147]. Moreover, the experimental results plotted in Fig. 6.5 for the teeth configuration are comparable with the numerical results in this study. Comparable results are found for all experimentally available Strouhal numbers, which gives confidence in the numerical results. Although the measurements were taken at different velocity (30 m/s), the scaling seems to be appropriate. Results from lower velocity slightly moves the maximum noise reduction to lower Strouhal numbers, but this can likely be corrected by a scaling based on displacement thickness.

Another interesting comparison is using the analytic relation derived by Howe [59, 148], which would give a reduction of $10\log_{10}\left[1+(4h/\lambda)^2\right] = 12.3$ dB for the teeth configuration. Integrating the noise reduction levels over the displayed Strouhal numbers results in an overall sound pressure level reduction with respect to the straight trailing edge of 4.1 dB for the teeth model and a 5.7 dB reduction for the combed teeth model (App. A).

This calculated 4.1 dB is much lower than the 12.3 dB predicted using Howe's model, but closer to the experimentally determined values presented before [150, 151, 155].

The dilatation snapshot in Fig. 6.4 showed the appearance of a convected dipole behavior, radiated towards the leading edge for $\Lambda/l = 1.7$. To observe this behavior in a more quantitative manner, a directivity analysis is performed. An array of 360 microphones positioned in a circle at mid-span around the trailing edge are used to record the acoustic pressure fluctuations derived from the FW-H integral solution method. Results are depicted in three different frequency bands in Fig. 6.6.

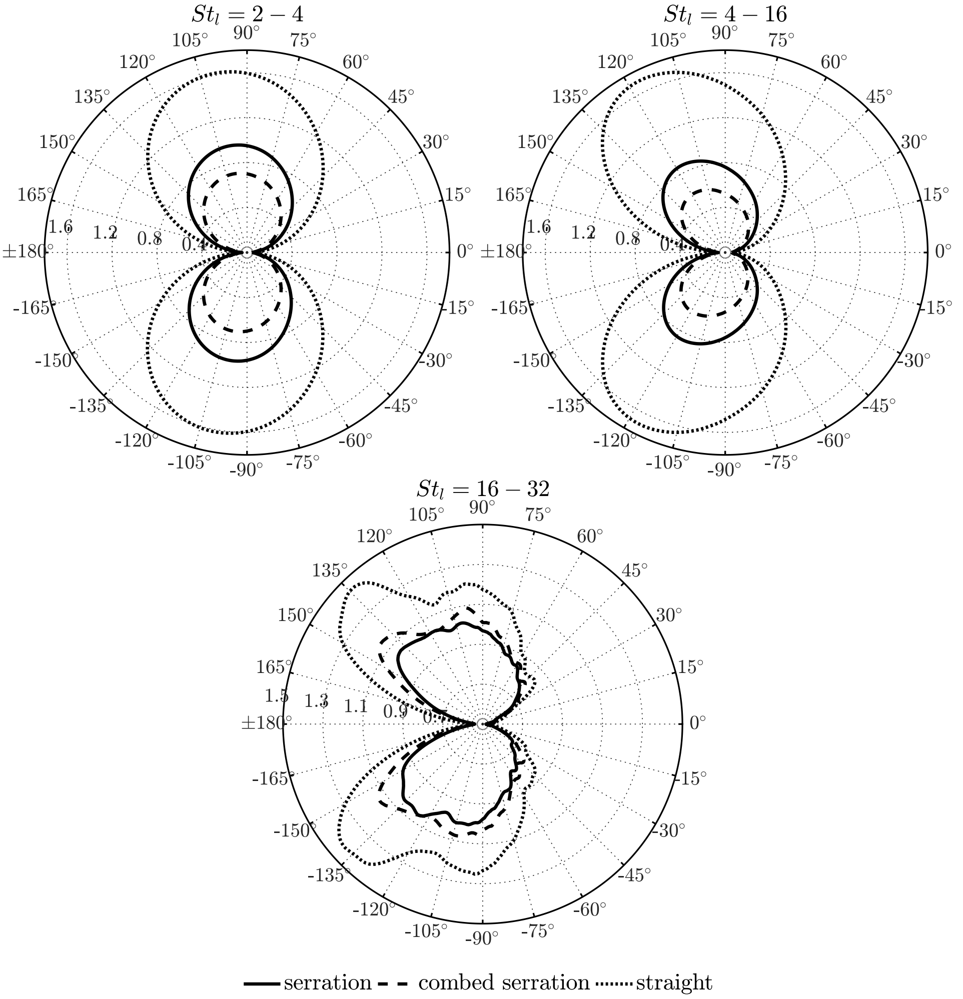

Figure 6.6: Directivity plot of $\Phi_{aa}(\alpha, \Delta f)/\Phi_{aa}(\Delta f)$ for the straight, teeth and combed teeth trailing edge models under different Strouhal numbers. Left $St_l = 2 - 8$ ($\Lambda/l = 8.5 - 2.1$), right $St_l = 8 - 16$ ($\Lambda/l = 2.1 - 1.1$) and bottom $St_l = 1.1 - 0.5$. Normalized by mean values of the straight edge case.

The behavior in terms of directivity is as expected; at low Strouhal numbers, a compact dipole source is observed. Increasing the frequency leads to a tilted dipole, directed towards the leading edge. When further increasing the frequency, non-compact behavior appears with multiple lobes. Between $St_l = 2-8$ and $St_l = 8-16$, noise reduction is observed in all directions for both the teeth and combed teeth model, with the largest reduction at upstream angles between 105 – 135 degrees. At higher frequencies the variations are smaller and the differences between the teeth and combed teeth model can almost be neglected. Also, it seems that the upstream traveling waves are canceled out more effectively with the trailing edge devices, resulting in a less upstream oriented directivity shape. This was hypothesized before by Jones and Sandberg [161] to be due to the out-of plane acoustic waves generated by the edge angle of the teeth.

6.4.3. MEAN FLOW OVER THE SERRATED EDGE

In order to determine the noise reduction mechanisms for the two investigated serrations, the mean flow over the serrated edge is discussed in this section. Earlier flow measurements [164] and computations [153, 161] showed that, even at small angles of attack, the turbulent flow tends to permeate into the empty space in between serrations. Both an outward (i.e., from the centerline toward the edge of the serration) and an inward (i.e., from the edge toward the centerline of the serration) flow characterizes the flow field at the root and the tip of the serrations, respectively. This flow distortion is found to reduce the effective angle seen by the turbulent flow convecting over the edge of the serrations, thus reducing the effectiveness of the serrations in reducing far-field noise [59, 148, 165].

The near-wall spatial distributions of the time-averaged mean velocity components are shown in Fig. 6.7 and Fig. 6.8 for the conventional teeth and the combed teeth geometry, respectively. Data are extracted at a plane close to the surface, i.e. $y/\delta = 0.05$ ($y = 0.5$ mm). Results from the conventional teeth geometry agree with previous studies [153, 155, 156, 161]; the mean streamwise velocity component increases from the root to the tip, corresponding to an acceleration of the flow with a thinning effect of the boundary layer (see also next section). Most notably, the flow tends to seep into the empty space in between serration (downward motion) as evidenced by the negative mean wall-normal velocity component ($\overline{v}$). As a direct consequence, the flow exhibits an outward motion as visible from the contour of the spanwise velocity component ($\overline{w}$).

For the combed teeth model, the streamwise component ($\overline{u}$) shows similar flow features, although the flow over the edge accelerates slightly faster. However, the downward motion of the wall normal velocity ($\overline{v}$) at the edge of the solid part of the teeth is much less pronounced. Furthermore, the spanwise component ($\overline{w}$) is almost totally canceled out, presumably due to the tangent orientation of the combs, starting already at the root. This results directly in a more streamwise, aligned streamline over the serrated edge ($\tan^{-1}\left(\overline{u}, \overline{w}\right)$). This effect is positive for noise reduction, as concluded before by Howe [59], and may explain why the combed teeth are more quiet than the conventional teeth.

6.4.4. BOUNDARY LAYER CHARACTERISTICS OVER THE SERRATED EDGE

Besides the mean flow direction, the boundary layer characteristics might also explain the noise reduction from the (combed) teeth. As mentioned in the introduction, the hydrodynamic velocity fluctuations in close vicinity of the surface will affect the surface

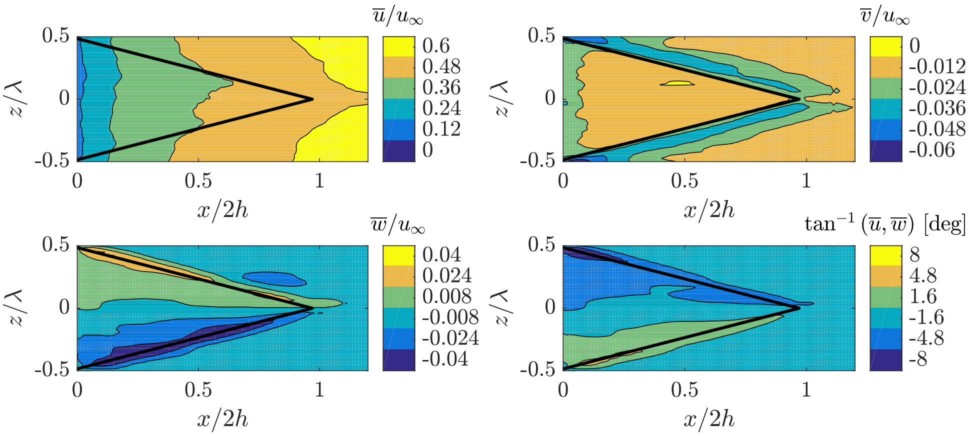

Figure 6.7: Contour of the mean velocity component over the teeth serration at $y/\delta = 0.05$: (top left) streamwise $\overline{u}$, (top right) wall-normal $\overline{v}$ and (bottom left) spanwise $\overline{w}$ velocity components. Projections of the solid serration on the $x-z$ plane are indicated by means of continuous black lines.

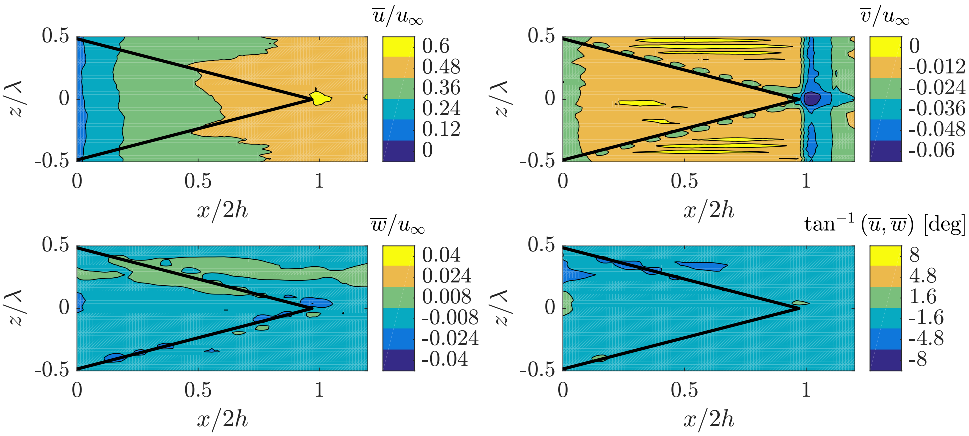

Figure 6.8: Contour of the mean velocity component over the combed teeth serration at $y/\delta = 0.05$: (top left) streamwise $\overline{u}$, (top right) wall-normal $\overline{v}$ and (bottom left) spanwise $\overline{w}$ velocity components. Projections of the solid serration on the $x-z$ plane are indicated by means of continuous black lines.

pressure fluctuations, which at edges act as an effective acoustic dipole source. It is interesting to study different key parameters in the boundary layer which could affect the noise production process at an edge. Three different points along the serrated edge are selected; the root, mid and tip of the teeth edge are compared to values obtained from the straight trailing edge. In addition, experimental data of the mean boundary layer flow obtained by Arce-León et al. [155] is added for convenience. The mean streamwise velocity and Reynolds shear stress profiles are extracted and plotted in Fig. 6.9, while the Reynolds normal stresses are plotted in Fig. 6.10. All plots are normalized according to the boundary layer parameters measured in mid-span at the trailing edge of the straight case, as defined in Tab. 6.1.

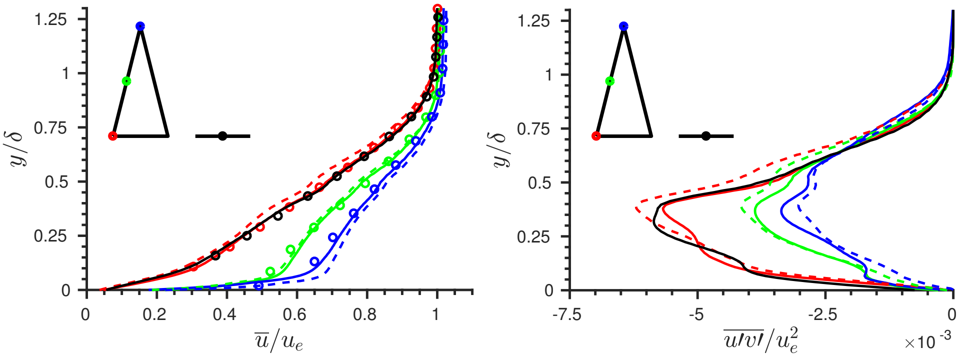

Figure 6.9: Mean velocity profile (left) and Reynolds shear stress (right) at different locations on the edge for the straight (black), teeth (solid) and combed teeth (dashed) case. Experimental data for the teeth, depicted by the circles, is extracted from Arce-León et al. [155].

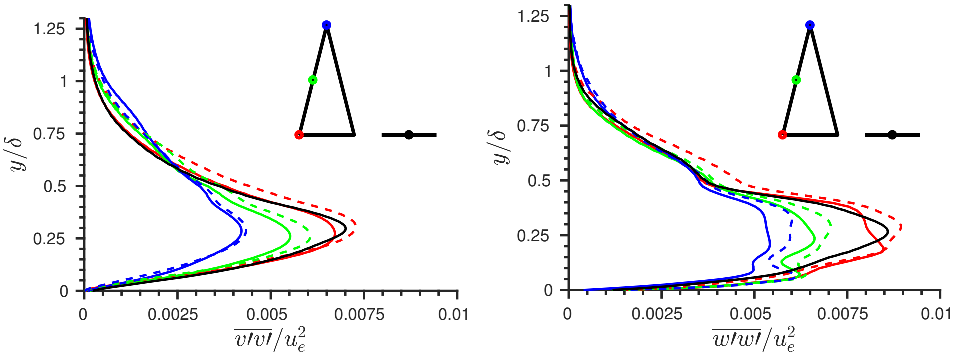

Figure 6.10: Reynolds normal stress profiles at different locations on the edge for the straight (black), teeth (solid) and combed teeth (dashed) case

The mean streamwise flow in Fig. 6.9 displays small variations for both serrated trailing edges when considering the point in the root of the serration (red line) with respect to the straight trailing edge (black). The boundary layer upstream of the trailing edge seems not to be affected by shape of the edge. A more turbulent profile is found downstream along the teeth edge (green and blue line), where a compression of the boundary layer shows a thinner boundary layer thickness. The experimental results, depicted by the circles, are in good agreement with the results from the LB simulation, giving confidence in the numerical results. Both trailing edge devices show similar trends, with higher mean streamwise velocity in the lower part of the boundary layer at the very tip of the serration. As the combs could be seen as a porous membrane, the flow will accelerate slightly faster on the solid surface of the teeth. Fig. 6.9 also shows the Reynolds shear stress, to provide information on structures sweeping and ejecting in the boundary layer, known as acoustic quadrupole sources in Lighthill's stress tensor [46]. This may be connected to surface pressure fluctuations, as is proposed by, for example Chong & Vathylakis [165]. As expected, all stresses in Fig. 6.9 drop down to zero for values of $y/\delta = 0$. The largest shear stresses are observed for upstream points, denoting a gradual decrease of shear over the edge of the serration. This is in agreement with previous experimental campaigns [155, 165]. The gradual decrease of shear over the edge of the serration may indicate that production of quadrupole noise sources is dominant at the root, as compared to the tip. The combed teeth trailing edge shear stress is slightly higher at the root. However, when going downstream, this difference changes in a slightly lower shear stress compared to the baseline teeth model. A maximum is observed at about $y/\delta = 0.3$ for all cases.

Reynolds normal stresses in wall-normal and spanwise direction, plotted in Fig. 6.10 at the edge location may also be relevant for the noise reduction mechanism from serrations. The general trend shows maximum amplitudes around $y/\delta = 0.3$ for both wall normal and spanwise stresses, with the largest amplitudes upstream along the edge. The upstream part of the serrated edges (i.e. the root) are therefore likely more effective in scattering acoustic waves, as more effective dipole sources are created in this region. Again, no significant variation in flow characteristics is observed when comparing the straight trailing edge with the serrated edges, indicating that the flow upstream remains unchanged. For both the wall-normal and spanwise normal stresses, the combed teeth configuration shows negligible higher fluctuations. Thus, the boundary layer characteristics do not seem to explain why the combed teeth are more quiet than the standard serrations. However, it is clear from this section, that the source of noise is mainly located around the root part of the teeth.

6.4.5. SURFACE PRESSURE FLUCTUATIONS

The far field noise is generated by the scattering of surface pressure fluctuations induced by the turbulent flow convecting over the edge of the serrations. To further understand the reasons behind the lower far field noise from the combed teeth configuration, the time-averaged surface pressure fluctuations ($\overline{p'p'}$) are depicted in Fig. 6.11. Both the spatial distribution as well as the intensity of the surface pressure fluctuations is similar for both cases. As can be seen, the intensity of the time-averaged surface pressure fluctuations is a function of the streamwise location, while it is only a weak function of the spanwise location. It decreases from the root to the tip, suggesting a variable intensity of the scattered pressure waves. In both cases, the intensity of $\overline{p'p'}$ is more than two times larger at the root than at the tip. This result reconfirms that, likely, most noise is produced at the root of the serration. This might be caused by the flow deviation imposed

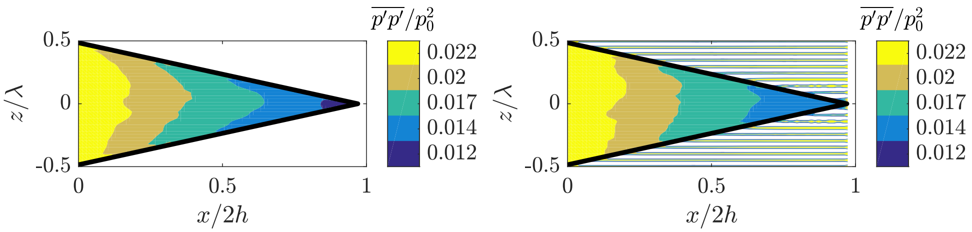

Figure 6.11: Intensity of the mean surface pressure fluctuation ($\overline{p\prime p\prime}/p_0^2$): (left) teeth and (right) combed teeth. The serration edge in the $x-z$ plane is indicated by means of continuous black lines.

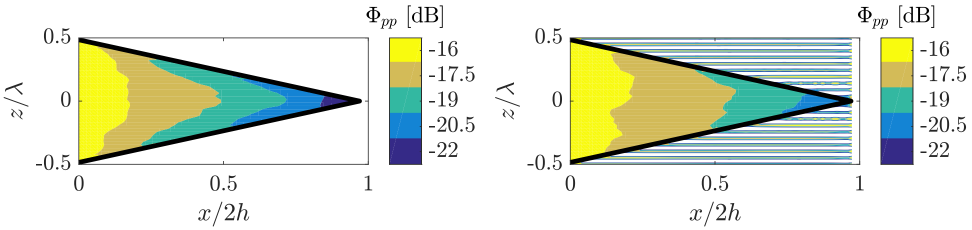

Figure 6.12: Intensity of the surface pressure fluctuation (Φ_{pp}) around $St_l = 4$: (left) teeth and (right) combed teeth. The serration edge in the $x-z$ plane is indicated by means of continuous black lines.

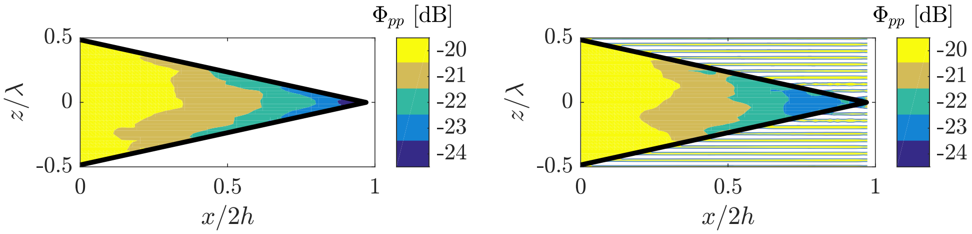

Figure 6.13: Intensity of the surface pressure fluctuation (Φ_{pp}) around $St_l = 10$: (left) teeth and (right) combed teeth. The serration edge in the $x-z$ plane is indicated by means of continuous black lines.

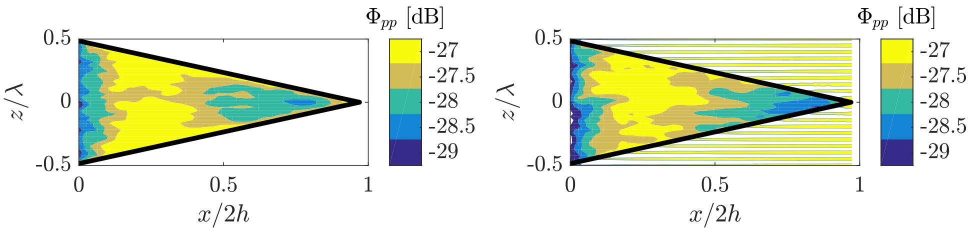

Figure 6.14: Intensity of the surface pressure fluctuation (Φ_{pp}) around $St_l = 20$: (left) teeth and (right) combed teeth. The serration edge in the $x-z$ plane is indicated by means of continuous black lines.

by the presence of the serration and the consequent variation of the pressure fluctuations. This assumption is supported by the mean wall-normal velocity components shown in Fig. 6.7 and Fig. 6.8, where $\overline{v}$ unequal to zero is measured for both configurations at $0 < x/2h < 0.1$. The pressure fluctuations on the combs do show slight spanwise variations: towards the tip, the combs show higher fluctuations for $-0.1 < z/\lambda < 0.1$.

All in all, the time averaged surface pressure fluctuations do not seem to explain the benefit of the combs. Therefore, it is interesting to observe trends at different frequencies, where we also observed the different noise reductions (Fig. 6.5). At Strouhal numbers of $St_l = 4$, $St_l = 10$ and $St_l = 20$, the intensity of surface pressure fluctuations (Φ_{pp}) are determined, and plotted in Fig. 6.12, Fig. 6.13 and Fig. 6.14 respectively. These results effectively display dipole sources on the surface [14]. Spectra were evaluated by using a periodogram method with Hamming windows of 128 elements with 50% of overlap. Fast Fourier Transform (FFT) was performed over 2048 elements thus resulting in a frequency resolution of approximately 15 Hz.

As expected, the time-averaged results presented in Fig. 6.11 before show close resemblance to the results at low Strouhal numbers (Fig. 6.12 and Fig. 6.13), which are dominant on the overall spectra in terms of amplitude (see Fig. 6.5). For both $St_l = 4$ and $St_l = 10$, the intensity of the surface pressure fluctuations is a function of the streamwise location, with a decreasing pattern from root to tip. This again suggests a variable intensity of the scattered pressure waves. At the tooth edges, the surface pressures decrease more gradually for the combed teeth than for the standard teeth, which might be related to the larger noise reduction at $St_l = 4$ and $St_l = 10$. A variation in this trend is observed when further increasing the frequency. At $St_l = 20$, a streamwise pattern is dominated by low levels at the root, high levels at mid and low levels around the tip of the teeth. This generally applies at the middle of the serration for both configurations. This suggests that the low-frequency noise is produced at the root of the serration, whereas the higher frequencies are generated further downstream on the tooth. A difference in both configuration is observed when looking at the surface pressure levels at the edges of the teeth. For the conventional teeth, the intensity stays high until the tip, whereas the combs seem to reduce the intensity again when going further downstream.

The fact that $\overline{p\prime p\prime}$ does not significantly depend on the serration geometry suggests that the lower far field noise generated in presence of the combed teeth geometry (Fig. 6.5) is mainly due to the effective angle seen by the turbulent flow approaching the edge of the serrations. To further confirm that the pressure fluctuations are only a function of the streamwise location and not of serration geometry, spectra of the wall-pressure fluctuations (Φ_{pp}), which were discussed previously, are now plotted in Fig. 6.15. Three reference points along the edge of the serrations are taken at $x/2h = 0$, 0.5 and 1. Spectra of the wall-pressure fluctuations show strong similarities between the two investigated configurations. The intensity of Φ_{pp} is slightly larger (approximately 2 dB) for the combed teeth geometry in the low frequency range ($5 < St_l < 10$), while the result from the straight trailing edge case is in line with the results from both roots.

With respect to the noise reduction mechanism of serrations in general, the results suggest that far field noise intensity benefits by both the reduced scattering efficiency due to the serration angle, and by streamwise variation of Φ_{pp} with respect to the root location ($\Delta\Phi_{pp} = \Phi_{pp}^{root} - \Phi_{pp}^{stream}$, where Φ_{pp}^{root} and Φ_{pp}^{stream} are the power spectra intensity at the root location and at the other streamwise points, respectively). As a matter of fact, in the frequency range where the $\Delta\Phi_{pp}$ is larger, the estimated far field noise reduction is higher. The cross-over frequency is observed at $St_l \approx 20$, which has been plotted before in Fig. 6.14. Interestingly, this corresponds to a $St_\delta \approx 1$ and matches earlier the cross-over frequency measured in the study of Gruber et al. [166]. The result in this section however, do not seem to explain the larger noise reduction of the combed teeth configuration.

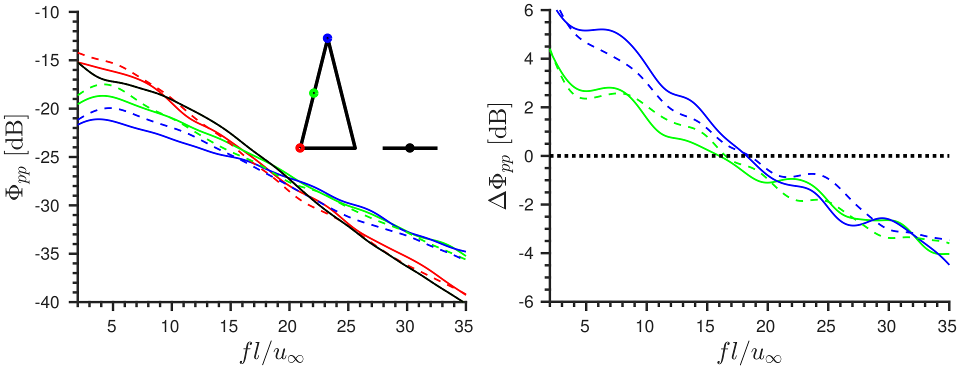

Figure 6.15: (left) Spectra of the surface pressure fluctuations (Φ_{pp}) at three streamwise locations corresponding to $x/2h = 0$ (red), 0.5 (green) and 1 (blue). The continuous and dashed lines represent the teeth and the combed teeth serrations respectively. (right) $\Delta\Phi_{pp} = \Phi_{pp}^{root} - \Phi_{pp}^{stream}$ with respect to the root location.

6.4.6. CONVECTION VELOCITY OVER EDGE

As trailing edge noise scales with velocity to the power five [11], it is important to analyze the convection velocity over the edge, to explore the phenomena of noise reduction from the (combed) teeth trailing edge. Convection velocity both influence the development of the turbulent fluctuations as well as the frequency at which the eddies are scattered. To determine the convection velocities near the edge, cross-spectral-densities are calculated using time series of surface pressure fluctuations. The surface pressure time series are compared for two points with a given $\Delta x = 1$ mm ($\Delta x = 0.005l$) spatial separation in streamwise direction. Here, the assumption is made of frozen turbulence right before the serrated edge. As the slope of the phase spectra, $\frac{\mathrm{d}\phi}{\mathrm{d}f}$, is relatively constant between frequencies of $St_l = 2-32$, the convection velocity can be determined as:

$$u_c = 2\pi\Delta x \frac{1}{\mathrm{d}\phi/\,\mathrm{d}f}, \tag{6.19}$$

with Δx being the streamwise distance between both measurement points. This procedure was used before by Chong & Vathylakis [165]. The results are depicted in Fig. 6.16.

Three observations can be made. Firstly, after the convection velocity slowly decreases, it increases from the root of the serration ($x/2h = 0$) towards the tip of the serration ($x/2h = 1.0$). This is in agreement with the mean velocity ($\overline{u}$) over the serrated edge, as seen in Fig. 6.7 and Fig. 6.8.

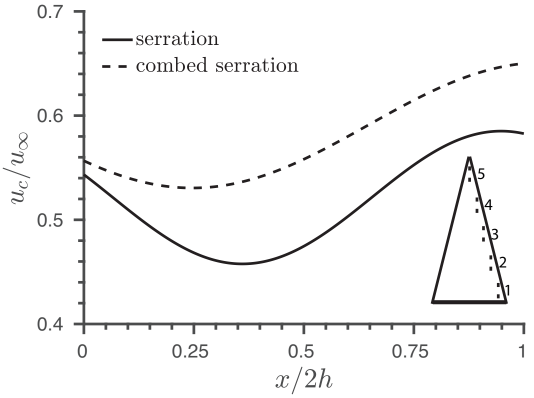

Figure 6.16: Streamwise convection velocity over tooth edge, extracted from surface pressure fluctuations. As an indication, a sketch is given of five measurement points.

Secondly, both models show a wavy pattern, where the convection velocity first reduces and then increases towards the tip. This pattern has been observed before in experimental studies [155, 165], with similar values for the absolute convection velocity. The waviness of the conventional teeth configuration may be related to the wall-normal ($\overline{v}$) and spanwise ($\overline{w}$) component of the mean velocity, which also vary slightly along the edge (Fig. 6.7 and Fig. 6.8). The waviness is reduced at the combed teeth model as the mean spanwise ($\overline{w}$) component is also reduced. This implies that on average, the acceleration of the flow has been reduced. A larger acceleration could be the reason of the higher noise levels for the baseline serrated case.

Lastly, the convection velocity of the combed teeth configuration is significantly larger than the teeth configuration. This would suggest that the combed teeth would scatter more effectively, when compared to the baseline teeth model. It should be noted though, that at the root of the tooth, where supposedly most noise is generated (see previous sections), the difference in convection velocity is only $2-3\%$, which would amount to a noise difference of only 0.5 dB. In any case, the edge convection velocity does not explain the larger noise reduction for the combed teeth.

6.4.7. SPANWISE COHERENCE

Another commonly discussed parameter in noise reduction, which might explain the superior acoustic performance of the combed teeth, is the decay of the spanwise coherence length [94, 95] (see Chap. 3 & App. C). The spanwise coherence length was determined using the coherence function γ^2 by means of auto-power and cross-power density of two surface pressure signals, separated by a given spanwise separation Δz. This representation is valid for the case that flow statistics are homogeneously distributed along the spatial dimension and stationary in time. Three different locations are analyzed; one just upstream of the straight trailing edge, one at the root of the serration and one at the tip of the serration. Results are displayed in Fig. 6.17. As can be seen, the characteristics just upstream the serration and straight edge are similar for all configurations, with

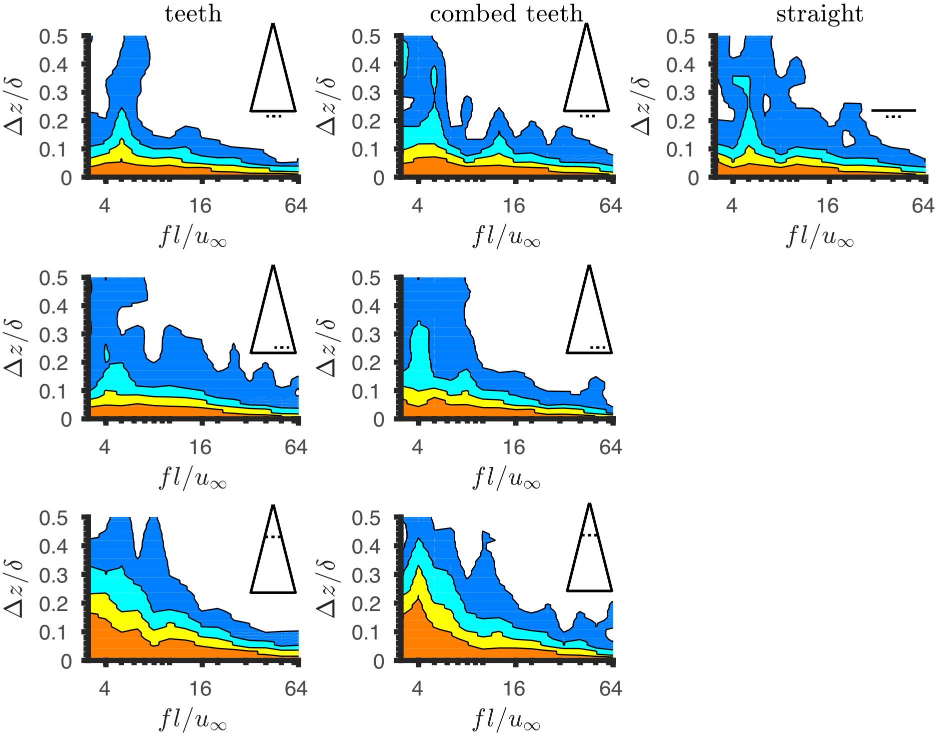

Figure 6.17: Contour plot of spanwise coherence function γ^2 for three geometries (left column teeth, central column combed teeth and right column straight trailing edge) for three different locations (top row trailing edge, central row root of serration and bottom row tip of serration). Colormap with steps of 0 : 0.2 : 1.0, the solid line the edge of the serration and the dotted line the spanwise, measurement location.

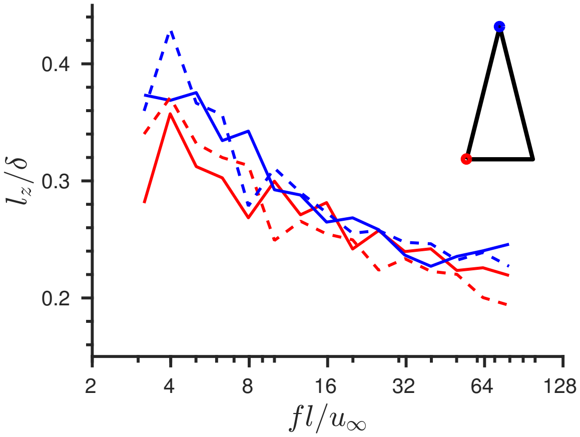

Figure 6.18: Spanwise coherence length l_z at two streamwise locations corresponding to $x/2h = 0$ (red) and $x/2h = 1$ (blue). The continuous and dashed lines represents the teeth and the combed teeth serrations respectively.

one large distinguished peak at $St_l \approx 4$. This is a common result and also found in, for example, the experiments of Pröbsting et al. [99]. The root and tip do show significant differences, and small variations between both serrated edges are observed. According to the spanwise coherence function results, the tip part is more coherent than the root and the combed teeth edge is more coherent than the teeth edge.

To confirm these observations, the coherence function is integrated along the spanwise separation distance for each single frequency band. This results in the estimation of the spanwise coherence length l_z, depicted in Fig. 6.18. The levels at the tip of the serration are consistently higher, as well as the decay towards a steady plateau around $St_l = 32$. Around $St_l = 8$, where the largest noise reductions were observed before (Fig. 6.5), the lines intersect and similar lengths for coherence length are found. This is in agreement with experimental results from Chong and Vathylakis [165]. When looking at the differences between both edges, the combed teeth model shows in general slightly higher levels at the low Strouhal numbers, but lower levels at the high Strouhal numbers. This could imply the presence of larger, spanwise, coherent structures near the tip of the combed teeth configuration, but does not explain the better noise performance.

6.4.8. SOURCE DETECTION AND LOCALIZATION

The previous sub-sections summarized the findings of the far-field acoustic spectra, where clearly both type of trailing edges were found to reduce the trailing edge noise from an airfoil, with various investigations of potential mechanisms explaining this large noise reduction of serrated edges. However, a clear localization of the noise sources is unfeasible with previous introduced methods, and hence, further investigations are required. One attempt, to localize the sources, is to split the airfoil and serration into different 'segments', as shown in Fig. 6.19. This technique is experimental and has only been validated for cases with airframe noise in the past [167]. The FW-H analogy is applied to all different segments, quantifying their separate contributions to the far field. In addition, the contribution of the entire region is calculated (part 0), as well as the energy sum of part 1 to part 9. This methodology may reveal which part of the airfoil and/or serration contributes the most to the far-field acoustic spectra. The method may also show the importance of constructive or destructive interference between the different segments, since acoustic interaction between the parts (such as reflection originating from the production of one segment to another) is not taken into account when analyzing them individually. Finally, it is important to mention that, by splitting the airfoil and serration in parts, artificial edges are likely created in the computational domain of the FW-H solver, thereby likely over-predicting the parts which not fully consisted of edges before.

The far-field spectra for the various segments of the standard tooth are displayed in Fig. 6.20 (left). One of the first observations tells us that the old location of the trailing edge still exhibits as main noise source, as part 3 is dominant for both configurations. However, not only the old trailing edge location, but also parts upstream of the edge (i.e. on the airfoil) have a significant contribution to the overall acoustic spectra. It is argued that this sudden increase of SPL is not physical and caused by the artificial edges created due to the splitting. The general trend is that, when going further downstream, the overall SPL levels gradually reduces. This trend is valid for $St_l < 16$, while at higher

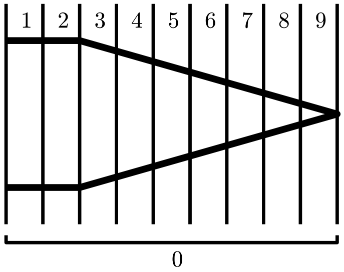

Figure 6.19: Splitting of a segment of the trailing edge as well as the entire serration

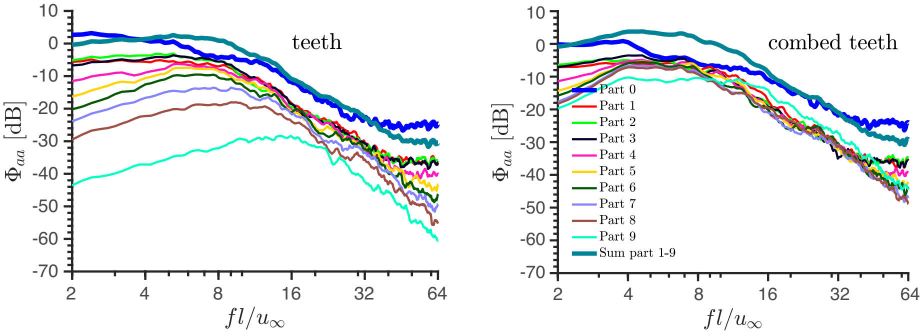

Figure 6.20: Contributions of different segments of the trailing edge and serration (see Fig. 6.19) to the far-field acoustic spectrum at an observer position above the trailing edge. Solutions obtained by applying FW-H analogy.

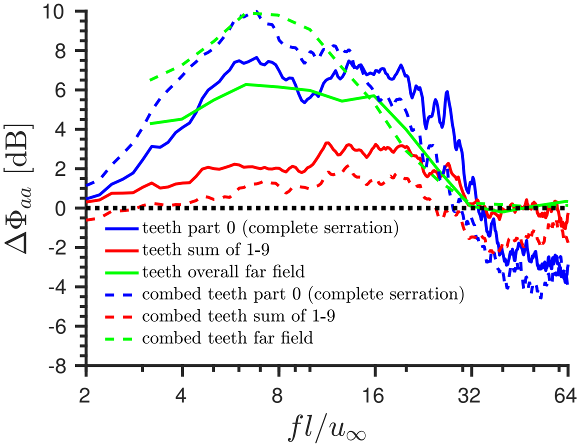

Figure 6.21: Comparison of sound pressure spectra reduction using part 0 (complete serration), a summation of segments 1 to 9 and the overall fari-field sound pressure spectra reduction from Fig. 6.5, all referenced to the straight trailing edge. Solutions obtained by applying FW-H analogy.

frequencies, the lines tend to fall on top of each other. This would imply that low frequency noise, which determined the overall sound level (Fig. 6.5), is generally generated at the root of the serration, while high frequency noise is found over the entire serrated edge. Similar trends were found before when analyzing the surface pressure fluctuations (Fig. 6.12, Fig. 6.12 & Fig. 6.14).

With respect to the combed teeth model (Fig. 6.20, right), it seems that the noise sources, predominately located at the root for the conventional teeth, are now distributed over the entire combed teeth. Most lines from downstream parts of the combed teeth serration (part 4 to 9) have increased amplitude compared to the conventional teeth, and are now within a 2 dB range of each other. Especially the trailing edge of the combs, part 9, has increased significantly, and is the dominant noise source for $St_l > 16$, as can be seen from Fig. 6.20. This reduced variation in SPL is contradictory to the surface pressure fluctuation results in Fig. 6.11, which suggested that the relative importance of the parts is the same for both the baseline teeth and combed teeth, but could be explained by looking at the results from Fig. 6.12. Here, along the edge (where noise is scattered), the variation of surface pressure fluctuations is larger for the standard teeth than the combed teeth model. Further research is needed to confirm this hypothesis.

Part 0 is further compared to the energy summation of segment 1 to 9 (thick lines). If no positive or negative interference between all segments appears, both lines should match. Clearly, from Fig. 6.20, it can be concluded that both methods show agreement in trend but are off in the range of $4 < St_l < 16$. In this range, the overall part for the combed teeth configuration shows 10 dB lower SPL than the summed part. The results suggest that destructive interference between the streamwise parts of similar SPL levels causes this noise reduction. Moreover, the overall part as well as the summation of all segments can be compared against the straight trailing edge case, see Fig. 6.21. In addition, the calculated far field noise reduction from Fig. 6.5 is also plotted for convenience. While the overall part 0 shows similar noise reduction trends as the overall far-field analysis performed before, the summation of segments fails in predicting correct noise reduction levels. This suggests that the individual segment approach does not capture the overall acoustic effect properly, but only locally. Possibly the calculated noise reduction for the sum of 1-9 is suppressed by the artificial edges.

To complement the results from the segment study, the FIND tool (see Sec. 6.2.3) is applied at $St_l = 4$ (Fig. 6.22), $St_l = 10$ (Fig. 6.23) and $St_l = 20$ (Fig. 6.24) to detect noise from co-rotating vortex pairs. These figures show iso-surfaces of P_{tot} (Eq. 6.17) at a value of −60, −50 and −45 dB and above, for $St_l = 4$, $St_l = 10$ and $St_l = 20$ respectively. At both $St_l = 4$ and $St_l = 10$, the combed teeth were found to be more quiet than the baseline teeth (Fig. 6.5). At $St = 4$, noise sources are mainly present at the root of the teeth design, while the combed teeth model hardly produce noisy co-rotating vortex pairs. Increasing the frequency to $St = 10$ (Fig. 6.23), the sources become more equally distributed over the entire teeth edge. The combed teethed edge shows high density sources at the trailing edge of the combs, which is in correspondence with the results from Fig. 6.20 (right, segment 9). Only when further increasing the Strouhal number (Fig. 6.24), the combed teeth is starting to produce noise sources in between the combs. These results suggest that, especially at $St_l = 4$ and $St_l = 10$, the combed teeth drastically improve the noise emission with respect to the conventional teeth configuration by reducing part of the

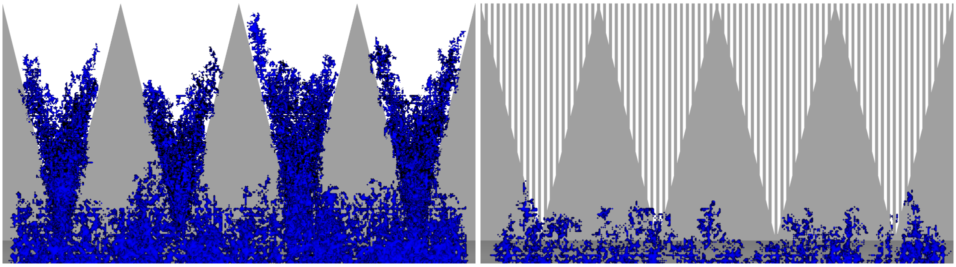

Figure 6.22: Iso-surfaces of flow induced noise detection at $St_l = 4$ (left) displaying acoustic sources for the teeth (left) and combed teeth (right) edge

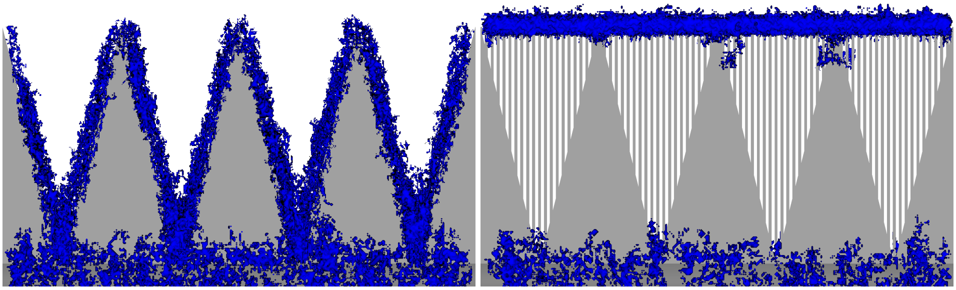

Figure 6.23: Iso-surfaces of flow induced noise detection at $St_l = 10$ (left) displaying acoustic sources for the teeth (left) and combed teeth (right) edge

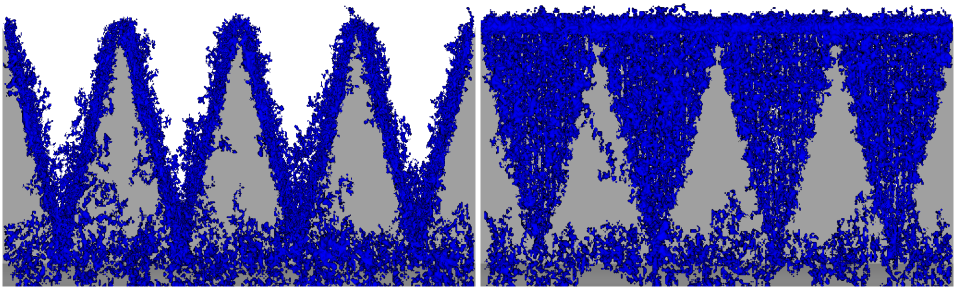

Figure 6.24: Iso-surfaces of flow induced noise detection at $St_l = 20$ (left) displaying acoustic sources for the teeth (left) and combed teeth (right) edge

co-rotating vortex pairs, which are scattering noise near the serrated edge.

6.5. CONCLUSION

The trailing-edge noise of a wind turbine blade is currently the most dominant noise source on a wind turbine and, therefore, understanding and modeling the physics associated with the generation and propagation of this noise is of paramount importance for the design of silent wind turbines. In the past, using both experiments and simulations, a serrated trailing edge has been shown to be efficient in reducing trailing edge noise. This study focused on the flow topology and noise emission around a toothed, combed toothed and straight edge configuration retrofitted on a NACA 0018 airfoil at zero angle of attack. The flow and pressure fields were analyzed by evaluating the fully explicit, transient, compressible Lattice Boltzmann equation. The far-field acoustic spectra were obtained using Ffowcs-Williams and Hawkings integral solution. The numerical results confirm that the combed teeth give a larger noise reduction than the standard teeth. Furthermore, the acoustic far-field results and boundary layer characteristics obtained from the simulation of the teeth configuration match earlier experiments.

It is hypothesized that the main noise-suppression mechanism, due to the application of the combs, is the change of the angle of the streamlines. In general, the flow tends to be less three-dimensional and more aligned with the serrated edge, as the mean spanwise velocity component is significantly lower for the combed teeth configuration, resulting in lower vorticity at the tooth edges. Other, more experimental numerical methods, such as the analysis of boundary layer characteristics, surface pressure fluctuations, the individual segment analysis and the flow induced noise detection, revealed that most noise is generated at the root of the teeth rather than the tip. It was also observed that surface pressure fluctuations at low frequencies are dependent of the streamwise location, suggesting a variable intensity of the scattered pressure waves along the streamwise serrated edge. Analysis of convection velocity and spanwise coherence did not explain the noise-reduction mechanism of the combs.

7

SHAPE OPTIMIZATION OF SERRATED TRAILING EDGES

The secret to creativity
is knowing how to hide your sources.

Albert Einstein

Previous chapter showed options of reducing trailing edge noise by the application of noise suppression add-ons, with a deeper understanding in the actual mechanism behind the reduction. To further improve the sawtooth geometry, far-field noise and hydrodynamic flow field over a novel trailing edge serration shape made as a concave triangle (named "iron-like" shape) are investigated. Numerical computations are performed using a compressible Lattice-Boltzmann solver. The iron-shaped serrations are compared to more conventional trailing edge serrations with a sawtooth geometry. Both serration geometries were retrofitted to a NACA 0018 airfoil at zero-degree angle of attack. The iron-shaped geometry is found to reduce far-field broadband noise of approximately 2 *dB more than the conventional sawtooth serrations for chord-based Strouhal numbers* $St_l < 15$*. At higher frequencies, the far-field broadband noise for the two serration geometries has comparable intensity. Near-wall velocity distribution and surface pressure fluctuations show that their intensity and spectra are independent on the serration geometry, but more a function of the downstream, streamwise location. It is found that the larger noise reduction achieved by the iron-shaped trailing edge serration is due to the mitigation of the scattered noise at the root. It is obtained by mitigating the interaction between the two sides of the serrations by delaying toward the tip both the outward, and the downward flow motions present at the root of the sawtooth.*

Parts of this chapter have been published in the Journal of Sound and Vibration (2017) [168].

7.1. INTRODUCTION

BROADBAND trailing edge noise generated by the scattering of the turbulent flow convecting over the trailing edge of an airfoil [7, 15] is one of the most relevant sources of nuisance in wind-turbine applications [147].

Many passive mitigation strategies have been proposed to reduce this source of noise. Amongst the most important serrations, acoustic measurements carried out both in wind tunnels and in-field, reported that sawtooth trailing edge serrations offer the most effective noise reduction, also taking into account the simplicity of the design [149, 151, 156, 164, 169–172]. Far-field noise reductions with respect to the straight trailing edge configuration, expressed as difference in Sound Pressure Level (SPL), of approximately 7 dB and 3 dB, were measured in both wind tunnels and in-field applications.

Many analytical approaches have been proposed [59, 148, 157, 159, 160] to predict trailing edge noise in presence of sawtooth trailing edge serrations. Howe [59, 148] formulated the first analytical model to predict broadband noise generated by a low Mach number turbulent flow over a flat plate at zero angle of attack with sawtooth trailing edge serrations. The model predicts an asymptotic noise-reduction value at relatively high frequencies of $10\log_{10}\left[1+(4h/\lambda)^2\right]$ dB where λ and $2h$ are the serration width and length, respectively. When compared to experimental results [151, 156, 164, 172, 173], the current triangular designs are not able to match the predicted noise reduction values. Moreover, the model cannot physically explain the characteristic “cross-over” frequency f_c corresponding to a Strouhal number $St_\delta = f_c\delta/U_\infty \approx 1$ (based on the free-stream velocity U_∞ and boundary layer thickness δ estimated with XFOIL [174] in the study of Gruber et al. [166]) after which noise increases again. Recently, Lyu et al. [159, 160] developed a new semi-analytical model applying Amiet’s trailing edge noise theory [95] to sawtooth trailing edges. Results showed that the predicted noise reduction are closer to the one experimentally measured. Lyu et al. [159, 160] detected two non-dimensional parameters that substantially affect the noise reduction: $k_1 \times 2h$ and $l_{zp}(f)/\lambda$, where k_1 is the wavenumber in the chordwise direction of the convective velocity, and $l_{zp}(f)$ is the spanwise correlation length of the pressure fluctuations on the surface of the airfoil. The studies of Lyu et al. [159, 160] concluded that far-field noise can be reduced when both $k_1 \times 2h$ and $l_{zp}(f)/\lambda$ are much larger than unity. This implies that the serration should be long enough to ensure a considerable phase difference of the scattered pressure waves at the edge of the serration. In addition, if the spatial range of these phase differences, i.e. λ, is sufficiently small compared to the correlation length in the spanwise direction, radiated sound waves may destructively interfere with each other.

More recent investigations of the actual flow fields [156, 161, 164, 165] have shown that the flow past serrated airfoils is strongly three dimensional, with vortical structures developing along the edges of the serrations. Because of the complex flow field and of the streamwise varying pressure gradient, both aerodynamic effects and acoustic scattering are mutually dependent [147, 175]. Flow measurements [156, 164] and computations [153, 161] showed that, even at small angles of attack, the turbulent flow tends to seep into the empty space in between serrations. More in details, both an outward (i.e., from the centerline toward the edge) and an inward (i.e., from the edge toward the centerline of the serrations) flow motions characterize the flow field at the root and the tip of the sawtooth trailing edge serrations, respectively [173]. This flow distortion is found to reduce the effective angle seen by the turbulent flow convecting over the edge of the serrations thus reducing the effectiveness of the serrations in reducing far-field noise [165].

Aiming at reducing the broadband far-field noise even further, several variations of the serration geometry were proposed and tested, e.g. brushed [176], sinusoidal [157], slitted [150, 153–155] and even randomly-shaped trailing edges [177]. More recently, it was proved that broadband far-field noise reduces, with respect to conventional serrations, by filling the empty space in between serrations with combs or slits [147]. However, a physical explanation behind the achieved noise intensity was not reported in this paper, but later by van der Velden & Oerlemans [146] (Ch. 6 of this thesis).

Based on previous experimental observations [156, 164] and previous chapter [146], curved solid trailing edge serrations may reduce the far field noise by mitigating the negative effect due to the outward and downward flow motions at the root of the serration. To overcome this, in this chapter, curved serrated trailing edge serrations, named as iron-like trailing edge serrations, are investigated with the commercial Lattice-Boltzmann Method (LBM) solver Exa PowerFLOW in terms of their far-field noise emission and hydrodynamic flow field. The iron-shaped serrations are compared to more conventional sawtooth trailing edge serration with same length ($2h$) and wavelength (λ). A similar concept was patented by Vijgen et al [178] with the purpose of improving lift and drag of lifting surfaces and by Oerlemans [179] for noise reduction. In the following study, the serrations are retrofitted to a NACA 0018 airfoil placed at zero angle of attack.

7.2. METHODOLOGY AND SOLVER

The commercial software package Exa PowerFLOW 5.3b was used to solve the discrete Lattice-Boltzmann equations for a finite number of directions. For a detailed description of the equations used for the flow field computations the reader can refer to Ch. 5 & Ch. 6, or studies of Succi [27] and van der Velden et al. [81].

The discretization used for this particular application consisted of 19 discrete velocities in three dimensions (D3Q19) involving a third-order truncation of the Chapman-Enskog expansion. The distribution of particles was solved using the kinetic equations on a Cartesian mesh, with the Bhatnagar-Gross-Krook (BGK) collision term operator [83]. A Very Large Eddy Simulation (VLES) was implemented as viscosity model to locally adjust the numerical viscosity of the scheme in regions that are under resolved [137]. The model consists of a two-equation $\kappa-\epsilon$ Renormalization Group (RNG) modified to incorporate a swirl based correction that reduces the modeled turbulence in presence of large vortical structures. A turbulent wall-model was used to resolve the near-wall region [84]. The particular choice of the wall model in combination with the subgrid scale model allows to obtain a reliable estimate of the boundary layer till the viscous sub-layer, with feasible turn-around times.

Due to the fact that the LBM is inherently compressible and it provides a time dependent solution, the acoustic pressure field was extracted directly from the computation domain. Sufficient accuracy is obtained when considering at least 16 lattices per wavelength for the LBM methodology [79].The obtained far field noise was further compared with noise estimated by using an acoustic analogy. For this purpose, the Ffowcs-Williams and Hawkings (FWH) [47] equation was employed. The time-domain FWH formulation developed by Farassat [48] was used to predict the far field sound radiation of the serrated trailing edge in a uniformly moving medium [49]. The input to the FWH solver is the time-dependent pressure field of a surface mesh provided by the transient LBM simulations.

Finally, to further detect the location of the noise sources in the near field, the dynamics of co-rotating flow structures was investigated [163]. The Flow-Induced Noise Detection (FIND) tool implemented in the LBM solver was used to detect and track the co-rotating flow structures in the flow field. Therefrom, the intensity of these noise sources was estimated based on the theory of vortex sound from Powell [53]. Details are found back in Ch. 6.

7.3. COMPUTATIONAL TEST-CASE

The studied test-case replicated the experimental conditions reported by Arce-León et al. [155, 164]. Computations were performed on a NACA 0018 airfoil with chord length l = 200 mm and 80 mm span (Fig. 7.1). The simulation domain size was $12l$ in both streamwise and wall-normal directions. The outer $2l$ were modeled as an anechoic outer-layer to damp acoustic reflections down. In spanwise direction, cyclic boundary-conditions were used. A variable mesh resolution in the computational field was employed. The grid size was changed by a factor two between adjacent resolution regions. The boundary layer was represented by two refinement regions, while the other refinement regions were placed outside, in uniform flow conditions, in the far field. Ten refinement regions allowed the first cell to be placed in the viscous sub-layer at $3.9 \cdot 10^{-4} l$ above the trailing edge location, corresponding to $y^+ \approx 3$. In total, around 150 million voxels were used for the discretization of the domain. Data sampling started after reaching a steady standard deviation of the lift and drag coefficient in the solution (approximately after 10 full flow-passes over the airfoil chord). The Courant–Friedrichs–Lewy (CFL) number is dependent on the wave propagation velocity and on the smallest voxel size in compressible simulations. With the current cell size and a unit CFL number, the resulting time-step equals $1.3 \cdot 10^{-7}$ s. The wall-pressure probes had the same size of the local voxel (i.e. $3.9 \cdot 10{-}4l$ at the trailing edge location and $7.8 \cdot 10^{-4} l$ along the rest of the airfoil). Flow data were sampled with frequency $f = 30$ kHz for 20 flow passes (App. B). The prescribed methodology was validated in a previous study by van der Velden et al. [81], see Ch. 5 of this thesis.

The trailing edge thickness of the airfoil was kept sharp with $t = 1$ mm ($t/l = 5 \cdot 10^{-3}$) in order to minimize any tonal noise component due to vortex shedding ($t/\delta \approx 0.1$ where δ is the boundary layer thickness discussed below) [120]. The free-stream velocity was $U_\infty = 20$ m/s, and the angle of attack was $\alpha = 0°$. Boundary-layer transition to turbulence was forced at $x/c = 0.2$ by means of serrated strip of height $3 \cdot 10^{-3} l$ and length $1.5 \cdot 10^{-3} l$ on both side of the airfoil [81].

The airfoil trailing edge was retrofitted with two serrated trailing edges: a conventional sawtooth and the iron-like geometry (Fig. 7.2). The latter was designed with a spline curve. At the root, it is perpendicular to the baseline trailing edge while, at the tip, it is tangent to the line obtained as intersection of the tip point with the point at $3/4 \times 2h$h (see dashed line in Fig. 7.2 right). Both serrations had length $2h/l = 0.2$ ($2h = 40$ mm) and wavelength $\lambda/l = 0.1$ ($\lambda = 20$ mm). The serration length was approximately four times the boundary layer thickness δ as in the reference experiment [155, 164].

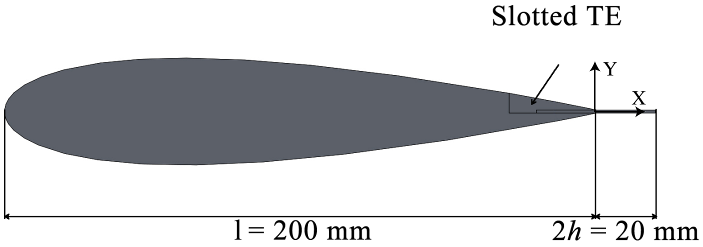
Slotted TE
Y
X
l = 200 mm
2h = 20 mm

Figure 7.1: Sketch of the airfoil (side view)

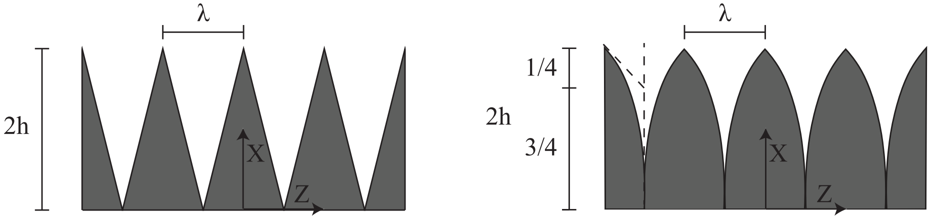
λ
2h
X
Z
λ
1/4
2h
3/4
X
Z

Figure 7.2: Sketch of the conventional (left) and iron-like (right) trailing edge serrations

The adopted Cartesian coordinate system (Fig. 7.1) for each configuration is defined as follows: the origin is chosen at the location of the baseline airfoil trailing edge; the z-axis coincides with the airfoil trailing edge; the x-axis is aligned with the chord of the airfoil (i.e., aligned with the serration surface); and the y-coordinate is perpendicular to the surface of the serrations. In presence of serrations, the origin coincides with the projection along the chord direction of a serration tip on the trailing edge of the baseline model.

Boundary-layer profiles of the mean streamwise velocity component and time averaged turbulent statistics [13] were inferred from the computed velocities at $x/l = 0$ for the straight trailing edge model. They are reported in Fig. 7.3 and summarized in Tab. 7.1. More in detail, $\delta_{95} = 7.9$ mm and $\delta = 9.5$ mm are the boundary-layer thickness parameters defined by the y-location corresponding to 95% and 99% of the local edge velocity (U_e), respectively $\delta^\star = 3.3$ mm and $\theta = 1.5$ mm are the displacement and momentum thickness, respectively. This results in a shape factor $H = \delta^\star/\theta$ of approximately 2.2. Results agree with the boundary layer integral parameters reported by Arce-León et al. [164], as mentioned before in Ch. 6. Tab. 7.1 also list the corresponding Reynolds numbers for the length scales addressed above.

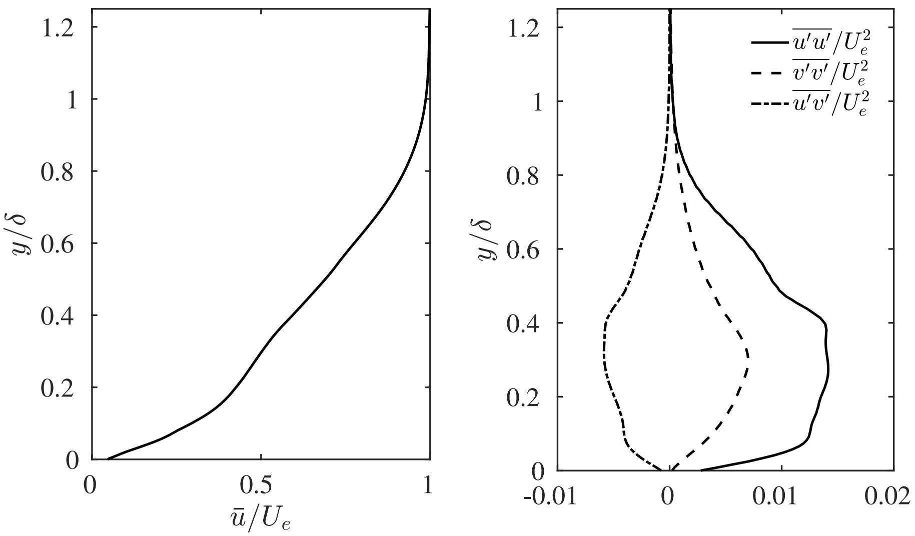

Figure 7.3: (left) Mean streamwise velocity component and (right) time-averaged turbulent statistics at $x/l = 0$ for the straight trailing edge model. U_e is the local edge velocity.

Given the flow similarities over the different serrations present in the computational domain and in order to further reduce the uncertainty of the mean and rms velocity fields, the computed fields were spatially averaged along the spanwise direction at points with the same relative spanwise location with respect to the chosen axis system (App. B). This procedure reduces the uncertainty by increasing the number of samples available for averaging by a factor of 8 (four serrations and symmetric flow conditions on top and bottom) [161].

Table 7.1: Boundary layer characteristics at $x/l = 0$

Parameter	Symbol	Quantity
Free stream velocity	U_∞	20 m/s
Edge velocity	U_e	18.75 m/s
Displacement thickness	$\delta^\star$	3.3 mm
Momentum thickness	θ	1.5 mm
Boundary layer thickness	δ	9.5 mm
	δ_{95}	7.9 mm
Reynolds number	Re_l	280,000
	$Re_{\delta^\star}$	4,600
	Re_θ	2,100
	Re_δ	13,300
Shape factor	H	2.2

7.4. RESULTS

The following sections contain results regarding the far field noise, mean and turbulent flow features, wall-pressure fluctuations and detection of noise sources.

7.4.1. FAR FIELD NOISE

Spectra of the scaled acoustic power spectrum (Φ_{meas}) are obtained from the time series of the pressure fluctuations sampled by a microphone located above the trailing edge of the baseline airfoil ($x/l = 0$, $z/l = 0$ and $y/l = 10$) using the FWH analogy [47], according to the setup prescribed in Sec. 7.2. Results presented in Fig. 7.4 are scaled to unity conditions as reported below:

$$\Phi_{aa} = \Phi_{meas} + 10\log_{10}\left(\frac{R^2}{bM^5}\right). \tag{7.1}$$

The adopted scaling is conventionally used in literature for trailing edge noise studies, where non-compact noise sources are the most relevant contributions [11, 140].

The scaled acoustic power spectrum (Φ_{aa}) for the baseline airfoil and the ones with the sawtooth and iron-like trailing edge serrations are plotted in Fig. 7.4 (left). Spectra were evaluated by using Hamming windows of 500 elements and 50% of overlap, thus resulting in a frequency resolution of approximately 20 Hz (App. C). Results in Fig. 7.4 were further integrated over 1/10 decade bandwidths. Spectra show broadband noise without any additional tonal component induced by vortex shedding at the trailing edge, as expected (cfr. Sec 7.3). Fig. 7.4 (right) quantifies the noise reduction with respect to the baseline airfoil without any add-on ($\Delta\Phi_{aa}$). In the same figure, the far field noise reduction measured by Arce-León et al. [155] at $U_\infty = 30$ m/s using the same sawtooth geometry is added as comparison. The measured noise reduction is comparable with the computed one, as both amplitude and frequency are scaled by the characteristic velocity of the specific test-case. Focusing on the computation results, the iron-shaped geometry reduces the far field broadband noise more than the conventional sawtooth geometry in the range of Strouhal number based on the chord $5 < St_l = fl/U_\infty < 15$. Both geometries

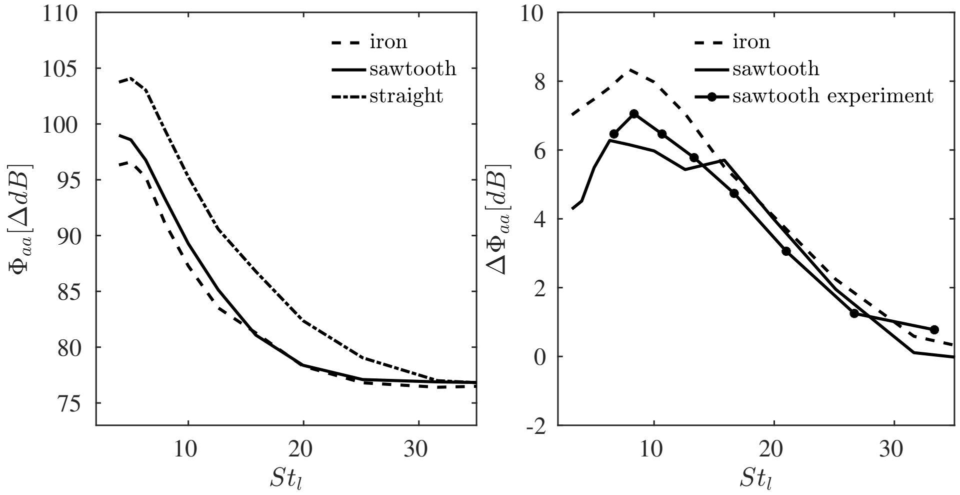

Figure 7.4: (left) Power spectra of the far field pressure fluctuations (Φ_{aa}) for the straight, sawtooth and iron-shaped trailing edge serrations. (right) noise reduction ($\Delta\Phi_{aa}$) with respect to the straight trailing edge noise. Experimental data are taken from Arce-León et al. [155] at U_∞ = 30 m/s with the same sawtooth geometry. Computational data are obtained by a microphone located above the trailing edge of the baseline airfoil (x/l = 0, $z/l = 0$ and $y/l = 10$).

show maximum noise reduction at approximately $St_l \approx 8$. The maximum noise reduction is equal 8 dB for the iron geometry while it is equal to 6 dB for the sawtooth one. The comparison between the two serrated trailing edges shows that the iron-shaped trailing edge serration has a positive effect on the far field noise, especially in the low frequency range.

To further compare the two serrated trailing edges, directivity plots are shown in Fig. 7.5. Data was obtained by sampling from an array of microphones positioned in a circle of radius $10l$ at the mid-span plane around the baseline trailing edge. Results were further averaged over the frequency band reported in each plot. As expected, at low frequencies (Fig. 7.5 top left), a compact dipole source is seen developing at the trailing edge. Increasing the frequency (Fig. 7.5 top right), the dipole is tilted toward the leading edge of the airfoil. Further increasing the frequency (Fig. 7.5 bottom left), a non-compact behavior appears only for the straight trailing edge with different upstream oriented lobes. In this frequency range, less pronounced lobes are visible for the serrated cases. It is argued that this change is generated by the addition of the serrated geometry, thereby locally transferring non-compact sources back to compact regime as the length scale to wavelength ratio changes. Noise reductions with respect to the baseline airfoil are observed at all angles with maximum for angles between 105 and 135 degrees. When comparing the two investigated serration geometries, it is evident that, at the highest simulated frequency, the two geometries generates the same noise intensity. It is clear that the modification of the serration geometry does not alter the directivity pattern in the simulated frequency range.

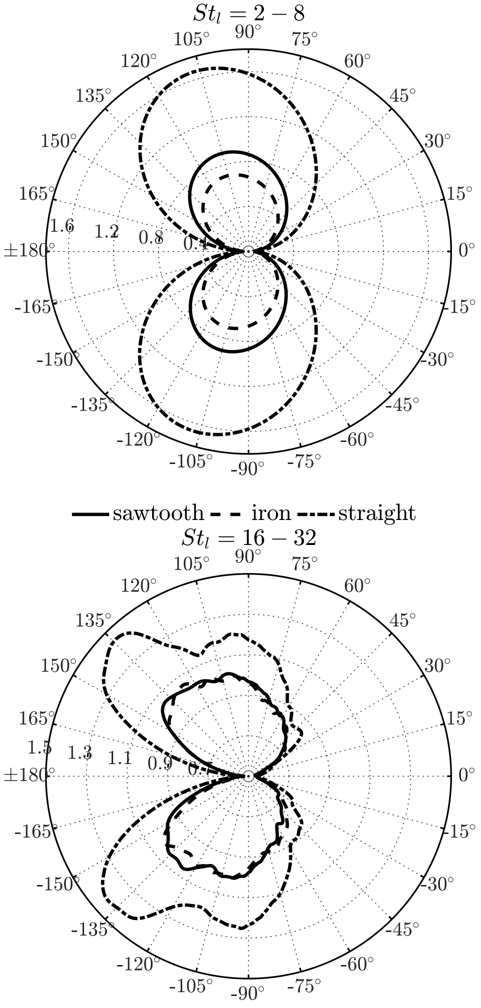

Figure 7.5: Directivity plot for the straight, sawtooth and iron-like trailing edge serrations. Data is obtained from an array of microphones positioned in a circle of radius $10l$ at the mid-span plane round the baseline trailing edge. Results are further averaged over the frequency band reported in each plot: (top left): $2 < St_l < 8$, (top right) $8 < St_l < 16$ and (bottom left) $16 < St_l < 32$.

7.4.2. MEAN AND TURBULENT FLOW FEATURES

In order to identify the physical mechanisms responsible for the larger noise reduction in presence of the iron-shaped serration, the mean and statistical flow fields are investigated.

Profiles of the time-averaged mean streamwise velocity component and of the time-averaged turbulent fluctuations are plotted in Fig. 7.6. Wall-normal profiles at two points located at the root ($x/2h = 0$) and at the tip ($x/2h = 1$) of the investigated serrations are shown. Results obtained from the baseline configuration are reported for the sake of completeness.

Data shows that the serrations mildly affect the boundary layer time-averaged mean and turbulent statistics at $x/2h = 0$ with respect to the baseline airfoil. Similar results were reported in the experiments carried out by Chong & Vathylakis [165] and Gruber et al. [166]. Strong similarities are present also at the tip ($x/2h = 1$). These results suggest that the turbulent flow convecting over the serration centerline is weakly sensitive to the serration geometry but it depends mainly on the streamwise location along the serration [156].

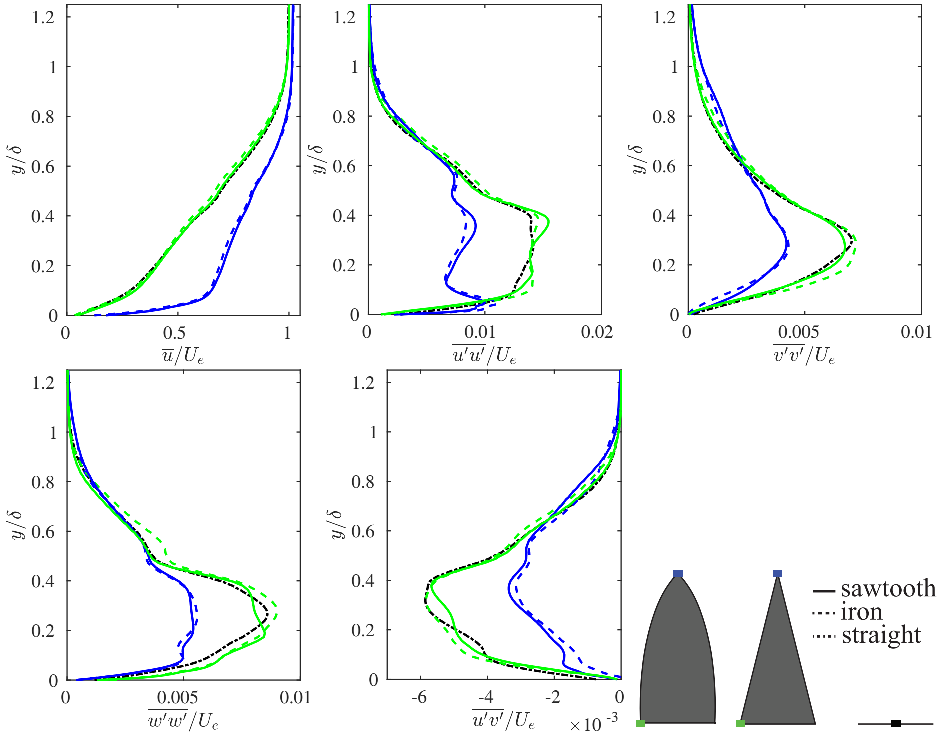

Figure 7.6: Comparison of the time-averaged mean streamwise-velocity component and of the time-averaged mean turbulent fluctuations at $x/2h = 0$ (green line) and $x/2h = 1$ (blue line). Profiles of the baseline configuration are extracted at $z/l = 0$ (black line). U_e is the local edge velocity.

In presence of spanwise variable geometries, such as the conventional sawtooth geometry, the spanwise flow variation, together with the wall-normal flow variation introduced because of the gap, may form a three-dimensional mixing layer consequently responsible for the streamwise oriented structures [180, 181]. Previous studies [153, 156] showed that the sawtooth trailing edge serrations induce distortion of the near-wall streamlines. Following Chong & Vathylakis [165], the distortion of the streamlines may reduce the effective flow edge angle seen by the turbulent flow convecting over the serrations and thus may locally increase the scattered noise with respect to an ideal flow over a sawtooth geometry, according to the theory presented by Howe [59, 148].

In order to compare the two investigated serrations and inspect the physical reasons behind the computed far field noise intensity, the near-wall spatial distributions of the time-averaged mean velocity components are discussed. They are reported in Fig. 7.7 and Fig. 7.8 for the conventional sawtooth and the iron-like geometry, respectively. Data are extracted at $y/\delta = 0.05$ ($y = 1.5$ mm). Results from the conventional sawtooth geometry agree with previous studies [153, 156, 161, 164, 173]. The mean streamwise velocity component increases from the root to the tip, corresponding to an acceleration of the flow with a thinning effect of the boundary layer. Most notably, the flow tends to seep into the empty space in between serration (downward motion) as evidenced by the negative mean wall-normal velocity component ($\overline{v}$). As a direct consequence, the flow over the serration exhibits an outward motion with respect to the edge, as visible from the contour of the spanwise velocity component ($\overline{w}$).

Similar flow features, but at a more downstream location ($x/2h > 0.5$), are present when retrofitting the airfoil with the iron-like serration. At the root, the reduced free space due to the tangent constraint delays both the downward and the outward motions discussed above. More in detail, up to $x/2h = 0.25$ the flow is characterized by $\overline{w} \approx 0$. At $x/2h \approx 0.75$, both the upward and downward motions are enhanced and larger values of both $\overline{v}$ and $\overline{w}$ are measured. A second major difference between the two serrations is present at the tip. While the sawtooth serration is characterized by $\overline{v}$ approximately equal to zero (i.e., flow approximately parallel to the serration surface), the iron-like geometry is characterized by a strong upwash. It is likely caused by the interaction between the vortical structures generated at the edge of the serration.

7.4.3. WALL-PRESSURE FLUCTUATIONS

The far field noise is generated by the scattering of turbulent flow convecting over the edge of the serrations. To further understand the reasons behind the lower far field noise generated by the iron-like geometry, the time-averaged wall-pressure fluctuations ($\overline{p\prime p\prime}$) are discussed (Fig. 7.9). Both the spatial distribution and the intensity of the wall-pressure fluctuations do not depend on the serration geometry. The intensity of the time-averaged wall-pressure fluctuations is a function of the streamwise location while it is a weak function of the spanwise location. It decreases from the root to the tip suggesting variable intensity of the scattered pressure waves. In both cases, the intensity of $\overline{p\prime p\prime}$ is more than two times larger at the root than at the tip. It might be caused by the flow deviation imposed by the presence of the serration and the consequent variation of the pressure fluctuations. This assumption is supported by the mean wall-normal velocity component shown in Fig. 7.7 and Fig. 7.8, where $\overline{v}$ unequal to zero is measured for both configurations at $0 < x/2h < 0.1$.

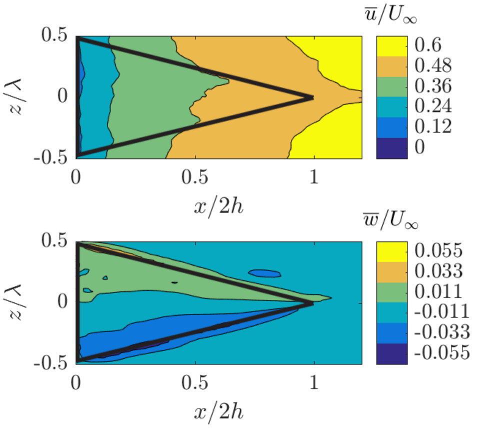

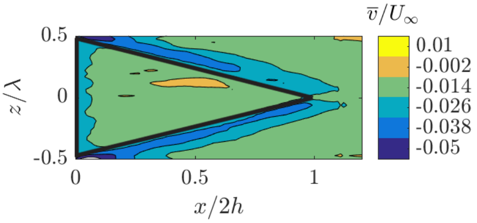

Figure 7.7: Contour of the mean velocity component over the sawtooth serration at $y/\delta = 0.05$: (top left) $\overline{u}$, (top right) $\overline{v}$ and (bottom left) $\overline{w}$ velocity components. Projections of the serration on the $x-z$ plane are indicated by means of continuous black lines.

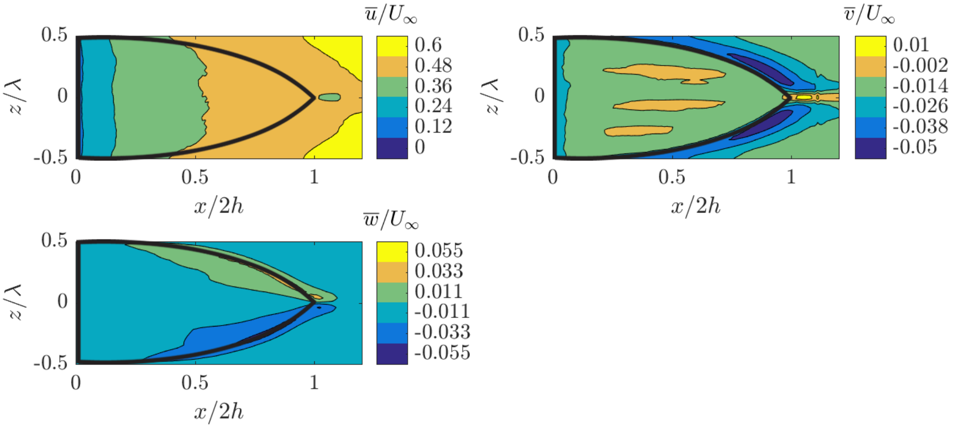

Figure 7.8: Contour of the mean velocity component over the iron-like serration at $y/\delta = 0.05$: (top left) $\overline{u}$, (top right) $\overline{v}$ and (bottom left) $\overline{w}$ velocity components. Projections of the serration on the $x-z$ plane are indicated by means of continuous black lines.

The fact that $\overline{p'p'}$ does not depend on the serration geometry suggests that the lower far field noise generated in presence of the iron-like geometry (Fig. 7.4) is mainly due to the effective angle seen by the turbulent flow approaching the edge of the serrations. To further confirm that the pressure fluctuations are only a function of the streamwise location, spectra of the wall-pressure fluctuations (Φ_{pp}) are plotted in Fig. 7.10. Spectra were evaluated by using a periodogram method with Hamming windows of 128 elements with 50% of overlap. Fast Fourier Transform was performed over 2048 elements thus resulting in a frequency resolution of approximately 15 Hz. Three reference points along the edge of the serrations are taken at $x/2h = 0$, 0.5 and 1.

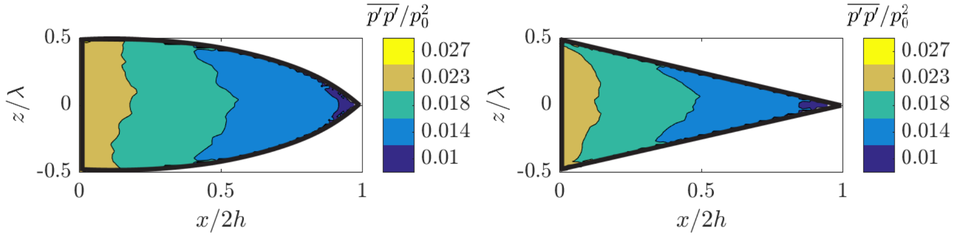

Figure 7.9: Intensity of the mean wall pressure fluctuation ($\overline{p'p'}/p_0^2$): (left) iron-like serration, (right) sawtooth serration. The serration on the $x-z$ plane are indicated by means of continuous black lines.

Spectra of the wall-pressure fluctuations show strong similarities between the two investigated geometries. In particular, no difference is measured at $x/2h = 0.5$ and 1, while minor differences are visible at $x/2h = 0$. At this location, the intensity of Φ_{pp} is slightly larger (approximately 2 dB) for the iron-like geometry in the low frequency range ($5 < St_l < 7$). Differently, at relatively higher frequencies ($St_l > 10$) the iron-like geometry shows lower intensity of approximately 0.5 dB.

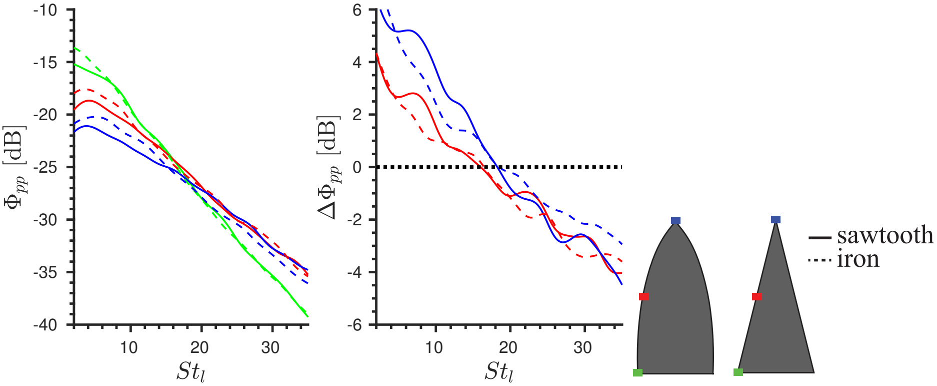

Figure 7.10: (left) Spectra of the wall-pressure fluctuations (Φ_{pp}) at three streamwise locations corresponding to $x/2h = 0$ (green), 0.5 (red), 1 (blue). The continuous and dashed lines represents the sawtooth and the iron-like serrations respectively. (center) $\Delta\Phi_{pp}$ with respect to the root location.

A deeper analysis of Fig. 7.10 suggests that far field noise intensity benefits by both the reduced scattering efficiency due to the serration angle, and by streamwise variation of Φ_{pp} with respect to the root location ($\Delta\Phi_{pp} = \Phi_{pp}^{root} - \Phi_{pp}^{stream}$, where Φ_{pp}^{root} and Φ_{pp}^{stream} are the power spectra intensity at the root location and at the other streamwise points, respectively). As a matter of fact, in the frequency range where the $\Delta\Phi_{pp}$ is larger, the estimated far field noise reduction is higher.

The overall good agreement further confirms that the wall-pressure fluctuations are only dependent on the effective length of the serration and not on the actual shape. These findings support the assumption behind the shaped geometry as discussed in the introduction; the effect of the introduced curvature of the serration edge is to reduce the scattered noise at the trailing edge root by mitigating both the interaction between the two sides of the airfoil and the negative effect induced by the outward and downward flow motions at this location (cfr. Fig. 7.7 and Fig. 7.8) [165]. The new geometry delays this effect downstream where the intensity of the pressure fluctuations is lower, thus contributing less to the far field noise.

7.4.4. DETECTION OF NOISE SOURCE

The above discussion showed that the iron-like trailing edge serration reduces noise in the low frequency range by mitigating noise sources at its root. In order to confirm these considerations, iso-surface of the noise sources, extracted from the FIND methodology, are plotted in Fig. 7.11 and Fig. 7.12 for $St_l = 4$ and 10, respectively [53, 163].

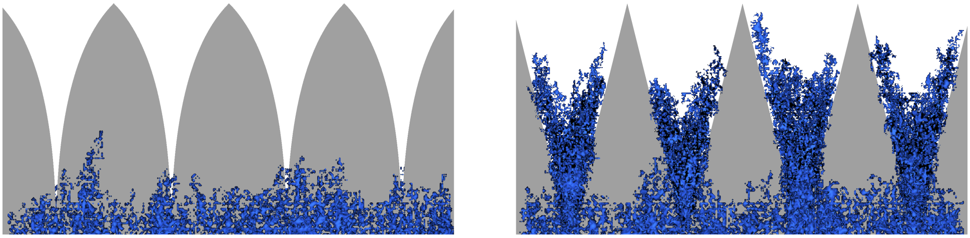

Figure 7.11: Iso-surface of noise sources at $St_l = 4$ ($f = 400$ Hz) for the iron-like (left) and sawtooth (right) trailing edge serrations.

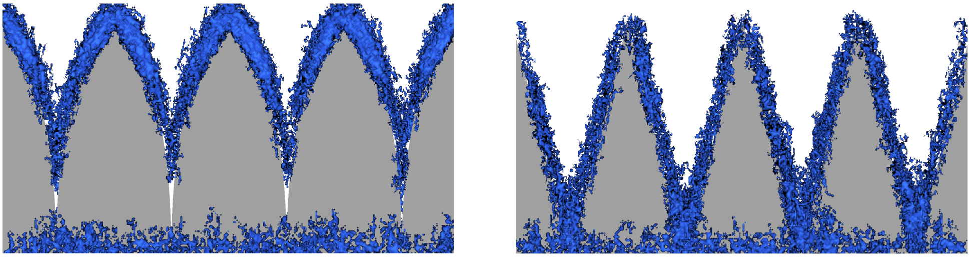

Figure 7.12: Iso-surface of noise sources at $St_l = 10$ ($f = 1000$ Hz) for the iron-like (left) and sawtooth (right) trailing edge serrations.

Fig. 7.11 shows that at low frequency, the sawtooth trailing edge serrations present noise sources between the serrations, near at the root. They are strongly mitigated in presence of the iron-like geometry. As discussed above, this fact can be related to the outward flow motion strongly reduced at the root location and to a more gradual interaction between the flow coming from the two sides of the airfoil. At a higher frequency (Fig. 7.12), noise sources are more uniformly distributed along the edges of the sawtooth serrations. Similarly, as above, the iron-like geometry shows reduced noise sources at the root. In this case, noise sources are stronger and located toward the tip where, as discussed in Sec. 7.4.2, the downward and the outward flow motion are dominant.

7.5. CONCLUSIONS

In this chapter, computations of the flow convecting over a conventional sawtooth and a new iron-like serration geometries were performed using the compressible, transient and explicit Lattice Boltzmann Method. The two investigated geometries had same length and wavelength and were retrofitted to a NACA 0018 airfoil. They were inspected in terms of both far field noise and hydrodynamic field.

The iron-like geometry reduces far field noise more by approximately 2 dB with respect to the conventional sawtooth geometry in the range $5 < St_l < 15$, without modifying the directivity of the noise propagation in the similar frequency range. The analysis of the time-averaged near-wall velocity components shows that the main effect of the proposed geometry is to mitigate both the outward and downward motion near the root of the serration. It results in a less strong interaction between the two sides of the airfoil at the root location and, in a larger effective angle seen by the turbulent flow approaching the edges. On the other hand, stronger outward and downward flow motions are present near the serration tip. However, at this location, the intensity of wall-pressure fluctuations is lower, thus scattering less noise. In order to confirm that the achieved lower far field noise is mainly due to the above mentioned flow effects, the time-averaged wall-pressure fluctuations and their spectra were inspected. It is found that they do not depend on the serration geometry, for a given serration aspect ratio, but they are a function of the streamwise location. This finding confirms that the intensity of the scattered pressure waves depends on the streamwise location. Finally, iso-surfaces of the noise sources confirm that the achieved noise reduction is mainly due to the mitigation of the noise sources at the root location.

EPILOGUE

8

CONCLUSION

The great thing about science is that you can get
it wrong over and over again because what you're after
- call it truth or understanding - waits patiently for you.
Ultimately, you'll find the answer because it doesn't change.

Dudley Herschbach

8.1. INTRODUCTION

HIGH fidelity computational aeroacoustic approaches have been applied in this thesis, for the purpose of predicting noise from wind turbine blades. For a large modern wind turbine, aerodynamic noise from the blades is generally considered to be the dominant noise source, provided that mechanical noise is adequately treated. Most of the aerodynamic blade noise sources, such as tip noise and blunt-trailing-edge noise, can be prevented by good design. Nevertheless, it is now widely accepted that turbulent boundary layer trailing edge noise (subsequently denoted as trailing edge noise) is the dominant noise source for modern large wind turbines. The research objective defined in this thesis was the following:

> *to develop a fast, reliable and accurate computational aeroacoustic methodology to identify, visualize and quantify primary noise sources and their underlying mechanisms on a wind turbine blade with and without noise suppression add-ons.*

In response to this main research objective, it was demonstrated how both incompressible and compressible computational fluid dynamics solutions (Tab. 1.1) can be employed to obtain both qualitative and quantitative descriptions of:

- The aeroacoustic sources (Part I, II & III)
- Aeroacoustic related parameters of a turbulent boundary layer (Part I)
- The predicted far-field acoustic pressure of trailing edge noise (Part II)
- The underlying mechanism of noise suppression add-ons (Part III)

With the obtained knowledge, new noise-suppression add-ons were analyzed, resulting in the optimization of trailing edge serrations (Ch. 7). The conclusions and recommendations for each part of this thesis are summarized below.

8.2. TURBULENT BOUNDARY LAYER

To ensure correct analysis of turbulent boundary layer trailing edge noise, it is important to investigate different governing flow equations and their corresponding solvers, and comment on their accuracy, easiness and effectiveness to generate physically correct turbulent boundary layer characteristics. For example, to force the flow from a laminar state into a turbulent state at a specific position of interest, a boundary layer transition trip is generally used. During more recent experimental campaigns, transition strips were used to match transition locations and boundary layer growth so that similar trailing edge flow characteristics were obtained when comparing, e.g. airfoil noise simulations with acoustical experiments.

Though the flow topology arising from the so-called bypass transition process has been extensively addressed in the past, the motivation for the current study was to understand the properties of simulated transition strips for future aeroacoustic simulations. A staggered grid of cubic blocks for transition was analyzed and compared with a more conventional, zigzag strip using flow results from the Lattice Boltzmann (LB) method. The velocity and pressure field was used to quantitatively visualize the flow topology field around both tripping devices.

The trips were shown to be successful to enforce transition. The observed transition scenario suggested that a zigzag strip is more efficient as a bypass transition process compared to the staggered grid of cubes, since the spanwise vortices were undulated more effectively from the trip. This could have been a result of a larger frontal area of the trip as well as a smaller wavelength of the zig-zag strip. These spanwise instabilities enhances the development of a canonical fully turbulent boundary layer.

Visualizations of the mean flow revealed periodic streamwise streaks behind the transition strips, with the most distinctive streaks being visible behind the staggered grid of cubes. In general, a canonical fully turbulent boundary layer was experienced after $40\delta_0$ for a zig-zag strip, while the staggered grid of blocks needed at least $80\delta_0$ to convergence to a fully developed turbulent boundary layer.

Furthermore, in another study, the prediction of the streamwise and spanwise coherence length of the pressure field below a turbulent boundary layer at low Reynolds number generated using a recycling inflow method, were estimated using different numerical LES models in an open-source Finite Volume based CFD package. Results have been compared to direct numerical simulations and experimental data.

Results for outer scaling mean and fluctuating velocity data were in good agreement with the PIV data, whereas the comparison with the DNS results showed small discrepancies in the viscous sub-layer. The trend of the pressure spectrum was confirmed by the empirical model of Goody, with a slightly faster decay at the higher frequencies.

Regarding the streamwise and spanwise pressure coherence, the spanwise coherence length was significantly smaller than the streamwise coherence length, indicating structures with lower coherence amplitude. For both spatial directions, the decay matched the analytic and reference result at intermediate and high frequencies. A mismatch in the low frequency regime of the coherence length estimation was found between Corcos model and both the numerical and experimental results. A closer look into the spanwise coherence showed that it is mainly limited by its small length and strength relatively to the mesh resolution. Increasing the spanwise mesh resolution enabled a better prediction of the coherent structures at the lower frequencies.

8.3. TRAILING EDGE NOISE

When uncorrelated boundary layers can be physically correctly generated, flow around trailing edges can be investigated. Efficient tools for the determination of trailing edge noise of wind turbine blades are necessary to further optimize and improve noise suppression add-ons, which will further reduce their noise footprint. These simulations should be computational efficient and should be able to capture acoustic sources in both the compact and non-compact regime, as the frequency range of interests covers both regimes. Hence, in this part, viable options for trailing edge noise prediction are discussed.

First, the prediction and computation of non-compact acoustic sources in the vicinity of a trailing edge was studied. Both integral and boundary element methods (BEM) were analyzed, while the latter also predicts the scattered acoustic pressure as well as proper propagation of the sources. The numerical model under consideration was a 25 degrees asymmetric beveled plate. When comparing an integral solution with a BEM with scattering effects, the compact source approximation was found to be valid for low frequencies up until the wavelength-chord ratio $\lambda/l = 1$. The integral solution started to deviate from the BEM when $\lambda/l > 1$. Here, the BEM solution started showing non-compactness by forming different lobes around the trailing edge.

The flow around a plate with an asymmetrically beveled 25° trailing edge was further analyzed by a solution of the fully explicit and transient compressible LB equation. In combination with a Ffowcs-Williams and Hawking (FW-H) aeroacoustic analogy, an estimation of the acoustic radiation in the far field was obtained. To validate the combination of these computational approaches for the prediction of trailing edge noise, a comparison was made between experimental data.

The flow field dynamics show similar trends and compare with a maximum deviation of less than 7% favorably for both the mean velocity field and turbulent fluctuations when compared to the experimental data. The simulations exhibited a slightly thicker boundary layer near the trailing edge, which may be a residual of the conservative thick tripping geometry selected for the simulation. The non-dimensional shedding frequency $St_h = 0.26$ agreed well between experiment and simulation.

Unsteady surface pressure measurements over the edge with the obtuse corner produced spectra for the turbulent boundary layer upstream of the edge and for the separated flow region. The general trends found in the simulated wall-pressure spectra show deviations of less than 2 dB when compared to their experimental counterparts for the broadband noise regime. A peak, originating from the coherent vortex shedding around the trailing edge, was present and similar for both experiment and simulation. At the shedding frequency, simulated and experimental results showed a maximum deviation of 5 dB with the simulated results being lower. Further away, downstream and upstream of the separation point, the wall pressure results were shown to be Reynolds independent for both experimental and numerical results.

Results of the acoustic far-field prediction were compared to acoustic measurements obtained from phased array measurements in combination with two beamforming methodologies. Vortex shedding resulted in a strong narrowband component centered at a fixed Strouhal number in the acoustic spectrum for both the simulation and experiment. Broadband noise was in excellent agreement with a similar maximum deviation of 2 dB as for the surface pressure spectra for $St_h > 0.3$. The typical cardioid-like directivity behavior was found for the acoustic pressure obtained from the FW-H analogy. In conclusion, the comparison between experiment and simulation presented here showed good agreement when compared to similar previous research efforts.

In general, a LB code with FW-H analogy is thus regarded to be sufficiently accurate for trailing edge noise prediction, in particular for broadband noise. Exact reproduction of the experimental conditions is regarded to be the major obstacle for an even closer agreement of the results. The major differences include numerical modeling of the tripping device, finite jet width in the experiment, and discretization of the geometry near the sharp corners.

8.4. NOISE SUPPRESSION ADD-ONS

Understanding and modeling the physics associated with the generation and propagation of trailing edge noise is of paramount importance for the design of more silent wind turbines. In the past, using both experiments and simulations, a serrated trailing edge has been shown to be efficient in reducing trailing edge noise. Although serration are now used quite often on wind turbine blades, the noise reduction mechanism is not fully understood.

Therefore, in this study, the flow topology and noise emission around a teeth, combed teeth and straight edge configuration retrofitted on a NACA 0018 airfoil at zero angle of attack is studied. The flow and pressure fields were analyzed by evaluating the fully explicit, transient, compressible LB equation. The far-field acoustic spectra were obtained from the FW-H integral solution.

The numerical results confirmed that the combed teeth give a larger noise reduction than the standard teeth. Furthermore, the acoustic far-field results and boundary layer characteristics obtained from the simulation of the teeth configuration match earlier experiments. It was hypothesized that the main noise-suppression mechanism, due to the application of the combs, is the change of the angle of the streamlines.

In general, the flow tends to be less three-dimensional and more aligned with the serrated edge, as the mean spanwise velocity component is significantly lower for the combed teeth configuration, resulting in lower vorticity at the tooth edges. Other, more experimental numerical methods, such as the analysis of boundary layer characteristics, surface pressure fluctuations, the individual segment analysis and the flow induced noise detection, revealed that most noise is generated at the root of the teeth rather than the tip. It was also observed that surface pressure fluctuations at low frequencies are dependent on the streamwise location, suggesting a variable intensity of the scattered pressure waves along the streamwise serrated edge.

The analysis of convection velocity and spanwise coherence did not explain the noise-reduction mechanism of the combs.

As previously was observed that most of the noise sources were located at the root of the serration, a shape optimization was proposed. Computations of the flow convecting over a conventional sawtooth and a new iron-like serration geometries were performed using the compressible, transient and explicit LB equation. The two investigated geometries had the same length and wavelength and were, again, retrofitted to a NACA 0018 airfoil. They were inspected in terms of both far field noise and hydrodynamic field.

The iron-like geometry reduced far field noise more by approximately 2 dB with respect to the conventional sawtooth geometry in the range $5 < St_l < 15$, without modifying the directivity of the noise propagation in the similar frequency range.

The analysis of the time-averaged near-wall velocity components showed that the main effect of the proposed geometry is to mitigate both the outward and downward motion near the root of the serration. It resulted in a less strong interaction between the two sides of the airfoil at the root location and, in a larger effective angle seen by the turbulent flow approaching the edges. On the other hand, stronger outward and downward flow motions were present near the serration tip. However, at this location, the intensity of wall-pressure fluctuations was lower, thus scattering less noise.

In order to confirm that the achieved lower far field noise is mainly due to the above mentioned flow effects, the time-averaged wall-pressure fluctuations and their spectra were inspected. It was found that they do not depend on the serration geometry, for a given serration aspect ratio, but they are a function of the streamwise location. This finding confirmed that the intensity of the scattered pressure waves depends on the streamwise location.

Finally, iso-surfaces of the noise sources confirmed that the achieved noise reduction is mainly due to the mitigation of the noise sources at the root location.

8.5. RECOMMENDATIONS

This thesis successfully presented a fast, reliable and accurate computational aeroacoustic methodology to identify, visualize and quantify primary noise sources on a wind turbine blade with and without noise suppression add-ons.

Further post-processing work should be related to further understand the noise reduction mechanism of both conventional and improved noise-suppression add-ons. As the first step has already been employed in Ch. 6, a continuation of the analysis of the same flow and acoustic data is obvious. One could think of:

- An improved version of the segment splitting tool, thereby investigating the instructive and destructive interference between the various parts. This can be obtained by an increasing summation of the segments (1, $1-2$, $1-2-3$, $1-2-3-4$, etc), rather than investigating the parts separately.

- Also the two-point auto- and cross-correlation phase could be further analyzed along the (serrated) edge of the serration, rather than sticking to a streamwise or spanwise direction. In a similar fashion, the coherence has to be determined. When windowing the signal, one could obtain the probability distribution function of the phase to see how dispersive the noise suppression add-ons are. This gives further insight in the instructive and destructive interference.

- Understanding of the wavy shape of the convection velocity could perhaps be obtained by looking at the analytical model of Biot-Savart [26]. This could also give insight in why the combed teeth model has higher convection velocities. Another investigation into the convection velocity could be focused on obtaining the convection velocity in the direction of the mean streamline, rather than sticking to the streamwise or spanwise direction.

The investigation of the near pressure field would benefit from a wavelet analysis [182] to decompose the hydrodynamic and acoustic pressure, assuming they contain the fully turbulent fluctuations and the coherent structures respectively. In this way, the nearly Gaussian background fluctuations are interpreted as acoustic pressure and are decomposed from the intermittent pressure peaks induced by the hydrodynamic components. This methodology could support the idea that the eddy edge interaction is Gaussian in nature, since it is not only related to the geometric interaction, but also to the interaction between two vortical systems. In the straight edge case, there is no vortex at the edge, because of the satisfaction of Kutta condition. On the contrary, for the serrated case, a local vortex along the edge exist which interacts with the boundary layer vortices, creating chaotic waves. If this is true, the combed toothed trailing edge configuration could produce weaker chaotic (hydrodynamic) pressure fluctuations, which would be another prove of larger noise reduction of the combed teeth.

As already mentioned in Ch. 7, the current test-case setup allows one to start an optimization process to further reduce the trailing edge noise. With the knowledge of the various noise reduction mechanisms in mind, new, innovative designs can be proposed, including, for example, new shapes and/or materials.

Finally, the presented CAA approach could be extended to industry related cases, involving cambered airfoils at non-zero angle of attack, high Reynolds numbers ($Re_l > 3 \cdot 10^6$) and improved trailing edge noise suppression devices. Both aerodyamic and aeroacoustic performances should be analyzed and compared to experimental campaigns. This will bring the approaches discussed in this thesis closer to industry.

REFERENCES

[1] F. van den Berg, E. Pedersen, J. Bouma, and R. Bakker. Windfarm perception: Visual and acoustic impact of wind turbine farms on residents. Technical report, University of Groningen, 2008.

[2] E. Maris, P.J.M. Stallen, R. Vermunt, and H. Steensma. Noise within the social context: Annoyance reduction through fair procedures. *Journal of the Acoustical Society of America*, 121(4):2000–2010, 2007.

[3] B. Howe, B. Gastmeier, and N. McCabe. Wind turbines and sound: Review and best practice guidelines. *Canadian Wind Energy Association*, 2007.

[4] H. Hubbard and K. Shepherd. Aeroacoustics of large wind turbines. *Journal of the Acoustical Society of America*, 89(6):2495–2508, 1991.

[5] G. Guidati, J. Ostertag, and S. Wagner. Prediction and reduction of wind turbine noise: An overview of research activities in europe. *18th ASME Wind Energy Symposium*, 0042, 2000.

[6] G. Leventhall and D. Bowdler. *Wind Turbine Noise: How it is produced, progated measured and received.* MultiScience, 2011.

[7] T.F. Brooks, D. Pope, and M. Marcolini. Airfoil self-noise and prediction. Technical report, NASA Reference Publication 1218, 1989.

[8] S. Pröbsting. *Airfoil self-noise - Investigation with Particle Image Velocimetry.* PhD thesis, Delft University of Technology, 2015.

[9] H. Arbey and J. Bataille. Noise generated by airfoil profiles placed in a uniform laminar flow. *Journal of Fluid Mechanics*, 134(33), 1983.

[10] C.J. Doolan, D.J. Moreau, and L.A. Brooks. Wind turbine noise mechanisms and some concepts for its control. *Acoustics Australia*, 40(7), 2012.

[11] W. Blake. *Mechanics of flow-induced sound and vibration, volumes I and II.* Academic Press, 1986.

[12] S. Moreau, M. Roger, and J. Christophe. Flow features and self-noise of airfoils near stall or in stall. *15th AIAA/CEAS Aeroacoustic Conference*, (3198), 2009.

[13] F. White. *Viscous Fluid Flow, 3rd edition.* McGraw-Hill, New York, 2006.

[14] N. Curle. The influence of solid boundaries upon aerodynamic sound. *Proceedings of the Royal Society of London*, 231:505–514, 1955.

[15] J.E. Ffowcs-Williams and L.H. Hall. Aerodynamic sound generation by turbulent flow in the vinictiy of a scattering half plane. *Journal of Fluid Mechanics*, 40(4):657–670, 1970.

[16] R.W. Paterson, P. Vogt, M.R. Vink, and C. Munch. Vortex noise of isolated airfoils. *Journal of Aircraft*, 10(296), 1973.

[17] T.F. Brooks and T.H. Hodgson. Trailing edge noise prediction from measured surface pressures. *Journal of Sound and Vibration*, 78(1):69–117, 1981.

[18] P. Sijtsma. Phased array beamforming applied to wind tunnel and fly-over tests. Technical Report NLR-TR-2010-549, NLR, 2010.

[19] E.C. Nash, M.V. Lowson, and A. McAlpine. Boundary layer instability noise on airfoils. *Journal of Fluid Mechanics*, 382(27), 1999.

[20] J.C. Yu and C.K.W. Tam. Experimental investigation of the trailing edge noise mechanism. *AIAA Journal*, 16(1046), 1978.

[21] D. Violato. *3D flow organization and dynamics in subsonic jets*. PhD thesis, Delft University of Technology, 2013.

[22] S. Oerlemans, P. Sijtsma, and B. Mendez Lopez. Location and quantification of noise sources on a wind turbine. *Journal of Sound and Vibration*, 299(4-5):869–883, 2007.

[23] W. Zhu. *Aero-Acoustic Computations of Wind Turbines*. PhD thesis, Technical University of Denmark, Department of Mechanical Engineering, 2007.

[24] M. Wang, J.B. Freund, and S.K. Lele. Computational prediction of flow-generated sound. *Annual Review of Fluid Mechanics*, 38:483–512, 2006.

[25] T. Colonius and S.K. Lele. Computational aeroacoustics: progress on nonlinear problems of sound generation. *Progress in Aerospace Sciences*, 40:345–416, 2004.

[26] J.H. Ferziger and M. Peric. *Computational Methods for Fluid Dynamics*. Springer, 2002.

[27] S. Succi. *The lattice Boltzmann equation for fluid dynamics and beyond*. Oxford University Press, 2001.

[28] R. Ewert, M. Meinke, and W. Schroder. Computation of aeroacoustic sound via hybrid CFD/CAA-methods. *RTO AVT Symposium on "Ageing Mechanisms and Control"*, pages 1–12, 2001.

[29] M. Wang and P. Moin. Computation of trailing-edge noise at low mach number using LES and acoustic analogy. *Center for Turbulence Research, Annual Research Briefs*, pages 91–106, 1998.

[30] E. Manoha, B. Troff, and P. Sagaut. Trailing edge noise prediction using Large Eddy Simulation and acoustic analogy. *AIAA Journal*, 38(4):575–583, 2000.

[31] B.A. Singer, K.S. Brentner, D.P. Lockard, and G.M. Lilley. Simulation of acoustic scattering from a trailing edge. *Journal of the Acoustical Society of America*, 105(950), 1999.

[32] B.A. Singer, D.P. Lockard, and K.S. Brentner. Computational aeroacoustic analysis of slat trailing-edge flow. *AIAA Journal*, 38(9):1558–1564, 2000.

[33] W. Bechara, C. Bailly, P. Lafon, and S.M. Candel. Stochastic approach to noise modeling for free turbulent flows. *AIAA Journal*, 32(3):455–463, 1994.

[34] C. Bailly, P. Lafon, and S. Candel. A stochastic approach to compute noise generation and radiation of free turbulent flows. *AIAA Journal*, 32(3):455–463, 1994.

[35] G. Kalizin, N. Kalitzin, and A. Wilde. A factorization scheme for RANS turbulence models and SNGR predictions of trailing edge noise. *6th AIAA/CEAS Aeroacoustic Conference*, (1982):1–10, 2000.

[36] C.K.W. Tam. Computational aeroacoustics: An overview of computational challenges and applications. *International Journal of Computational Fluid Dynamics*, 18:547–567, 2004.

[37] W.C.P. van der Velden, J.T. Akhnoukh, and A.H. van Zuijlen. Low order finite-volume based riemann solver for application to aeroacoustic problems. *Journal of Computational Acoustics*, 2017.

[38] W. de Roeck, W. Desmet, M. Baelmans, and P. Sas. On the prediction of near-field cavity flow noise using different CAA techniques. *Proceedings of ISMA*, pages 369–388, 2004.

[39] C.A. Wagner, T. Huttl, and P. Sagaut. *Large-Eddy simulation for Acoustics*. Cambridge, 2007.

[40] C. Schram. A boundary element extension of Curle's analogy for non-compact geometries at low-Mach numbers. *Journal of Sound and Vibration*, 322:264–281, 2009.

[41] R. Ewert and W. Schröder. Acoustic perturbation equations based on flow decomposition via source filtering. *Journal of Computational Physics*, 188:365–398, 2003.

[42] J. Seo and Y. Moon. Perturbed compressible equations for aeroacoustic noise prediction at low Mach numbers. *AIAA Journal*, 43:1716–1724, 2005.

[43] H. Si, W. Shen, and W. Zhu. Effect of non-uniform mean flow field on acoustic propagation problems in computational aeroacoustics. *Aerospace Science and Technology*, 28:145–153, 2013.

[44] J. Sesterhnenn. A characteristic-type formulation of the Navier-Stokes equations for high order upwind schemes. *Computers and Fluids*, 30:37–67, 2001.

[45] S.A. Karabasov and V.M. Goloviznin. New efficient high-resolution method for nonlinear problems in aeroacoustics. *AIAA Journal*, 45(12):2861–1871, 2007.

[46] M.J. Lighthill. On sound generated aerodynamically. part i. general theory. *Proceedings of the Royal Society of London*, 211:564–587, 1952.

[47] J.E. Ffowcs-Williams and D.L. Hawkings. Sound generation by turbulence and surfaces in arbitrary motion. *Philosophical Transactions of the Royal Society of London*, 264:321–342, 1969.

[48] F. Farassat and G. Succi. A review of propeller discrete frequency noise prediction technology with emphasis on two current methods for time domain calculations. *Journal of Sound and Vibration*, 71(3):399–419, 1980.

[49] G.A. Bres, F. Perot, and D. Freed. A Ffowcs Williams-Hawkings solver for Lattice-Boltzmann based computational aeroacoustics. *16th AIAA/CEAS Aeroacoustic Conference*, (3711):1–14, 2010.

[50] D. Casalino. An advanced time approach for acoustic analogy predictions. *Journal of Sound and Vibration*, 261(4):583–612, 2003.

[51] H.S. Ribner. New theory of jet noise generation, directivity and spectra. *Journal of the Acoustical Society of America*, 31:245–246, 1959.

[52] O.M. Phillips. On the generation of sound by supersonic turbulent shear layers. *Journal of Fluid Mechanics*, 9:1–28, 1960.

[53] A. Powell. Theory of vortex sound. *Journal of the Acoustical Society of America*, 36(1):177–195, 1964.

[54] G.M. Lilley. Theory of turbulence generated jet noise: Generation of sound in a mixing region. Technical Report AFAPL-TR-72-53 Volume IV, United States Air Force, 1972.

[55] M.S. Howe. Trailing edge noise at low Mach numbers. *Journal of Sound and Vibration*, 225(2):211–238, 1999.

[56] W. Möhring, E.H. Müller, and F. Obermeier. Problems in flow acoustics. *Review of Modern Physics*, 55:707–724, 1983.

[57] P. Doak. Fluctuating enthalpy as the basic generalized acoustic field. *Theoretical Computational Fluid Dynamics*, 10:115–133, 1998.

[58] T. Lutz, A. Herrig, W. Würz, M. Kamruzzaman, and E. Krämer. Design and wind tunnel verification of low noise airfoils for wind turbines. *AIAA Journal*, 45(4), 2007.

[59] M.S. Howe. Aerodynamic noise of a serrated trailing edge. *Journal of Fluids and Structures*, 5:33–45, 1991.

[60] R. van Rooij and W. Timmer. Roughness sensitivity considerations for thick rotor blade airfoils. *Journal of Solar Energy Engineering*, 125:468–478, 2003.

[61] A. Braslow and E. Knox. Simplified method for the determination of critical height of distributed roughness particles for boundary layer transition at Mach numbers from 0 to 5. Technical Report 4363, NACA TN, 1958.

[62] R. Adrian. Hairpin vortex organization in wall turbulence. *Physics of Fluids*, 19(041301), 2007.

[63] E. Reshotko. Transition issues for atmospheric entry. *45th IAA Aerospace Science Meeting and Exhibit*, (304), 2007.

[64] P.S. Klebanoff and K.T. Tidstrom. Mechanism by which a two-dimensional roughness element induces boundary-layer transition. *Physics of Fluids*, 15(7):1173–1188, 1972.

[65] M. Dalle and L. Meyer. Turbulent convective heat transfer from rough surfaces with two-dimensional rectangular ribs. *International Journal of Heat and Mass Transfer*, 20(6):583–620, 1977.

[66] R.J. Volino, M.P. Schultz, and K.A. Flack. Turbulence structure in a boundary layer with two-dimensional roughness. *Journal of Fluid Mechanics*, 635:75–101, 2009.

[67] C. Lyon, M. Selig, and A. Broeren. Boundary layer trips on airfoils at low Reynolds number. *35th AIAA Aerospace Science Meeting and Exhibit*, (511), 1997.

[68] G. Elsinga and J. Westerweel. Tomographic-PIV measurement of the flow around a zigzag boundary layer trip. *Experiments in Fluids*, 52:865–876, 2012.

[69] L. Erm and P. Joubert. Low-Reynolds number turbulent boundary layers. *Journal of Fluid Mechanics*, 230:1–44, 1991.

[70] S. Leonardi, P. Orlandi, R.J. Smalley, L. Djenidi, and R.A. Antonia. Direct numerical simulations of turbulentchannel flow with transverse squarebars on one wall. *Journal of Fluid Mechanics*, 491:229–238, 2003.

[71] S. Lee and H. Sung. Direct numerical simulation of the turbulent boundary layer over a rod-roughened wall. *Journal of Fluid Mechanics*, 584:125–146, 2007.

[72] J.H. Lee and H.J. Sung. Very-large-scale motions in a turbulent boundary layer. *Journal of Fluid Mechanics*, 673:80–120, 2011.

[73] P. Andersson, M. Berggren, and D. Henningson. Optimal disturbances and bypass transition in boundary layers. *Physics of Fluids*, 11:134–150, 1999.

[74] L. Brandt, P. Schlatter, and D. Henningson. Transition in boundary layer subject to free-stream turbulence. *Journal of Fluid Mechanics*, 517:167–198, 2004.

[75] X. Wu and P. Moin. Direct numerical simulation of turbulence in a nominally zero-pressure gradient flat-plate boundary layer. *Journal of Fluid Mechanics*, 630:5–41, 2009.

[76] D. Lockard, L. Luo, and B.A. Singer. Evaluation of the Lattice-Boltzmann equation solver PowerFLOW for aerodynamic applications. Technical report, NASA Reference Publication 210550, 2000.

[77] A. de Jong and H. Bijl. Airfoil sharp trainling edge aeroacoustics using a Lattice Boltzmann method. *AIAA Workshop on Benchmark problems for Airframe Noise Computations*, 1:103–126, 2010.

[78] F. Perot, M.S. Kim, M. Meskine, and D. Freed. NREL wind turbine aerodynamics validation and noise predictions using a Lattice Boltzmann Method. *18th AIAA/CEAS Aeroacoustic Conference*, (2290):1–13, 2012.

[79] K. Habibi, H. Gong, A. Najafi-Yarzdi, and L. Mongeau. Numerical simulations of sound radiated from internal mixing nozzles with forced mixers using the Lattice Boltzmann Method. *19th AIAA/CEAS Aeroacoustic Conference*, (2143):1–15, 2013.

[80] M. Sanjose, C. Meon, V. Masson, and S. Moreau. Direct numerical simulation of acoustic reduction using serrated trailing-edge on an isolated airfoil. *20th AIAA/CEAS Aeroacoustics Conference*, (2324):1–15, 2014.

[81] W.C.P. van der Velden, S. Pröbsting, A.H. van Zuijlen, A.T. de Jong, Y. Guan, and S.C. Morris. Numerical and experimental investigation of a beveled trailing-edge flow field and noise emission. *Journal of Sound and Vibration*, 384:113–129, 2016.

[82] U. Frisch, D. D'Humiéres, B. Hasslacher, P. Lallemend, Y. Pomeau, and J. Rivet. Lattice gas hydrodynamics in two and three dimensions. *Complex Systems*, 1:649–707, 1987.

[83] P.L. Bhatnagar, E.P. Gross, and M. Krook. A model for collision processes in gases: Small amplitude processes in charged and neutral one-component systems. *Physical Review*, 94(3):511–525, 1954.

[84] S. Chen and G.D. Doolen. Lattice Boltzmann method for fluid flows. *Annual Review of Fluid Mechanics*, 30:329–364, 1998.

[85] J. Preston. The minimum Reynolds number for a turbulent boundary layer and the selection of a transition device. *Journal of Fluid Mechanics*, 3:373–384, 1958.

[86] J. Gibbings. On boundary layer transition wires. Technical Report CP-462, Aeronautical Research Council, 1959.

[87] M. Calaf, C. Meneveau, and J. Meyers. Large eddy simulation of fully developed wind-turbine array boundary layers. *Physics of Fluids*, 22(015110):1–16, 2010.

[88] P. Schlatter and R. Orlu. Assesment of direct numerical simulation data of turbulent boundary layers. *Journal of Fluid Mechanics*, 659:116–126, 2010.

[89] S. Ghaemi and F. Scarano. Counter-hairpin vortices in the turbulent wake of a sharp trailing edge. *Journal of Fluid Mechanics*, 689:317–356, 2011.

[90] S.K. Robinson. Coherent motions in the turbulent boundary layer. *Annual Review of Fluid Mechanics*, 23(1):601–639, 1991.

[91] P.S. Klebanoff, K.T. Tidstrom, and L. Sagent. The three dimensional nature of boundary layer instability. *Journal of Fluid Mechanics*, 12:1–34, 1962.

[92] I. Castro and E. Epik. Boundary layer development after a separated region. *Journal of Fluid Mechanics*, 374:91–116, 1998.

[93] A. Alving and H. Fernholz. Turbulence measurements around a mild separation bubble and downstream of reattachment. *Journal of Fluid Mechanics*, 322:297–328, 1996.

[94] W.C.P. van der Velden, A.H. van Zuijlen, A.T. de Jong, and H. Bijl. Estimation of spanwise pressure coherence under a turbulent boundary layer. *AIAA Journal*, 53(10):3134–3138, 2015.

[95] R.K. Amiet. Noise due to turbulent flow past a trailing edge. *Journal of Sound and Vibration*, 47(3):387–393, 1976.

[96] G. Corcos. The structure of the turbulent pressure field in boundary layer flows. *Journal of Fluid Mechanics*, 18(3):353–378, 1964.

[97] J. Christophe. *Application of hybrid methods to high frequency aeroacoustics*. PhD thesis, Université Libre de Bruxelles, 2011.

[98] S. Pröbsting, M. Tuinstra, and F. Scarano. Trailing edge noise estimation by tomographic Particle Image Velocimetry. *Journal of Sound and Vibration*, 346:117–138, 2015.

[99] S. Pröbsting, F. Scarano, M. Bernardini, and S. Pirozzoli. On the estimation of wall pressure coherence using time-resolved tomographic PIV. *Experiments in Fluids*, 54:1567–1582, 2013.

[100] H. Jasak. *Error analysis and estimation for the Finite Volume Method with applications to fluid flows*. PhD thesis, Imperical College London, 394 p, 1996.

[101] OpenFOAM. *OpenFOAM: The Open Source CFD Toolbox Programmer's Guide*. ESI-Group, 2012.

[102] R.I. Issa. Solution of the implicitly discretised fluid flow equations by operator-splitting. *Journal of Computational Physics*, 62:40–65, 1986.

[103] M. Germano, U. Piomelli, P. Moin, and W. Cabot. A dynamic subgrid-scale eddy viscosity model. *Physics of Fluids*, 3(7):1760–1765, 1991.

[104] P. Sagaut, E. Montreuil, and O. Labbé. Assessment of some self-adaptive SGS models for wall bounded flows. *Aerospace Science and Technology*, 6:335–344, 1999.

[105] J. Boris, F. Grinstein, E. Oran, and R. Kolbe. New insights into Large Eddy Simulation. *Fluid Dynamics Research*, 10(4-6):199–229, 1992.

[106] T. Lund, X. Wu, and K. Squires. Generation of turbulent inflow data for spatially-developing boundary layer simulations. *International Journal of Computational Physics*, 140(2):233–258, 1998.

[107] D. Palumbo. Determining correlation and coherence lengths in turbulent boundary layer flight data. *Journal of Sound and Vibration*, 331(16):3721–3737, 2012.

[108] S. Pirozzoli. Generalized conservative approximations of split convective derivative operators. *Journal of Computational Physics*, 229(19):7180–7190, 2010.

[109] M. Bernardini and S. Pirozzoli. Wall pressure fluctuations beneath supersonic turbulent boundary layers. *Physics of Fluids*, 23(8):85–102, 2011.

[110] J. Österlund. *Experimental studies of zero-pressure gradient turbulent boundary-layer flow.* PhD thesis, KTH Stockhold, Sweden, 2000.

[111] P. Welch. The use of fast fourier transform for the estimation of power spectra; a method based on time averaging over short modified periodograms. *IEEE Trans Audo Electroacoustics*, 15(2):70–73, 1967.

[112] M. Goody. Empirical spectral model of surface pressure fluctuations. *AIAA Journal*, 42(9):1788–1794, 2004.

[113] B. Efimtsov. Characteristics of the field of turbulent wall pressure fluctuations at large Reynolds numbers. *Sov Phys Acoustics*, 28(4):289–292, 1982.

[114] W.C.P. van der Velden, A.H. van Zuijlen, A.T. de Jong, and H. Bijl. Acoustic non-compactness of a beveled trailing edge using incompressible flow source data. *AIAA Journal*, 2017.

[115] D.W. Shannon and S.C. Morris. Experimental investigation of a blunt trailing edge flow field with application to sound generation. *Experiments in Fluids*, 41(5):777–788, 2006.

[116] D. Casalino and M. Barbarino. Stochastic method for airfoil self-noise computation in frequency domain. *AIAA Journal*, 49:2453–2469, 2011.

[117] D. Lockard. An efficient, two dimensional implementation of the Ffowcs-Williams and Hawkings equation. *Journal of Sound and Vibration*, 229(4):897–911, 2000.

[118] T. Takaishi, M. Miyazawa, and C. Kato. A computational method of evaluating noncompact sound based on vortex sound theory. *Journal of the Acoustical Society of America*, 121(3):1353–1361, 2007.

[119] LMS-SYSNOISE. LMS SYSNOISE rev 5.6, computational vibro-acoustics, on-line user's manual. *LMS International NV, Interleuvenlaan 68, Leuven, Belgium*, 2002.

[120] P.W. Bearman. Investigation of flow behind a two-dimensional model with a blunt trailing edge and fitted with splitter plates. *Journal of Fluid Mechanics*, 21:241–255, 1965.

[121] M.E. Greenway and C.J. Wood. The effect of a beveled trailing edge on vortex shedding and vibration. *Journal of Fluid Mechanics*, 61:323–335, 1973.

[122] P. Spalart. Numerical simulation of boundary layers: Part 1. weak formulation and numerical method. Technical report, NASA Reference Publication 882222, 1986.

[123] D.W. Shannon and S.C. Morris. Trailing edge noise measurements using a large aperture phased array. *International Journal of Aeroacoustics*, 7(2):147–176, 2008.

[124] Y. Guan, S. Pröbsting, D. Stephens, A. Gupta, and S. C. Morris. On the wake flow of asymmetrically beveled trailing edges. *Experiments in Fluids*, pages 57–78, 2016.

[125] M. Wang and P. Moin. Computation of trailing-edge flow and noise using Large-Eddy simulation. *AIAA Journal*, 38(12):2201–2209, 2000.

[126] M. Wang. Computation of trailing-edge aeroacoustics with vortex shedding. *Center for Turbulence Research, Annual Research Briefs*, pages 379–388, 2005.

[127] W.C.P. van der Velden, A.H. van Zuijlen, A.T. de Jong, and H. Bijl. On the aeroacoustic properties of a beveled plate. *E3S Web of Conferences, 2nd Symposium on OpenFOAM in Wind Energy, Boulder*, 5(04001):1–11, 2015.

[128] W.C.P. van der Velden, A.H. van Zuijlen, A.T. de Jong, and H. Bijl. Noise estimation of beveled trailing edges using an integral and boundary element method. *54th AIAA Aerospace Sciences Meeting*, (260):1–10, 2016.

[129] D. Casalino, A.F.P. Ribeiro, E. Fares, and S. Nolting. Lattice-Boltzmann Aeroacoustic Analysis of the LAGOON landing-gear configuration. *AIAA Journal*, 52(6):1232–1248, 2014.

[130] P.T. Lew, A. Najafi-Yarzdi, and L. Mongeau. Numerical simulation of sound from flow over an airfoil with a blunt trailing edge. *16th AIAA/CEAS Aeroacoustic Conference*, (3879):1–20, 2010.

[131] S. Pröbsting, M. Zamponi, S. Ronconi, Y. Guan, S. C. Morris, and F. Scarano. Vortex shedding noise from a beveled trailing edge. *International Journal of Aeroacoustics*, pages 1–19, 2016.

[132] T.J. Mueller, D.F. Scharpf, S.M Batill, R.B. Strebinger, C.J Sullivan, and S. Subramanian. The design of a subsonic low-noise, low-turbulence wind tunnel for acoustic measurements. *17th AIAA/CEAS Aeroacoustic Conference*, (3883):1–14, 1992.

[133] M.J. Bilka, S.C. Morris, C. Berntsen, J.C. Silver, and D.W. Shannon. Flow field and sound from a blunt trailing edge with varied thickness. *AIAA Journal*, 52(1):52–61, 2014.

[134] Y. Guan, C. R. Berntsen, M. J. Bilka, and S. C. Morris. The measurement of unsteady surface pressure using remote microphone probe. *Journal of Visualized Experiments*, page 1, 2016.

[135] T.F. Brooks and W.M. Humphreys. A deconvolution approach for the mapping of acoustic sources (DAMAS) determined from phased microphone arrays. *Journal of Sound and Vibration*, 294:856–879, 2006.

[136] R. Amiet. Refraction of sound by a shear layer. *Journal of Sound and Vibration*, 58:467–482, 1978.

[137] H. Chen. Extended Boltzmann kinetic equation for turbulent flows. *Science*, 301(5633):633–636, 2003.

[138] B. Crouse, D. Freed, M. Senthooran, S. Ullrich, and S. Fertl. Analysis of underbody windnoise sources on a production vehicle using a Lattice Boltzmann scheme. *SAE Technical Paper*, 2400(2007), 2007.

[139] R.H. Kraichnan. Pressure fluctuations in turbulent flow over a flat plate. *Journal of the Acoustical Society of America*, 28(3):378–390, 1956.

[140] J.E. Ffowcs-Williams. Hydrodynamic noise. *Annual Review of Fluid Mechanics*, 1:197–222, 1969.

[141] P. Költzsch. *Strömungsmechanisch erzeugter Lärm*. PhD thesis, Technische Universität Dresden, 1974.

[142] M. Roger and S. Moreau. Extensions and limitations of analytical airfoil broadband noise models. *International Journal of Aeroacoustics*, 9(3):273–305, 2010.

[143] S. Oerlemans and P. Sijtsma. Determination of absolute levels from phased array measurements using spatial source coherence. Technical report, National Aerospace Laboratory NLR, 2002.

[144] A. Oberai, F. Roknaldin, and T. Hughes. Trailing edge noise due to turbulent flows. 02-002, Boston University, 2002.

[145] R. Ewert and W. Schröder. On the simulation of trailing edge noise with a hybrid LES/APE method. *Journal of Sound and Vibration*, 270:509–524, 2004.

[146] W.C.P. van der Velden and S. Oerlemans. Numerical analysis of noise reduction mechanisms on improved trailing edge serrations using the Lattice Boltzmann method. *35th ASME Wind Energy Symposium*, pages 1–15, 2017.

[147] S. Oerlemans. Reduction of wind turbine noise using blade trailing edge devices. *22nd AIAA/CEAS Aeroacoustics Conference*, (3018), 2016.

[148] M.S. Howe. Noise produced by a sawtooth trailing edge. *Journal of the Acoustical Society of America*, 90:482–7, 1991.

[149] A.G.M. Dassen, R. Parchen, J. Bruggeman, and F. Hagg. Results of a wind tunnel study on the reduction of airfoil self-noise by the application of serrated blade trailing edges. *Proceeding of the European Union Wind Energy Conference and Exhibition*, pages 800–803, 1996.

[150] M. Gruber, P.F. Joseph, and M. Azarpeyvand. An experimental investigation of novel trailing edge geometries on airfoil trailing edge noise reduction. *19th AIAA/CEAS Aeroacoustic Conference*, (2011), 2013.

[151] S. Oerlemans, P. Sijtsma, and B. Mendez Lopez. Reduction of wind turbine noise using optimized aifoils and trailing-edge serrations. *AIAA Journal*, 47:1470–1481, 2009.

[152] R. Parchen, W. Hoffmans, A. Gordner, and K. Braun. Reduction of airfoil self-noise at low Mach number with a serrated trailing edge. *International Congress on Sound and Vibration*, pages 3433–3440, 1999.

[153] W.C.P. van der Velden, A.H. van Zuijlen, and D. Ragni. Flow topology and noise emission around straight, serrated and slitted trailing edges using the Lattice Boltzmann methodology. *22nd AIAA/CEAS Aeroacoustics Conference*, (3021), 2016.

[154] C. Arce-León, F. Avallone, D. Ragni, and S. Pröbsting. PIV investigation of the flow past solid and slitted sawtooth serrated trailing edges. *54th AIAA Aerospace Sciences Meeting*, (1014), 2016.

[155] C. Arce-León, R. Merino-Martínez, D. Ragni, F. Avallone, and M. Snellen. Boundary layer characterization and acoustic measurements of flow-aligned trailing edge serrations. *Experiments in Fluids*, 57(182), 2016.

[156] F. Avallone, S. Pröbsting, and D. Ragni. Three-dimensional flow field over a trailing-edge serration and implications on broadband noise. *Physics of Fluids*, 28:1–20, 2016.

[157] M. Azarpeyvand, M. Gruber, and P.F. Joseph. An analytical investigation of trailing edge noise reduction using novel serrations. *19th AIAA/CEAS Aeroacoustic Conference*, (2009), 2013.

[158] S. Pröbsting, J. F. Schneiders, F. Avallone, D. Ragni, C. Arce-León, and F. Scarano. Trailing-edge noise diagnostics with low-repetition-rate tomographic PIV. *22nd AIAA/CEAS Aeroacoustics Conference*, (3023), 2016.

[159] B. Lyu, M. Azarpeyvand, and S. Sinayoko. Prediction of noise from serrated trailing edges. *Journal of Fluid Mechanics*, 793:556–588, 2016.

[160] B. Lyu, M. Azarpeyvand, and S. Sinayoko. A trailing-edge noise model for serrated edges. *21st AIAA/CEAS Aeroacoustics Conference*, (2362):1–24, 2015.

[161] L.E. Jones and R.D. Sandberg. Acoustic and hydrodynamic analysis of the flow around an aerofoil with trailing edge serrations. *Journal of Fluid Mechanics*, 706:295–322, 2012.

[162] R. Arina, R. Della Ratta Rinaldi, A. Iob, and D. Torzo. Numerical study of self-noise produced by an airfoil with trailing-edge serrations. *18th AIAA/CEAS Aeroacoustic Conference*, (2184), 2012.

[163] A. Mann, M.S. Kim, J. Wu, F. Perot, J. Grilliat, M.C. Jacob, and M. Colman. Airfoil tip leakage aeroacoustics predictions using a Lattice Boltzmann based method. *22nd AIAA/CEAS Aeroacoustics Conference*, (2825):1–17, 2016.

[164] C. Arce-León, D. Ragni, S. Pröbsting, F. Scarano, and J. Madsen. Flow topology and acoustic emissions of trailing edge serrations at incidence. *Experiments in Fluids*, 57(91), 2016.

[165] T.P. Chong and A. Vathylakis. On the aeroacoustic and flow structures developed on a flat plate with a serrated sawtooth trailing edge. *Journal of Sound and Vibration*, 354:65–90, 2015.

[166] M. Gruber, P.F. Joseph, and T.P. Chong. Experimental investigation of airfoil self noise and turbulent wake reduction by the use of trailing edge serrations. *16th AIAA/CEAS Aeroacoustic Conference*, (3803):1–23, 2010.

[167] Q. Bouvy, T. Rougier, A. Ghouali, D. Casalino, J. Appelbaum, and C. Kleinclaus. Design of quieter landing gears through lattice-boltzmann cfd simulations. *21st AIAA/CEAS Aeroacoustics Conference*, (3529):1–21, 2015.

[168] F. Avallone, W.C.P. van der Velden, and D. Ragni. Benefits of concave serrations on broadband trailing-edge noise reduction. *Journal of Sound and Vibration*, 2017.

[169] D.J. Moreau and C.J. Doolan. Noise-reduction mechanism of a flat-plate serrated trailing edge. *AIAA Journal*, 51:2513–22, 2013.

[170] T.P. Chong and P.F. Joseph. Airfoil self noise reduction by non-flat plate type trailing edge serrations. *Applied Acoustics*, 74:607–13, 2013.

[171] M. Gruber, P.F. Joseph, and T.P. Chong. On the mechanisms of serrated airfoil trailing edge noise reduction. *17th AIAA/CEAS Aeroacoustic Conference*, (2781):1–23, 2011.

[172] M. Gruber. *Airfoil noise reduction by edge treatments*. PhD thesis, University of Southampton, 2012.

[173] F. Avallone, S. Pröbsting, K.P. Lynch, and D. Ragni. Tomographic-piv investigation of the flow over serrated trailing-edges. *54th AIAA Aerospace Sciences Meeting*, (1012):1–14, 2016.

[174] M. Drela. Xfoil: An analysis and design system for low reynolds number airfoils. *Springer Berlin Heidelberg*, pages 1–12, 1989.

[175] H. Clemons and R.W. Wlezien. Modification of flow structures associated with broadband trailing edge noise. *46th AIAA Fluid Dynamics Conference*, (3627):1–18, 2016.

[176] M. Herr and W. Dobrzynski. Experimental investigations in low-noise trailing edge design. *AIAA Journal*, 43:1167–75, 2005.

[177] T.P. Chong, A. Vathylakis, P.F. Joseph, and M. Gruber. Self-noise produced by an airfoil with nonflat plate trailing-edge serrations. *AIAA Journal*, 51:2665–77, 2013.

[178] P.M.H.W. Vijgen, F.G. Howard, D.M. Bushnell, and B.J. Holmes. Serrated trailing edges for improving lift and drag characteristics of lifting surfaces. Technical report, US 5088665 A, 1989.

[179] S. Oerlemans. Arrangement to reduce noise of a wind turbine rotor blade. Technical report, EP2851553 A1, 2015.

[180] I. Wygnanski, P. Tewes, H. Kurz, L. Taubert, and C. Chen. The application of boundary layer independence principle to three-dimensional turbulent mixing layers. *Journal of Fluid Mechanics*, 675:336–46, 2011.

[181] R.W. Wlezien and V. Kibens. Passive control of jets with indeterminate origins. *AIAA Journal*, pages 1263–70, 1986.

[182] S. Grizzi and R. Camussi. Wavelet analysis of near-field pressure fluctuations generated by a subsonic jet. *Journal of Fluid Mechanics*, 698:93–124, 2012.

APPENDIX

A

VARIABLES FOR ACOUSTICS

A near-field pressure signal can be considered as a combination of acoustic fluctuations and an hydrodynamic or pseudo-sound contribution induced by the eddy structures. We assume that the hydrodynamic contribution is related to local eddies, while the acoustic counterpart is given by the more weaker, but more homogeneous fluctuations. Hence, sound waves, or acoustic waves, can be defined as fluctuations build up from usually weak pressure p_a, velocity u_a and/or density waves ρ_a in a compressible fluid and can travel in each direction. In air, the local pressure deviation, further denoted as sound pressure, can be measured using a microphone. The SI unit is in Pascal (Pa). Its intensity (W/m^2), the energy flux transmitted per unit area by the propagation of sound, is defined as:

$$I = p_a u_a. \tag{A.1}$$

The sign of the intensity is dependent on the direction of propagation. The sound intensity is related to the pressure through its specific acoustic impedance $\rho_0 c_0$. When definining the effective pressure amplitude as $p_e = \left(\overline{p_a^2}\right)^{1/2}$, i.e. the root-mean-square of p_a, the intensity for pure plane harmonic waves can be rewritten as:

$$I = \frac{p_e^2}{\rho_0 c_0}. \tag{A.2}$$

To extract the sound power P (W) from a source, the intensity is integrated over the surface S with outward normal $\mathbf{n}$ as:

$$P = \int_S I \cdot \mathbf{n} \, \mathrm{d}S \tag{A.3}$$

It is difficult to plot this parameter as the range can vary significantly; e.g. from the threshold until the deafening of hearing. Therefore, often a decibel scale is used, commonly known as the Sound Pressure Level (SPL) in (dB):

$$SPL = 20 \log_{10}\left(\frac{p_e}{p_{ref}}\right), \tag{A.4}$$

with p_{ref} defined as 20 μPa. SPL is usually defined per chosen frequency band, with the bandwidth varying from constant bandwidth to, e.g. one-third octave or one-tenth decade bands. The Overall Sound Pressure Level ($OASPL$) is effectively an integration of all bands, resulting in a single value for each SPL plot.

In a similar way, the Intensity Level (IL) is defined in a decibel scale:

$$IL = 10\log_{10}\left(\frac{I}{I_{ref}}\right), \tag{A.5}$$

with $I_{ref} = 10^{-12}\ W/m^2$. Finally, the Sound Power Level (SWL) can be written in decibel scale using:

$$SWL = 10\log_{10}\left(\frac{P}{P_{ref}}\right), \tag{A.6}$$

with $P_{ref} = 10^{-12}\ W$.

B

SAMPLING FOR AEROACOUSTICS

As aeroacoustic approaches require high fidelity flow source data in both spatial and temporal resolution, it is important that one proper sample its data. Some key criteria are given in this appendix.

INITIAL TRANSIENT PHASE

It is important that one start proper sampling their data after the initial transient phase has been removed. As guidance, different criteria are given for when starting sampling seems to be appropriate:

1. Consider to use the lift and drag coefficient as the convergence factor and start sampling once you meet your selected criterion. This means that:

   $$t_{start} \text{ if } \Delta C_L \text{ or } \Delta C_D < \epsilon, \tag{B.1}$$

   with C_L and C_D being the lift and drag coefficient respectively. ϵ would be set at the desired convergence level for a small interval.

2. For any compressible simulation, start sampling after 6 total reflections throughout your entire computational domain. This could mitigate the adverse effects of numerical noise generated during initialization and lead to cleaner spectra. Hence:

   $$t_{start} \leq \frac{6L}{c}, \tag{B.2}$$

   with L the length of the computational domain and c the speed of sound.

3. A sufficient number of flow passes over the object of interest are required before sampling. From previous experience, consider at least 10 flow passes:

   $$t_{start} \leq \frac{10l}{u_\infty}, \tag{B.3}$$

   with l the length of the object of interest, e.g. the airfoil chord and u_∞ the undisturbed flow speed.

4. The initial field set in the computational domain should be fully removed. Hence, allow one flow pass throughout the entire domain:

$$t_{start} \le \frac{L}{u_{\infty}}, \tag{B.4}$$

Please note that all criteria should be fulfilled before starting sampling. Therefore consider the most conservative one (i.e. largest t_{start}).

SAMPLING RATE AND TIME

The temporal resolution is further based on the selection of sampling rate, taken into account the Nyquist criterion ($2f_{max}$). It should be able to capture all frequency ranges of interest, i.e. f_{max}. However, if memory allows, oversample by a factor of three or four ($3\ 4f_{max}$) to improve the resolution. Likely, the upper bound of your simulation is either dependent on your local grid size with respect to the acoustic wavelength (for the LBM simulations in this thesis at least 16 voxels per wavelength were used) or on the background noise levels due to the undisturbed flow.

The lower bound of the spectrum is dependent of the duration of the sampling. In general, the more data, the more accurate the result at low frequencies. From previous experience, consider at least 20 flow passes over the object for converged spectra up to object based Strouhal numbers of $St_l = 2$. This is lowest frequency of interest when dealing with trailing edge noise problems.

C

STATISTICAL DATA ANALYSIS

STATISTICAL data analysis is often applied in this thesis work. Below, the most important relations are given in summary to understand the process. For simplicity, the variable A is taken as general variable along the various statistical calculations.

REYNOLDS DECOMPOSITION

For any statistical analysis of boundary layers often the flow variable A is decomposed into a time average part, $\overline{A}$ and a fluctuating part $A\prime$. This is known as the Reynolds decomposition and can be performed for any variable;

$$A(\mathbf{x},t) = \overline{A}(\mathbf{x}) + A\prime(\mathbf{x},t). \tag{C.1}$$

with $\mathbf{x}$ the spatial location vector and t the time dependency. For further calculations in this section, the spatial location is only used whenever needed.

MEAN

The time averaged part is commonly known as the mean. It is the first category of a statistical calculation and will reduce a time series to a single value:

$$\text{mean}(A) = \frac{1}{N}\sum_{j=0}^{N-1} A(t_j) \tag{C.2}$$

with N the total number of temporal samples and j the time increment.

VARIANCE

For turbulence measurements, the time history of flow variables contain a lot of information about the random processes occuring in the flow. The variance, known as the second category of a statistical calculation provides this information by looking at the spread of the distribution around the mean. It is defined as:

$$\mathrm{var}(A) = \frac{1}{N}\sum_{j=0}^{N-1}\left[\left(A(t_j) - \mathrm{mean}(A)\right)^2\right] \tag{C.3}$$

Furthermore, the standard deviation is defined as the positive root of the variance:

$$\mathrm{stdev}(A) = \sqrt{\frac{1}{N}\sum_{j=0}^{N-1}\left[\left(A(t_j) - \mathrm{mean}(A)\right)^2\right]} \tag{C.4}$$

This calculation is commonly called the RMS, or root-mean-square value, and can be assigned to the fluctuating part of the Reynolds decomposition.

COVARIANCE

The covariance of two signals is the mean of the product of the fluctuations of each signal around its mean. If we consider A to be variable one, and B to be variable two, one can write:

$$\mathrm{cov}(A,B) = \frac{1}{N}\sum_{j=0}^{N-1}\left[\left(A(t_j) - \mathrm{mean}(A)\right)\left(B(t_j) - \mathrm{mean}(B)\right)\right] \tag{C.5}$$

CORRELATION

If the degree of dependence it interested between the two signals, the correlation coefficient can be employed. The correlation coefficient is defined as the covariance between the two signals, normalized by the standard deviation of each signal separately:

$$\mathrm{corr}(A,B) = \frac{\mathrm{cov}(A,B)}{\mathrm{stdev}(A)\mathrm{stdev}(B)} \tag{C.6}$$

The auto-correlation and cross-correlation calculations are statistical functions, mostly used to describe the variation of a signal (auto) or two signals (cross) as a function of the time separation between any two time values. The relation for cross-correlation is defined as:

$$\begin{aligned}\mathrm{crosscorr}(B,A) = \frac{1}{N-|m|}\sum_{j=max(0,-m)}^{min(N-1,N-1-m)} & \left[\left(A(t_{j+m}) - \mathrm{mean}(A)\right)\right. \\ & \left.\left(B(t_j) - \mathrm{mean}(B)\right)\right],\end{aligned} \tag{C.7}$$

with

$$\begin{aligned} m &= -N/2+1, -N/2+2, ..., N/2-1, N/2, \text{when } N \text{ is even} \\ m &= -N/2, -N/2+1, ..., N/2-1, N/2, \text{when } N \text{ is odd.}\end{aligned}$$

In a similar way, the auto-correlation can be written as: $\mathrm{autocorr}(A) = \mathrm{crosscorr}(A,A)$.

SPECTRAL DENSITY

Many analyses performed in this thesis are with respect to frequency, and not with respect to time. A Fourier series represents the time series using a summation of cosines and sines, preceded by complex value coefficients. Each cosine or sine forms a mode of a particular frequency, and can be determined using the following relation:

$$F_k = \frac{1}{N}\sum_{j=0}^{N-1} A(t_j)e^{-i2\pi k t_j/P}, \tag{C.8}$$

with i denoting the imaginary number, k the mode index and $P = N\Delta t$ the period of the signal. This is determined using the commonly used fast Fourier transform algorithm (FFT), assuming constant Δt and 2^n sampling. The $e^{-i2\pi k t_j/P}$ term can be rewritten in a term including cosines and sines. Now the auto power spectrum, defined as the contribution to the power from a single mode, is determined by:

$$\mathrm{power}_k(A) = |F_k|^2 \tag{C.9}$$

In a similar fashion, the cross spectrum can be determined using the product of two Fourier transforms (F_k and G_k). The conjugate is applied to the transform of the primary variable, to ensure consistency with the idea of using the second signal as a reference.

$$\mathrm{cross}_k(B,A) = G_k^* \cdot F_k \tag{C.10}$$

It is often useful to represent the power spectrum for a smaller number of modes. The purpose is to present a smoother, or more averaged, solution of the power spectrum. This is accomplished by averaging the spectra using a series of windows. In general, in this thesis, a Hamming window with 50% is used [111].

COHERENCE

The coherence, or coherence squared function, is a statistical calculation defined by the squared magnitude of the cross spectrum of two signals, divided by the power spectrum of both signals at each frequency. It is a real-valued calculation and only reported for positive frequencies:

$$\mathrm{coh}_k(A,B) = \frac{|\mathrm{cross}_k(B,A)|^2}{\mathrm{power}_k(A)\cdot \mathrm{power}_k(B)} \tag{C.11}$$

The coherence is sometimes defined as the positive square root of the above formula.

ACKNOWLEDGEMENTS

In science one tries to tell people,
in such a way as to be understood by everyone,
something that no one ever knew before.
But in poetry, it's the exact opposite

Paul Dirac

So hence, let's also be tried to be understood in this chapter. This thesis marks the ending of a four-year journey in which I developed myself from MSc to PhD. It has been a time in which I met an enormous number of people ranging from the best people in the field of research, to colleagues turning into life-long buddies. Don't think a journey to become a doctor goes without any frustration. There are times in which you feel lonely, there are times in which you try to investigate new things but miserably fail, and there are times in which your expectations do not fulfill the outcome. Whenever you find yourself doubting how far you can go, just remember how far you have come. Remember everything you have faced, all the battles you have won, and all the fears you have overcome. For the rest, rely on the help and support of your family, girlfriend, friends and supervisors, which I also frequently did during those four years.

"A drunk mind speaks a sober heart" is a saying often attributed to French Enlightenment philosopher Jean-Jaques Rousseau, himself quite a drunk. The idea is that when we are drunk we lose our inhibitions and allow ourselves to verbalize our true thoughts and feelings. I would therefore suggest you to read the next paragraphs with a bottle of Bourbon, as most parts are also written with it ;-)!

I will start with my two buddies and already old colleagues; Rogier and Kyle. One married and started a living in Munich, another one still hopping around in the US. However, there is no week without contact and no three to six months without a visit. I know, we are all three globetrotters, we have all three (I must say almost) a PhD in aerodynamics and we all like to hang out in a bar, but still, what is the chance you will find such good friends at work? I should thank you both for your critical advises; both personal as work related, it helped me structuring my life and to start off with my PhD. Furthermore, I want to thank you both for the various trips we made during, but also after the PhD. Although I don't prefer another 29 hours' bus drive in Sumatra (which by the way should have taken only 13 hours) consorting my body to the surroundings, it is alright for me to let the sunburn be faster than the motorbike next time. See you soon guys.

There is no complete PhD party group without further acknowledging Koen and Jan. I enjoy the nights and travels with you guys, it always gives an extra spark of entertaining during the (work) trips. I can't find other friends with similar work-live-party balance then you two. Good luck with the last parts of your PhD. Have a good one!

More research related, although soon escalated into more study elusive activities, I found two Italian compagni, Daniele and Francesco. Sure, everyone knew we started to have research meetings when my PhD was coming to an end. However, it positively affected 100% of this PhD thesis. I am very grateful for all the high-level discussions and assistance, especially the ones ending late night in bars! Saluti gentlemen and I hope you guys will once show me Italy :-)

Credits and thanks to Arjen, Roberto, Stefan and Carlos; it was a real pleasure to work with you guys on various aeroacoustic topics. Many of our interesting (off course at work) and fun conversations (often accompanied with beer on a exotic place on earth) led to direct input of my PhD thesis, I am really thankful for that!

Of course, there were several other great colleagues which deserve to be mentioned. Just to mention a few (yes in alphabetical order): Beppe, David, Dhruv, Giuseppe, Illias, Iya, Jacopo, Liesbeth, Martin, Mustafa, Rakesh, Shaafi, Theo, Thijs, Tiago, Vahid and Valeria. Work was much more fun with you around.

Furthermore, I want to give credits to both Colette and Nico for taking care of a lot of stuff which I should have done myself. They were always willing to assist and helped me with a lot of organizational matters. And besides that, they were always in the mood for a nice talk.

I would also would like to take this opportunity to thank my master students that I got to work with during my time as PhD candidate; Michel, Jurriaan, Jaap and Pranav, it has been a pleasure to work with all of you. You guys kept me sharp which directly affected the quality of my PhD thesis.

You could think, if you would stop reading now, that work-related friends were the only ones which kept me alive during those four years. Nothing is farther from the truth. Let me alone mention my travel soul mate Diederick, which (luckily) kept me away from work during the endless trips over the entire globe. For example, I enjoyed the two months of back-backing in Myanmar and the Philippines, traveling to terrific good (and bad) places. Let alone the shorter holidays (here I consider the definition of two weeks or less) to the US and Iceland, or the visit to Paris to enjoy one of the best performers. Even a regular Saturday at home was not safe anymore since we decided to try out all coffee bars and restaurants. Thanks for keeping me alive!

There are more good friends I must thank for their support. When I think about good quality talks, drinks, food and fun I think about mornings with coffee, afternoons with beer, evenings with the galloping gourmet cooking club and nights with scotch and Cuban cigars. A wonderful life which kept me busy during the weekends. Thanks, Darryll, Jasper and Oscar.

I also should thank my best buddies from field-hockey, not only for the last four years but almost for my entire 20 years of playing. While sport is an excellent tool for getting rid of the hassle at work, I would consider a team sport to be even more important as it provides important lessons on personal values and creates friendships. For both first and second half of the match, there was always a third half which usually lasted hours longer than planned. And not only on the pitch, also outside the pitch parties and festivals were planned. Thanks, Olivier, David, Wesley, Luc, Ruud, Tim en Michiel.

Finally, I would like to conclude with a message to my dear family and girlfriend, who always stood by my side. As we will all grow older, we will grow closer, no matter what happens in the future!

Wouter Cornelis Pieter van der Velden
Delft, December 2016

CURRICULUM VITÆ

Wouter Cornelis Pieter VAN DER VELDEN

24-04-1989	Born in Rotterdam, the Netherlands.

EDUCATION

2001–2007	Pre University Education (VWO NG + NT) Scholengemeenschap Spieringshoek, Schiedam, the Netherlands *Thesis:* Medical Ultrasonography
2007–2010	Bachelor of Science (BSc) in Aerospace Engineering Delft University of Technology, Delft, the Netherlands *Thesis:* Design of a competitive VTOL business aircraft
2010–2012	Honours track in Bio-mechanical Engineering Design Delft University of Technology, Delft, the Netherlands *Thesis:* Design and prototyping of an improved biopsy punch
2010–2012	Master of Science (MSc) in Aerodynamics Delft University of Technology, Delft, the Netherlands *Thesis:* Numerical investigation of an upper airway in a patient suffering from stridor
2013–2017	Doctor of Philosophy (PhD) in Aeroacoustics Delft University of Technology, Delft, the Netherlands Siemens Wind Power, Brande, Denmark *Thesis:* Computational aeroacoustic approaches for wind turbine blade noise prediction *Promotor:* Prof. dr. ir. drs. H. Bijl

LIST OF PUBLICATIONS

JOURNAL PAPERS

6. F. Avallone, **W.C.P. van der Velden**, D. Ragni, *Benefits of concave serrations on broadband trailing-edge noise reduction*, Journal of Sound and Vibration, *under consideration*, (2017).

5. **W.C.P. van der Velden**, A.H. van Zuijlen, A.T. de Jong, H.Bijl, *Acoustic non compactness of a beveled trailing edge using incompressible flow source data*, AIAA Journal, *in press*, (2017).

4. **W.C.P. van der Velden**, J.T. Akhnoukh, A.H. van Zuijlen, *Low order finite-volume based Riemann solver for application to aeroacoustic problems*, Journal of Computational Acoustics, *in press*, (2017).

3. **W.C.P. van der Velden**, S. Pröbsting, A.H. van Zuijlen, A.T. de Jong, Y. Guan, S.C. Morris, *Numerical and experimental investigation of a beveled trailing-edge flow field and noise emission*, Journal of Sound and Vibration, **384**, 113-29 (2016).

2. **W.C.P. van der Velden**, A.H. van Zuijlen, A.T. de Jong, C.T. Lynch, L.H. Hoeve, H.Bijl, *Acoustic simulation of a patient's obstructed airway*, Computer Methods in Biomechanics and Biomedical Engineering, **19**, 2, 144-58 (2016).

1. **W.C.P. van der Velden**, A.H. van Zuijlen, A.T. de Jong, H.Bijl, *Estimation of spanwise pressure coherence under a turbulent boundary layer*, AIAA Journal, **53**, 10, 3134-38 (2015).

CONFERENCE PAPERS

9. R. Merino-Martinez, **W.C.P. van der Velden**, F. Avallone, D. Ragni, *Acoustic measurements of a wind turbine cambered airfoil with flow-misaligned serrations in a closed wind tunnel test section*, 7th International Conference on Wind Turbine Noise, Rotterdam, the Netherlands, *in press*, (2017).

8. **W.C.P. van der Velden**, S. Oerlemans, *Numerical analysis of noise reduction mechanisms on improved trailing edge serrations using the Lattice Boltzmann method*, 35th ASME Wind Energy Symposium, Grapevine, TX, USA, (2017).

7. **W.C.P. van der Velden**, A.H. van Zuijlen, D. Ragni, *Flow topology and noise emission around straight, serrated and slitted trailing edges using the Lattice Boltzmann methodology*, 22nd AIAA/CEAS Aeroacoustic Conference, Lyon, France, 3021 (2016).

6. **W.C.P. van der Velden**, *BANC IV Workshop - Trailing edge noise emission from a DU96 airfoil*, 22nd AIAA/CEAS Aeroacoustic Conference, Lyon, France, (2016).

5. **W.C.P. van der Velden**, A.H. van Zuijlen, A.T. de Jong, H. Bijl, *Noise estimation of beveled trailing edges using an integral and boundary element method*, 54th AIAA Aerospace Sciences Meeting, San Diego CA, USA, 0260 (2016).

4. **W.C.P. van der Velden**, S. Pröbsting, A.T. de Jong, A.H. van Zuijlen, Y. Guan, S.C. Morris, *Numerical and experimental investigation of a beveled trailing edge flow and noise field*, 21st AIAA/CEAS Aeroacoustic Conference, Dallas TX, USA, 2366 (2015).

3. **W.C.P. van der Velden**, A.H. van Zuijlen, A.T. de Jong, H.Bijl, *On the noise prediction of a serrated DU96 airfoil using the Lattice Boltzmann Method*, 6th International Conference on Wind Turbine Noise, Glasgow, United Kingdom, 692-702 (2015).

2. **W.C.P. van der Velden**, A.H. van Zuijlen, A.T. de Jong, H.Bijl, *On the aeroacoustic properties of a beveled plate*, E3S Web of Conferences, 2nd Symposium on OpenFOAM in Wind Energy, Boulder, CO, USA, **5**, 04001 (2015).

1. **W.C.P. van der Velden**, A.H. van Zuijlen, A.T. de Jong, H.Bijl, *On the estimation of spanwise pressure coherence of a turbulent boundary layer over a flat plate*, ECFD VI: 6th European Conference on Computational Fluid Dynamics, Barcelona, Spain (2014).